AN ANALYSIS OF RESISTIVITY SURVEYS AT NORRIS HOT SPRINGS

by Janet L. Peterson

Butte, Montana

March 1, 1983

TABLE OF CONTENTS

TABLE OF FIGURES

TABLE OF FIGURES CONTINUED

LITHOLOGY

The geology in the area of study, Figure 2, is summarized from a map in the Billings Geological Society Guidebook, Volume 11, Plate 1, by Adretta and Alsup, and from a map by Vitaliano and others published by the Geological Society of America. Lithology consists mainly of quartzofeldspathic gneiss with thin Quaternary alluvium covering the topographic lows. Approximately a mile west of Norris, Tertiary volcanics outcrop about a quarter of a mile south of Hot Springs Creek. Small outcrops of hornblende gneiss and ultramafic intrusives occur near the volcanics. About a mile furthur to the west lies the Tobacco Root Batholith.

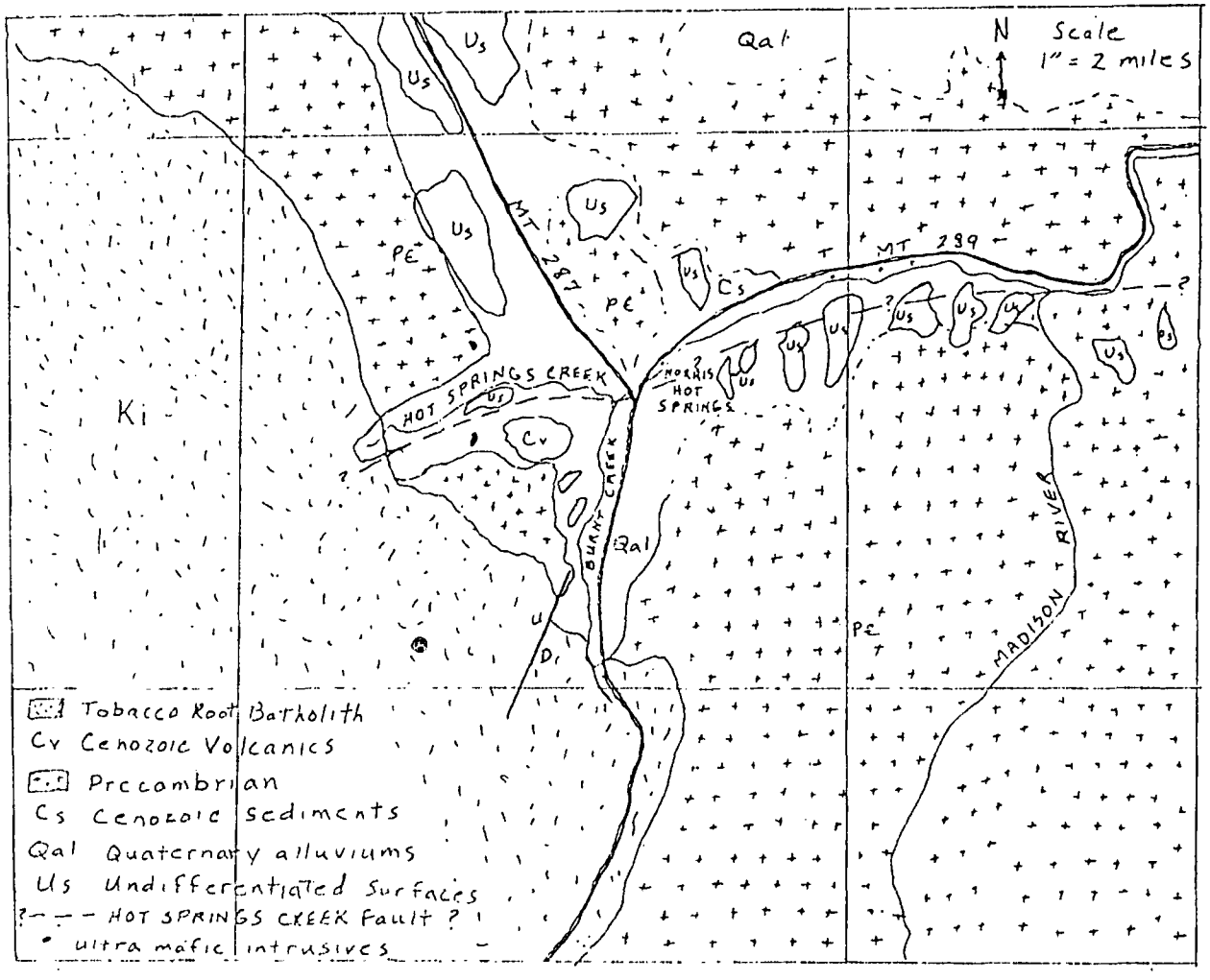

Figure 2. Generalized Geology of Norris Hot Springs area, adapted from Andretta, Vitaliano, and others.

STRUCTURAL GEOLOGY

Structures generally trend north to northwest in the area with Norris Hot Springs lying over a northwesterly plunging anticline (Chadwick and Leonard, 1979). The anticline may be obliquely intersected by a fault, which is speculated to follow Hot Springs Creek (Andretta, ibid.). The fault/anticline contact may be the pathway used by the hot water (Chadwick, ibid.), which forms geothermal seepages at Norris Hot Springs.

A normal fault (Vitaliano, et. al., ibid.) is located about a mile south of the Tertiary volcanics and intersects an arm of the Tobacco Root Batholith's eastern extension into the Madison Valley.

GEOPHYSICAL BACKGROUND

Previous studies of Norris Hot Springs were made by Robert A. Chadwick and others, 1978. A shallow Wenner array electrical sounding was interpreted by Chadwick to delineate a low of 30 ohm-meters at 20 meters of depth roughly circular around Hot Springs Creek. At 100 meters of apparant depth the area lessens in extent, elongates in the northeast direction, and increases in resistivity to 50 ohm-meters.

A hammer seismic survey (Chadwick, ibid.), with penetration to about 70 meters of depth began at a well, which bottoms at 23 meters in granitic gneiss, and was profiled in the east-north-east direction over the low. A resulting seismic pattern of velocities is interpreted by Chadwick to show alluvium up to about 30 meters deep underlain by what is probably granitic and mafic gneiss respectively. The thickest alluvium is at the array center and is directly underlain by the mafic rock.

ELECTRICAL SURVEYS

In the summer of 1982, resistivity measurements in the area were made using a symmetrical Schlumberger array with a portable transmitter and receiver. Figure 3 shows the locations of fourteen soundings in the Norris geothermal area.

Five soundings at half spreads of less than 50 meters will aid in determining resistivities of outcropping rocks for correlation. Six soundings at half spreads of 300 to 1000 meters will help delineate the geographical extent and possibly the depth limit of the geothermal area and may help locate a possible source. Two soundings at half spaces of 100 meters were obtained at desired locations, but were limited in extent because of physical access or restraints. These will be useful in correlation of the data and somewhat in delineation of the area.

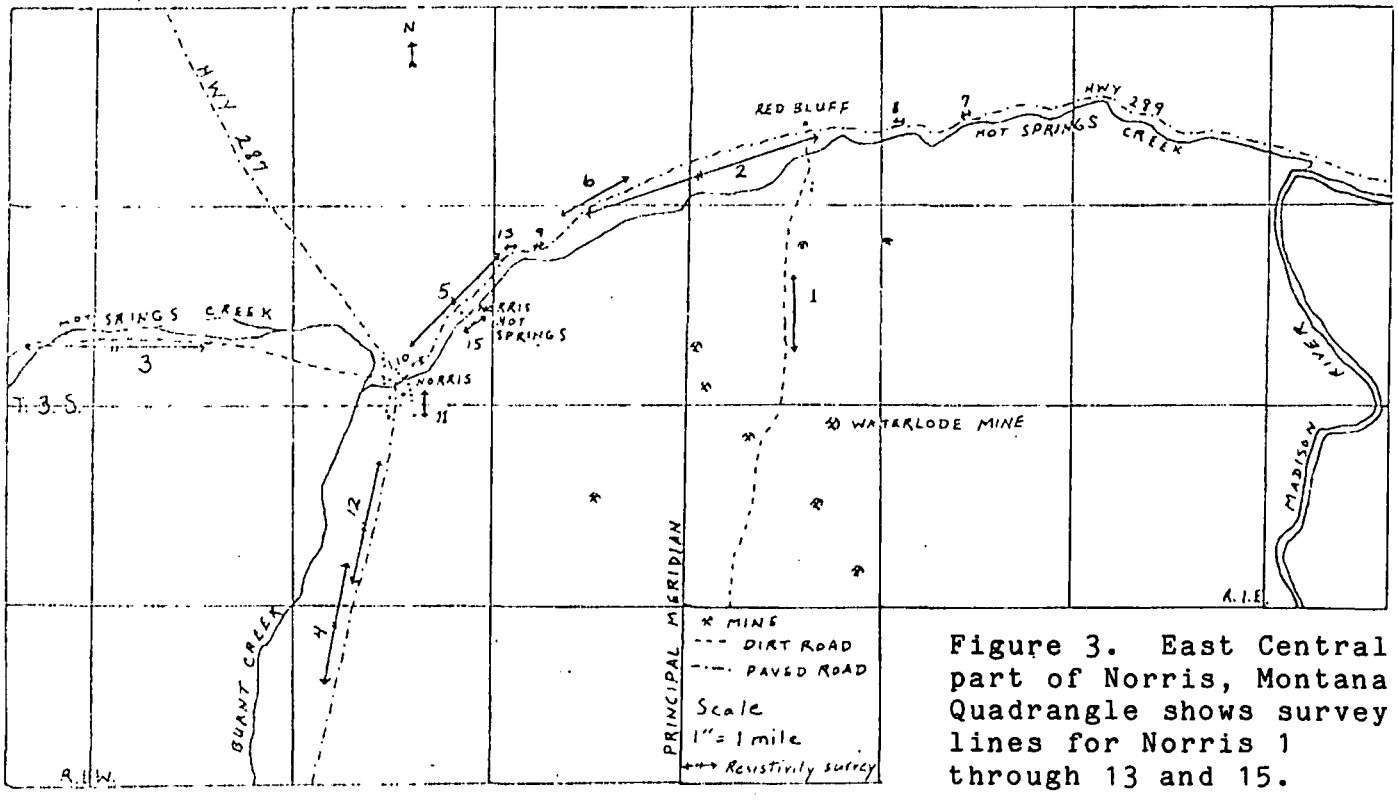

Figure 3. East Central part of Norris, Montana Quadrangle shows survey lines for Norris 1 through 13 and 15.

INTERPRETATION METHODS

Field data was interpreted using forward modeling by computer methods. A resistivity and depth are given for each layer as deduced from a log-log plot of field data. The first two layers are based on curve matching methods, the other layers are estimated. Resistivity and depth are varied until a curve, which best fits the data points, is produced.

Figures 4 through 17 are computer plotted curves of the fourteen resistivity surveys. The x's are the field data points and the curved line is the computer simulated match based on the layer resistivities and thicknesses listed in the upper right hand corner of the graph. Due to the limits of the plotting programs some curves show a basement thickness of 0.00, which means no basement thickness was given to compute the curve and implies an infinite thickness.

Various combinations of resistivities and thicknesses can produce similar curves because the parameter constant used to compute the curve is resistivity times thickness. However, resistivity contrasts, which are evident from the changes in the curve, are relatively valid. There are conductive layers between more resistive layers in most of these curves or a bottoming out of the conductive layer in other curves, due to limited depth probing.

GENERAL INTERPRETATION

Curves one and two are modeled on data taken east of the Hot Springs. Both indicate a high-low-high resistivity pattern, as shown in Figures 4 and 5 Norris one is a north-south array, while Norris two is along the north side of Hot Springs Creek.

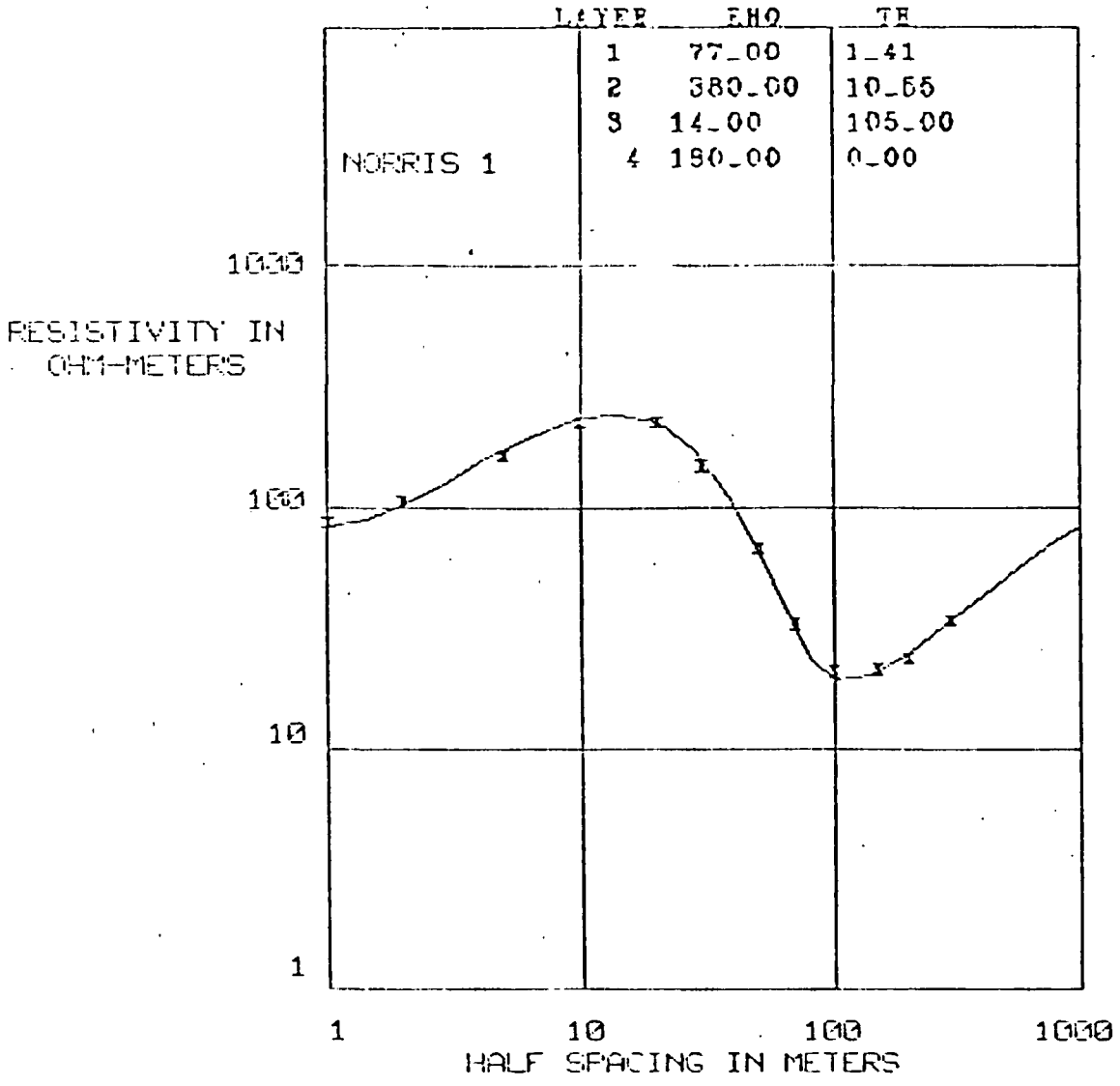

Figure 4. Norris one - the field data points are x's. The smooth curve is simulated by computer using the layer data in the upper right hand corner.

Norris one shows a thicker but more resistive low than Norris two. The suspected fault (Andretta, ibid.) or shear zone along the Hot Springs creek is possibly a cause of the conductive layer in Norris two. Warm water may ascend along a fracture zone and then percolate laterally through alluvial sediments.

The conductive layer of Norris one is more difficult to explain as Norris one is situated not over alluvium but over highly elevated metamorphic rocks. Norris one lies near inactive mines, an indication of mineral enrichment, which may be the result of hydrothermal alteration due to ascending waters along fracture zones.

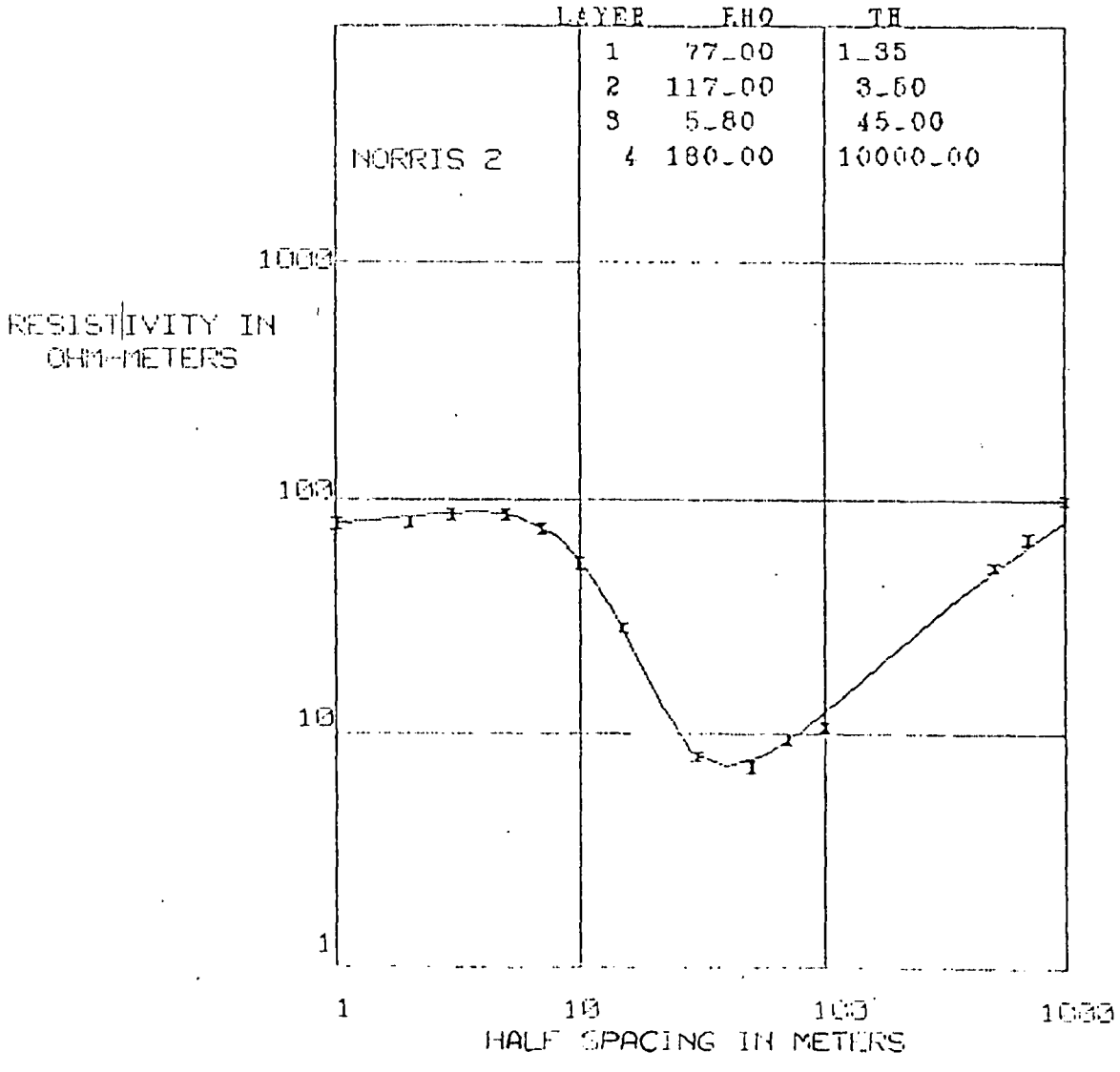

Figure 5. Norris two - the field data points are x's. The smooth curve is simulated by computer using the layer data in the upper right hand corner.

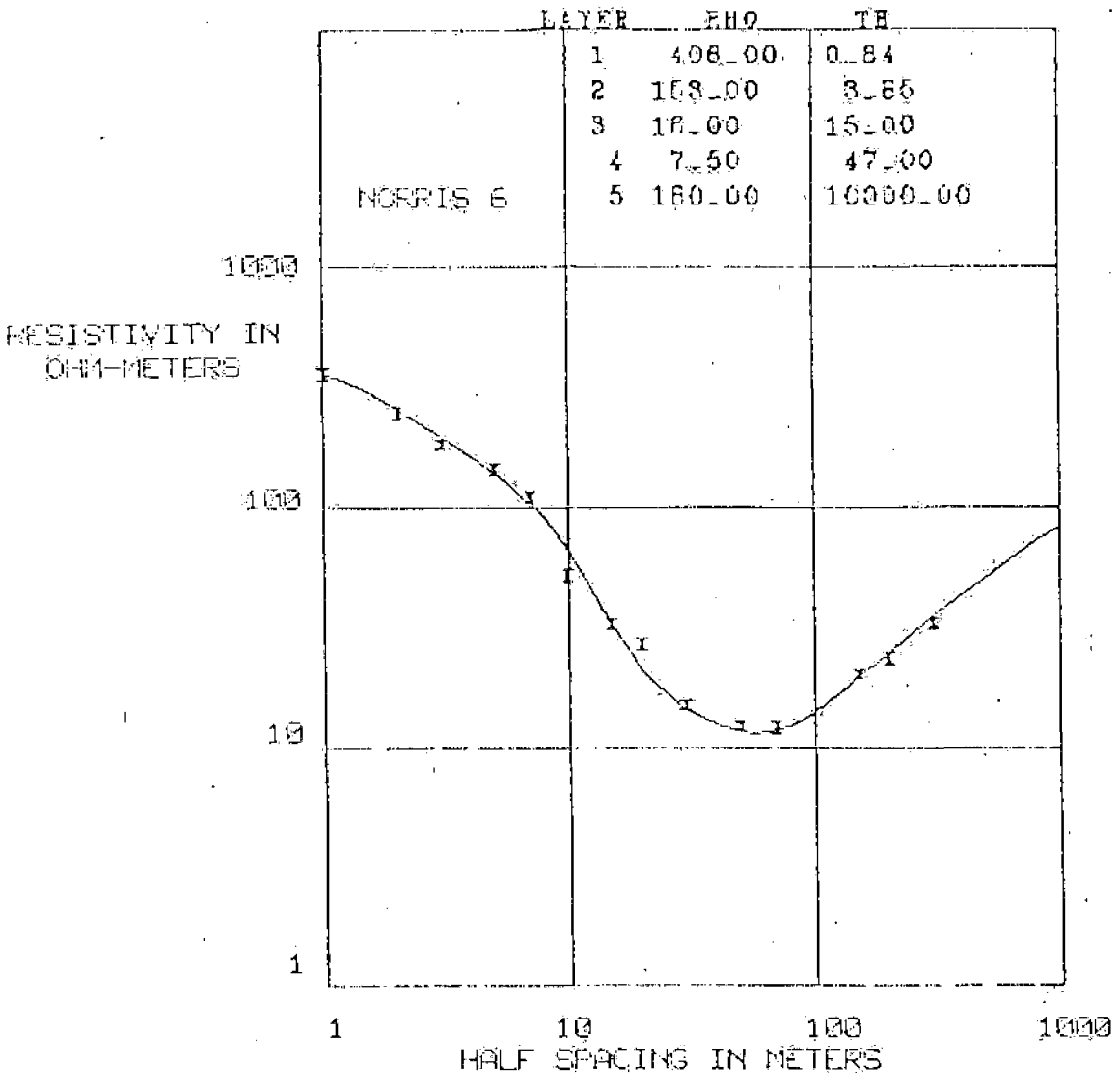

Figure 6. Norris six - the field data points are x's. The smooth curve is simulated by computer using the layer data in the upper right hand corner.

Norris six, shown in Figure 6, is across Highway 289 from Norris two. The conductive layer is slightly thinner and more resistive than found in Norris two, but definitely exists. The similar low furthur supports a probable shear zone along which hot water may ascend to saturate the alluvium and lower the resistivity.

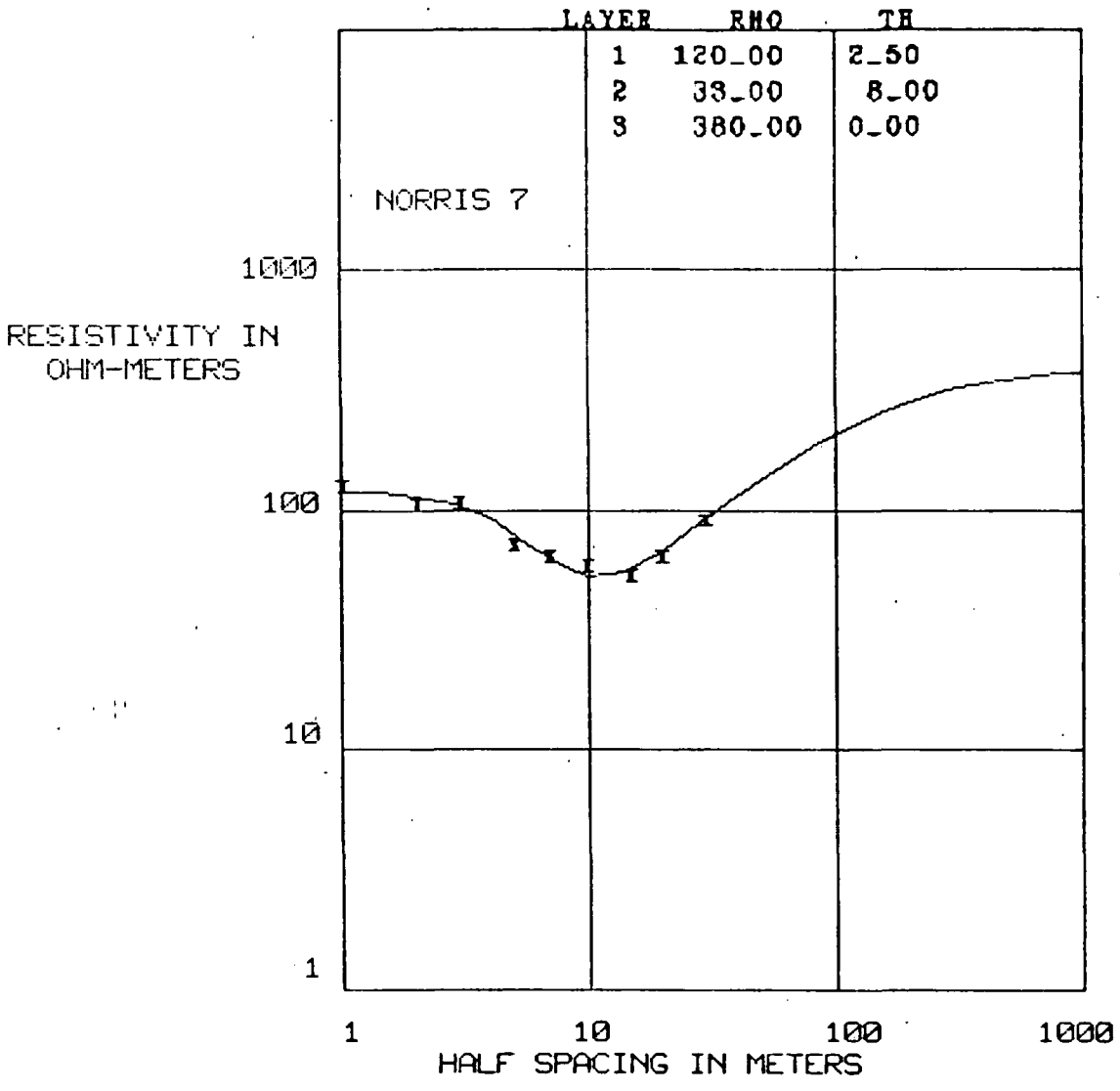

Figure 7. Norris seven - the field data points are x's. The smooth curve is simulated by computer using the layer data in the upper right hand corner.

The shallow resistivity curves, Figures 7 through 11, indicate three ranges of resistivities. Shallow alluvium, which varies in resistivity, a type layer of about 180 ohm-meters, and a third type layer of about 380 ohm-meters.

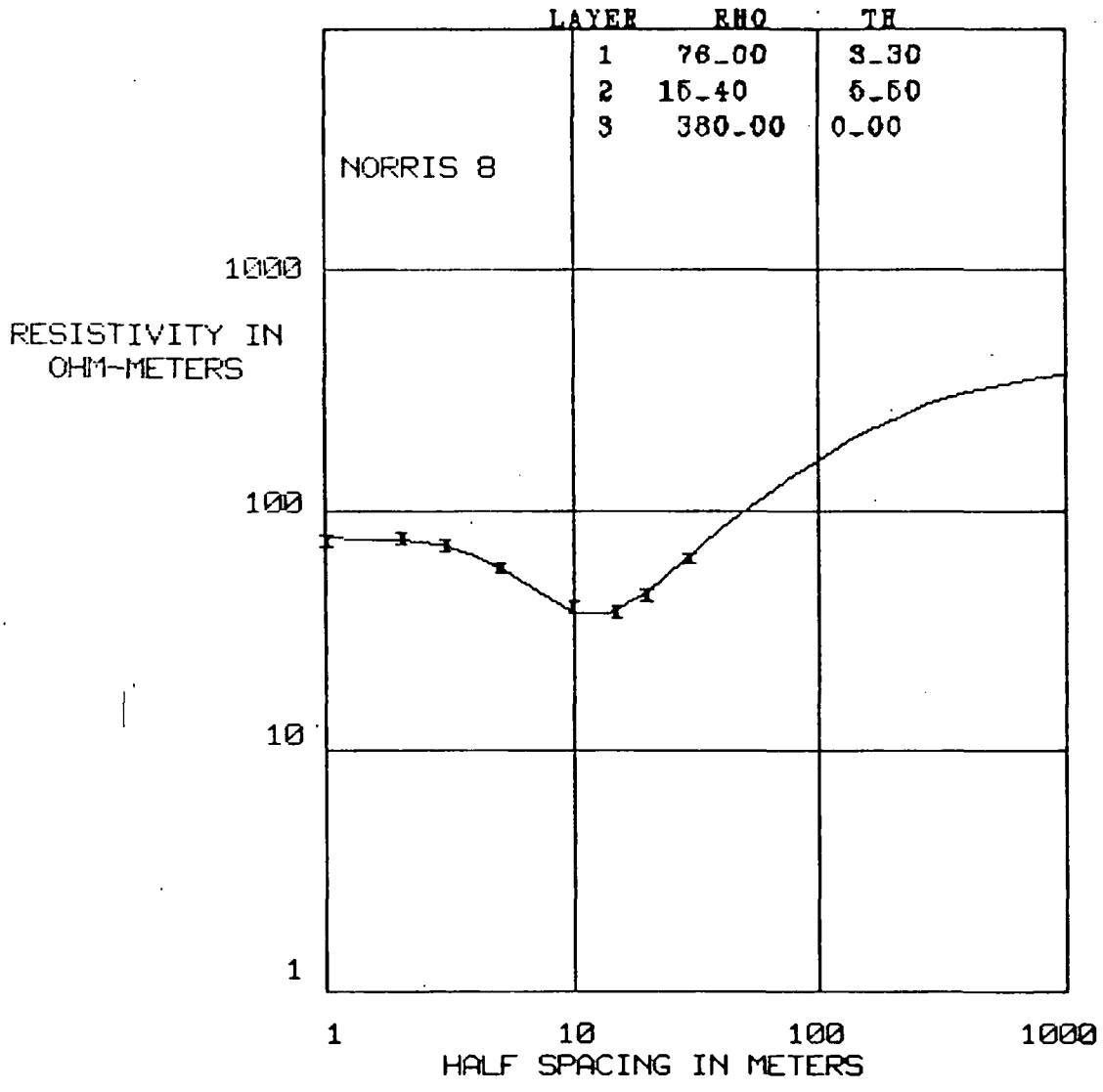

Figure 8. Norris eight - the field data points are x's. The smooth curve is simulated by computer using the layer data in the upper right hand corner.

Norris seven and eight show a layer about eight meters in thickness of 30 ohm-meter and 15 ohm-meter material respectively, which may be warm water saturated or altered alluvium. Beneath these layers, resistivity increases to around 380 ohm-meters.

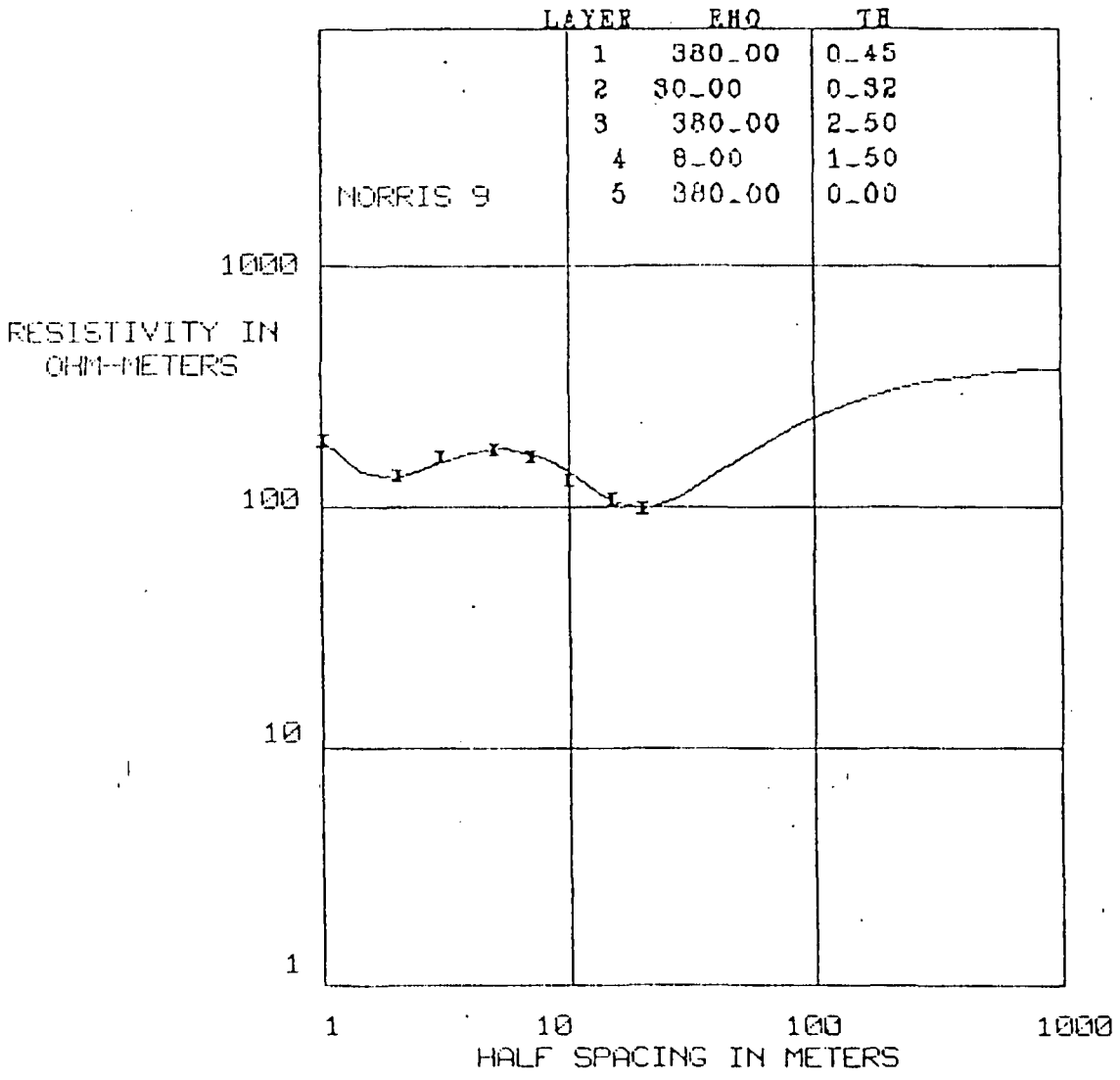

Figure 9. Norris nine - the field data points are x's. The smooth curve is simulated by computer using the layer data in the upper right hand corner.

Norris nine and thirteen, being next to each other, produce complimentary curves. Norris nine is assumed to turn up, but, because it was measured to a twenty meter depth, the actual data points only show an asymptotic low. A thin conductive layer between the 380 ohm-meter layers may be a localized zone of hydrothermal alteration or possibly a vein or lens.

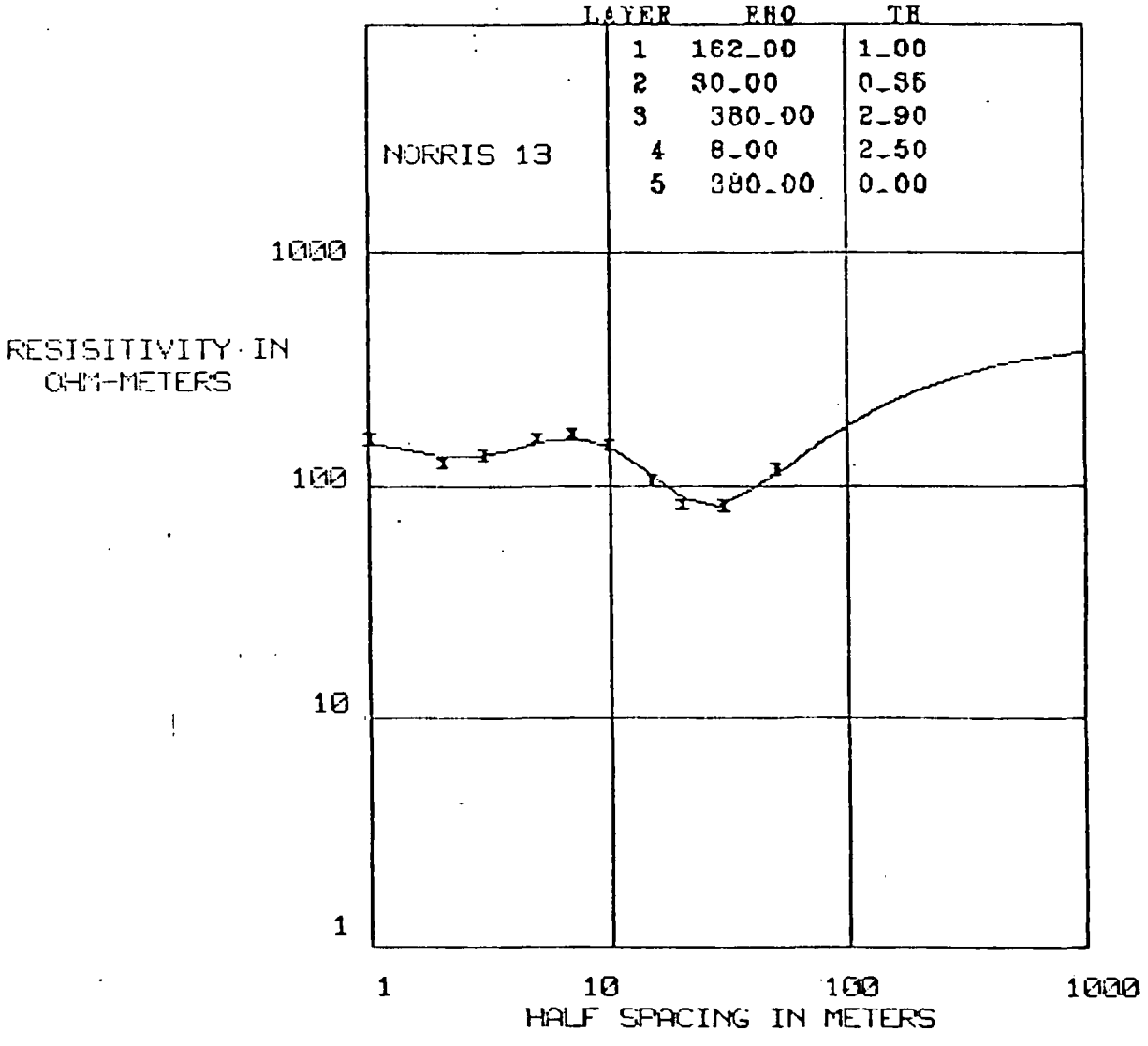

Figure 10. Norris thirteen - the field data points are x's. The smooth curve is simulated by computer using the layer data in the upper right hand corner.

Norris ten shows a 380 ohm-meter layer with a gradual decline in resistivity to about 160 ohm-meters, which may indicate the contact between the two types of metamorphic rocks interpreted by the seismic velocity findings of Robert A. Chadwick mentioned in the geophysical history section on page 3.

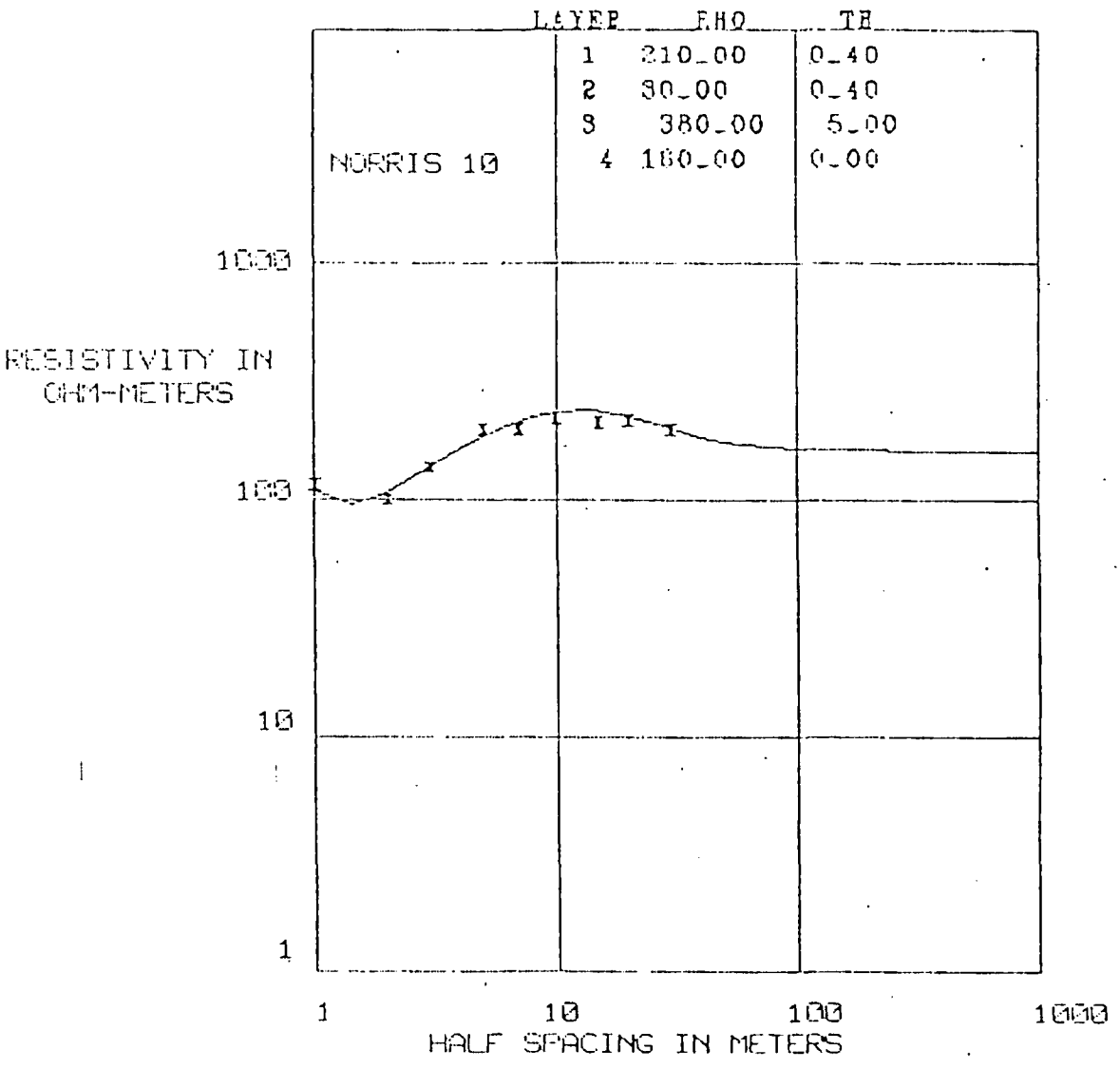

Figure 11. Norris ten - the field data points are x's. The smooth curve is simulated by computer using the layer data in the upper right hand corner.

Norris five, shown in Figure 3, lies between Norris ten and thirteen directly across Highway 289 from Norris Hot Springs. A matched curve for Norris five (see Figure 12) shows two adjacent layers of intermediate resistance with higher resistivities above and below them. The sounding was centered approximately over the anticlinal feature (Chadwick and Leonard, 1979) shown in Figure two.

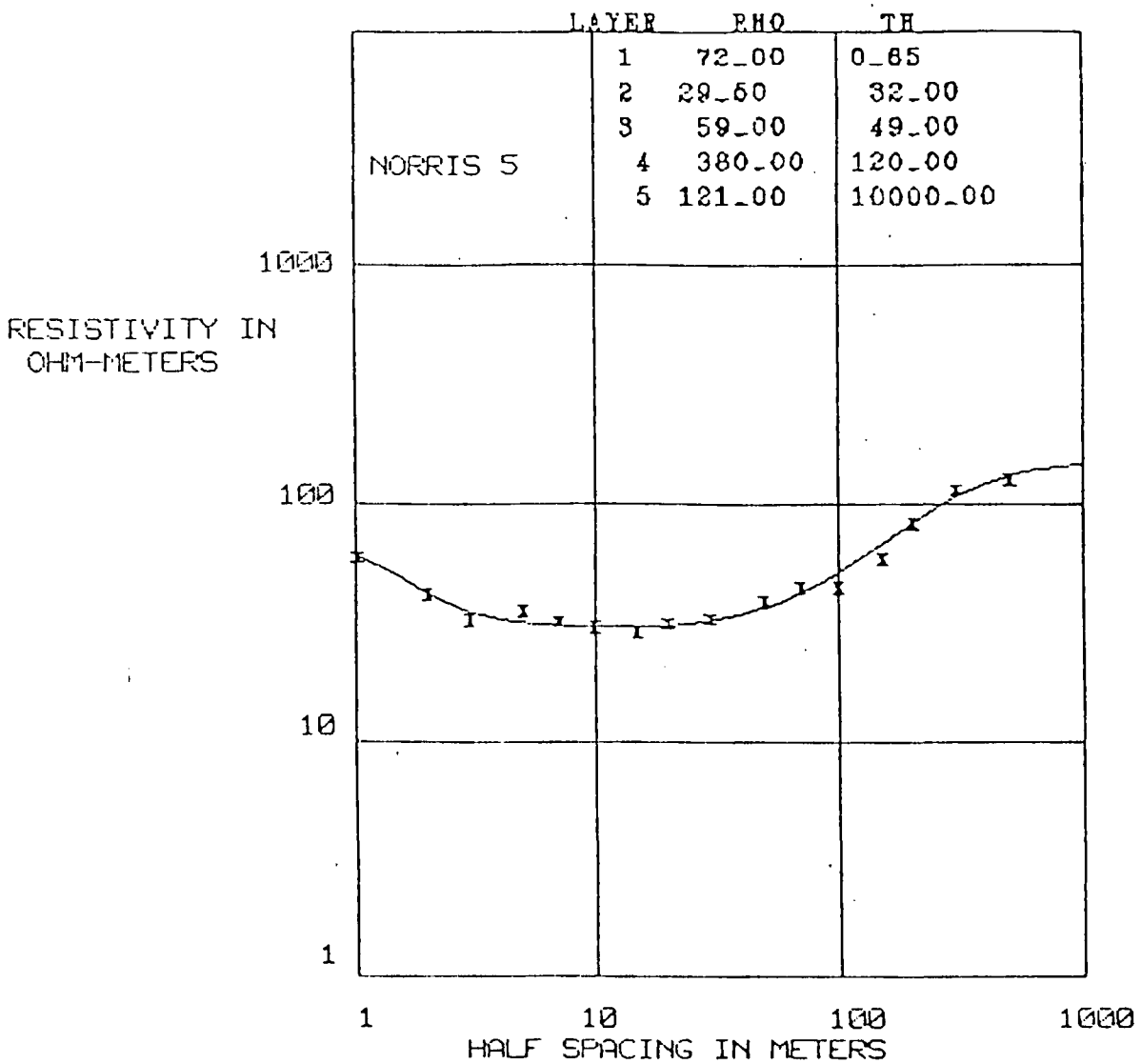

Figure 12. Norris five - the field data points are x's. The smooth curve is simulated by computer using the layer data in the upper right hand corner.

Norris fifteen sounding, shown in Figure 13, was conducted about a month later than the other surveys due to inaccessibility because of Hot Springs Creek flooding.

Norris fifteen, situated across the creek from the hot springs, shows a shallow layer of 15 ohm-meters and beneath it a layer of about 24 ohm-meters. The sounding is in an area of thickest alluvium, which may act as a reservoire for the ascending hot water.

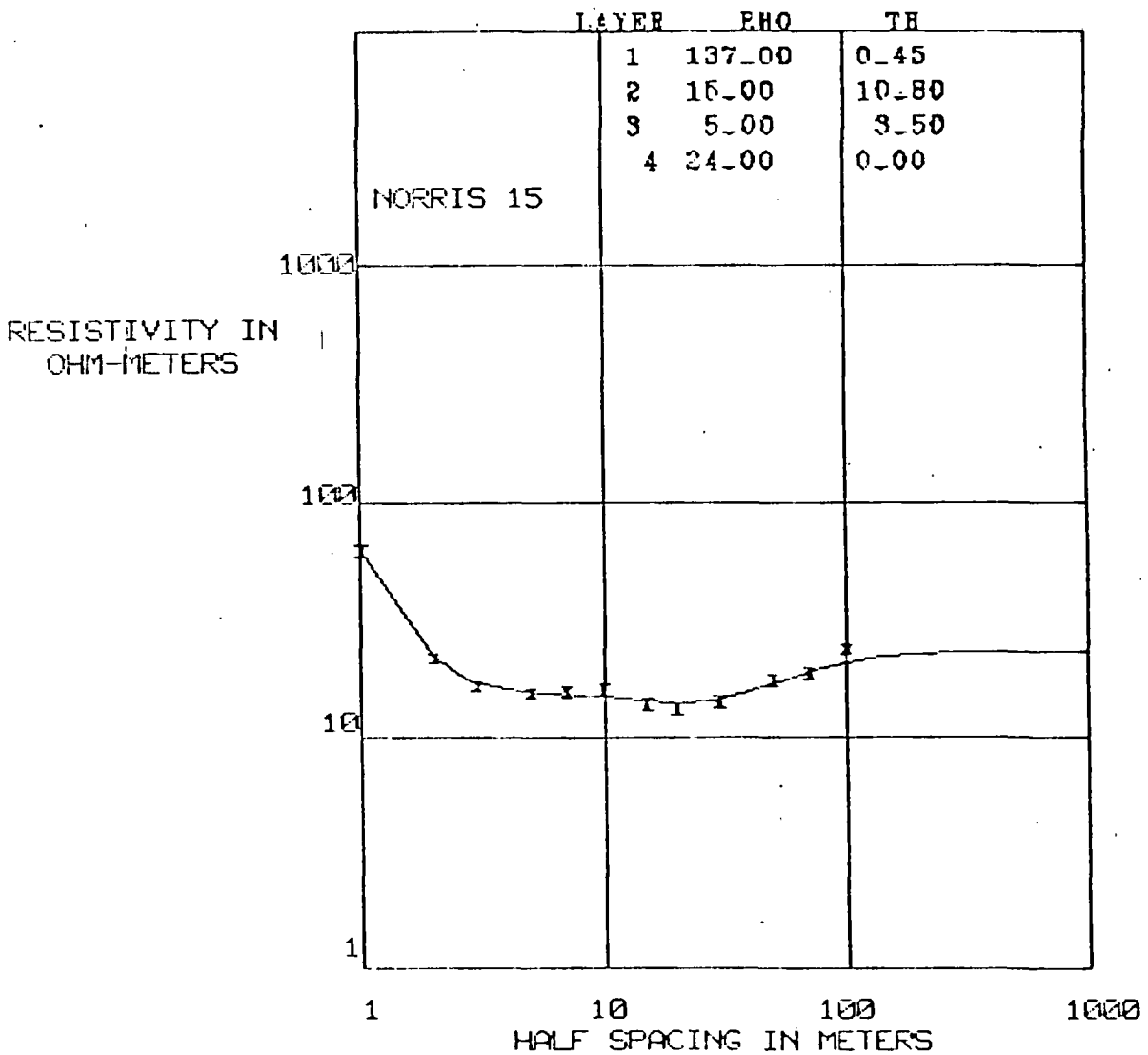

Figure 13. Norris fifteen - the field data points are x's. The smooth curve is simulated by computer using the layer data in the upper right hand corner.

Norris eleven is a north-south sounding about a half mile southwest of the hot springs, see Figure 14. Though about ten times furthur from the main spring than Norris fifteen, Norris eleven shows a greter low, which may indicate fracturing and shearing extends to the southwest.

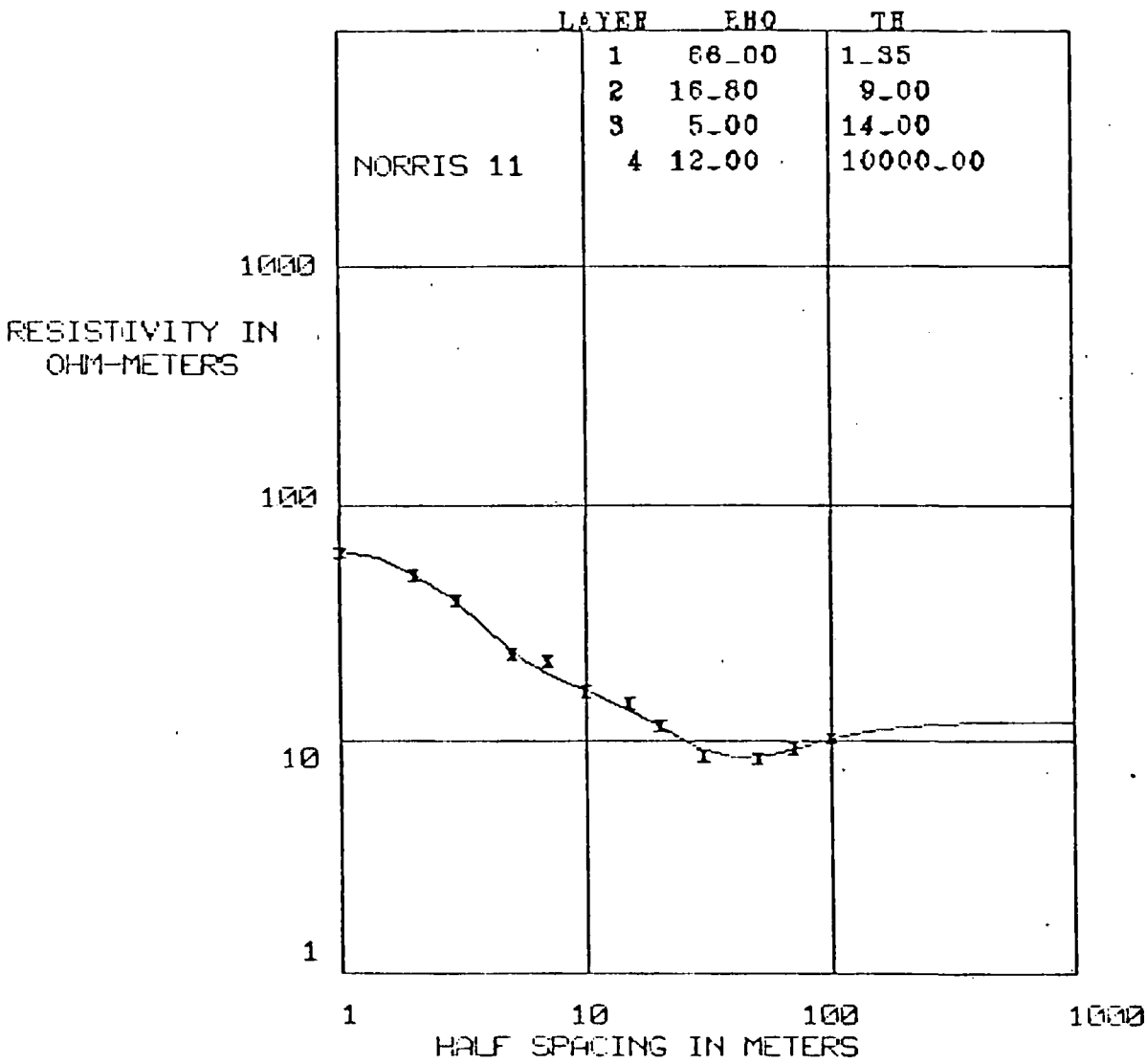

Figure 14. Norris eleven - the field data points are x's. The smooth curve is simulated by computer using the layer data in the upper right hand corner.

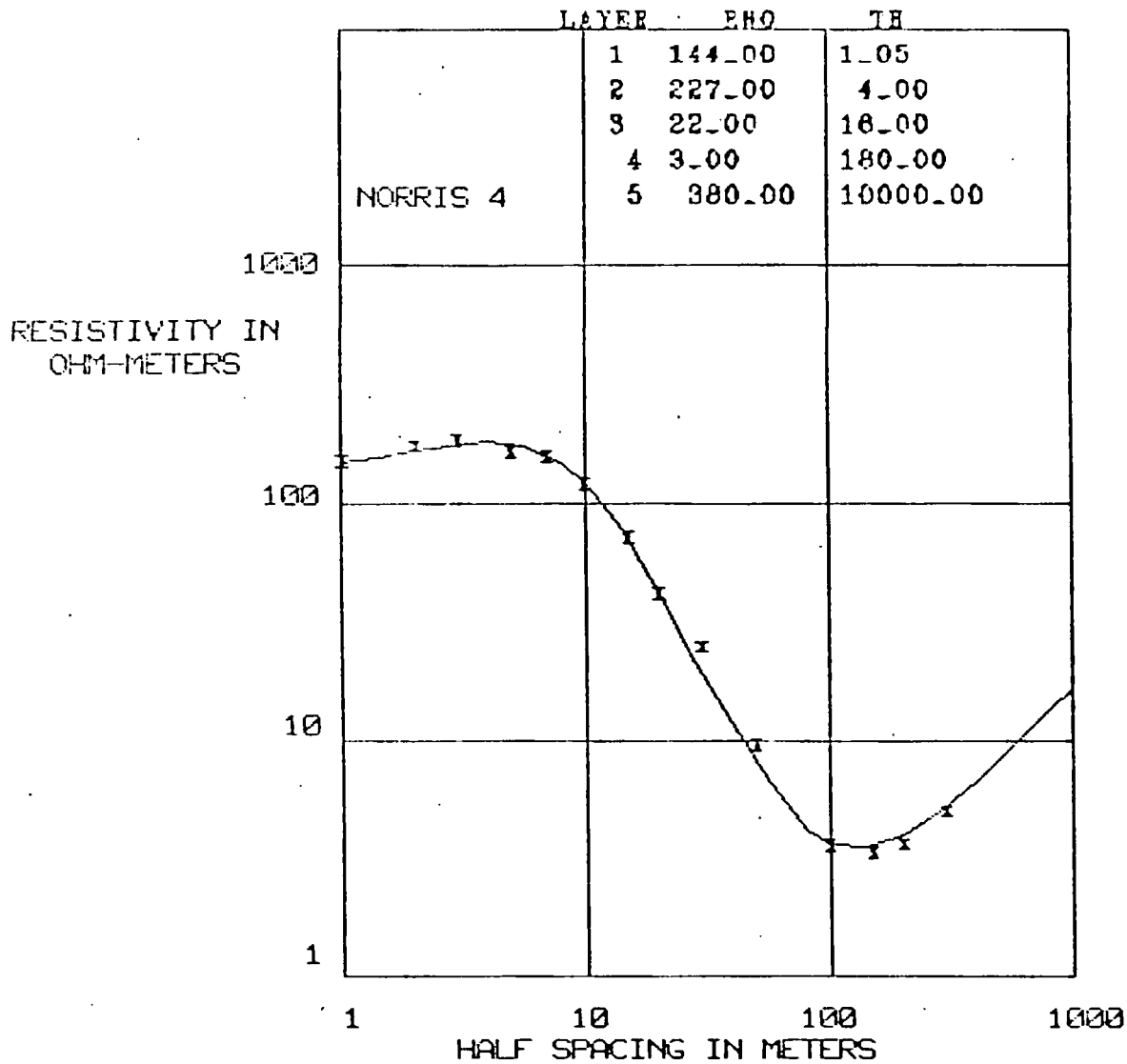

Figure 15. Norris four - the field data points are x's. The smooth curve is simulated by computer using the layer data in the upper right hand corner.

Norris four and twelve exhibit a thick conductive layer as shown in Figures 15 and 16, respectively. Norris four is west of the normal fault mentioned in the structural geology section. This fault may help control geothermal fluids in the Norris Hot Springs vicinity. Norris four and twelve show the greatest low and propose the interesting possibly of being nearest the source.

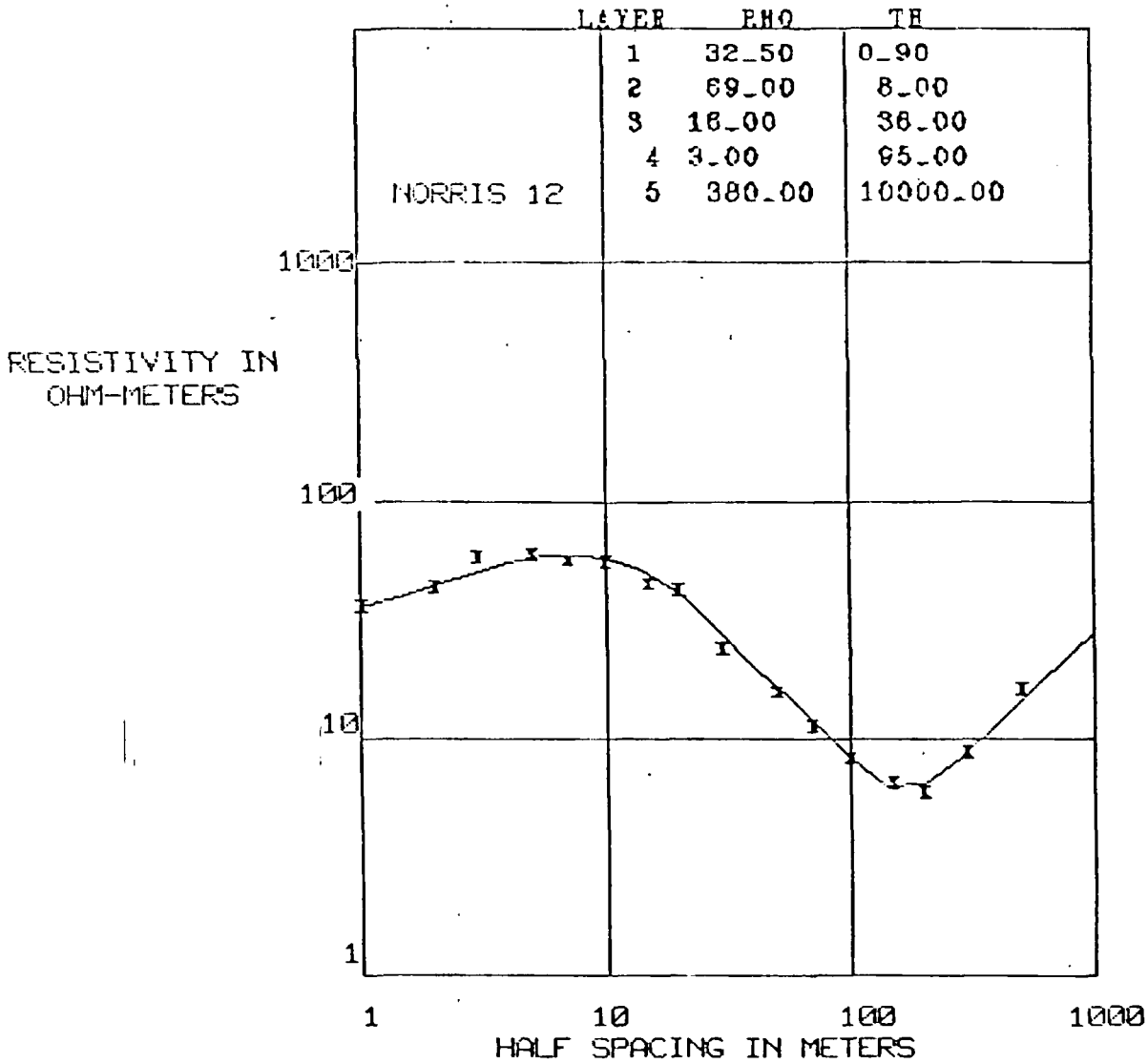

figure 16. Norris twelve - the field data points are x's. The smooth curve is simulated by computer using the layer data in the upper right hand corner.

It is of interest to note that Norris twelve is about a half mile south of Norris eleven, which also shows a greater low than was measured nearer the hot springs surface manisfestations. A possible southwest trend of a thickening conductive layer will be explored furthur by geoelectric section later in this report.

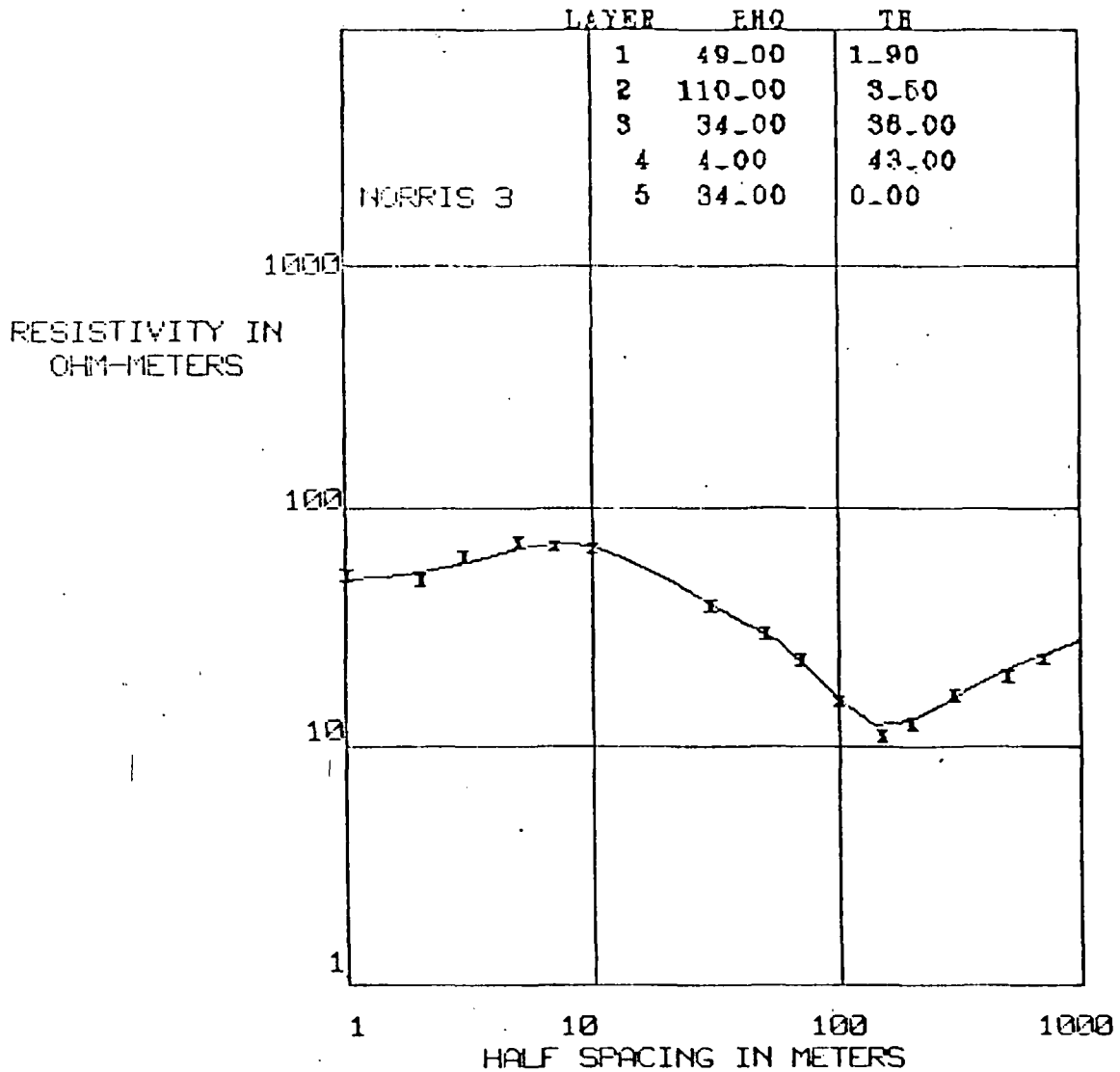

Figure 17. Norris three - the field data points are x's. The smooth curve is simulated by computer using the layer data in the upper right hand corner.

Norris three, in Figure 17, also has a conductive layer at about the same depth as the layer in Norris 12. These last three curves, shown in Figures 15 through 17, make a good case for a nearby source, or possibly water circulation at depth due to a deep seated fault.

GEOELECTRIC SECTION INTERPRETATION

Six geoelectric sections are included as Figures 18 through 23. Figure 18 is a northwest to southeast line which intersects Norris one, two, and six. Because cross-section one does not intersect the centers of the arrays it is assumed there is lateral continuity in each array, which may not be the case.

Cross-section one shows a consistant low beneath Norris two and six, broadening to a much thicker though slightly more resistant layer below Norris one. Basement resistivity is at least 180 ohm-meters and could possibly be higher according to the curve of Norris two, which shows about a 45 degree slope between data points taken at 100 and 1000 meters.

The Hot Springs Creek fault (Andretta, ibid.) is not apparent from the resistivity cross-section. Lateral migration of warm water through alluvium or hydrothermally altered rock may be causes of the low. However, a shear zone or fault can not be precluded from aiding in the spread of warm waters into the wide range they enjoy.

The existance of warm water throughout the area is supported by temperature measurements of discharge water at the Waterlode Mine. Located about a quarter mile southeast of Norris one, it has an anomalous water temperature year round. The mean annual temperature for Montana is about 7 degrees centigrade. The water temperatures of the Waterlode were measured to be 10 degrees centigrade in August, 1976 and about 9.4 degrees centigrade in February, 1978 (Lawson and Sonderegger). More resistivity surveys may help pinpoint the source of warm water.

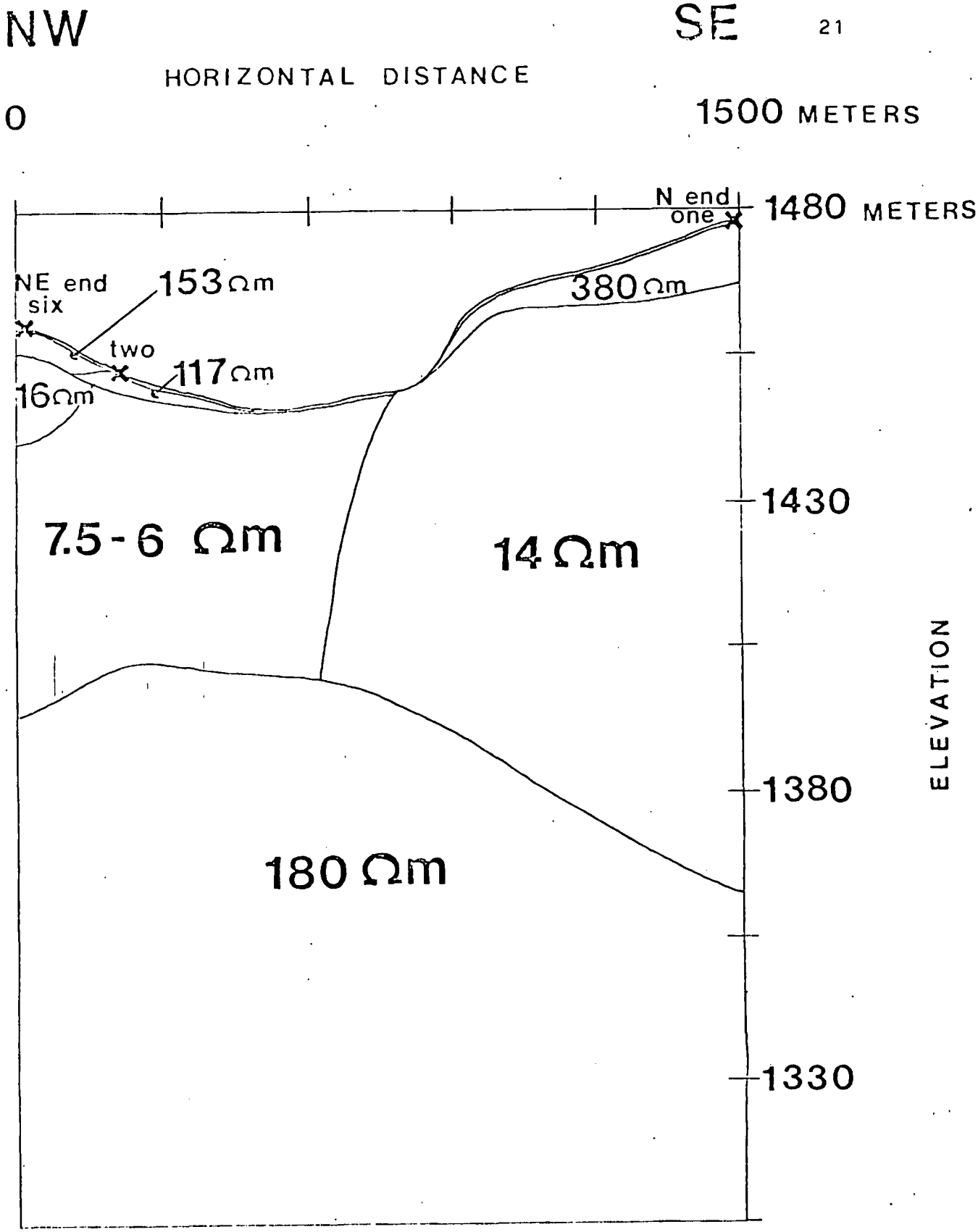

Figure 18. Geoelectric section one, incorporating data from Norris soundings one, two, and six (locations are marked with x's), shows interpreted layer resistivities in ohm-meters. Vertical exaggeration is 12:1.

Figure 19 is a geoelectric section along a line, which lies north and nearly parallel to Hot Springs Creek. Section two intersects Norris six, two, seven and eight. A conductive layer thins to the east and a resistant basement is found at a shallower depth. Soundings seven and eight seem to mark the eastern limit of the Norris geothermal area. The conductive layer's termination may be due to the speculated Hot Springs Creek fault (Andretta, ibid.) or to the natural thinning of warm water saturated or altered alluvium.

Figure 20 shows geoelectric section three, through Norris nine, thirteen, five and ten. The section begins approximately at the western limit of Figure 19. The attitiude is more northeast to southwest, but continues to roughly parallel the north bank of Hot Springs Creek. No conductive layer is evident from this geoelectric section three. The deeper probe, Norris five, approximately in the center of the section, has a broad intermediate low which gradually increases in resistivity at about 75 meters of depth; Then, it rises more steeply (see Figure 12) to an interpreted layer of 380 ohm-meters. At a minimum of 200 meters of depth, resistivity decreases asymptotically to 121 ohm-meters. Inspection of geoelectric section three and the contributing curves (Figures 10 through 13) may indicate a northern limit of the geothermal area or a location at a disadvantage with respect to shear zones and ascending warm water.

Geoelectric section four, shown in Figure 21, lies along a line which is oblique to section three. It crosses the creek passes through Norris Hot Springs, which lies between Norris five and fifteen, and then roughly parallels the creek on its south bank.

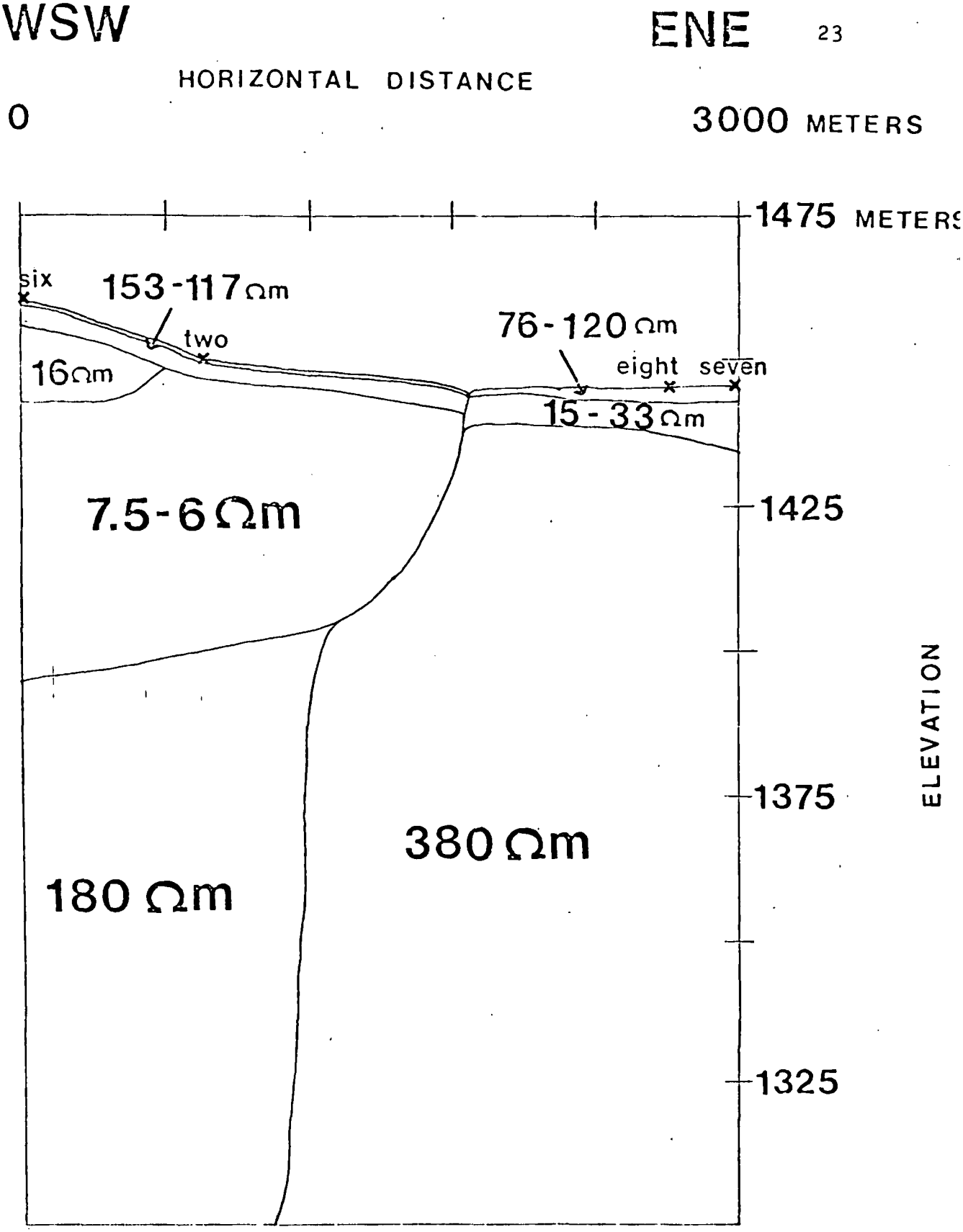

Figure 19. Geoelectric section two, incorporating data from Norris soundings seven, eight, two, and six (locations are marked with an x), shows interpreted layer resistivities in ohm-meters. Vertical exaggeration is 24:1.

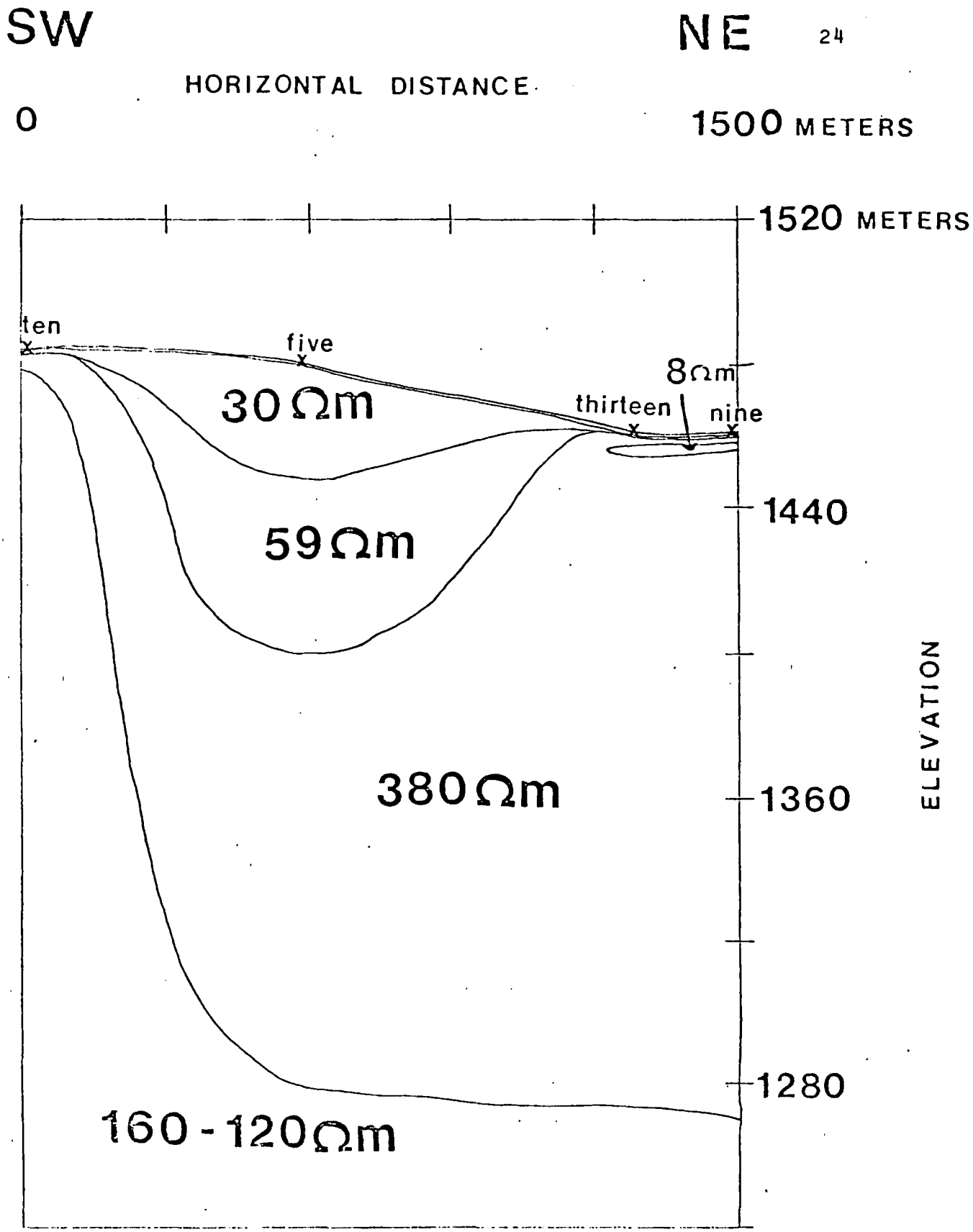

Figure 20. Geoelectric section three, incorporating data from Norris soundings nine, thirteen, five, and ten (locations are marked with an x), shows interpreted layer resistivities in ohm-meters. Vertical exaggeration is 7.5:1.

The inconsistancy between layers in Norris five and fifteen is evident from geoelectric section four. The abrupt break between resistivity layers may be due to the Hot Springs Creek fault, which is inferred by Andretta and others.

The thickness of the conductive layer can only be surmised from the soundings of Norris eleven and fifteen because probing was limited to a half-spacing of 100 meters. The fact that conductance increases to the southwest may indicate a source direction.

Geoelectric section five (Figure 22) extends geoelectric section four (Figure 21) to include Norris twelve, but, because it is slightly offset from section four, it does not intersect Norris fifteen. Again the increase in conductivity and thickness of the conductive layer to the southwest is obvious.

A section through Norris four was not drawn. However, a look at the curves in Figures 15 and 16 indicates a continuing trend towards a thicker and more conductive layer. Because Norris four obliquely crosses a power line, the data is questionable. Norris twelve was obtained along this same stretch, but north of the power line, to substantiate the low resistivities of Norris four. An electric survey south of Norris four would furthur confirm a south to southwestern trending low.

The last geoelectric section connects Norris three and twelve and moves northwest of the previous section. A conductive layer exists, but thins slightly in this direction. The basement is of a much lower resistivity than previously encountered for a sounding with a 1000 meter half spacing. An outcrop of Tertiary basalts, located about a quarter of a mile to the south, may cause the low if they are thick enough to appear as basement rock.

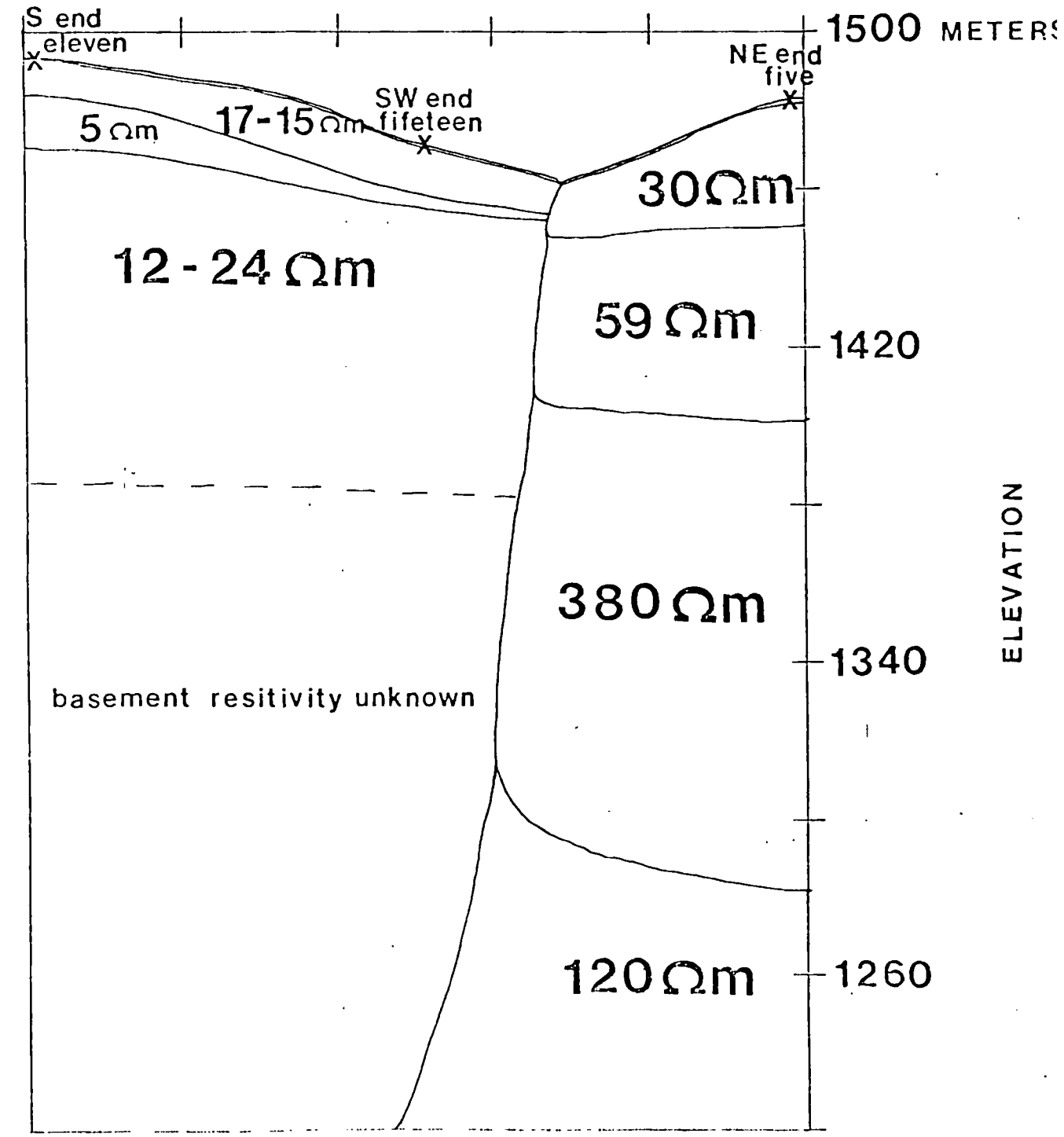

figure 21. Geoelectric section four, incorporating data from Norris soundings five, fifteen, and eleven (locations are marked with an x), shows interpreted layer resistivities in ohm-meters. Vertical exaggeration is 7.5:1.

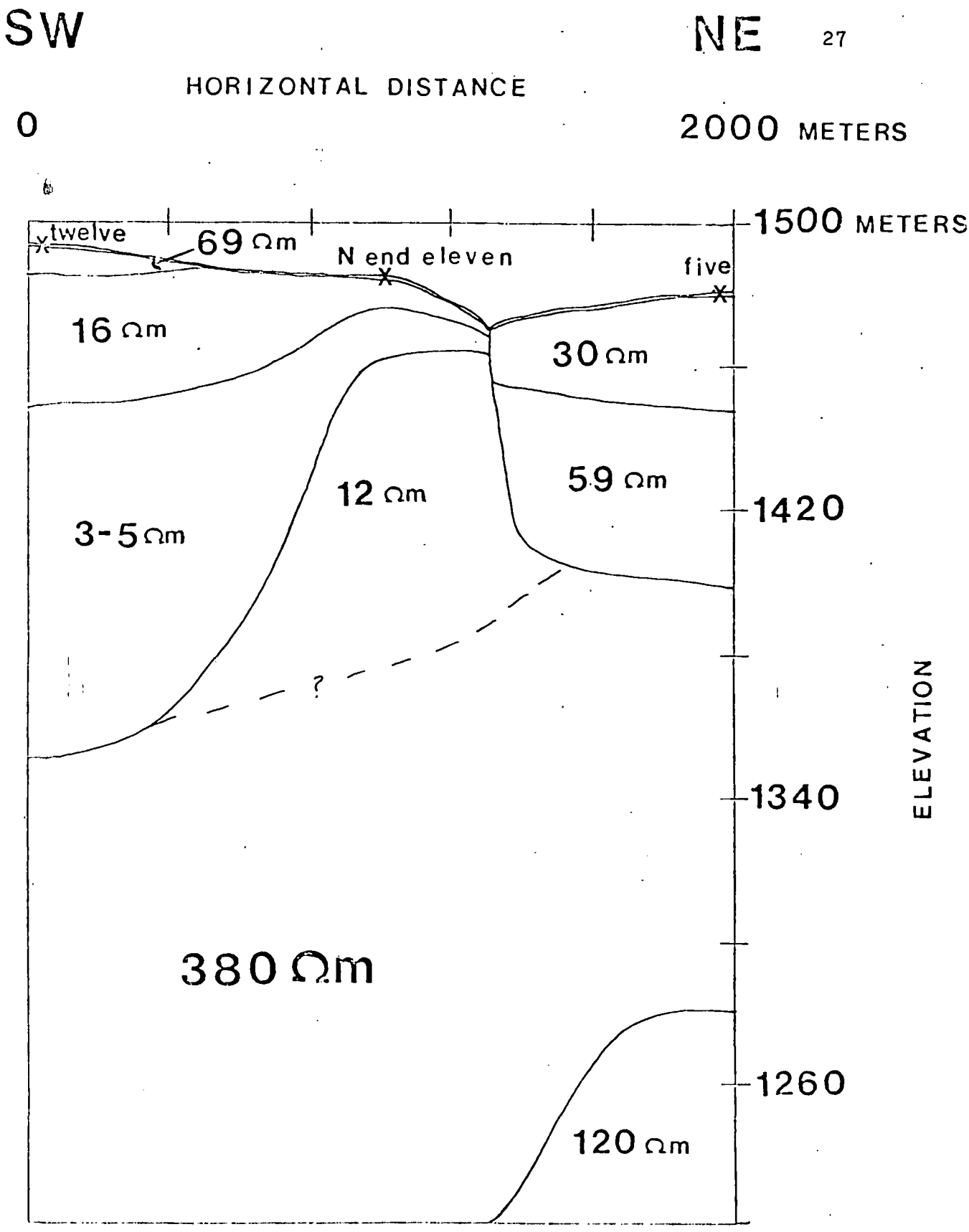

Figure 22. Geoelectric section five, incorporating data from Norris soundings five, eleven, and twelve (locations are marked with an x), shows interpreted layer resistivities in ohm-meters. Vertical exaggeration is 10:1.

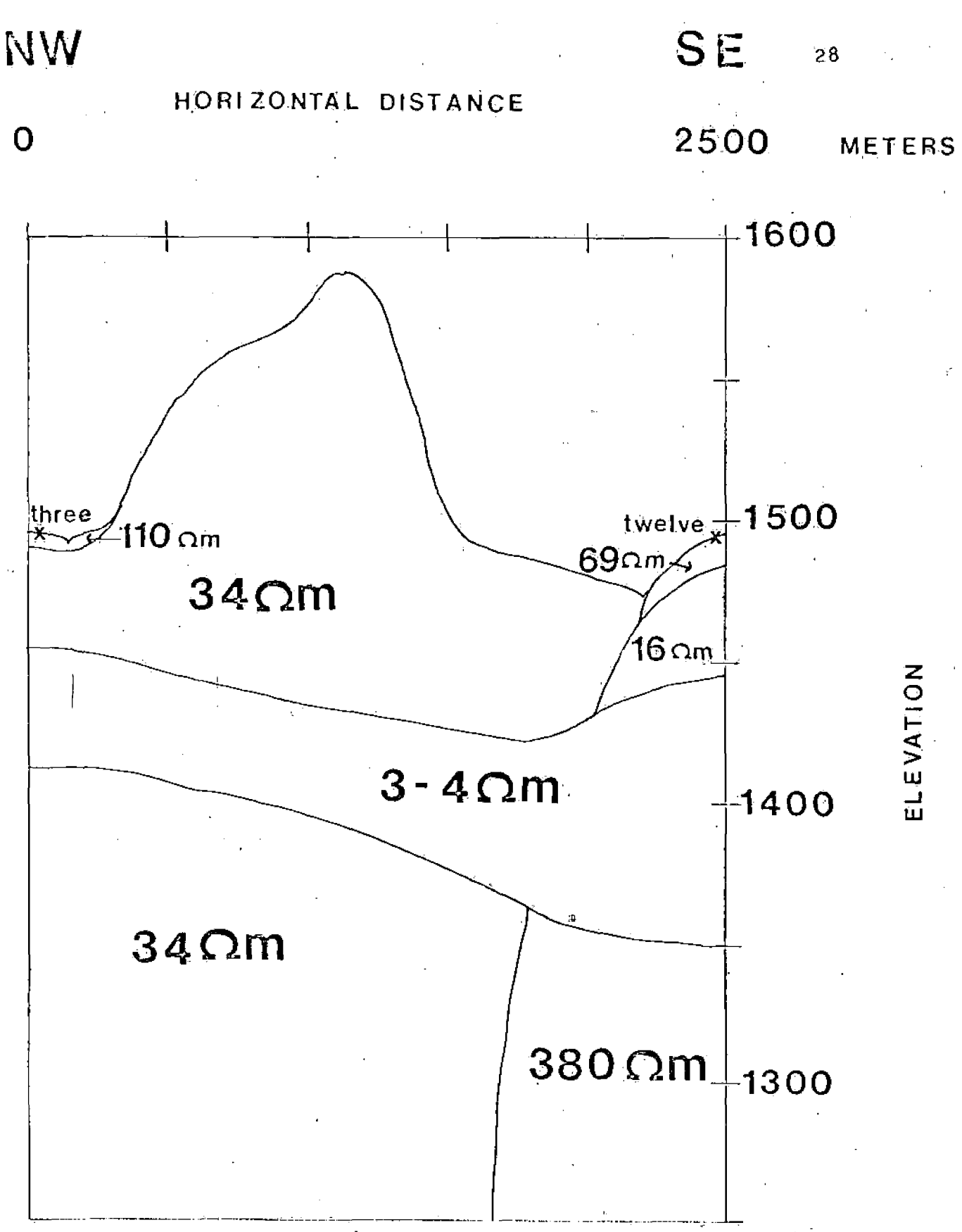

Figure 23. Geoelectric section six, incorporating data from Norris soundings twelve and three (locations are marked with an x), shows interpreted layer resistivity in ohm-meters. Vertical exaggeration is 10:1.

CONCLUSIONS

A conductive anomaly is evident from the electrical surveys and their geoelectric sections. The anomaly extends roughly over an eight square mile area of which the southwestern portion shows the most promise as to source direction. A fault (Vitaliano and others, 1979), shown near Burnt Creek in Figure 2, lies southwest of Norris four and may provide a pathway for thermal waters. Furthur work near Burnt Creek is needed to explore the southwest trending low. Lateral flow into shallow alluvium, which probably acts as a reservoire for the warm water, may be responsible for the wide range of low resistivities, measured throughout the area.

Norris one, though not nearly as anomalous as twelve or four, is interesting because it is not located in a structurally favorable area. Because of the anomalous mine water it would be instructive to do another electrical survey in the area, perhaps nearby the Waterlode Mine, to help determine if a relationship exists between the warm mine water and Norris Hot Springs.

BIBLIOGRAPHY

Abdul-Malik, Muhamed M.; "A Geophysical Investigation of the Silver Star Area of Madison County, Southwest Montana"; Masters Thesis; Montana College of Mineral Science and Technology, Butte, Montana, May, 1977.

Andretta, D. B. and Alsup, S. A.; "Geology and Cenozoic History of the Norris-Elk Creek Area, Southwest Montana"; Billings Geological Society, 11th Annual Field Conference, 1960; Campau, D. E. and Anisgard, H. W., editors; pages 185-190.

Chadwick, Robert A. and Kaczmarek, Michael B.; "Geothermal Investigations of Selected Montana Hot Springs"; Montana Geological Society; 22nd Annual Publication; Billings, Montana, 1975; pages 209-215.

Chadwick, Robert A. and Leonard, Robert B.; "Structural Controls of Hot-Spring Systems in Southwestern Montana"; U.S. Geological Survey, open file report no. 79-1333; Helena, Montana, September, 1979.

Chadwick, Robert A.; Weinheimer, G. J.; Rose', C. C.; Boyer, C. I.; "Geophysical Investigation and Thermal Water Circulation at Hunters and Norris Hot Springs, Montana"; Northwest Geology, Volume 7; Alt and Moore, editors; University of Montana, Missoula, Montana, 1978; pages 27-33.

Keller, G. V.; and Frischknecht, E. C.; "Electrical Methods in Geothermal Prospecting"; New York, Pergamon Press, 1966.

Leonard, Robert B.; Brosten, Tordis M. and Midtlyng, Norman; "Selected Data from Thermal-Spring Areas, Southwestern Montana"; U.S. Geological Survey open file report no. 78-438; Helena, Montana, May 1978; pages 32-33.

Lawson, Don and Sonderegger, John; "Geothermal Data Base Study: Mine Water Temperatures"; Montana Bureau of Mines and Geology, Special Publication 79, July, 1978.

Perry, Eugene S.; "Montana in the Geologic Past"; Montana Bureau of Mines and Geology, Butte, Montana, March, 1962.

Telford, W. M.; Geldart, L. P.; Sheriff, R. E.; Keys, D. A.; "Applied Geophysics"; Cambridge University Press; Cambridge, England, 1976.

Vitaliano, Charles and others, geological map of southern Tobacco Root Mountains, Madison County, Montana; published by the Geological Society of America, Inc.; Boulder, Colorado, 1979.

Convection Currents in the Earth's Mantle

The steady motion of the plates that form the earth's crust is evidence for convection currents on a vast scale. Laboratory studies indicate that there should be smaller currents as well

by D. P. McKenzie and Frank Richter

Geophysicists have long conjectured that the rock of the earth's mantle, the deep plastic region below the earth's rigid crust, must be churning slowly in vast convection cells, rising in some regions, cooling and sinking in others. In the past dozen years, with the general acceptance of the concept of plate tectonics, the existence of convection has become apparent on a global scale. The crust of the earth is made up of large quasi-rigid plates that grow outward from rifts in the ocean floor where molten rock wells up and eventually plunge back into the mantle in the vicinity of deep ocean trenches. The motion of the plates from a mid-ocean ridge to a trench provides the visible half of the convection loop. The mass of the plunging plate must be conserved and the loop closed by a deep return flow of material from the trench to the ridge. Since the horizontal dimension of the loop corresponds to the dimensions of a plate, the complete loop is now often called the large-scale circulation. In the case of the Pacific plate the horizontal dimension reaches 10,000 kilometers.

Although the large-scale circulation can now be accurately described, and almost certainly represents a form of thermal convection in the earth's upper mantle, there is still no satisfactory theory explaining how the circulation is maintained for tens of millions of years. Attempts to answer the question with the help of laboratory experiments and computer simulation have yielded evidence for the possibility of convection on a smaller scale, where the convection cells would have a horizontal dimension comparable to their depth: about 700 kilometers. The experiments suggest that such cells could explain the flow of heat under old sections of oceanic plates, which is greater than one would expect, and perhaps could account for gravity anomalies in the ocean floor. Small-scale convection cells might also provide the rising jets of hot material that create oceanic chains of volcanoes such as the Hawaiian Islands. Finally, the experiments suggest that the small-scale convection cells may be aligned in long parallel cylinders under plates that are moving as fast as the Pacific plate. It has not yet been possible, however, to simulate in the laboratory the large-scale convection that is apparent in the overall motion of the plates.

The Motions of the Plates

In any effort to understand the forces that drive the plates the most straightforward approach is to start from theoretical models of worldwide plate motions, which impose some constraints on the possible driving mechanisms. Almost all large earthquakes are triggered by plate motions, so that the energy released by earthquakes must be provided by the forces driving the plates. Many mechanisms have been proposed as a source of the energy, but few are adequate to account for it. The only mechanisms that easily provide enough energy are convective flow in the mantle and the process of differentiation by which iron present in the mantle became dissociated from other elements and sank to form the earth's core. As we shall see, thermal convection can give rise to a large variety of flow patterns; the neat hexagonal arrangement of convection cells so common in textbooks is extremely rare in nature.

Thermal convection involves the transport of heat by the coherent motion of material rather than by radiation or diffusion. In the type of convection that is of interest in plate tectonics the heat is transported upward and the flow is driven by the difference in density between the hot fluid and the cold. Even the most conservative estimates of the buoyancy forces resulting from plate motions are much larger than the forces involved in earthquakes. This argument has convinced many geophysicists, but by no means all of them, that the plate motions are maintained by some form of convection.

Geophysical observations can tell us a little about how deep the convective flow extends. No earthquake focus has yet been accurately located whose depth is greater than 700 kilometers. Furthermore, the slabs sinking under the arcs of islands where plates converge are in compression at all depths when their advancing edge extends to depths of more than 600 kilometers, whereas they are in tension at depths of less than 300 kilometers if their leading edge does not reach 300 kilometers. The simplest explanation of this behavior is that the slab meets great resistance to its motion at 600 kilometers and is unable to penetrate below 700 kilometers. The in-

SHADOW PATTERNS OF CONVECTION CELLS are seen from above in a laboratory apparatus designed to simulate conditions that may produce convection in the plastic rock of the earth's upper mantle. The patterns are made visible in the apparatus by shining light through a transparent viscous fluid from below (*see illustrations on page 80*). The rays are refracted away from hot regions and toward cold ones, giving rise to light and dark patterns. The changes in laboratory conditions responsible for the various patterns can be summarized in terms of the Rayleigh number, a dimensionless quantity that is proportional to the temperature difference across the layer of fluid and to several other parameters, including the thickness of the layer. When the Rayleigh number is less than about 1,700, there is no convection. When the Rayleigh number is between 1,700 and about 20,000, convection takes the form of two-dimensional parallel cylinders, as is shown in the top photograph on the opposite page. At Rayleigh numbers between 20,000 and 100,000 two sets of cylinders at right angles to each other are generated (*middle photograph*). This convection pattern is called bimodal flow. At still higher Rayleigh numbers the flow assumes an intricate spoke pattern in which sheets of rising hot fluid and sinking cold fluid radiate out from multiple centers (*bottom photograph*).

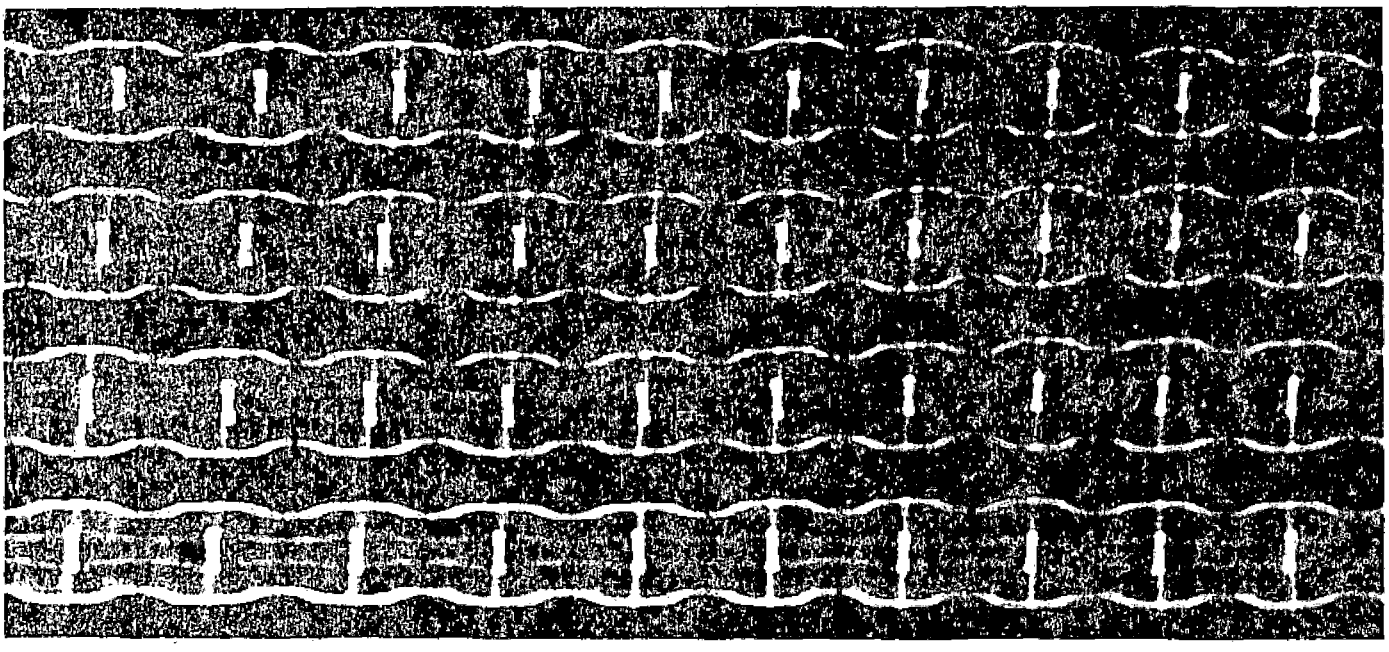

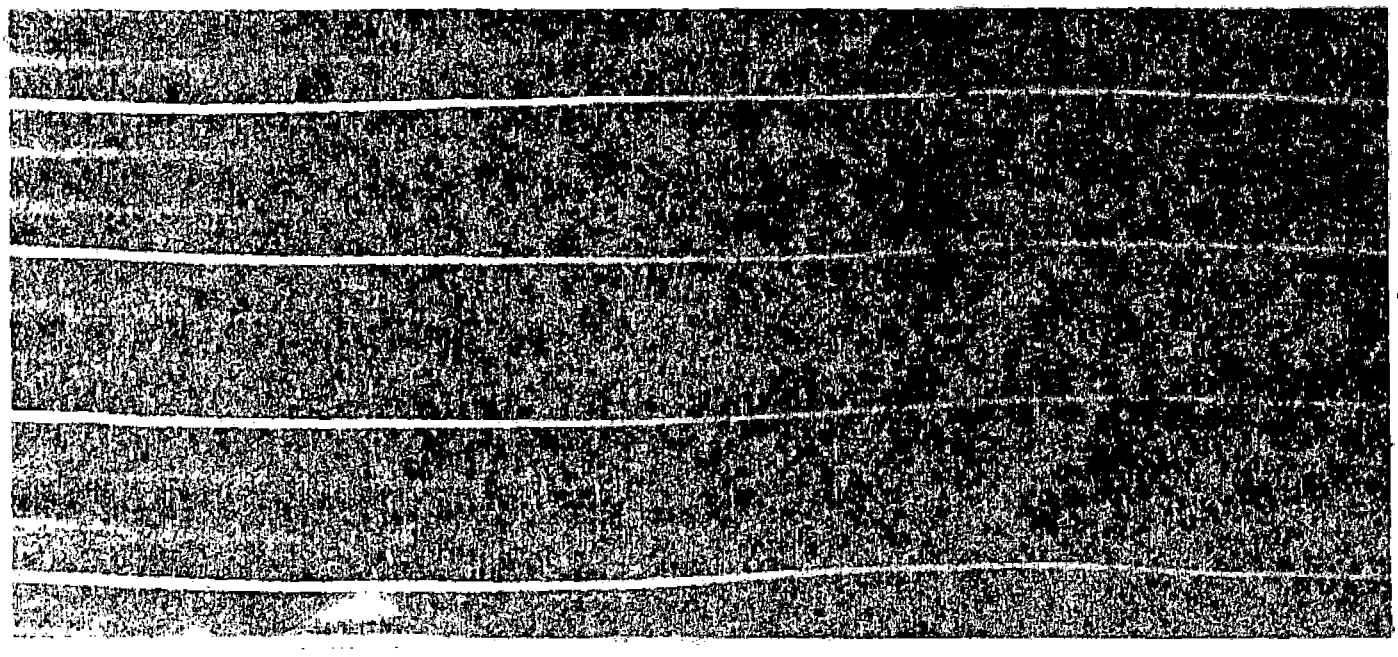

crease in the resistive force is probably associated with a change in the crystal structure of iron and magnesium silicates that occurs at this depth. Whatever the explanation, the behavior of sinking slabs strongly suggests that the convective circulation of which the plates are a part is confined to a region 700 kilometers deep. What happens deeper in the mantle need not concern us here (although it seems likely that convection also occurs in the lower mantle).

It is difficult to say much more about the form of the flow from geophysical observations alone. The plates are large and strong, and their rigid motions conceal the more complicated three-dimensional motions in the mantle below. It is much harder to study convection in the mantle than it is to study the circulation of the ocean or of the atmosphere. There is no drill that can bore through a plate; the deepest boreholes sample only the top 10 percent of it. And even if one could penetrate to the mantle, one would have the problem of measuring convection currents that move at velocities of only a few centimeters a year.

The Rayleigh and Reynolds Numbers

Fortunately mathematical physicists have been interested in convection since the 19th century, so that there is considerable understanding of how convection currents behave. Perhaps the most striking finding is how complicated the convective flow can be even in a layer of fluid uniformly heated from below. Undoubtedly convection in the earth's mantle is more complicated still.

Two of the leading contributors to the mathematical description of fluid flow, including convection, were Lord Rayleigh and Osborne Reynolds. Largely as a result of their work it is possible to describe any type of convective flow with only a few numbers, named after Rayleigh and Reynolds, that are dimensionless combinations of various physical parameters such as viscosity, thermal conductivity and the coefficient of thermal expansion. With the aid of these numbers one can simulate the convection in the earth's mantle in a layer of fluid a few inches thick. The reason is that convection depends on the combined properties of the fluid layer and not on the properties taken singly. The Rayleigh number depends in part on the ratio between the cube of the depth and the viscosity, so that one can model a system such as the upper mantle, which has a very high viscosity and a depth of hundreds of kilometers, with a fluid of moderate viscosity. One can also speed up the passage of time so that processes that could take millions of years in the earth take only a few hours in the laboratory model.

The Rayleigh number is particularly significant for modeling convection. It is proportional to the temperature difference between the top and the bottom of the fluid and to several other parameters. In a convecting fluid the Rayleigh number is in practice proportional to the ratio between the time needed to heat a layer of fluid by thermal conduction and the time needed for a particle of fluid to circulate once around the convection cell. A familiar example of a convecting fluid with a large Rayleigh number is water being heated in a saucepan but not yet boiling. The fluid inside an egg placed in the pan represents a system with a small Rayleigh number because the contents of the egg are much more viscous than water. (As a result the heat that cooks the egg is distributed by conduction rather than by convection.)

The Reynolds number is concerned not with heat but with momentum. It measures the ratio between the forces accelerating the fluid and the viscous forces resisting its motion. When the Reynolds number is small, the inertia of the fluid is not important and the flow is fairly simple. If the number is large, however, eddies are likely to form and the flow can become turbulent and extremely complex. Examples of flow with a high Reynolds number are water gushing from a faucet or a mountain stream tumbling over rocks. Atmo-

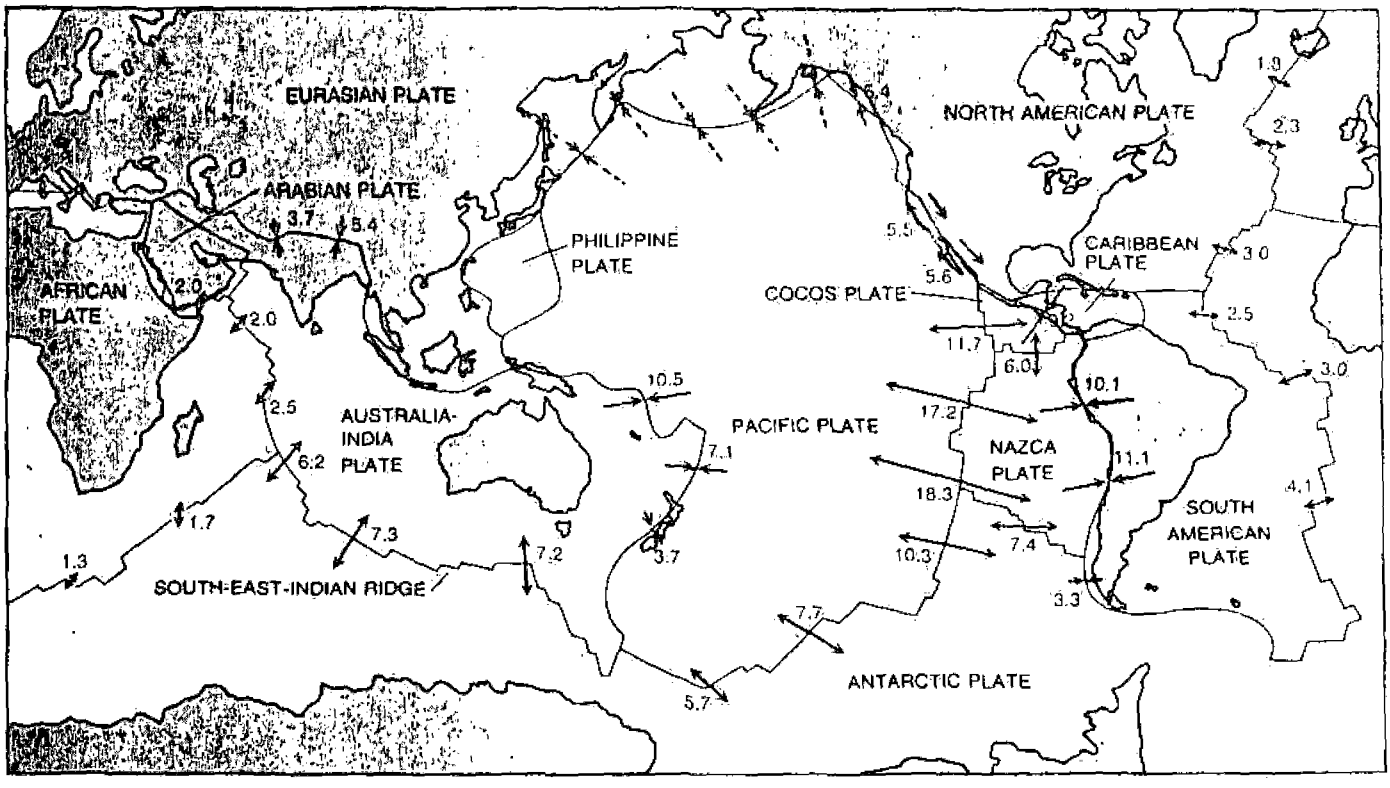

EVIDENCE FOR CONVECTION IN THE MANTLE is supplied by the motions of the dozen or so plates into which the earth's crust is divided. Material is added to the plates by upwelling of molten rock along rifts in the ocean floor that mark the center of a ridge extending continuously for some 40,000 miles through the Atlantic, Indian and Pacific oceans. The plates plunge back into the mantle at subduction zones that coincide with oceanic trenches. The lines with arrowheads pointing outward show where plates are moving apart at ridges; numbers indicate the relative velocity in centimeters per year. The Australia-India, Pacific and Nazca plates are moving the most rapidly. Lines with opposed arrowheads show where plates are moving toward each other, usually at trenches. The Himalayas are a major exception. Plates can also slide past each other along transform faults such as San Andreas fault on west coast of North America.

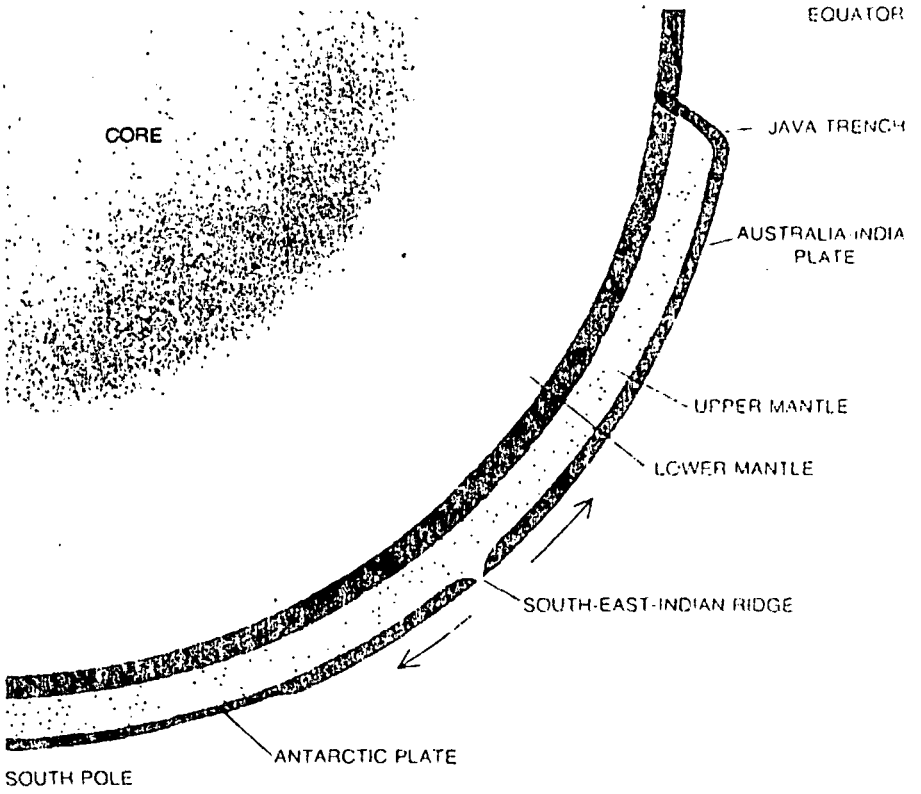

SECTION THROUGH THE EARTH depicts in true scale the configuration of plates from the Equator to the South Pole along the meridian at 110 degrees east. Plates (*color*) are created at mid-ocean ridges and usually descend into mantle at trenches adjacent to island arcs. Movement of plates transports by convection about half of the heat passing through upper mantle.

spheric disturbances are another example. Such flows are difficult to model and to understand.

The viscous material flowing in the earth's mantle has a very small Reynolds number, about 10^{-10}, and the momentum of the flow is negligible. One might expect convection in the mantle to be strongly influenced by the earth's rotation, but it can be shown that rotation has no direct effect. The Rayleigh number is of much greater significance because it is quite large. Although estimates vary, the lower limit is about 10^6, and the number could be higher by a factor of 10 or more. It is not difficult to produce such Rayleigh numbers in the laboratory by heating a fluid such as glycerin or silicone oil in a layer a few centimeters thick confined between two plates.

When the Rayleigh number in such a

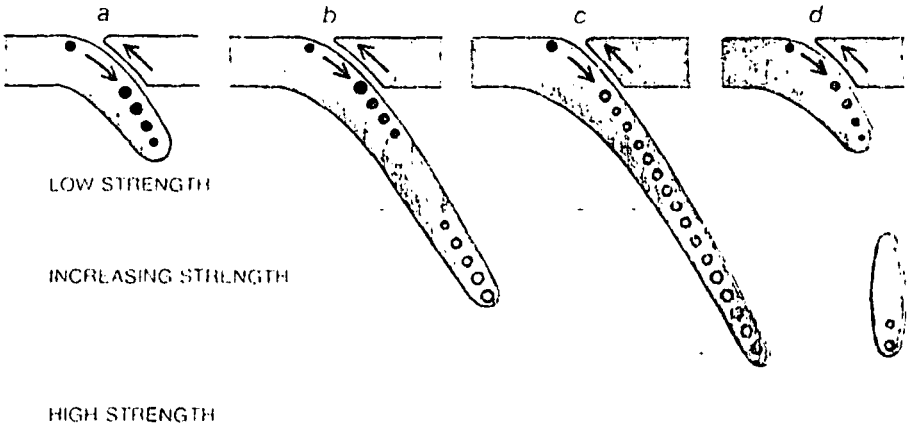

DESCENDING PLATES meet increasing resistance as they penetrate deeper into the upper mantle. At a depth of 200 kilometers in *a* the slab is in tension and pulling apart, as is shown by solid dots. In *b* the upper section is still in tension but the part of the slab below 300 kilometers is in compression (*open circles*). In *c* the tip of the slab, below 600 kilometers, meets such resistance that the entire slab is in compression. In some cases (*d*) pieces of slab break off and sink to about 600 kilometers. Such observations suggest that the convective flow involving the motions of the plates is confined to depths in mantle shallower than 700 kilometers.

system is less than 1,708, thermal convection cannot occur; heat travels directly by conduction from the hot lower plate to the cool upper plate. If a small disturbance is created in the fluid, the disturbance dies away with time. Such a state is described as stable, but it need not be static. When the Rayleigh number is increased to between 1,708 and about 20,000, the system becomes unstable and small disturbances can grow into convection cells. The shape of the cells and their horizontal arrangement in the layer, called the plan form of the convection, depend on the form of the initial disturbance.

Types of Cells

The simplest plan form consists of two-dimensional cells: cylinders that rotate on their long axes. Three-dimensional cells can be produced by a three-dimensional initial disturbance. We know that in the range of Rayleigh numbers between 1,708 and 20,000 two-dimensional cylindrical cells are stable in the presence of small disturbances. We also believe all three-dimensional flows slowly evolve toward the two-dimensional configuration. We cannot be sure, however, because the evolution is very slow. Even experiments lasting several months have not completely resolved the question.

If the Rayleigh number is increased to 20,000 or so, two-dimensional cylindrical cells are no longer stable. Another set of cylinders at right angles to the original one grows to give rise to a three-dimensional network of rectangular cells, a pattern of flow called bimodal convection. If these cells are generated with great care in the laboratory, they are all virtually identical. Obviously if the plan form is not two-dimensional at the lower Rayleigh numbers where cylindrical cells are stable, there is no sudden shift to three-dimensional flow as the Rayleigh number is increased.

At Rayleigh numbers larger than about 100,000 the bimodal pattern breaks down in a rather complicated way. Where the two sets of cylindrical cells cross in the bimodal pattern there are points at which the fluid sinks or rises faster than it does elsewhere. As the Rayleigh number is increased these points move together and distort the bimodal pattern. The resulting plan form consists of a number of points of intense upwelling joined to one another by vertical sheets of sinking fluid (or points of downwelling joined by sheets of rising fluid). This plan form is called the spoke pattern.

What happens at still larger Rayleigh numbers, comparable to those of the material of the earth's mantle? This question is difficult to answer because the Reynolds number of spoke convection in laboratory experiments is the rel-

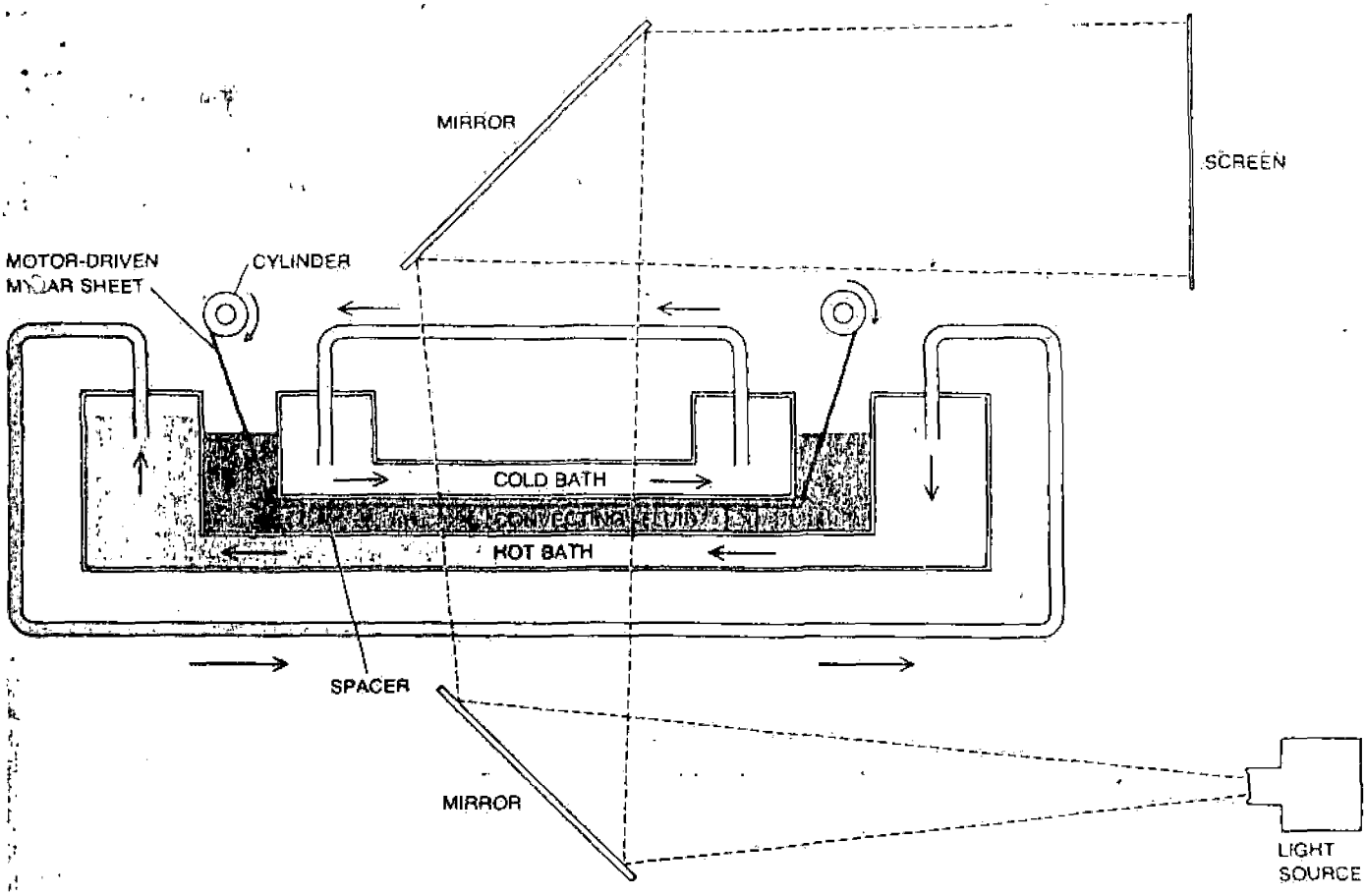

APPARATUS FOR CONVECTIVE FLOW simulates conditions thought to prevail in the earth's upper mantle. The convecting fluid is a viscous silicone oil, which is heated from below and cooled from above. The properties of the oil, in combination with suitable heat flows and depths of fluid, reproduce Rayleigh numbers in the range from about 1,700 to 10^6. The depth of the fluid can be varied from about 1.6 to seven centimeters. The convecting region measures about 100 centimeters on a side. To simulate the effect of a moving plate on the convection patterns a thin sheet of Mylar can be moved across the surface of the oil. Usually only a few hours are needed to reproduce events that would take millions of years on the scale of the earth. Light shining from below makes convection patterns visible.

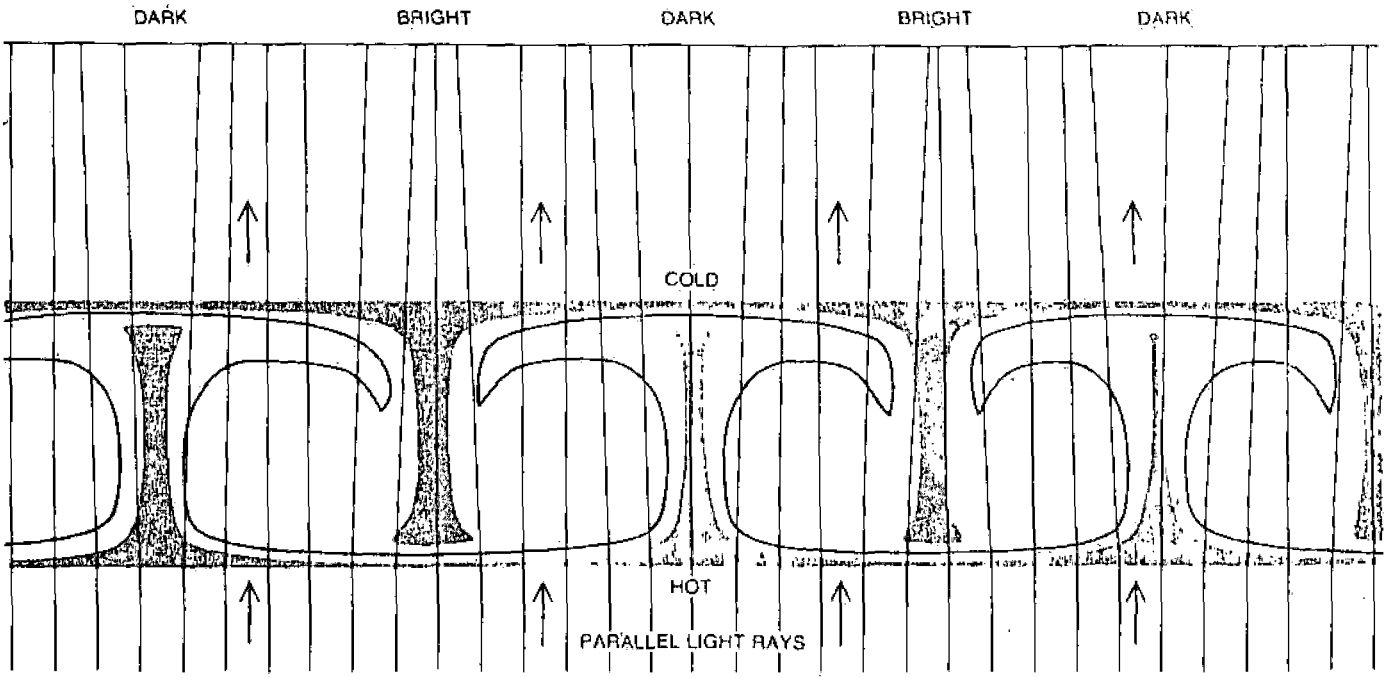

SIMPLE CONVECTION CELLS, consisting of two-dimensional cylindrical cells, seen here end on, make a shadowgraph such as the one reproduced at the top of page 73. Parallel rays of light shine through the fluid from below. The rays are refracted away from hot regions and toward cold ones. Thus hot, rising sheets of fluid are marked by a dark line, which sometimes has a thin bright line on each side. Cold, sinking sheets of fluid are marked by a bright line. Convection cells in general tend to be as wide as they are deep.

atively large number of about 1, even when the fluid is very viscous, and momentum effects begin to become important. The convection becomes time-dependent, that is, its pattern changes with time. It still looks like the spoke pattern, but the hubs of the spokes are farther apart and the position of the rising and sinking sheets is constantly shifting. We suspect that this behavior occurs only when the Reynolds number is not small.

The most striking feature of the cylindrical, bimodal and spoke patterns is that the horizontal distance between the rising and sinking regions is always about the same as the depth of the layer. For a given difference in temperature between the bottom and the top of the layer, cells that are approximately square transport more heat than cells with other shapes. This behavior does not, however, offer much help in the effort to devise a model of the large-scale convection that moves the earth's plates (assuming that the flow in the mantle does not extend below 700 kilometers). What we should like to produce in laboratory experiments is convection cells whose width is many times their depth.

The Heating of the Fluid

The mantle is not a uniform fluid heated from below. It contains radioactive elements, and their decay partly heats it from within. Moreover, the viscosity of the mantle material and its resistance to deformation vary sharply with temperature. It is because of this variation that the cool, thin plates that form out of the material are so rigid. Indeed, the variation is so great that many geophysicists question whether the mantle material can adequately be described as a viscous fluid. How seriously do such considerations complicate the effort to develop a model of the mantle's convective flow? It is true that most of the work done so far has involved fairly simple convection systems in which the fluid layer is heated only from below. Nevertheless, some significant discoveries about convection have been made, chiefly through experiments performed with computers.

As we have seen, when convection is driven by heating from below, heat is transported by hot jets or sheets of fluid rising from the lower boundary of the fluid and by cold fluid sinking from the upper boundary. At large Rayleigh numbers this type of flow gives rise to a thin horizontal layer of hot fluid adjacent to the lower boundary and a similar layer of cold fluid adjacent to the upper boundary. Between these two boundary layers is a region where there is little change in temperature from top to bottom. As the Rayleigh number increases, the turnover time decreases and the boundary layers become thinner. When the heat is generated internally, however, there is no lower boundary layer. Heat must be transported to the upper boundary by all the fluid's passing close enough to it for the heat to be conducted out. There is no longer a "passive" region in the center of the cell.

This state of affairs destabilizes the cold upper boundary layer and gives rise to complicated time-dependent behavior when the Rayleigh number exceeds about 40,000. Both jets and sheets of sinking fluid materialize spontaneously through instabilities of the upper boundary layer. Once they have formed

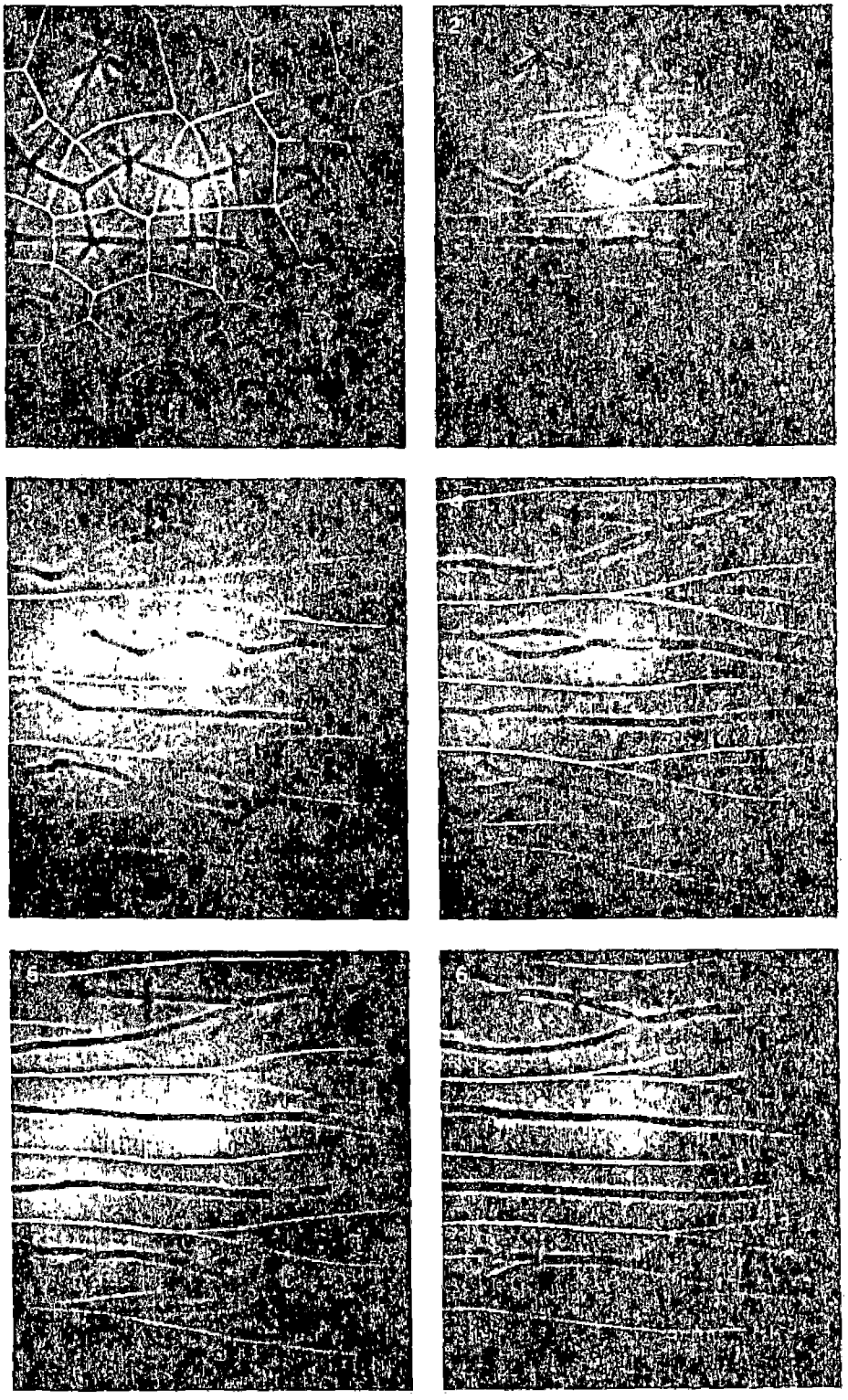

EFFECT OF SHEAR ON SPOKE PATTERN has been studied in the apparatus depicted on the opposite page. After a convective pattern characteristic of a Rayleigh number of 140,000 has become stabilized (*first picture*) the sheet of Mylar is set in motion to simulate a plate moving across the mantle. Successive pictures, made at equal intervals, show the rearrangement in pattern resulting from the motion of the Mylar plate as it travels from left to right. The shear converts the spoke pattern into cylinders whose axes are parallel to the direction of plate motion. The small black bar at upper left in each photograph indicates the depth of the fluid.

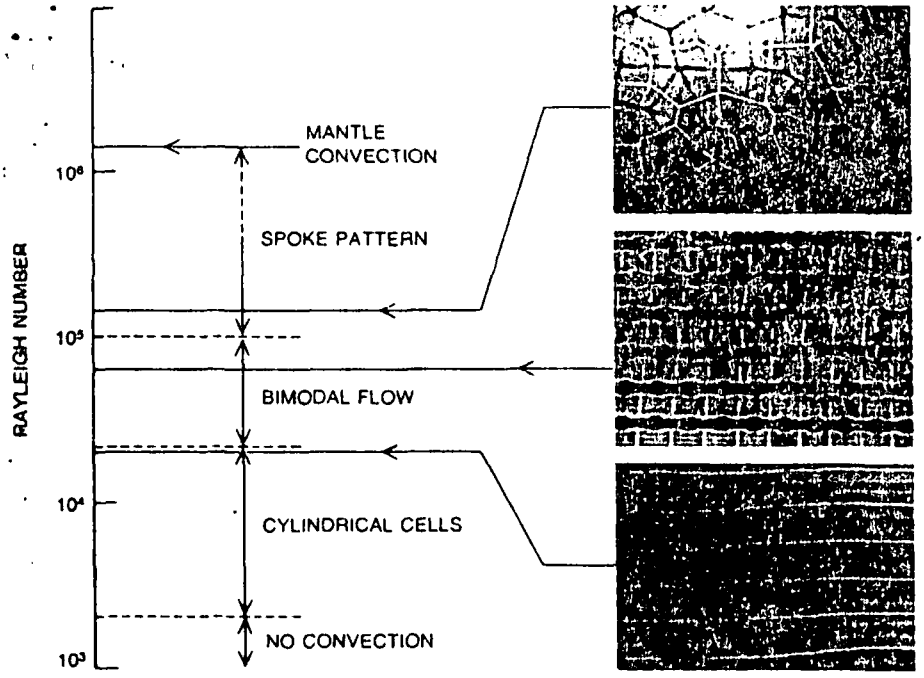

CONVECTION IN THE MANTLE is thought to involve Rayleigh numbers lying somewhere between 10^6 and 10^7. Laboratory experiments show that convection patterns develop in complexity from cylinders to bimodal flows to spoke patterns as Rayleigh number increases.

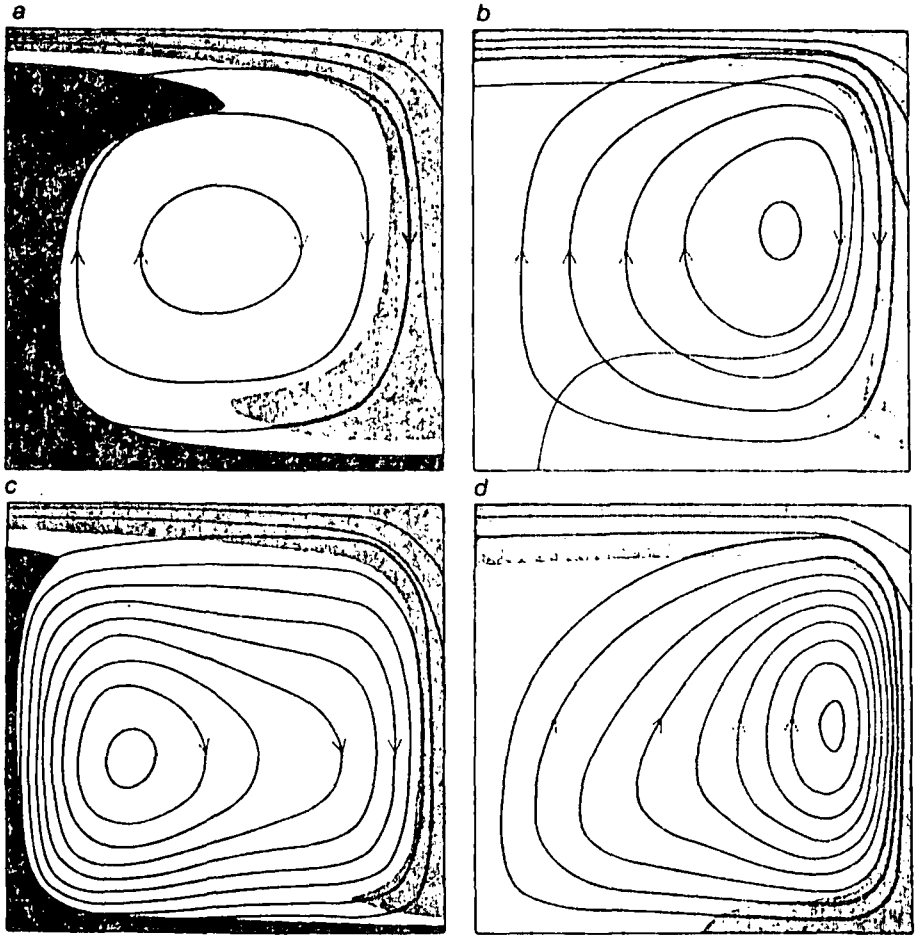

COMPUTER SIMULATIONS of convection cells show how patterns are affected by variations in fluid viscosity and by the mode of heating. When the viscosity is constant and the fluid is heated entirely from below (*a*), the rising and sinking sheets of fluid are nearly symmetrical. When the heat is supplied uniformly throughout the interior of a fluid of constant viscosity (*b*), convection consists of thin sinking sheets of cold fluid with hot fluid upwelling everywhere else. When the computer simulation is repeated for a fluid whose viscosity decreases markedly with temperature, heating from below (*c*) produces a convection cell in which the hot rising sheet is significantly thinner than the cold sinking sheet. When the heat is supplied from within variable-viscosity fluid (*d*), pattern is little changed from that seen when viscosity is constant.

they travel toward other sinking regions and combine with them in moving toward the interior of the fluid. The cycle is then repeated. The general form of the flow closely resembles the plate motions, with a thin, cold upper boundary layer and sinking sheets in motion, but the horizontal dimension of the motion is once again similar to the depth of the convecting layer.

In all the laboratory experiments the hot fluid is less viscous than the cold fluid, but this variation in viscosity only affects the flow strongly when the hot region is less viscous than the cold region by a factor of 10 or more. When the convection is driven by heating from below, the hot, low-viscosity, rising region becomes thinner and the sinking region broader than would be the case if there were little difference in viscosity. When the heat is supplied from within the fluid, there is no pronounced change in the form of the flow even where there are large differences in viscosity. The rather limited experiments on internal heating that have been conducted so far suggest that such heating has a more important influence on the form of the convection than differences in viscosity do. Recently computer experiments have been performed on convection in fluids that not only show variations in viscosity but also behave according to more complicated and more realistic laws of flow found by deforming rocks at high temperature. Somewhat surprisingly the introduction of these laws has little influence on the form of the flow.

Although there is clearly much more to be learned about the plan forms of convection in fluids of various viscosities or of convection driven by internal heating, all convection cells with a width five or more times greater than the depth of the convecting layer have been found to be unstable. Several workers have reported generating stable cells, but the flow was stable only because boundary-layer instabilities were artificially suppressed.

The Small-Scale Convection

One obvious way to reconcile the geophysical observations, which demonstrate that the cells extend at least 10,000 kilometers horizontally, with the laboratory and computer experiments is to assume that mantle convection extends from the surface to the region where the mantle meets the earth's core at a depth of 2,900 kilometers. There are several objections to such a model. The most important is the great resistance sinking slabs encounter at a depth of 700 kilometers. Another objection is more complex. If the flow extends throughout the mantle, it must be almost entirely driven by internal heating, which implies a Rayleigh number of at least 50 million. As we have seen, under these conditions many jets and sheets sink

from the cold upper surface and the distance between them is only a small fraction of the depth of the convecting layer. To achieve conditions where this type of small-scale flow does not occur one must decrease the Rayleigh number by a factor of at least 1,000, or to about 50,000. Although our knowledge of the physical parameters of the earth's interior is not very precise, there seems no way to reconcile a figure of 50,000 with the estimated minimum value of 50 million required for deep convection in the mantle. We prefer a model in which the convection is confined to the mantle's outer 700 kilometers. The flow is then driven partly by heat generated within the fluid and partly by heat generated in the lower mantle and perhaps in the core, with the latter heat entering the base of the upper mantle by conduction.

The experimental results clearly imply that there is small-scale convection in the upper mantle, with a distance of about 700 kilometers between the rising and sinking regions. In addition, however, there must be a large-scale convection to account for the geophysical observations, in particular the motion of the surface plates. Convection involving high Rayleigh numbers often occurs on several scales. The circulation of the atmosphere and of the oceans, driven by large-scale differences in density, provides familiar examples. In both cases large-scale motions are superimposed on small-scale convective features. Clouds are such a convective feature. Convection in the mantle, however, is quite different from the convection seen in the atmosphere and in the oceans because in the mantle the Reynolds number is small and momentum is unimportant.

To test the hypothesis that there are two scales of convective flow in the mantle we need geophysical evidence that the small-scale flow exists. One would also like to understand how the large-scale flow can be stable, as it so obviously is. The plan form of the small-scale flow probably depends on how strongly the surface plates and the mantle are coupled. If there is no slippage between a moving plate and the mantle, a substantial layer of the upper mantle will be dragged along by the plate. In that case the mantle under the moving layer will be strongly sheared.

We can simulate such a condition in our laboratory apparatus by arranging matters so that a sheet of the plastic Mylar, representing a plate, moves across the top of the convecting fluid at a steady rate. When the velocity of the plastic sheet exceeds a certain low value, the convection takes the form of rotating cylinders whose axes are aligned in the direction of the shear. The shearing merely transports the fluid along the cylinder and therefore has no effect on the small-scale convection. Convective cylinders in sheared flow are often seen in the atmosphere, where they take the form of cloud "streets": parallel rows of puffy clouds all about the same size. The shear required to change the three-dimensional bimodal or spoke patterns into cylindrical ones depends on the Rayleigh number. In the laboratory the cylindrical convection cells develop when the speed of the plastic sheet corresponds to a plate velocity of about 10 centimeters a year for a convecting layer 700 kilometers thick (assuming that there is no slippage between the plate and the mantle).

This general understanding of the physics of vigorous convection is obviously a great help in understanding convection in the earth's mantle. Instead of trying to apply the limited geophysical observations to guess the form of the flow, we can apply them to test models that are compatible with laboratory experiments. As we noted at the outset, however, the plates are so rigid they mask most of the effects that might be associated with small-scale convection. Two of the important effects that are not masked are regional variations in gravity and in the depth of the ocean.

Gravity anomalies extending over a distance of 1,000 kilometers or more originate with differences of density in the mantle and associated deformations of the surface. Variations in the depth of the ocean are slightly less easy to interpret. The most obvious variation in depth results from the cooling and shrinking of a plate as it moves away from the axis of a mid-ocean ridge, where the growth of the plate begins

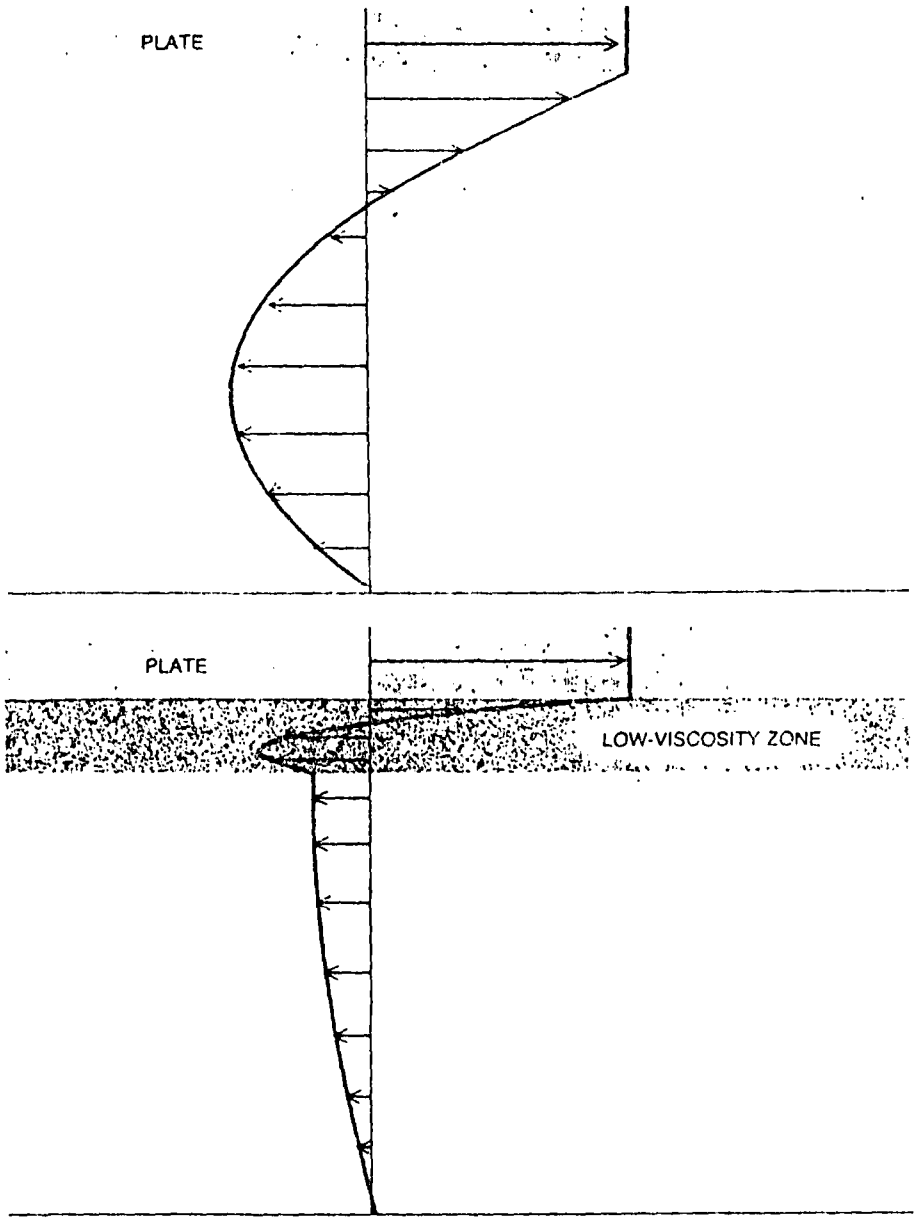

FLOW UNDER PLATES may follow either of two general schemes. In one model (*top*) the viscosity of the material under the plates is uniform. Thus a considerable layer of fluid is swept along by the plate motion. In order for mass to be conserved there must be a strong reverse flow deeper in the mantle. If, however, there is a thin layer of low-viscosity material under the plates (*bottom*), surface motions are decoupled from mantle and basically only mass of plates themselves need be carried by return flow. Geophysical observations favor decoupled model.

with the upwelling of hot material from the mantle. Because all plates cool the same way the depth of the ocean should be a function of the age of the plate material at that point, unless other forces are at work. The expected depth can readily be calculated. When this is done carefully, regional departures from the expected depth are revealed that correspond closely to the gravity anomalies. There are good reasons to believe the variations in depth and gravity are associated with convection currents at the base of the plates.

The first question we must answer is whether the moving plates sweep the upper part of the mantle along with them or whether they are decoupled from the convection cells in the mantle by a thin layer of low-viscosity material. If the plate motion sweeps much material along with it, there must be some kind of return flow at greater depth; otherwise mass would not be conserved. The return flow must be driven by a drop in pressure between the deep ocean trenches, where the plate plunges into the mantle, and the mid-ocean ridge. The required pressure difference should cause the top of the plate to slope. No such slope has been detected, and there is no obvious gravity anomaly produced by the material being carried into the trench and its return flow. Therefore the geophysical observations favor the decoupling of the plate from the mantle by a low-viscosity layer. The existence of such a layer was proposed independently of plate-tectonic theory to account for the observed damping of earthquake waves. The layer is conceivably created by the partial melting of rock between the crust and the mantle.

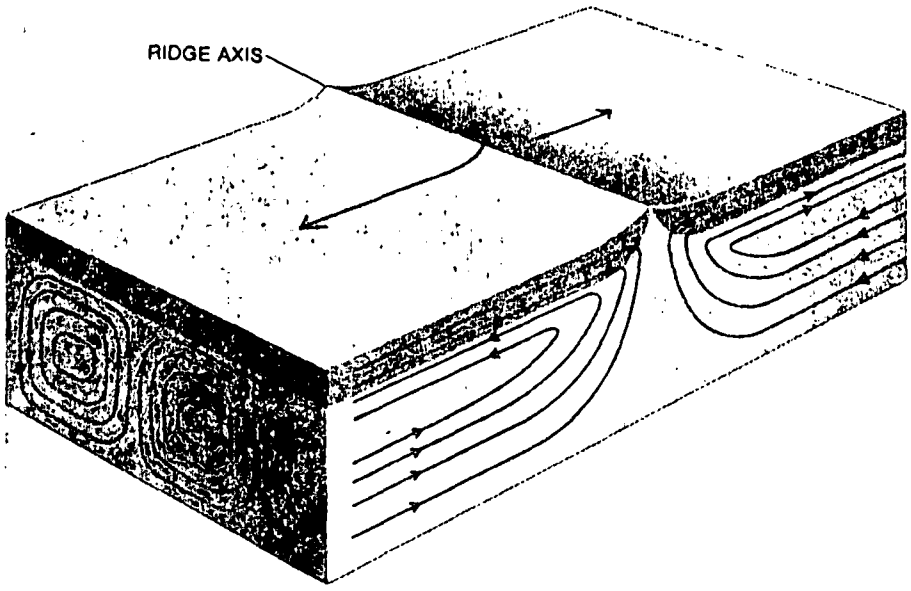

POSSIBLE MODEL OF CONVECTION under plates in the vicinity of a mid-ocean ridge visualizes flow on two scales. If the plates are moving apart fast enough, by 10 centimeters or more a year, the small-scale convection may be transformed into longitudinal cylinders with axes parallel to the plate motion. Exactly how the large-scale convection associated with the plate motion would interact with the longitudinal convection cylinders remains to be clarified.

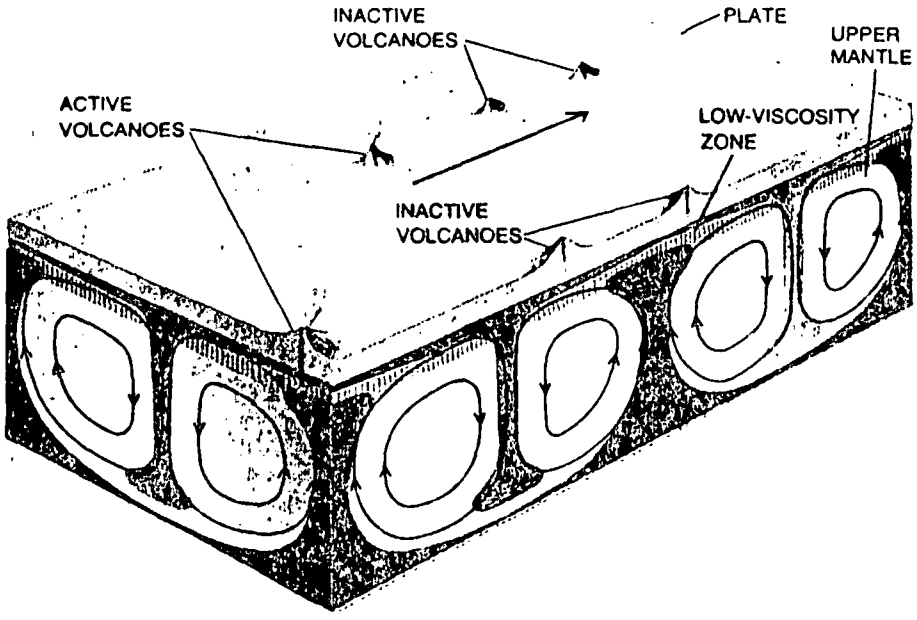

ALTERNATIVE MODEL OF MANTLE CONVECTION may explain the creation of chains of volcanoes in which the site of active volcanism does not move as fast as the plates. This diagram attempts to show only the small-scale convection cells; the large-scale circulation is omitted. The small-scale flows are somewhat decoupled from the plates by a thin, low-viscosity layer that may be partially molten. Part of the heat needed to drive the small-scale circulation comes from the lower mantle and part from the decay of radioactive isotopes within the layer. Since the viscosity decreases with temperature the heat from below produces thin rising jets of hot material. The internal heating creates cold sinking sheets and jets, which dominate the overall flow. Because of the decoupling layer the hot rising jets can erupt as active volcanoes that do not move with the plate, whereas lava cones of extinct volcanoes do move.

The Decoupling of the Plates

Recent attempts to determine the forces acting on plates by analyzing their motions in some detail have also suggested that they are decoupled from the mantle. Little is known, however, about the viscosity of the layer responsible for decoupling, which is probably less than 50 kilometers thick. If the plates and the mantle are indeed decoupled, the resistance to plate motions is greatly reduced, and the various sources of convective energy associated with plate motions can easily provide enough power to drive the large-scale flow at the velocities observed. The most obvious source of energy is the upwelling of hot material from the mantle, which pushes the plates apart at the mid-ocean ridges. Even more important is the sinking of the cold, dense plates back into the mantle, which would tend to pull the plates toward the trenches.

There is little direct evidence of small-scale flow in the mantle. If the plates and the mantle are not decoupled, under plates that are moving rapidly such flows should take the form of rotating cylinders. If a low-viscosity layer provides decoupling, we expect the small-scale flow to be three-dimensional and complicated. We expect it to consist of both hot rising material and cold sinking material in the form of jets and sheets. Since roughly half of the convective layer's heat comes from conduction through the base of the layer and half comes from within, we expect more sinking regions than rising ones, and we also expect the variation of viscosity with temperature to make the rising flows narrower than the sinking ones.

Attempts have been made to detect the small-scale convection, but they have met with only marginal success. Not all geophysicists accept the gravity

anomalies and depth variations as convincing evidence for small-scale flow. Nevertheless, there is good evidence for some type of convective heat transport other than that directly associated with the plate motions. The increase in the depth of the ocean with the age of the plate at the bottom agrees closely with the subsidence calculated for a plate about 120 kilometers thick. If the mantle below a depth of 120 kilometers could cool by conduction, the oldest parts of the Atlantic and the Pacific would be about a kilometer deeper than they actually are. Such cooling can be prevented only if heat is transported to the base of the plate by convection. The ocean-depth observations do not, however, supply any information about the plan form of the inferred convection. Although it seems likely that small-scale convection of the type we have described is responsible, any form of convective heat transport would account for the observations.

There is one other set of observations that offers evidence for both decoupling and small-scale convection: the chains of volcanoes that form ridges in parts of the deep ocean. The best-known example is the Hawaiian Ridge in the Pacific. The two currently active volcanoes are on the island of Hawaii at the southeast end of the ridge. The volcanic rocks that form the ridge increase steadily in age with their distance from Hawaii. Several ridges in the Indian Ocean and the Atlantic resemble the Hawaiian Ridge.

The interesting point is that the motion of an active site of such volcanism with respect to another active site is only one or two centimeters a year, whereas the motion of one plate with respect to another is more than 10 centimeters a year. These measurements indicate that the source of the lava for the volcanoes lies under the plates and does not move with them. According to this view, the volcanoes are the surface expression of jets of hot material that rise to the surface from the base of the mantle.

The principal objection to this concept comes from the computer models of the behavior of internally heated fluids, which show that although sinking cold jets are generated, hot rising ones never are. No such difficulty arises, however, if convection is confined to the upper 700 kilometers of the mantle. Since this region is heated both from below and from within, hot jets should be able to form in it. Furthermore, such jets will not move with the plates, because they are decoupled. On the basis of the laboratory experiments one would expect the small-scale convection to be time-dependent. Hence it is not surprising that there is a certain amount of slow movement in the jets that have given rise to the volcanoes of the oceanic chains.

We should obviously like to have more information about the form of the small-scale flow, but it is nonetheless pleasing that we can account for all the relevant geophysical observations with a model based on laboratory experiments. The fact remains that the observations are all too few. With recent advances in the measurement of the earth's gravity by satellites, however, our knowledge of the gravity anomalies under the oceans should increase rapidly over the next few years. And laboratory experiments at large Rayleigh numbers (10^6 to 10^7) and small Reynolds numbers are possible, although difficult, and they should help us to understand the features detected by the satellites.

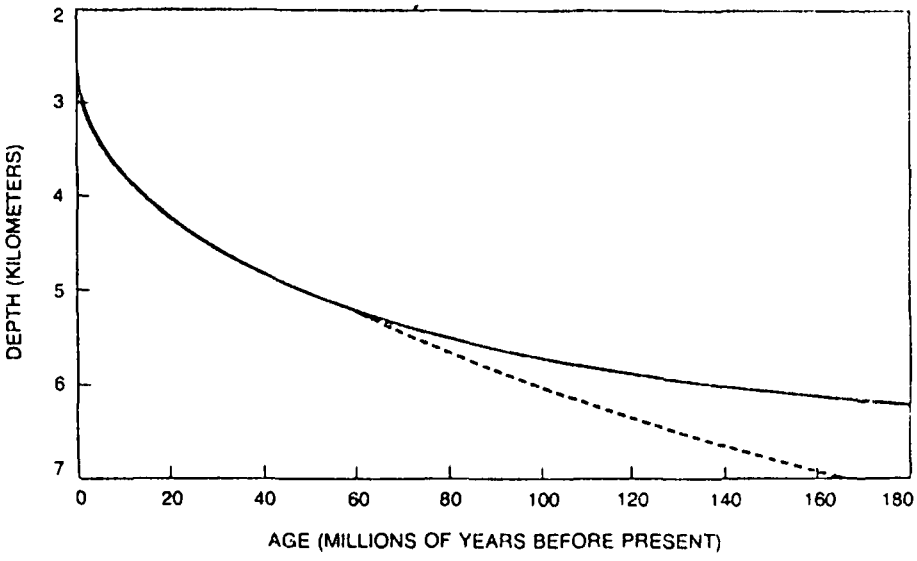

DEPTH OF THE OCEAN increases with the age of the sea floor because of thermal contraction as the plate cools from a high uniform temperature at the axis of the mid-ocean ridge. If the cooling continued uniformly with age as the plate moved away from the ridge, the depth of the ocean should follow the broken curve. Actual depth measurements, however, yield solid curve, which conforms to cooling of plate 120 kilometers thick whose base is at 1,200 degrees Celsius. It appears that heat is supplied from below, probably by small-scale convection.

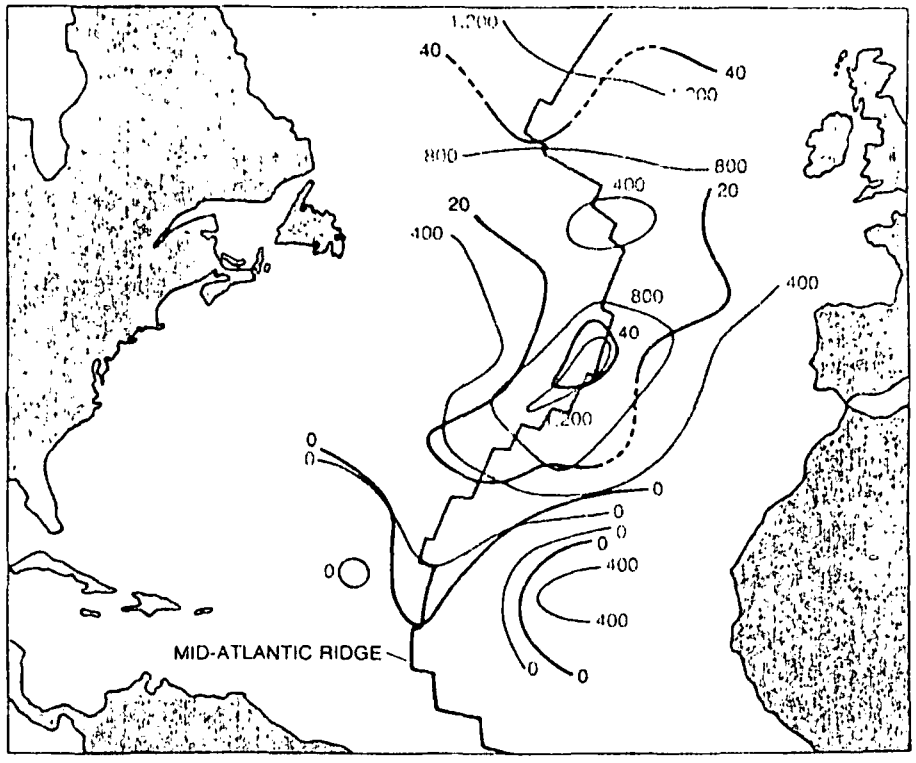

DEPTH OF THE NORTH ATLANTIC is shown in meters (*color*) after removal of the effect of cooling of the plate by age. Black lines show contours of the gravity field in milligals. The variations in the two features seem to be closely related and could be evidence for a region in which hot mantle material is carried upward by small-scale convection currents. Neither the depth of the ocean nor the gravity field seems to bear much relation to Mid-Atlantic Ridge (*gray line*), where the North American plate and the Eurasian plate are being pushed apart.

occur in island-arc regions in subsidiary amounts; these may be generated by partial fusion within the ultramafic mantle rocks which overlie the slip-zone.

In the processes operating at plate margins we see possible mechanisms for generating the Earth's crust. By partial fusion of the mantle, it is possible to generate oceanic crust; by a second cycle of partial fusion, in which the oceanic crust is itself partially fused, it is possible to generate the more silicic rocks of the continental crust.

The theory of Plate Tectonics has therefore gone some way towards providing a unifying theory for understanding the wide variety of Earth phenomena which were previously neither understood in themselves nor in any wider context. We see some pattern in the distribution of world-wide seismicity and volcanicity, a mechanism for the generation of the two main crustal types, clear evidence of large-scale motions between crustal plates and between the continents which some of them contain. We see that, whilst oceanic crust is 'disposable', continental crust cannot return into the mantle. Is it too presumptuous to assert that the general outline of the processes we have discussed is sufficiently consistent internally to suggest that it is probably correct?

DIVISION OF ENGINEERING

DEEP CRUSTAL STUDIES OF THE EARTH (PROJECT MOHOLE)*

Gordon Lill

National Science Foundation, Washington, D.C.

Introduction

The National Science Foundation has initiated a program for studying the crustal section of the earth and the upper portion of the mantle beneath that is within reach by direct observation. These studies will be made possible by drilling for core samples on the continents as well as into the bottom of the deep sea floor. The continental program has been devised on a world-wide scale by the Upper Mantle Committee of the International Union of Geodesy and Geophysics (IUGG); a member of the International Council of Scientific Unions (ICSU).

Plans for drilling into the crust underlying the deep oceans of the world had a different origin than the International Upper Mantle program and preceded it by about a year. However, it is included as a part of the United States program and contributed directly to the formation of plans for studying the crust and mantle on an international scale.

The subject of this paper is Project Mohole, the most spectacular part of the Upper Mantle Program that is to be found in any nation. It involves drilling in oceanic depths of 12,000 to 14,000 feet and on through the crust to perhaps a total depth of 35,000 feet below sea level. Special techniques and equipment have been developed to make this possible.

Drilling to the mantle beneath the sea is a difficult engineering feat, but the Foundation has for some time considered this objective as only one aspect of a program with the much broader aim of studying the earth as a planet. Eighty-five per cent of the earth by volume is in the mantle. If we can sample it, we will surely obtain a better understanding of the earth as a body in space rather than thinking of it piecemeal as a continent or an ocean, a deep sea canyon or a high mountain peak.

The Science

Within the earth's mantle lie the sources of stress that cause the great tectonic features that confront the geologist. These all must somehow be explained: volcanism, mountain building, earthquakes, continents and oceans. The geologist has always had to rely upon what he finds in the rocks in order to interpret the history of the earth and to infer the processes that have operated to produce the features at the earth's surface. First, he collected evidence from the field. Then, especially during the last twenty years, he has been greatly assisted (and at times even surpassed) by the physicist,

* This paper, illustrated with slides, was presented at a meeting of the Division on October 13, 1965.

chemist and hydrodynamicist. But now, having gone around the circuit through postulate and theory, we find ourselves back once again with the rocks. The reason is simple. Our theories about the earth have been invented largely from what we know of less than 1 per cent of its volume and 30 per cent of its surface. We have never had rocks from the deep crust or mantle, and, until quite recently, we have not even had rocks from the top of the oceanic crust of the deep sea basins. As in all sciences, we must now check theory with direct evidence if we are to progress. Theory without experimental proof more often than not remains sterile.

Careful geochemical analysis of the basalt recovered during Phase I of the Project in 1961 has already called into question some of our thoughts on the magmatic differentiation of continental crust from mantle, the origin of the continents, the chemical nature of the mantle, the nature of the Mohorovicic Discontinuity which divides crust from mantle, and our concepts of heat flow from the mantle outward through the crust of the ocean basins and continents.

Quite recently, additional developments in other fields have made an understanding of the nature of the earth's mantle increasingly important to the orderly growth of science. For example, the largest and most exciting technical and scientific project in any nation, landing men on the moon and returning with samples of its surface material, is approaching realization. In addition, in the past few months we have received the first close-up photographs of the planet Mars. Because of these developments, it is not only timely but urgently necessary that we know enough about the interior of the earth to enable us to interpret effectively the returns expected from the nation's planetary and lunar programs. Knowledge of the chemical phases and composition of the mantle will bear directly on the theories that deal with the differentiation of the earth-moon system and the solar system as a whole. Without earth-mantle data, further development of these theories will not have adequate foundation.

The recent development of a new hypothesis on the origin of linear magnetic anomalies over the oceans opens up a possibility of understanding convection within the mantle and may place limits on its velocity. The size and shape of the magnetic anomalies indicate that their origin cannot be more than 10 km. deep and perhaps is in the upper 1 km. of the ocean crust. Mohole drilling through the crust should provide answers to the question of mantle convection which would have a large impact on problems of the earth's interior.

There is a growing amount of evidence that would indicate that the continents have drifted, while, at the same time, new theories are being proposed in an attempt to prove that the continents cannot possibly have drifted. Drilling into the deep sea crust will either add to, or detract from, the belief in continental drift depending upon whether or not extensive thicknesses of sedimentary rocks are found in the deep sea basins. If the ocean basins as we see them today are permanent features, then the continents cannot have moved, and we should find approximately 10,000 feet of sedimentary rock beneath the sea. If the sedimentary rocks are not present, then the ocean basins cannot be permanent or near permanent features, and the continents may well have drifted.

This problem has a direct bearing upon the amount of carbon dioxide that may be stored in the rocks beneath the sea in the form of limestone ($CaCO_3$)

or dolomite $CaMg(CO_3)2$
cycle during past geolog
today. If we are effecti
much is in the rocks, in
as carbon dioxide, in the
are among them all. Th
has taken in geologic hi
standing of the carbon c
found at the base of the
earlier forms of life tha
of the gaps in our knowle

Some of the theories
the universe, are based u
elements. The primary
knowledge of the distribu
inadequate since 85 per
has never been sampled.

As the Project has de
of the earth's interior h
now able to proposed t
corollary to drilling at
the world for the purpos
upper mantle. As a re
earth have been develope
sciences, and which mus
to advance.

The engineering aspe
that are either an integ
drilling platform. The sys

1. Drilling platform
2. Positioning system
3. Drilling system
4. Pipe racking system
5. Inspection and maint
6. Hole re-entry syste
7. Logging system
8. Riser casing system

The drilling platform
The design and specific
prime contractor, and Gi
photograph of the latest m

Size of upper platform
Height of upper platform
Diameter of supporting
Total height, keel to upp
Derrick height

or dolomite $CaMg(CO_3)2$. This, in turn, affects our estimates of the carbon cycle during past geologic ages as well as our estimates of the carbon cycle today. If we are effectively to account for the carbon, we must know how much is in the rocks, in the seas as calcium bicarbonate, in the atmosphere as carbon dioxide, in the plants and animals, and what the rates of exchange are among them all. The origin of life on earth and the various forms life has taken in geologic history are also intimately involved with our understanding of the carbon cycle. In addition, if very old sedimentary rocks are found at the base of the oceanic crust, we may also find fossil remnants of earlier forms of life than are presently known which would help to fill some of the gaps in our knowledge of the evolution of life.

Some of the theories of the origin of the universe, and of the stars within the universe, are based upon our knowledge of the distribution of the chemical elements. The primary base line available to the astrophysicist is his knowledge of the distribution of the elements in the earth. This knowledge is inadequate since 85 per cent of the earth by volume is in the mantle, and it has never been sampled.

As the Project has developed, a great deal of new interest in the problem of the earth's interior has been stimulated. Students of the solid earth are now able to proposed that a large number of holes be drilled on land as a corollary to drilling at sea. National committees have been formed around the world for the purpose of recommending research programs to study the upper mantle. As a result, a host of new geophysical theories about the earth have been developed that represent an enormous contribution to earth sciences, and which must be checked by actual sampling if the theories are to advance.

The Engineering

The engineering aspects of the project are contained in several systems that are either an integral part of, or are involved in the operation of, the drilling platform. The systems are listed below.

1. Drilling platform
2. Positioning system
3. Drilling system
4. Pipe racking system
5. Inspection and maintenance systems
6. Hole re-entry system
7. Logging system
8. Riser casing system

The drilling platform is the major technological development of the project. The design and specifications were prepared by Brown & Root, Inc., the prime contractor, and Gibbs & Cox, Inc., working as a team. FIGURE 1 is a photograph of the latest model. The principal dimensions follow.

Size of upper platform	279 ft. × 234 ft.
Height of upper platform	23 ft.
Diameter of supporting columns	31 ft.
Total height, keel to upper deck	135 ft.
Derrick height	196 ft.

Overall height, keel to top of radar mast	375 ft.
Diameter of lower hulls	35 ft.
Length of lower hulls	390 ft.
Light ship displacement	13,500 tons at 28 ft. draft
Normal drilling displacement	21,500 tons at 60 ft. draft

Brief specifications of the Mohole drilling platform are listed below.

Total horsepower	19,500 to 21,000
HP for positioning	4,500 to 6,000
HP main propulsion	15,000
Total complement	160
Standard speed	10 to 12 knots
Hook load on the derrick	1,000,000 pounds
Drill pipe and/or casing	35,000 ft.

Positioning system - automatic, dynamic, acoustic
One 30-ton rotary deck crane
Two 50-ton rotary deck cranes.

The platform is designed to stay on station and drill under conditions prevailing with 30-knot winds, fully developed seas (28 to 30 foot waves) and 3-knot surface currents. Work would cease under worse conditions, but the site would have to be abandoned only under near hurricane or hurricane conditions.

In order to imagine adequately the size of this proposed platform, one should stand on a street corner and gaze upward to the tenth story of a building and let your eyes rove down the street to the middle of the next block. It helps also, in thinking of the size, to note that the platform cannot go under the Golden Gate Bridge or through the Suez Canal.

Mounted beneath each of the six vertical columns of the platform are positioning engines that will deliver from 750 to 1,000 shaft horse power each. These engines are automatically tied through computers to the positioning system that is shown in FIGURE 2.

The Positioning System consists of both a long and short base line of bottom-mounted acoustic transponders sending variable signals of from 9 to 27 kilocycles to hydrophones that are lowered beneath the platform. As signals are received, the platform's position among the transponders is computed and signals are sent to the positioning engines for the required thrust and direction for keeping the platform centered above the hole.

In 12,000 feet of water, the platform must be kept within a radius of 300 feet of the hole in order to keep the bending stress on the drill stem within tolerable limits. The 300 feet is an empirical number based on the limited experience during the Phase-I drilling off Guadalupe in 1961. Only further experience will give us a better limiting distance on the horizontal excursion of the platform.

Also involved in the matter of position keeping is a third system called the riser casing. This system is shown schematically in FIGURE 3. The riser, which is casing in sea water, serves two purposes. In this case it brings the drill hole up to the surface, thus solving the problem of hole re-entry, and it provides a closed system within which is contained the drilling fluid or mud. The mud flows under pressure down the inside of the drill stem, out the bit, and up to the pumps between the drill stem and riser casing.

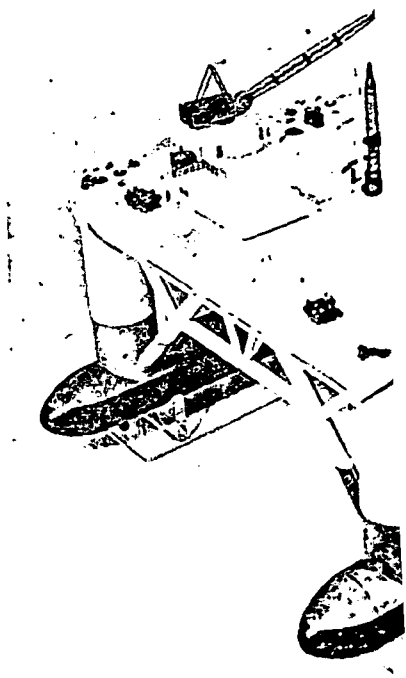

FIGURE 1. Model of

The mud cools and lubricates t
the rock cuttings up to the surface

The riser casing is cemente
between hard rock and sediment.
on the bottom and is held upright
buoys pulling upward with a total
buoyancy system is also provide
or severe storms.

Academy of Sciences

st	375 ft.
	35 ft.
	390 ft.
	13,500 tons at 28 ft. draft
	21,500 tons at 60 ft. draft

lling platform are listed below.

	19,500 to 21,000
	4,500 to 6,000
	15,000
	160
	10 to 12 knots
	1,000,000 pounds
	35,000 ft.

ic, acoustic

on station and drill under conditions eloped seas (28 to 30 foot waves) and ease under worse conditions, but the under near hurricane or hurricane

size of this proposed platform, one upward to the tenth story of a build- treet to the middle of the next block. ote that the platform cannot go under ez Canal.

ertical columns of the platform are rom 750 to 1,000 shaft horse power ed through computers to the position-

both a long and short base line of sending variable signals of from 9 e lowered beneath the platform. As osition among the transponders is positioning engines for the required rm centered above the hole.

must be kept within a radius of 300 ding stress on the drill stem within irical number based on the limited ff Guadalupe in 1961. Only further istance on the horizontal excursion

n keeping is a third system called n schematically in FIGURE 3. The erves two purposes. In this case it us solving the problem of hole re- thin which is contained the drilling essure down the inside of the drill en the drill stem and riser casing.

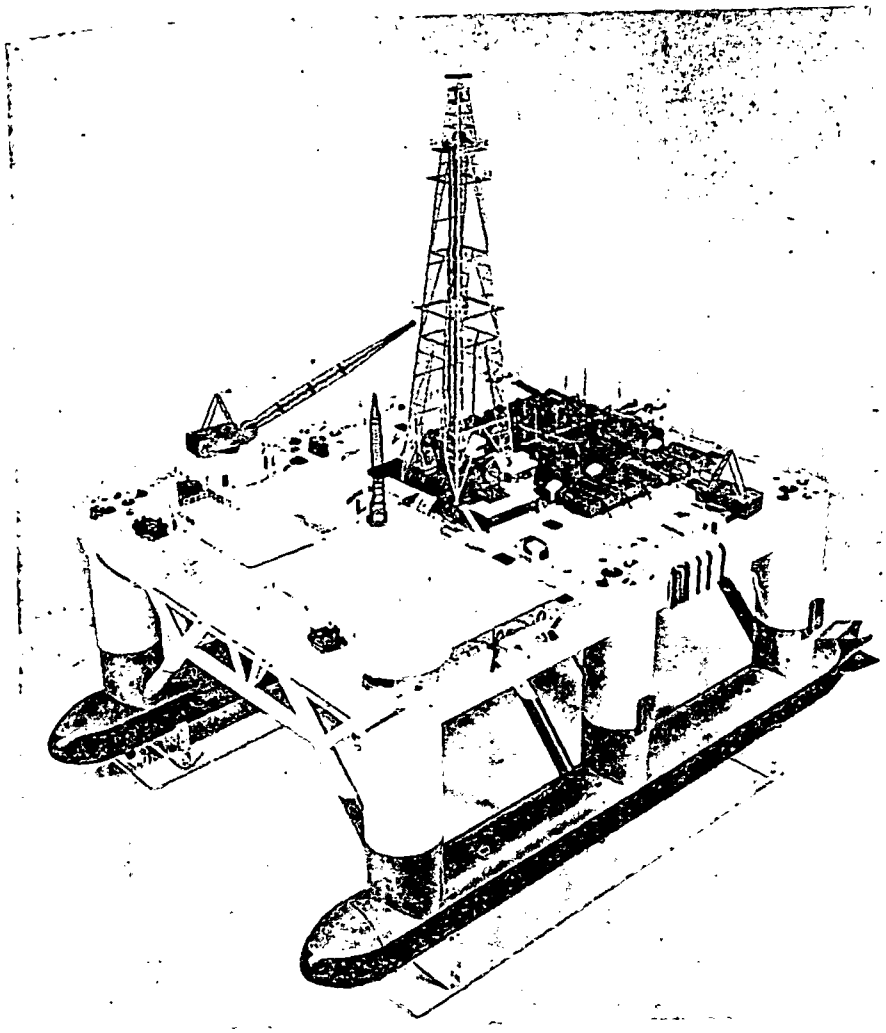

FIGURE 1. Model of the Mohole Drilling Platform.

The mud cools and lubricates the bit and keeps the hole open by carrying the rock cuttings up to the surface where they may be examined.

The riser casing is cemented well into the bottom below the boundary between hard rock and sediment. It is partially supported by a landing base on the bottom and is held upright, much like a taut wire by a series of static buoys pulling upward with a total buoyancy of 2,000,000 pounds. A variable buoyancy system is also provided for emergencies such as strong currents or severe storms.

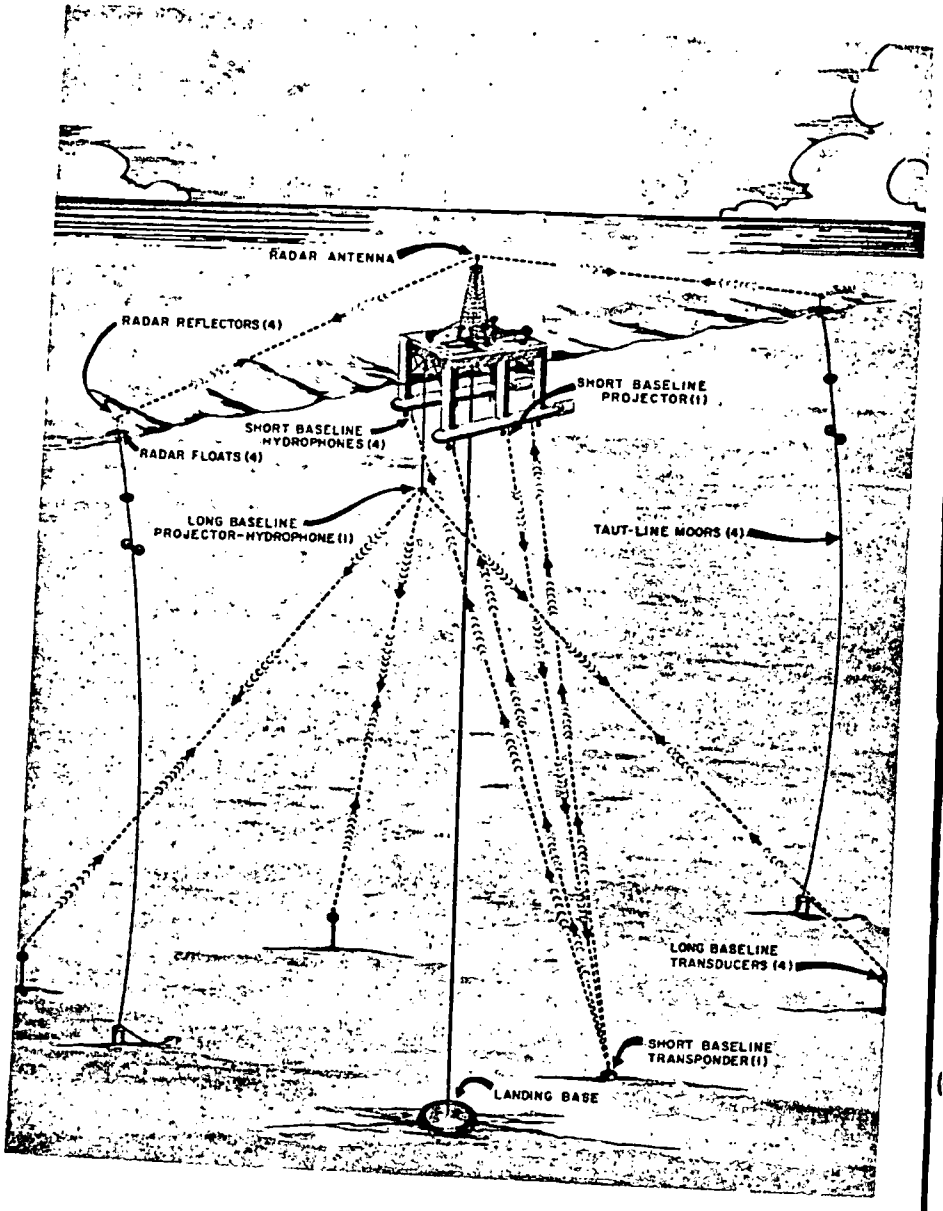

FIGURE 2. Mohole Project Positioning System.

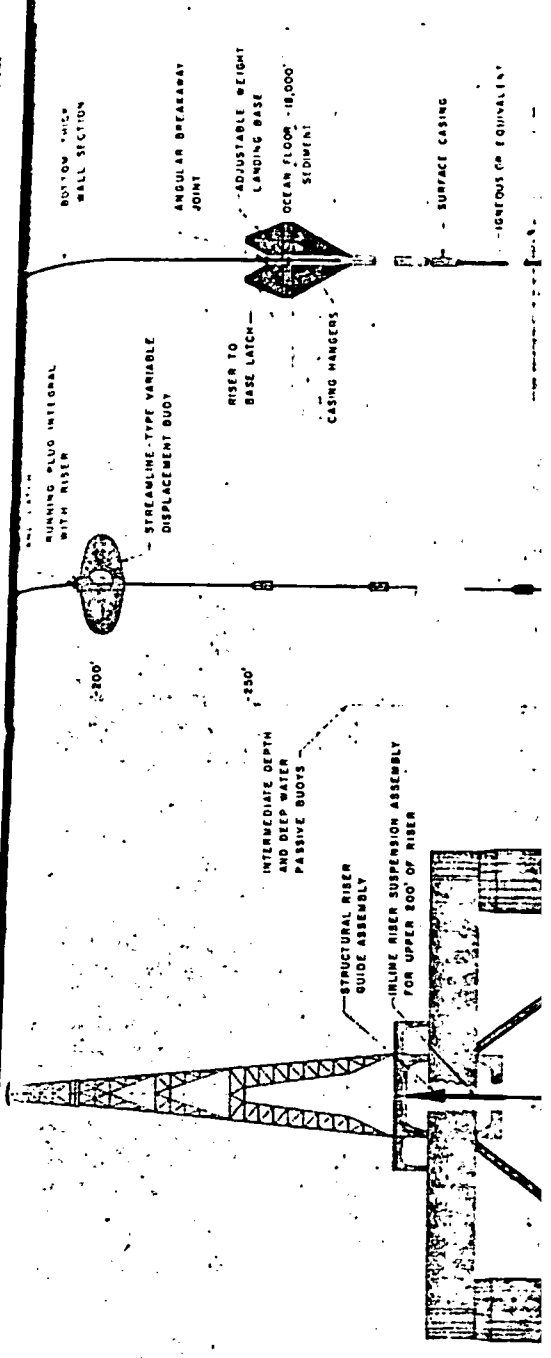

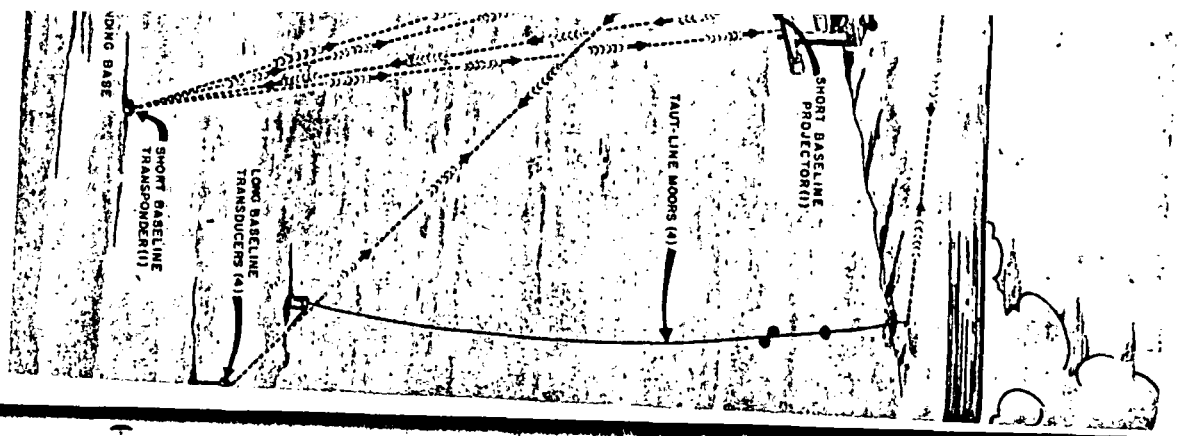

sitioning System.

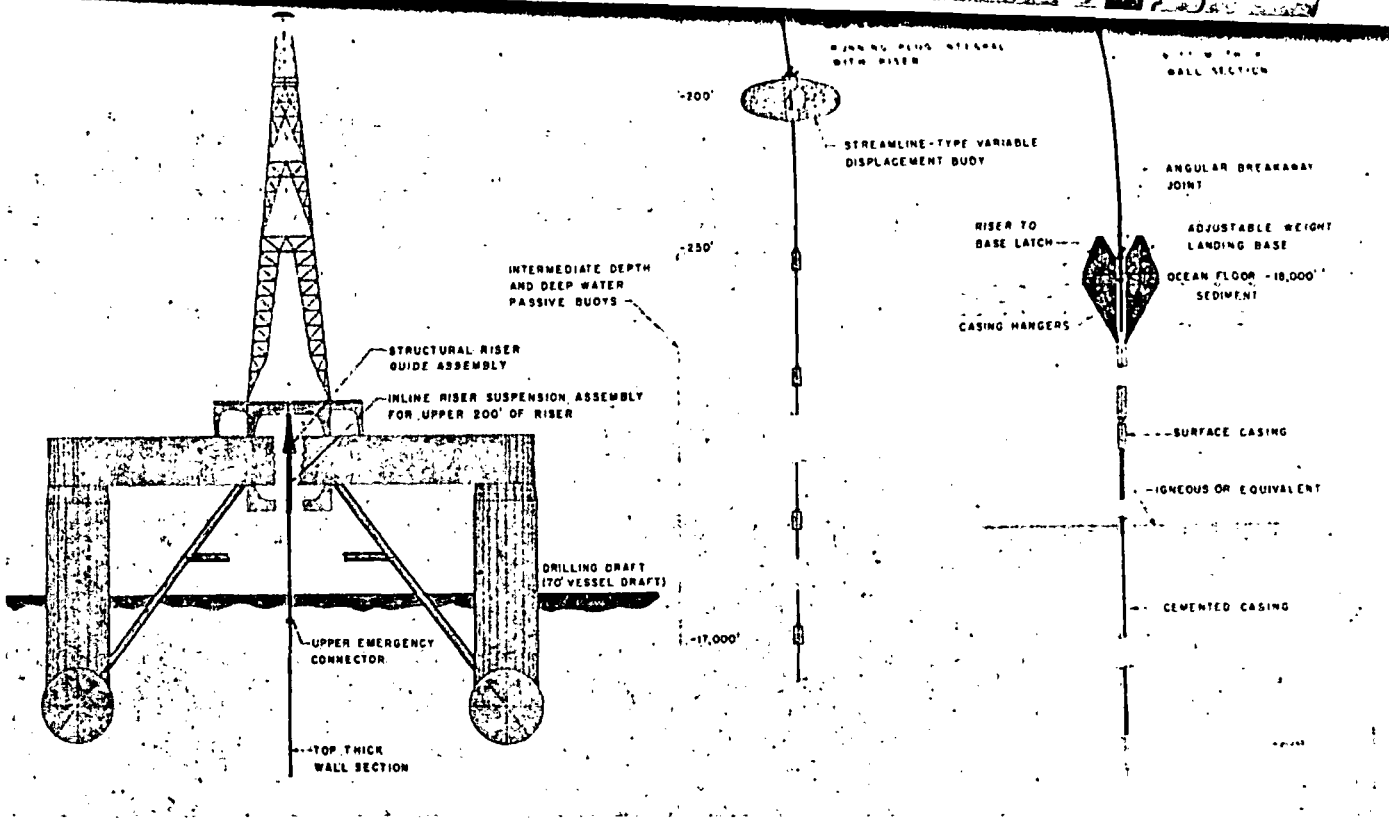

FIGURE 3. One of the schemes showing how the riser casing will be supported by both static and variable displacement buoys.

The best material for the buoys appears at this time to be a syntact foam called Inlyte. It consists of an epoxy base containing minute, hollow gla beads.

The riser casing will be fitted with telescoping joints, called bumper sub at the upper end to absorb the vertical motion of the platform.

The drilling system is quite similar to that found in the offshore drilli industry except for its increased size. The automatic pipe racking system i an innovation but is complicated and is worthy of separate treatment in it own right, as are the other systems which will not be discussed here.

Test Drilling

I shall now discuss the test drilling that has been done to check variou parts of the program as we have proceeded with the job.

The first drilling, called Phase-I, was completed in March and April 196 off LaJolla and off Guadalupe Island. The major purpose of Phase-I was t prove that drilling could be done in 12,000 feet of water. The drilling sit is shown in FIGURE 4. At this site we drilled through 540 feet of soft, gray green, silty clay and on down 60 feet into a hard glassy basalt. The drilling wa accomplished from the Global Marine Company's drilling barge CUSS-I show here in FIGURE 5. CUSS-I is a 260-foot converted, ex-Navy YNFB barge She still is one of the busiest rigs in Global's fleet. For the first time durin Phase-I, the second layer of the oceanic crust was sampled. It proved to b the volcanic rock basalt. The results of its analysis have already been men tioned under the section on science.

The second experimental drilling was done at Mayaguez, Puerto Rico, in 1962. The major purpose there was to check the drilling characteristics of the igneous rock called serpentinite. The location of the hole is shown o the index map, FIGURE 6.

Serpentinite, a hydrous magnesium silicate, generally gray-green i color, is presumed by some geologists to form the upper mantle and perhaps a part of the lower crust. Since this is a likely supposition, it seemed wise to determine its drilling and structural characteristics. Continuous core samples were taken at Mayaguez. The serpentinite was highly fractured o faulted and tended to flow rather easily under pressure. The drilling was carried out by Boyles Brothers of Salt Lake City, Utah. The drilling rate averaged about 1.5 ft. per hour.

The most recent test drilling was completed at Uvalde, Texas, in Decem ber, 1964. Here, again, we wished to test the drilling characteristics of one of the rocks we know we will find in some undetermined thickness beneath the sea. The rock is basalt similar to that found at Guadalupe; the difference in the Uvalde test is that we had some new equipment with which to experiment.

The drilling was done in a volcanic plug which penetrated the surrounding sediments to within about 500 feet of the surface. A total depth of 3,479 feet was drilled, out of which 1,884 of core was recovered.

The most noteworthy equipment tested was the Dresser Industries (Dallas, Tex.) coring turbodrill, although logging instruments, and diamond bits from various manufacturers were tested as well. The turbocorer drilled a total of 1,194 feet in 216 hours and 10 minutes for an average penetration rate of 5-1/2 feet per hour. This exceptional drilling tool is shown in FIGURE 7. The

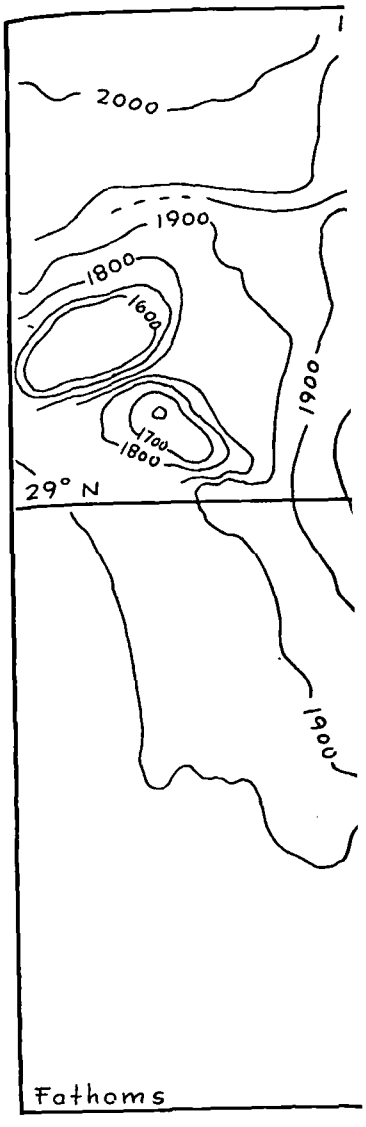

FIGURE 4. Project Mohole expe

or the buoys appears at this time to be a syntacti
sists of an epoxy base containing minute, hollow glas

be fitted with telescoping joints, called bumper subs
o the vertical motion of the platform.
s quite similar to that found in the offshore drillin
creased size. The automatic pipe racking system i
plicated and is worthy of separate treatment in it
r systems which will not be discussed here.

Test Drilling

ıe test drilling that has been done to check various
e have proceeded with the job.
ed Phase-I, was completed in March and April 196
ılupe Island. The major purpose of Phase-I was t
l be done in 12,000 feet of water. The drilling site
t this site we drilled through 540 feet of soft, gray-
vn 60 feet into a hard glassy basalt. The drilling was
obal Marine Company's drilling barge CUSS-I shown
S-I is a 260-foot converted, ex-Navy YNFB barge,
est rigs in Global's fleet. For the first time during
of the oceanic crust was sampled. It proved to be
The results of its analysis have already been men-
ı science.
ıtal drilling was done at Mayaguez, Puerto Rico,
se there was to check the drilling characteristics
l serpentinite. The location of the hole is shown on

ıS magnesium silicate, generally gray-green in
ıe geologists to form the upper mantle and perhaps
Since this is a likely supposition, it seemed wise
and structural characteristics. Continuous core
yaguez. The serpentinite was highly fractured or
v rather easily under pressure. The drilling was
others of Salt Lake City, Utah. The drilling rate
our.
illing was completed at Uvalde, Texas, in Decem-
e wished to test the drilling characteristics of one
will find in some undetermined thickness beneath
similar to that found at Guadalupe; the difference
ad some new equipment with which to experiment.
a volcanic plug which penetrated the surrounding
500 feet of the surface. A total depth of 3,479 feet
184 of core was recovered.
ıipment tested was the Dresser Industries (Dallas,
ıough logging instruments, and diamond bits from
e tested as well. The turbocorer drilled a total
and 10 minutes for an average penetration rate of
ceptional drilling tool is shown in FIGURE 7. The

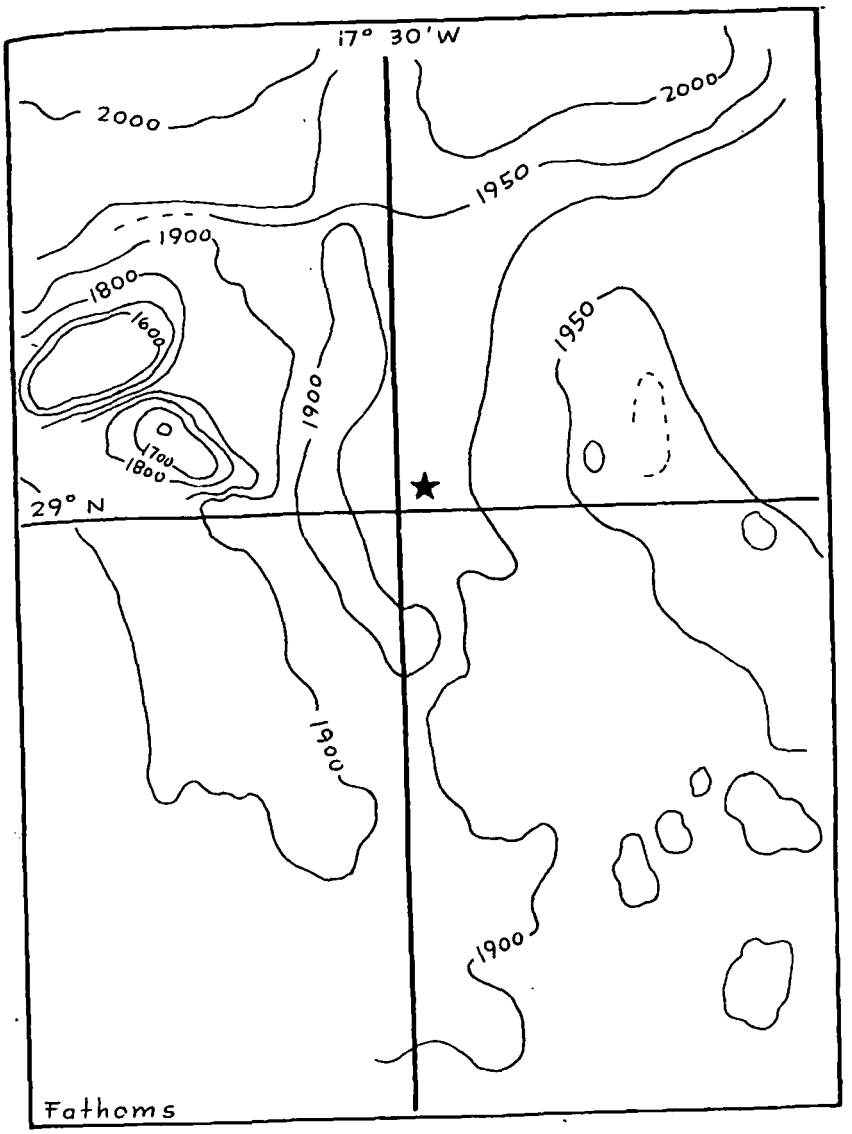

FIGURE 4. Project Mohole experimental drilling site (from Kraus & Menard).

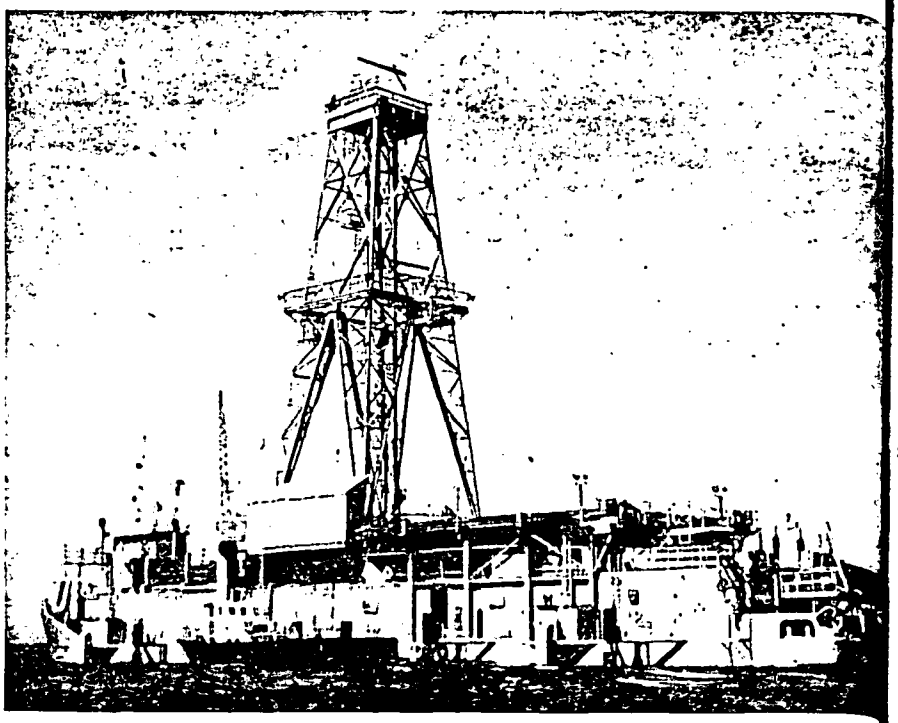

FIGURE 5. Cuss-I Global Marine, Inc., Los Angeles, drilling ship.

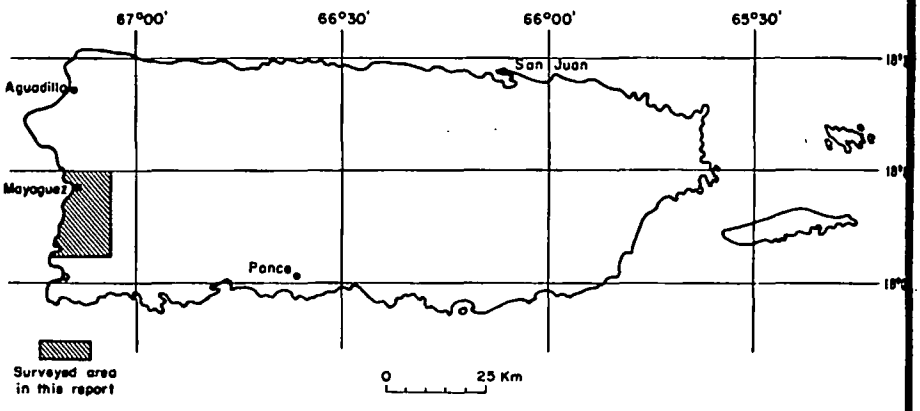

FIGURE 6. Index map of Puerto Rice showing area of survey.

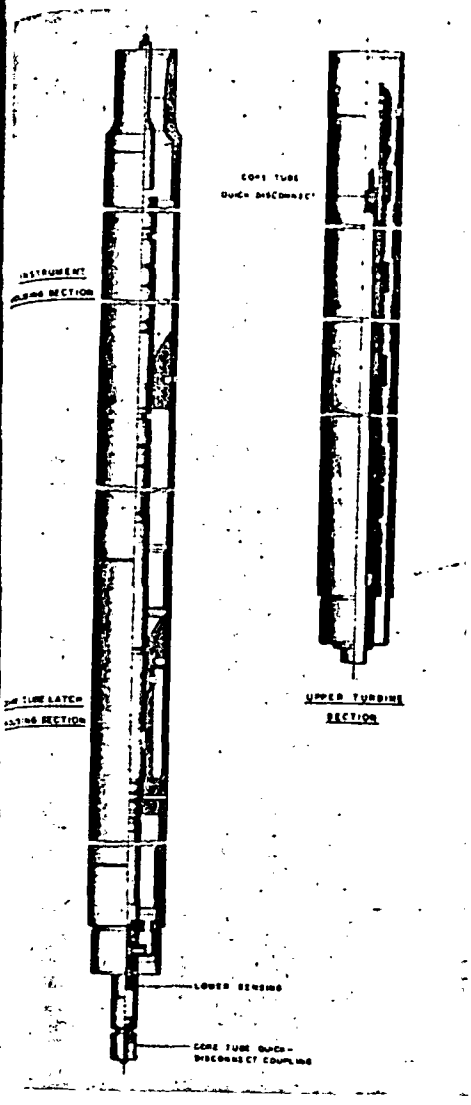

FIGURE 7. Eight and one-hal

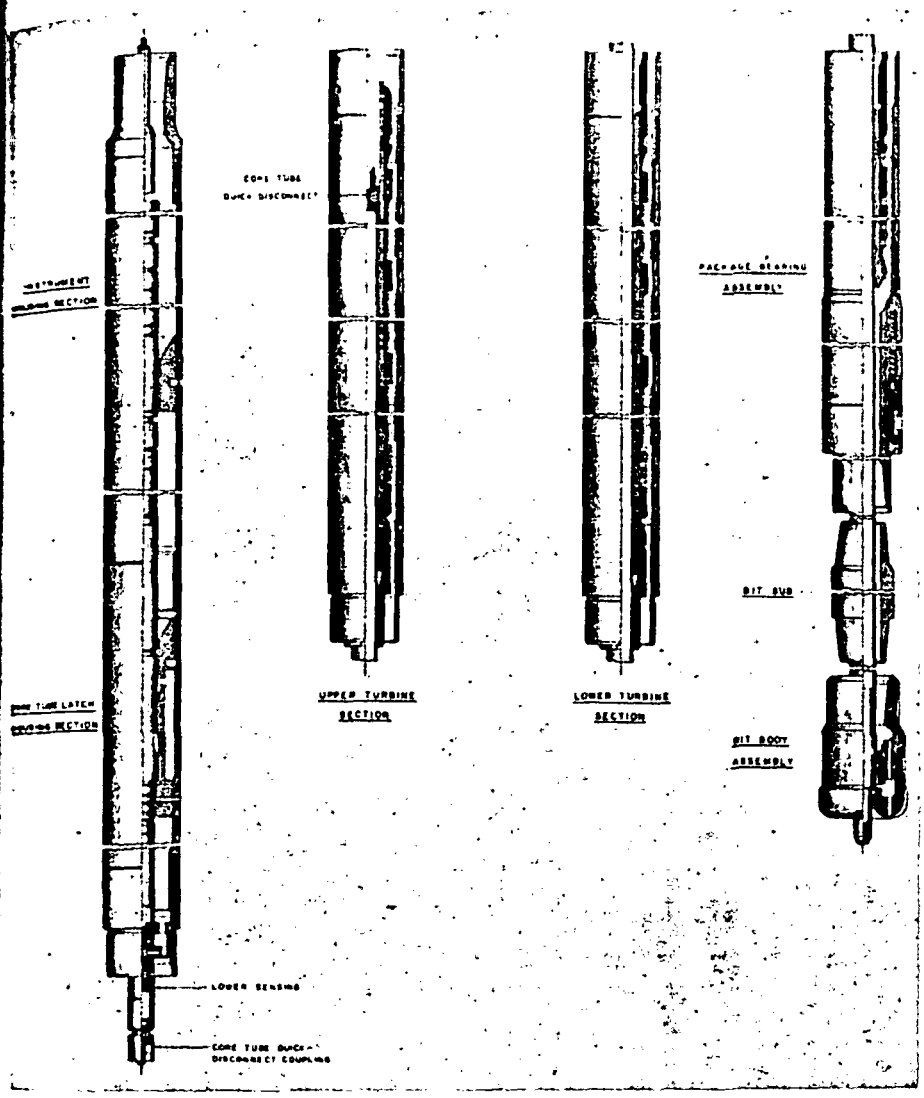

FIGURE 7. Eight and one-half inches coring turbodrill.

ngeles, drilling ship.

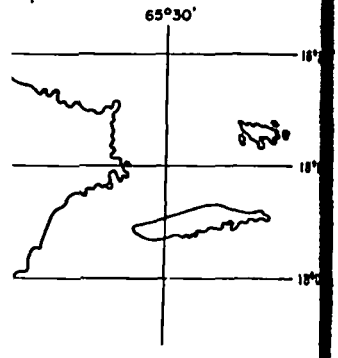

; area of survey.

turbocorer bit was rotated at 600 RPM throughout its use. Total maximum wear on the radial thrust bearings was only 2/32 of an inch.

Site Selection

The crust under the world's ocean averages somewhat over 39,000 feet in thickness, which in most places would put the mantle about 4,000 feet beyond our reach. This means that, with the present state of technology, it is estimated that drill stem in excess of 35,000 feet in length would fail through tension introduced by its own weight.

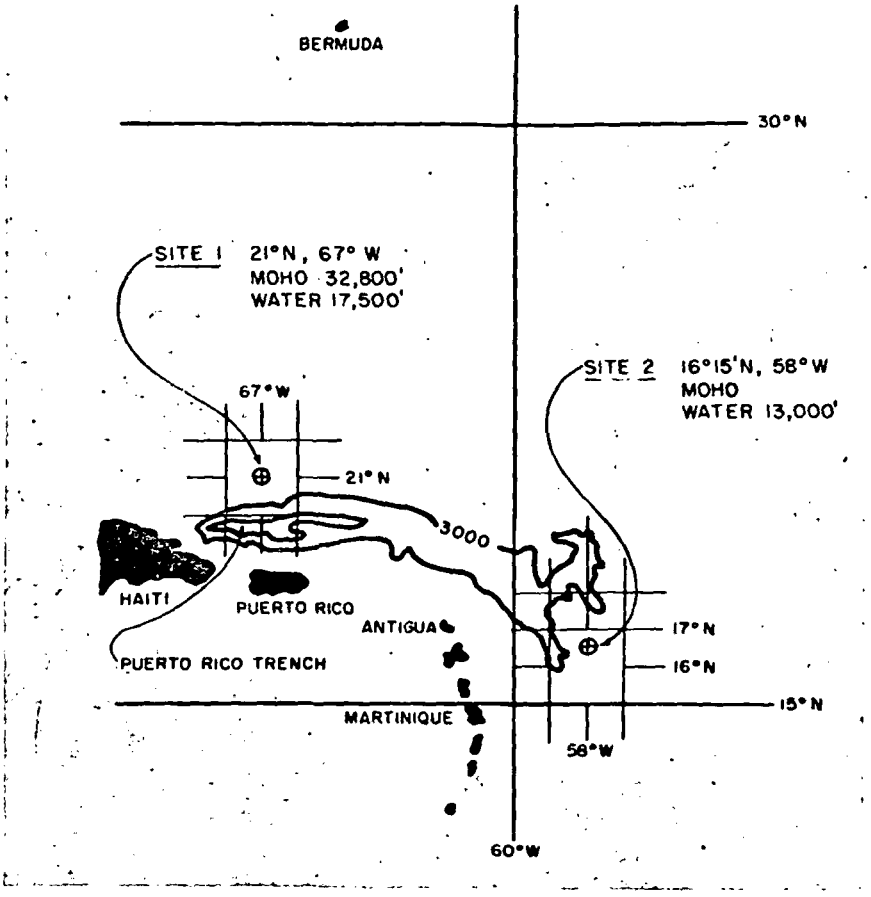

FIGURE 8. Location of possible Mohole Drilling Sites north of Puerto Rico and east of Antigua.

In order to find spots wh
vantage was taken of geophysi
graphic institutions. Having loc
and gravity surveys were con
of Puerto Rico; 200 miles eas

The Puerto Rican and Anti
The crustal rocks north of
faulted. Seismic evidence show
that it could be penetrated. H
hurricanes, because of the frac
has been abandoned as an imme

To the east of Antigua is a
this locality it was supposed
that the mantle might be easily

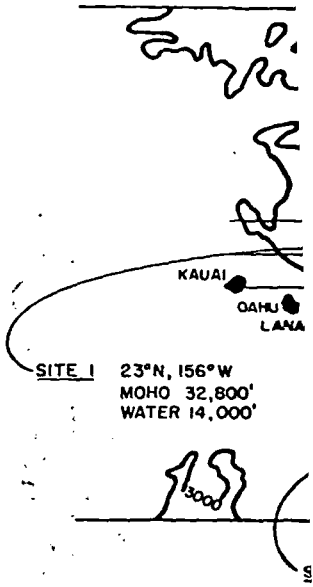

FIGURE 9. Two possible drilling
Maui has been chosen.

In order to find spots where the crust is thin enough to penetrate, advantage was taken of geophysical surveys already conducted by the oceanographic institutions. Having localized likely areas, detailed seismic, magnetic and gravity surveys were conducted in the following areas: 200 miles north of Puerto Rico; 200 miles east of Antigua; and 120 miles northeast of Oahu.

The Puerto Rican and Antiguan areas are shown together in FIGURE 8. The crustal rocks north of Puerto Rico proved to be badly fractured and faulted. Seismic evidence showed the crust to be about 31,000 feet thick, so that it could be penetrated. However, because the area is highly subject to hurricanes, because of the fracturing and the strong ocean currents, the site has been abandoned as an immediate possibility for mantle drilling.

To the east of Antigua is a region called the Barracuda Fault Scarp. At this locality it was supposed that the crust had been fractured upward so that the mantle might be easily reached. Detailed seismic surveying revealed

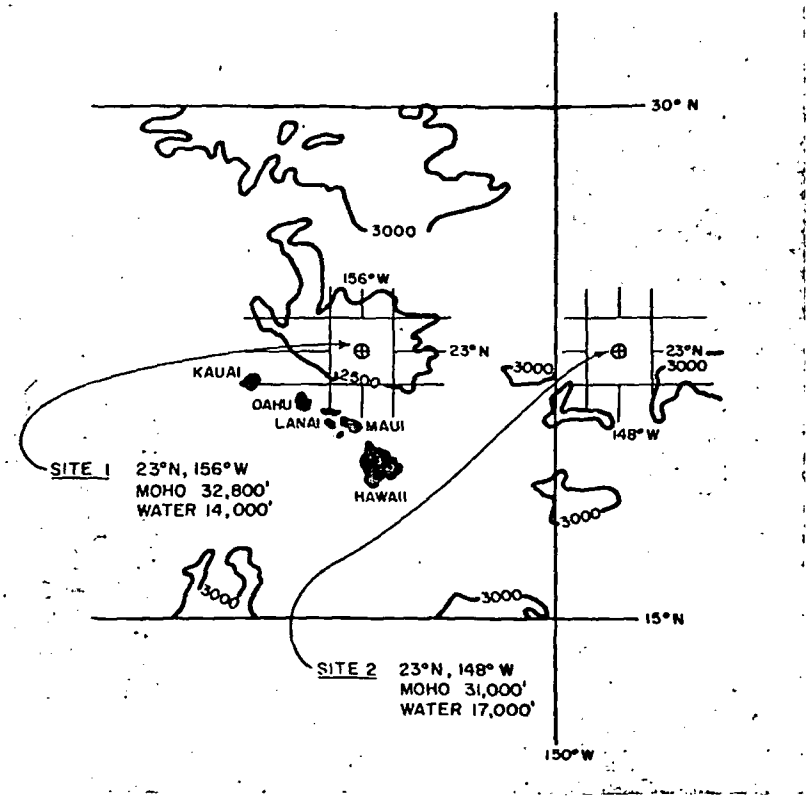

FIGURE 9. Two possible drilling sites on the Hawaiian arch. The area north of Maui has been chosen.

that a four-layer, instead of a three-layer, crust existed and that the depth to the mantle was about 39,000 feet. The seismic records from the Barracuda Fault Scarp will be given further detailed checking.

Seismic surveying along the Hawaiian Arch, in the locality shown in FIGURE 9, revealed that the crust there may be as thin as 31,800 feet. This fact, coupled with the generally good weather, oceanic conditions and easy logistic support, dictated that we should choose this site for our first attempt to reach the mantle. Further seismic surveying along the Hawaiian Arch is indicated in order to find out if we have actually located the thinnest part of the crust.

The Future

As most of you know, from newspaper and journal accounts, the future of the Mohole Project has always been in doubt.

Scientific and engineering arguments, cost escalations, and budgetary problems have all taken their toll in slippage of schedule. However, if all goes well, we should be drilling at sea sometime in 1969.

DIVISION C

THE RUR

Joel

Russian Research Center, Ha

Ill fares the land, t
Where wealth accu
Princes and lords r
A breath can make
But a bold peasantr
When once destroye

In a note of dedication of his p
smith remarked that some quest
countryside, and he countered by
have written . . . I have taken all
for these four or five years past, to

While the poet's moral implica
are perhaps debatable, his basic ob
a hundred years later, in 1867, Ka
plications of the changes observed
agriculture, modern industry has a
for this reason, that it annihilates th
and replaces him by the wage-labou
of the Agricultural Population from
associated measures in highly emc
with regard to their impact on the ri

Marx's comments on the peasan
of course, been well publicized (e.
his statement in *The Communist Ma*
the country to the rule of the to
greatly increased the urban populat
thus rescued a considerable part o
life" (in Eastman, Ed., 1932: 325).

But, regardless of the attitude we
tations of Goldsmith, it is clear from
that the current condition in the Unite
of the total population is involved i
drastic impact on the existing social
beginning of the eighteenth century nc
in towns, yet by the latter part of that c
mately half of the population was u
the development of urban industry a

*This paper was presented at the meeting
†"The Deserted Village (originally publ
Oliver Goldsmith. J. M. Dent & Sons, Lo

SUBJ
GPHYS
Drill
BPP

U.S. GEODYNAMICS COMMITTEE
WORKSHOP ON CONTINENTAL DRILLING FOR SCIENTIFIC PURPOSES
17-21 JULY, 1978

BACKGROUND PAPER ON PRACTICAL AND ORGANIZATIONAL ASPECTS

By

H. R. Gould, J. W. Harris, M. K. Horn, C. J. Mankin
P. H. Stark, and E. R. Turner, Jr.

Organizational Structure

One of the objectives of the workshop will be to consider an organizational plan that will best accomplish the scientific objectives of the program. The basic elements of such a plan were identified by the 1974 Ghost Ranch Workshop on Continental Drilling and are reproduced here in Attachment 1. In response to the U.S. Geodynamics Committee request for suggestions on ways to implement the recommendations of the Ghost Ranch Workshop, a panel of the Federal Committee on Solid Earth Sciences (CSES) recommended a more detailed organizational scheme, which is reproduced in Attachment 2. This plan was conceived as a national program that would accommodate not only the interests of Federal agencies in drilling for scientific purposes but those of all qualified scientists.

The plan calls for establishment within ERDA [now the Department of Energy (DOE)] of a Continental Drilling Program (CDP) Office with overall management responsibility. This office would receive policy direction from an Interagency Steering Group, scientific advice from a broadly based Scientific Advisory Committee, data handling and coordination assistance from an Information and Data Management Unit, and advice on drilling, sampling, and well logging technology from a Drilling Technology Advisory Committee. The Nevada Operations Office of DOE would manage field operations and provide drilling, logging, and other common services and support from commercial sources. The Operations Manager of DOE, Nevada, would receive assistance of an Environmental Impact Group, a Drilling Services and Contract Unit, and a Facilities Planning Board. The collection and analysis of scientific field data would be carried out under the guidance and sponsorship of the agency or agencies (DOE, USGS, NSF, DOD) having principal programmatic interest.

Further details regarding the proposed organizational structure and the responsibilities of individual management units are contained in the report of the 1974 Ghost Ranch Workshop, Continental Drilling (published by the Carnegie Institution of Washington, June 1975) and the report on Recommendations of the Panel on Continental Drilling of the FCCSET Committee on Solid Earth Sciences (April 1977), copies of which have been furnished to all Workshop participants. We recommend that all attendees, particularly those participating in the Panel on Practical and Organizational Aspects, familiarize themselves with these documents so that the best decision can be reached regarding organizational structure.

Comments on Specific Practical and Organizational Aspects

In the following sections, we provide additional information and suggestions on several specific practical and organizational matters which we believe will help the program attain its objectives. These concern the Information and Data Management Unit; arrangements for utilization of holes drilled for other purposes; and cooperation of State geological surveys and related agencies; professional societies; and industry.

Information and Data Management Unit

The four primary tasks for this unit were defined in the 1975 Report of the Ghost Ranch Workshop as follows:

1. To provide information on subsurface data banks and sample and core repositories which contain information relative to project objectives.

2. To provide information on new wells to be drilled by industry which offer opportunity for solving scientific problems and would be appropriate for cooperative efforts.

3. To organize and manage a sample repository and computer ized data bank for samples and drill-hole data acquired in the project.

4. To ensure timely publication of results of all studies.

We support these tasks and offer the following supplementary information and suggestions:

1. Information on Data Banks, Sample and Core Repositories

It is important to know what technological data banks and repositories are available to support the work of CDP. The assembly and cataloging of pertinent files and repositories should be the first task of the information unit.

Although the number of pertinent files is large and expanding rapidly, several available compilations can be used to start this task.

a. The USGS has compiled a directory to available core and sample repositories in North America (Open File Report 77567).

b. The USGS has purchased Petroleum Information Corporation's (PI) Well History Control System that contains well histories on more than 1,000,000 U.S. wells. This is the largest available well data file in the U.S.

c. Other files, such as the Petroleum Data System oil and gas field file, the AAPG CSD drilling statistics file plus additional commercial, professional society, and governmental data banks, are also available. Attachment 3 contains a listing of publications describing several of these not listed in the 1975 report on Continental Drilling. The Information Unit should compile annotated references to these and other resource files for scientific users. The AAPG Committee on Computer Applications may be able to provide some assistance in this regard.

2. Information on New Wells to be Drilled

All new wells to be drilled for oil and gas in the United States are permitted by State agencies and announced in daily publications by PI. Most significant wildcats in remote locations or that test new depths or unique geological environments also are published in special news releases by PI or industry trade journals, such as World Oil and Oil and Gas Journal. Data on all weekly new well starts in the U.S. also are available by remote terminal access through PI.

The concern of CDP is to define the areas, depths, and environments that are of interest for scientific purposes. The announcement of intent to drill in these areas can then trigger the response of interested scientific groups to participate in gathering data from the drilling.

3. To Organize and Manage a Sample Repository and Computerized Data Bank

The information unit should insure that samples, cores, and pertinent scientific data obtained by CDP are securely stored and accessible to users. It is suggested that the many excellent sample repositories operated by State surveys, geological societies, and other government agencies be utilized wherever possible. If, however, a suitable storage facility does not exist, the Information Unit may find it necessary to fund a facility. It is likely that an existing facility would welcome the support and would provide excellent service at far less cost than a new single purpose storage.

There are many existing resource data bases and associated management systems. It is suggested that data obtained by CDP be compiled and stored in an existing format and system that provides maximum compatibility with other subsurface data and is readily accessible for retrieval and application programs. The previously mentioned PI Well History Control System is such a system. New data, including laboratory analyses and engineering testing on wells drilled for the Eastern Gas Shale project, Michigan Basin Devonian study, NURE and Alaska NPR-A projects, are being added to this file. This large well data system already has compatible formats for capture of subsurface data that will be gathered by CDP, and comprehensive retrieval and mapping programs are available. Consequently, the Information Unit should evaluate this system to determine if it satisfies the information storage and application requirements.

Other systems also should be evaluated. The Illinois Geological Survey, for instance, has a well data system that may be suitable. Many oil companies have large well data bases that also are based on the Well History Control System, and many research laboratories and universities have data base management systems and special resource evaluation systems that might be evaluated. The Information Unit should avoid, however, the temptation to develop a new system.

The Information and Data Management Organization must be advised of what data are to be stored and what applications are to be made of the data. These two factors depend, of course, on a clear definition of scientific objectives. As a consequence, it is important that the Data Management staff participate in planning and defining objectives and procedures. The definition of information system standards, such as formats, codes, and application capabilities including retrieval, custom reports, and graphic displays, such as plots and maps, is directly related to project objectives. Lack of coordination of these functions will certainly lead to failure of the information system. It is important, therefore, that the Information and Data Management group be a staff function that reports directly to CDP Operations Management. This organization should highlight the service aspect of the Information Group and facilitate their inclusion in planning scientific objectives that can be properly supported by the information system.

4. To Ensure Timely Publication of Results

The information system should be used to support publications by providing rapid access to stored data and generation of summary reports, graphs, and maps that can speed interpretation and preparation of publication materials. Results of geochemical analysis in NPR-A, for instance, will be displayed by computer graphics for publication. The Information Unit also should find access to suitable scientific journals or government publications and provide funds for timely publication.

Utilization of Holes Drilled for Other Purposes

Before any new holes are proposed by CDP, every effort should be made to determine whether the scientific objectives can be met by use of holes drilled by the petroleum industry or other holes drilled for highly specific and applied purposes. The attraction of such dual purpose holes is that the additional scientific information should be obtainable at relatively small incremental costs. While some dual purpose holes have proved successful in the past, many have not or have failed at the negotiation stage. The chief problems have been lack of sufficient lead time, failure to reach agreement on financial and legal arrangements, and inadequate planning for in-hole operations (logging, coring, instrumentation, etc.).

Following are suggestions which we believe will help to avoid these pitfalls and lead to more successful operations.

To insure adequate lead time, every effort should be made to learn as early as possible about proposed new oil and gas wells in areas of special scientific interest. In addition to the information sources already noted, local geological societies can assist by identifying proposed new wells or the names of companies with large lease blocks likely to be drilled in the areas of interest. The operators or owners of the leases should then be contacted and an explanation presented to them of the project and the data needed from the well or wells to be drilled.

In negotiating arrangements for obtaining the desired scientific data from the well, CDP should be prepared to pay all costs above and beyond usual exploratory well cost calculated by the operator. This includes:

1. Coring time and coring equipment rental.

2. Delay time involved in coring, such as delivering of equipment or equipment breakdown, and fishing or redrilling costs if related to coring.

3. Added cost of rig capable of drilling deeper than planned exploratory well depth.

4. Added costs of larger hole size and casing program required to drill deeper than planned exploratory well depth together with associated costs of larger mud volumes.

5. Cost of additional electric logs including company charge plus rig time involved.

6. All costs of drilling beyond planned total depth of exploratory well.

7. All rig time necessary for various scientific data recording (seismic, magnetometer, gravity, etc.)

8. Blowout insurance on portion drilled for CDP. Since most policies have a deductible, it should be agreed that CDP would assume costs up to the deductible limit.

9. Reasonable overhead charge by exploratory well operator plus a management fee.

10. CDP should assume all plugging cost if well is taken over at total exploratory depth for deeper drilling.

There should be adequate time in advance of spudding a well to prepare for all instrumentation and other programs deemed necessary by CDP. The cost of wells is a vital part of the exploratory operator's business and hurried-up programs would cause him additional cost burdens. CDP should agree to hold all parties harmless and accomplish the well work so that it does not cost the operator one dollar more than he would have spent in drilling his well.

As a matter of agreement, it should be understood if the well discovers oil or gas and the operator decides to complete it as an oil or gas well that all CDP activity must cease and that CDP will pay all costs accrued in its program up to that time, whether or not any data have been obtained. Part of the reasoning for this action is that the lease with the landowner may demand completion of the well to maintain the lease. Drilling for scientific purposes alone may not extend the lease.

Also, as a matter of agreement, if CDP takes over operation of a well for deeper drilling and discovers oil or gas below the original proposed total depth of the well, then the well must be offered back to the operator for completion purposes. The original operator will own the minerals discovered and will pay a prorata share of the deepening, being the actual costs less scientific evaluation charges.

Those wells drilled on private lands will need prior approval from the landowner for drilling to be done only for scientific purposes unless the lease specifically allows this. Most leases do not. If wells are drilled on Federal land, it is assumed the government agency administering the land (DOI, Forestry Service, etc.) would need to give permission.

Cooperation of State Geological Surveys, Professional Societies, and Industry

These organizations all have a definite interest in CDP and can provide valuable assistance in helping to achieve its scientific objectives.

The State geological surveys and related agencies, in additon to their core repositories and data files on oil and gas wells, maintain records and samples from water wells and holes drilled in minerals exploration that can be of use. As these agencies also issue permits for all wells drilled within the States, they can be helpful in identifying in advance wells that might be suitable for dual purpose drilling in areas of scientific interest. To enlist the assistance of the State agencies, it is suggested that a "Liaison Committee for Continental Drilling for Scientific Purposes" be established within the Association of American State Geologists.

Professional geological and geophysical societies, especially those with expertise in subsurface investigations, can also be of help. Reflecting its interest in the program, the American Association of Petroleum Geologists (AAPG) recently endorsed the CDP in principal and established a special "Subcommittee on Drilling for Scientific Purposes" within the AAPG Research Committee. The purpose of this Subcommittee is to serve as a focus within AAPG to provide advisory and other assistance to CDP. Similar committees within the Society of Exploration Geophysicists (SExG), the Society of Economic Geologists (SEcG), the Society of Petroleum Engineers (SPE), and perhaps other earth science organizations would be most helpful. Accordingly, it is suggested that invitations be extended to these societies to establish such committees.

Industrial organizations, especially the petroleum and mining companies, can provide valuable assistance in many ways. The petroleum industry has been most supportive of the Deep Sea Drilling Project (DSDP) and is currently providing advisory assistance to the geophysical investigations of the deep crust and upper mantle by the Consortium for Continental Reflection Profiling (COCORP). This project is developing information critical to the selection of suitable sites for accomplishing CDP's scientific objectives requiring deep drilling. Representatives of both the petroleum and mining industries have and are participating in plans for CDP, and their continued assistance should be utilized as the program develops.

6.12.78

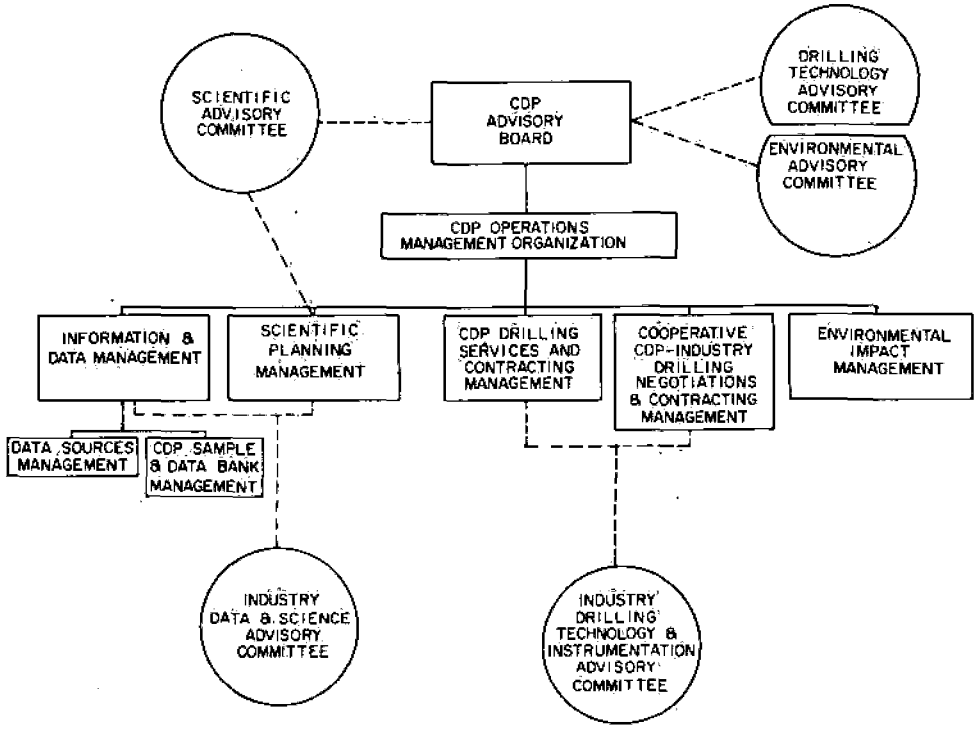

Figure 7. Suggested management structure for Continental Drilling Project.

CONTINENTAL DRILLING PROGRAM

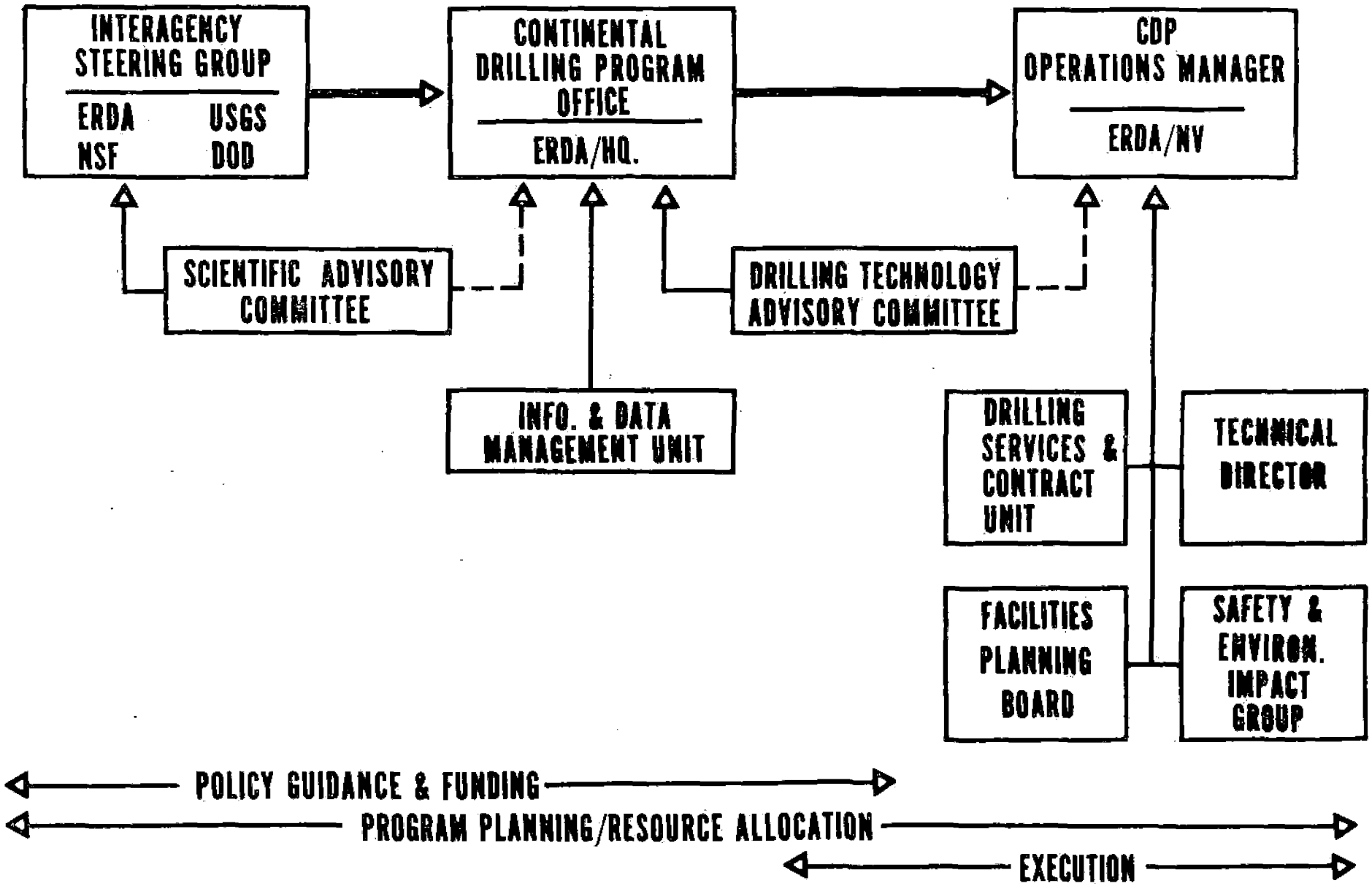

Attachment 3

ADDITIONAL REFERENCE TO
KEY SOURCES OF DRILL HOLE INFORMATION
NOT CONTAINED IN 1975 REPORT ON CONTINENTAL DRILLING

1. Report on the USGS Rocky Mountain Core Repository.

2. Kansas Geological Society supplemental edition "Catalog of Electrical Logs."

3. Tulsa Geological Society publication, "Tulsa's Physical Environment."

4. Wyoming Geological Association Core Book, Greater Green River Basin Symposium.

5. USGS Proposal for Development of Integrated Nationwide Physical and Chemical Properties Data Bank.

6. Catalog Sample Library, Utah Geological and Mineralogical Survey, Circular #55.

7. Brochure Geological Information, Library of Dallas.

6.10.78

SUBJ
GPHYS
Drill
CscB

Core system, chain bit get field test

Newly designed pressure coring system cuts faster, keeps drilling mud out of the core, developers say. Continuous chain drilling bit will cycle new cutting edge into place without pulling the bit out of the hole.

A NEWLY developed pressure coring system featuring faster penetration and a continuous chain drill bit that cycles new cutting surfaces into place without the bit being removed from the hole have undergone their first field test.

The coring system, developed by Sandia Laboratories, Albuquerque, N.M., and Diamond Oil Well Drilling Co. (Dowdco), Midland, Tex., cut 17 eight-ft-long cores at an average rate of 20 ft/hr during the test.

And a special fluid used in the process kept drilling mud from invading the core.

In its field test, the continuous chain bit, which consists of diamond-studded cutting links mounted on a chain, used six cutting surfaces to drill 250 ft of granite, according to the developer, Sandia.

The chain bit drilled an average 41 ft in granite before the cutting surface wore out and had to be changed. By comparison, two conventional diamond bits lasted an average of 28 ft before wearing out in the same granite formation, Sandia says. Both bit types drilled about 4 ft/hr.

Coring bit. The pressure coring system uses a 6½-in. bit, which cuts a 2½-in.-diameter core. It is fitted with man-made diamond cutters instead of natural diamonds used in conventional coring bits.

Developers report that the penetration rate is about seven times faster than natural diamond core bits tested in the same 5,000-ft-deep dolomite-anhydrite formation near Denver City, Tex.

Two coring runs also used a Sandia-developed, brine-based, polymer fluid stored in the core retriever to form an 1/8-in.-thick gelatin-like protective film around the core as it entered the retriever barrel.

A comparison. Although current pressure coring methods seal a core to maintain downhole pressure, their relatively slower drilling rate permits drilling mud to wash away residual fluids, the developers say.

Studies show that the longer it takes to cut a core, the more time drilling mud has to wash away these fluids, says L. E. Baker of Sandia's drilling technology division. Loss of the fluids makes it hard to know how much resource is in the study area, he said.

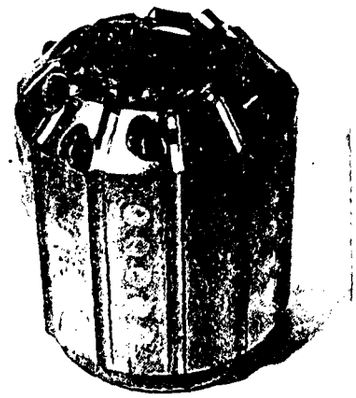

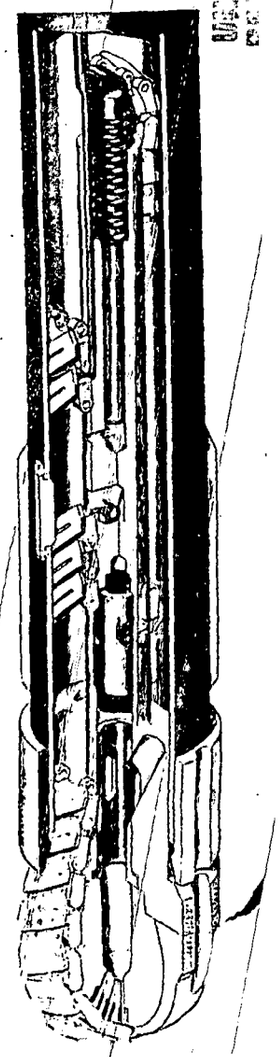

CORING BIT, above, used with pressure coring system. Continuous chain drill bit, right, is 4¾ in. slim hole model designed mainly for exploration drilling.

"This first test of the new, fast bit and the special fluid shows that they can make core analysis much more accurate," Baker said.

"The rapid cutting speed alone significantly reduces core washing. When used in combination with the protective fluid, we get a good picture of what the strata contain."

System makeup, operation. The new system's bit contains fifteen ½-in. stud mounted polycrystalline diamond cutters (PDCs), which protrude 1/10-in. above the bit face, compared with a protrusion of 8/1,000-in. for natural diamonds on conventional coring bits. This increased exposure permits deeper cuts and faster cutting rates, Baker said.

The PDCs also are sharper than natural diamonds, and they machine the core much like a lathe. Because of the cutting speed and the bit design, a core is exposed to regular drilling mud for only a short time before entering the barrel and being coated with the fluid sealant.

The noninvading coating fluid used is hydroxyethyl cellulose polymer. It is easily distinguishable from hydrocarbons in laboratory testing of core samples, Baker said. The fluid contains calcium carbonate particles which plug small holes in the core, helping to prevent the protective gel from invading the core.

In operation, once coring begins, about 3 gal of fluid is sto th core retriever. As the core int the retriever, fluid is disp oat ing the core, and cleaning ling the bit in conjunction wit ing mud.

The new fluid doesn't ily and generally can be ed off a frozen core.

Sandia provided the n of the system. Dowdco design layout and ma bit.

Other field tests ar a bit slightly redesign and to coat cores m protective fluid.

Tests also will be a similar PDC bit d by Sandia. It will

a 1-in.-long PDC pilot bit designed to reduce core invasion by drilling muds ahead of the core bit.

Chain bit design. Each cutting surface in the new chain bit consists of five adjacent chain links wrapped around a hemispherical bit head. When the five 2¼ by 1½-in. links are worn, the next five are remotely cycled into place and drilling resumed.

Each link is set with 100 diamonds totaling about 10 carats. In the center of every fifth link are six synthetic diamonds which serve as the nose of the cutting surface. These diamonds, which protrude 0.065 in. above the surface, increase bit life and penetration rate, Sandia reports.

During its test, the bit contained only 30 links—six cutting surfaces. But commercial versions are ultimately expected to have up to 75 links, or 15 cutting heads. The chain, in that case, would be about 7½ ft long.

Its greatest advantage, Sandia says, is expected to be the savings which would accrue with fewer bit trips in deep, hard rock drilling.

With the chain bit, a new cutting surface can be cycled into place in 6 min by stopping the mud pump and raising the bit a few feet off bottom. This activates a spring which moves a new cutting surface into position.

Bit cost. Commercial versions of the chain bit are expected to cost about $30,000 in the 4¾-in. size—10 times the cost of a conventional diamond bit.

However, depending on well depth and daily drilling costs, Sandia says, a chain bit with 15 cutting heads would reduce drilling costs 30-50% even though the life of each head were no longer than that of a conventional bit.

"The added life of each cutting surface demonstrated in the test provides an additional bonus," says Sam Varnado, supervisor of Sandia's drilling technology division. "If this extended life continues in subsequent tests, the new bit will be even more competitive."

The bit, under development by Sandia since 1977, will undergo a second field test later this year. The test will be conducted to determine bit wear and reliability more precisely and to improve mud flow around the bit.

In the first test, rock chips partially clogged nozzles in the bit, preventing proper cooling and cleaning of the diamonds.

Filters are now being added to the system.

The cutting surfaces are designed for a uniform wear rate under normal hydraulic conditions at the bottom of the hole and for a maximum load of 120 lb/diamond.

Sandia wants to team up with an industry partner to develop a larger diameter—6⅛ to 8½-in.—chain bit which would have more general uses. Ultimately, it hopes to transfer final development and commercialization of the continuous chain drill bit to private industry.

Interior details changes in onshore leasing

THE Interior Department has proposed major changes in noncompetitive leasing of U.S. government lands to carry out many of the reforms announced by Interior Sec. Cecil Andrus June 4.

The new proposals, however, don't include required payment of higher rentals during the last 5 years of the lease term if exploration hasn't started before the end of the fifth year. Such a rule requires consultation with the Department of Energy, which is now under way.

Nor do the new proposals expand the areas beyond present known geologic structures for competitive leasing. Legislation to do that is now pending on Capitol Hill, following its submission by the administration Aug. 9.

In issuing the new proposals, Andrus said, "With our increasingly serious energy problem, it is vitally important that we do everything possible to make sure that noncompetitive leasing leads to exploration. We feel our proposed changes will encourage exploration and eliminate possible abuses and inefficiency in the present noncompetitive onshore leasing system."

What would be changed. Under the present noncompetitive leasing system, tracts are awarded once a month in Bureau of Land Management offices. All applications received by the filing deadline are considered to have been submitted simultaneously. When there is more than one application for a given tract, the winner is chosen by drawing—a lottery.

A major change would switch the frequency of the drawings from monthly to quarterly to permit assembly of larger, more desirable tracts for exploration.

Andrus said the department's research shows that in some states as many as 70% of existing parcels could be combined with other parcels which become available within a 3-month period as opposed to about 20% on a monthly basis.

By switching to quarterly drawings, Andrus said, applicants could be given an additional 10 days in which to file their entry cards. Winners of leases could be given an additional 15 days in which to pay the first year's rental. Applicants now have difficulty in meeting the deadline under the present system.

Another big change proposed by Interior would increase the maximum size of tracts offered for noncompetitive leasing to 10,240 acres from 2,560 acres.

However, Andrus emphasized that this doesn't mean that all noncompetitive leases will be that size. Many will continue to be issued for less than the current maximum of 2,560 acres. But wherever appropriate, larger tracts will be used.

Other major proposed changes include:

- Only handwritten signatures would be accepted on drawing entry cards. A card signed by anyone other than the applicant must reveal the name of the applicant and the signer and the relationship between them. Only cards fully completed and signed by the applicant or those fully completed and signed by an agent on the applicant's behalf would be accepted by BLM. All cards would have to be signed within the filing period.
- Only the applicant's personal or business address could be used as the return address on the drawing entry card. A filing service couldn't use its address for a client. Agents would be required to submit copies of all agreements with their clients relating to federal leasing.
- While entry cards would continue to be used for the drawing, the lease form would replace the entry cards as the official lease offer and would require the signature of the applicant. When the lease is issued, only the applicant could pay the first year's rental.
- It would be illegal for an agency to have a prior agreement to resell a lease. Andrus said this proposed change would outlaw "kickbacks" to filing services from oil companies to middlemen.

GEOPHYSICS, VOL. 45, NO. 11 (NOVEMBER 1980); P. 1659-1666.

Electrical, electromagnetic, and magnetotelluric methods

S. H. Ward*

Application of electrical methods began with Robert W. Fox's 1830 observation of self potentials associated with copper vein deposits in Cornwall. Conrad Schlumberger introduced the direct current equal potential line resistivity method in 1912. Harry W. Conklin received the first patents on the electromagnetic (EM) method in 1917. From these beginnings, the history of the development of the resistivity induced-polarization (IP), magnetotelluric and EM methods are traced to the present time.

It is of interest to note that application of electrical methods flourished from about 1920 to 1930, but then the methods were developed slowly until after World War II when a major burst of development activity took place. However, the interpretational basis of the methods remained poor until the last several years when application of numerical techniques using computers permitted forward and inverse solutions to electrical boundary value problems in two and three dimensions.

Field hardware gradually evolved from 1960 through 1980 to permit precise broadband IP, electromagnetic, and magnetotelluric data acquisition with coherent detection and remote reference noise rejection, in-field digital data processing and interpretation. The future of electrical methods is briefly sketched, with trends largely toward better numerical interpretation schemes, more broadband applications, more sophisticated use of in-field digital acquisition processing and interpretation schemes, and accommodation of more channels of information.

EARLY HISTORY

The early chronology of applications of electrical methods of exploration has been carefully preserved in the literature (e.g., Kelly, 1950; Kunetz, 1966; Van Nostrand and Cook, 1966). From those preservations and others, one learns that the first attempt to utilize electrical methods dates back to Robert W. Fox (1830) when he observed that electrical currents, flowing in Cornish copper mines, were the result of chemical reactions within the vein deposits, i.e., self potentials. According to Kelly, "The first recorded discovery of a sulfide body by electrical methods is to be credited to him, as the result of the investigations which he carried out in 1835, in the Penzance Mine of Cornwall."

As early as 1882, Carl Barus conducted experiments at the Comstock Lode, Nevada, which convinced him that the method could be used to prospect for hidden sulfide ores. To Barus goes the credit for introducing the nonpolarizing electrode. Conrad Schlumberger put the method on a commercial basis in 1912. The first plan map of self potential over a metallic deposit was prepared by Schlumberger in 1913 and was published in 1918; it depicted the pyrite mines at Sain-Bel, France. Roger C. Wells, of the U. S. Geological Survey, contributed the first chemical understanding of the passive self-potential phenomena in 1914. Kelly (1957) introduced the self-potential method to Canada and the United States in 1924.

Fred H. Brown, in the era 1883 to 1891, and Alfred Williams and Leo Daft in 1897, first attempted to determine differences in earth resistivity associated with ore deposits and were granted patents on their methods. In 1893, James Fisher measured the resistivity of copper bearing lodes in Michigan (Broderrick and Hohl, 1928). In 1900, N. S. Osborne did equipotential work in the same district. The first practical approach to utilizing active electrical methods, wherein the earth is energized via a controlled source and the resulting artificial potentials are measured, was due to Schlumberger in 1912. At that time he

*Director, Earth Science Laboratory, University of Utah Research Institute, Salt Lake City, UT 84108.
0016-8033/80/1101-1659 $03.00.

introduced the direct-current equipotential line method (Schlumberger, 1920).

The concept of apparent resistivity was introduced in about 1915 by both Wenner (1912) of the U.S. Bureau of Standards and by Schlumberger (1920). The field techniques for apparent resistivity were then developed by O. H. Gish and W. J. Rooney of the Carnegie Institution of Washington and by Marcel Schlumberger, E. G. Leonardon, E. P. Poldini, and H. G. Doll of the Schlumberger group. Wenner used the equal-spaced electrode array which today bears his name, while the Schlumberger group standarized an electrode configuration in which potential electrodes are sufficiently close together that the potential gradient, i.e., the electric field, is measured midway between the current electrodes (the Schlumberger array).

The earliest attempt to understand telluric currents is generally credited to Charles Mateucci (1867) of the Greenwich Observatory. It was not until 1934 that Conrad Schlumberger (1939, p. 272–273) made commercial use of the method.

According to Sumner (1976), "Conrad Schlumberger was the first to describe a *polarization provoquée*, i.e., induced polarization, in 1920 although he dropped the concept in favor of the self-potential method."

Harry W. Conklin, an American mining engineer, took out basic patents on the electromagnetic (EM) method in 1917. The first successful application of the Sundberg EM method, the forerunner of the horizontal loop method, occurred in 1925 (Sundberg et al, 1925); hence, the beginning of the Swedish thrust in EM prospecting which Lundberg and Sundberg fostered. The Bieler-Watson (1931) method of measuring the ellipse of magnetic field polarization in the vicinity of a large horizontal transmitting coil appeared next.

These were the foundations of the development of the theory and application for electrical methods of geophysical exploration. In the next decade or so, numerous books and treatises appeared which rapidly expanded the foundations. Most notable among these were Ambronn (1928), Eve and Keys (1929), and Broughton Edge and Laby (1931). The three *Geophysical Prospecting* volumes of the Transactions of the American Institute of Mining and Metallurgical Engineers (AIME), in 1929, 1932, and 1934, provided forums for dissemination of knowledge of this rapidly growing field of electrical geophysical prospecting. These volumes were followed by *Geophysics*, 1940, v. 138 and *Geophysics*, 1945, v. 164 of the Transactions of AIME. The Society of Exploration Geophysicists published six papers on electrical methods in *Early Geophysical Papers*. Most of these papers dealt with oil and gas exploration. The first paper on electrical methods to appear in GEOPHYSICS (v. 1) was by Statham (1936). From these beginnings, the electrical methods slowly developed, with most of the development taking place after World War II. Highlights of these developments follow.

THE RESISTIVITY METHOD

The theoretical basis for the electrical resistivity method became more firmly grounded with the forward solutions developed for horizontally layered earths by Stefanesco et al (1930), and others. This work culminated in the publication of an album of curves for the Schlumberger array (Compagnie General de Geophysique, 1955) and for the Wenner array by Mooney and Wetzel (1956). Until recently, matching of observed and theoretical curves using such albums was the standard method of interpreting resistivity data over horizontally layered earths. Roy and Apparao (1971) and Madden (1971) demonstrated, respectively, the depth of exploration for various electrode arrays and the resolving power of resistivity sounding for thin conductive and thin resistive beds.

Langer (1933) and Slichter (1933) were the first to develop formulation of the inverse problem in resistivity sounding of horizontally layered structures. Koefoed (1968) and Ghosh (1971) did much to make inversion practical. Zohdy (1975) developed a method of direct interpretation with which he obtained good results. However, none of the above investigations used the method of the generalized inverse introduced by Backus and Gilbert (1967). Inman et al (1973) introduced the use of the latter method to resistivity sounding, demonstrating that it was the most powerful technique for estimating parameters of a layered earth and for describing the nonuniqueness of the inverse solutions. Vozoff and Jupp (1975), Petrick et al (1977), and others used simultaneous inversion of resistivity and other data sets.

Tagg (1930) computed apparent resistivity curves for Wenner array resistivity profiles across a vertical fault. Logn (1954) developed expressions for the apparent resistivity over thin vertical sheets. Lundberg and Zuschlag (1931) computed potential-drop ratio curves over a vertical fault and a vertical dike. Many other workers pursued these initial leads. The dipping-bed problem in electrical geophysical applications was first solved by Skal'skaya (1948), and her work was extended by many others. Frank and

von Mises (1935) gave the exact solution for the potential due to a point current electrode over a horizontal buried cylinder. Van Nostrand and Cook (1966) presented an excellent summary of 1-, 2-, and 3-D models available for interpretation of resistivity data to that time.

In recent years, the development of practically realizable numerical methods, (e.g., the finite-difference, finite-element, transmission-line, and integral equation methods) has permitted the computation of sounding-profiling results for any electrode configuration over 2-D inhomogeneities of arbitrary shape. Madden (1972) introduced the transmission-line method, Jepsen (1969) the finite-difference method, and Coggon (1971), the finite-element method, while Snyder (1976) introduced the integral-equation method.

The inversion of 2-D resistivity data is in its infancy. Pelton et al (1978) developed an approach to inversion of 2-D dipole-dipole resistivity and IP data, using the transmission surface method, which relied upon storage in a computer of a data bank of forward solutions. Tripp et al (1979), following a suggestion by Madden (1972), utilized Telegen's theorem and the transmission surface analogy to produce a true ridge regression generalized inverse solution for the dipole-dipole array over a 2-D earth structure.

Petrowsky (1928) first studied the potential distribution at the surface of the earth due to a buried electrically polarized sphere. Stefanesco (1950) first presented the very interesting and powerful alpha center approach to 3-D modeling of resistivity data. Cook and Van Nostrand (1954) calculated a wide variety of resistivity curves over and near filled sinks, appropriate to the Lee and Wenner arrays. Seigel (1959) presented the response of a polarizable sphere in a half-space. The first 3-D numerical solution was presented by Hohmann (1975) in a GEOPHYSICS paper which received a Best Paper award. Pridmore (1978) used the finite-element method to calculate apparent resistivities over a complex 3-D earth. Dey and Morrison (1979) used the finite-difference method to calculate apparent resistivity distributions for the dipole-dipole array over 3-D inhomogeneities.

If in the Schlumberger array the current electrodes are far apart, and the potential electrodes are moved in-line between the current electrodes, then the *gradient array* is achieved. The pole-dipole and dipole-dipole arrays seem to have been promulgated by Madden and his students, but they have their roots in the Eltran array (West, 1940). The vector bipole-dipole array (e.g., Doicin, 1976) has achieved prominence in recent years, but it has yet to prove its value. The Lee, potential-drop ratio, equipotential line, and Wenner arrays have not survived the test of time. Van Nostrand and Cook (1966) provided an extensive coverage of resistivity arrays.

Edwards (1974) provided the basis for the magmetometric method of mapping resistivity. This technique is intended for deeper exploration than conventional resistivity methods because it relies upon measurement of magnetic field rather than electric field.

The Schlumberger and Wenner arrays are frequently referred to as dc resistivity methods. At various early times, dc and ac sources such as batteries and the commutated Megger have been used. In more recent years reliance has been placed on low-frequency (10^{-2} to 10^{2} Hz) generators. In the last decade, these generators have provided synchronized signals at the receiver either by (1) wave form recognition, (2) hard-wire link, or (3) synchronized clock link. Also in the last decade, digital receivers in the field have facilitated various frequency or time-domain procedures for data processing such as stacking, noise rejection, and band-pass filtering (e.g., Sumner, 1976). Current technology, via in-field microprocessors and a time reference between transmitter and receiver, permits processing, plotting, and interpretation of data in the field.

THE INDUCED-POLARIZATION METHOD

Subsequent to Schlumberger's (1920) discovery of the IP method, the next record of its study is attributed to Dakhnov (1941). Seigel (1949) provided the first proof that the method could detect disseminated sulfides. Bleil (1953) was sufficiently encouraged by Seigel's work to publish his own work. Madden and his students put the method on a sound phenomenological and interpretational basis through a series of publications (e.g., Hallof, 1957; Marshall and Madden, 1959). Angoran and Madden (1977) summarized the history of our understanding of IP phenomenology and made important contributions of their own. Commercial application of the method rapidly developed in the decade 1950 to 1960.

As equipment evolved to provide coherent detection over a broad spectrum, either in the time or frequency domain, routine collection of IP data as a function of frequency or time delay became practical (e.g., Van Voorhis et al, 1973). Broadband IP measurements permit recognition of the deleterious EM coupling effect and can aid in its removal. Mineral discrimination by broadband IP surveys is an elusive but much desired current goal of IP surveys.

Grounded structures such as fences and pipelines constitute a major source of noise in many IP surveys and can be dealt with by calculation in some instances (Nelson, 1977).

Interpretation of IP survey data in terms of 2-D earth structures is now routine (Coggon, 1971; Madden, 1971). Hohmann (1975) introduced a 3-D algorithm. Electromagnetic coupling has been computed over a homogeneous earth by Millet (1967) and over a layered earth by Hohmann (1973). Magnetic induced polarization (Seigel, 1974) offers a promise of better detection of polarizable bodies beneath very conductive overburden. Research on nonlinear IP phenomena was initiated by Shaub (1965) and Ryss et al (1967), but no commercial application of this method of mineral discrimination is evident yet. The text by Sumner (1976) contains a comprehensive list of references on the IP method.

THE MAGNETOTELLURIC METHOD

The magnetotelluric (MT) method is generally attributed to Tichonov (1950) and Cagniard (1953), with most of the credit going to Cagniard. However, Fournier et al (1963) noted that the roots of the method actually extend back to the work of Van Bemmelen (1908). Wait (1954) used the transmission line analogy to produce a compact form of the impedance of a layered earth to an incident plane wave. While these early workers treated the earth as a homogeneous or horizontally plane layered isotropic medium, Cantwell (1960) recognized the importance of resistivity anisotropy or two-dimensionality and hence introduced the notion of an impedance tensor which permitted determination of apparent resistivity as a function of angular orientation. He rotated his observed data into directions of maximum and minimum apparent resistivities. There followed many applications of the MT method in either scalar (Cagniard) or tensor form (Sims et al, 1971). Vozoff (1972) gave an excellent summary of the processing of tensor MT data and of the earth response functions which can be derived from them. While the tensor MT method recognizes anisotropy and/or two-dimensionality in earth structure, its routine application has been in terms of 1-D, i.e., plane, horizontally layered earths. That this approach is erroneous in general application has been clearly demonstrated by Wannamaker (1980, personal communication); in fact, he establishes that even a 2-D model is inadequate and that a 3-D model is usually required. This then requires the use of a 3-D modeling algorithm such as that of Ting and Hohmann (1980). Where the earth is 1- or 2-D, available forward and inverse algorithms can be applied (e.g., Petrick et al, 1977; Jupp and Vozoff, 1977). Improvement of signal-to-noise ratio is made possible by the innovative remote reference method of Gamble et al (1979).

THE ELECTROMAGNETIC METHOD

Development of the electromagnetic (EM) method was largely dormant in the interval 1930 to 1950, with notable exceptions being some scale-model results by Slichter (1932), Bruckshaw (1936), and Hedstrom (1940) and some theoretical and field work described in Slichter (1932). However, a flurry of significant developments occurred in the next 30 years, initiated by the enormous creative theoretical works of J. R. Wait (e.g., 1951, 1953, 1955, 1958) and the equipment development and field applications of the staff of McPhar Engineering Co. (e.g., Ward, 1952; Ward and Harvey, 1954; Ward, 1957; Ward et al, 1958). It was during 1950 to 1960 that the first broadband ground EM system, the first airborne EM system, the first drillhole EM system, ground Afmag, and airborne Afmag were developed by McPhar engineers, G. H. McLaughlin, W. O. Cartier, H. A. Harvey, and W. A. Robinson. McLaughlin later went on to develop the time-domain PEM system now manufactured by Crone Geophysics (Crone, 1979) and the EMP time-domain system now used by Newmont Mining Co. (Nabighian, 1977). Articles by Tornquist (1958), Paterson (1961), Barringer (1962), Fraser (1972), Seigel and Pitcher (1978), and Becker (1979) trace the evolution of the airborne EM method to digital recording, automatic-interpretation, and continuous apparent resistivity estimates.

A great many ground EM systems, both time domain and frequency domain, have evolved in the years between 1950 and 1980, and these were reviewed by Ward (1979). The trend is toward broadband systems employing coherent detection and microprocessor technology. These systems attempt to solve the problems encountered by the EM method when faced with a real earth consisting of overburden, host rock, surface topography, buried topography, disseminated and massive sulfides, and graphite.

Attempts to design an optimum waveform have been made by Lamontagne and West (1976). Won (1980) performed laboratory experiments with a sweep frequency generator.

Over the years, scaled physical modeling has been used to develop interpretation schemes, utilizing metallic sheets to simulate thin ore veins, metallic spheres to simulate equidimensional ore deposits,

or slabs of carbon/graphite to represent tabular base metal deposits. The variety of geometries of such models is great. Until about 10 years ago, the earth was modeled by placing sheets, spheres, or slabs in air and totally ignoring all other elements of the real earth. That application of the EM method was successful when using such crude models for interpretation is surprising.

Analytical solutions for a variety of simple earth models are available. These include: electric or magnetic dipoles over a homogeneous earth (Wait, 1953, 1955); electric or magnetic dipoles over a layered earth (Wait, 1958); a uniform alternating magnetic field incident upon a sphere or cylinder in free space (Wait, 1951); magnetic dipoles near a spherical body in free space (Nabighian, 1971); and magnetic dipoles near a sphere in a conductive half-space (Singh, 1973).

In recent years solutions have been found to previously intractable EM boundary value problems (e.g., Coggon, 1971; Swift, 1971; Hohmann, 1975; Lajoie and West, 1976; Stoyer and Greenfield, 1976; and Pridmore, 1978). The earliest of these articles dealt with 2-D inhomogeneities in the fields of line sources; this is a true 2-D problem. The article by Stoyer and Greenfield (1976) describes a 2-D inhomogeneity in the field of a 3-D source (the 2-D/3-D problem) while the articles by Hohmann (1975), Lajoie and West (1976), and Pridmore (1978) described a 3-D inhomogeneity in the field of a 3-D source (the full 3-D problem). Petrick et al (1979) developed a 3-D inversion scheme based on Stefanesco's alpha center concept.

While numerous algorithms exist for the inversion of resistivity and MT data in terms of a layered earth, such is not the case for active source EM methods. The paper of Glenn et al (1973) was the first of only five papers published on the subject at the time of writing.

THE SELF-POTENTIAL METHOD

An in-depth understanding of the self-potential method was first presented by Sato and Mooney (1960); Nourbehecht (1963) made the next major contribution in this direction. Corwin and Hoover (1978) demonstrated that very low noise levels can be obtained in self-potential surveys provided care is exercised in preparing electrodes. Some modeling with various source mechanisms has been done (e.g., Nourbehecht, 1963; Corwin and Hoover, 1978), but this activity is only now emerging. Morgan et al (1979) performed laboratory experiments designed to elucidate streaming potentials thought to be the cause of self-potential anomalies observed over geothermal systems.

THE FUTURE

The direction for the future of electrical methods would appear to focus on six main issues:

(1) Increased application of 2- and 3-D forward and inverse solutions applicable to resistivity, IP, self-potential, EM, and magnetotelluric methods;

(2) increased application of broadband IP and EM methods to permit identification of various members of the typically complex geoelectric section and to permit elimination of geologic noise;

(3) increased use of in-field microprocessors for acquisition processing and interpretation of field data to permit quicker exploration decisions and adjustment of survey design;

(4) development of optimum schemes for enenhancement of signal-to-noise ratio, such as use of a remote reference;

(5) facility in-field hardware for accommodating data from multiple sensors; and

(6) a resurgence of use of electrical methods in oil field and uranium exploration.

Some of the more difficult interpretation problems facing electrical methods are now yielding to solution; thus, more use of the methods is to be expected for all commodities. Microprocessors in the field will continue to allow electrical methods to be cost competitive vis-á-vis other geophysical methods.

REFERENCES

Ambronn, R., 1928, Elements of geophysics: New York, McGraw-Hill Book Co., Inc.

Angoran, Y., and Madden, T. R., 1977, Induced polarization: A preliminary study of its chemical basis: Geophysics, v. 42, p. 788–803.

Backus, G. E., and Gilbert, J. F., 1967, Numerical applications of a formalism for geophysical inverse problems: Geophys. J. Roy. Astr. Soc., v. 13, p. 247–276.

Barringer, A. R., 1962, A new approach to exploration—The Input airborne electrical pulse prospecting system: Min. Cong. J., v. 48, p. 49–52.

Becker, A., 1979, Airborne electromagnetic methods, *in* Geophysics and geochemistry in the search for metallic ores: P. J. Hood, Ed., Geol. Surv. Can., econ. geol. rep. 31, p. 33–43.

Bleil, D. F., 1953, Induced polarization: A method of geophysical prospecting: Geophysics, v. 18, p. 636–661.

Broderick, T. M., and Hohl, C. D., 1928, Geophysical methods applied to exploration and geologic mapping in the Michigan copper district: Econ. Geol., v. 23, p. 489–574.

Broughton Edge, A. B., and Laby, T. H., 1931, The report of the Imperial Geophysical Experimental Survey (of Australia): Cambridge, Cambridge University Press.

Bruckshaw, J. McG., 1936, Experiments on conducting

laminae in periodic magnetic fields: Proc., Phys. Soc., v. 48, p. 63.
Cagniard, L., 1953, Basic theory of the magnetotelluric method of geophysical prospecting: Geophysics, v. 18, p. 605–635.
Cantwell, T., 1960, Detection and analysis of low-frequency magnetotelluric signals: Ph.D. thesis, MIT.
Coggon, J. H., 1971: Electromagnetic and electrical modelling by the finite-element method: Geophysics, v. 36, p. 132–155.
Compagnie General de Geophysique, 1955, Abaques de sondages electriques: Geophys. Prosp., v. 3, supplement no. 3.
Cook, K. L., and Van Nostrand, R. G., 1954, Interpretation of resistivity data over filled sinks: Geophysics, v. 19, p. 761.
Corwin, R. F., and Hoover, D. B., 1978, The self-potential method in geothermal exploration: Geophysics, v. 44, p. 226–245.
Crone, J. D., 1979, Exploration for massive sulfides in desert areas using the ground pulse electromagnetic method, *in* Geophysics and geochemistry in the search for metallic ores: R. J. Hood, Ed, Geol. Surv. Can., econ. geol. rep. 31, p. 745–755.
Dakhnov, V. N., 1941, Electrical well logging interpretation of electric logs: Moscow.
Dey, A., and Morrison, H. F., 1979, Resistivity modeling for arbitrarily shaped three-dimensional structures: Geophysics, v. 44, p. 753–780.
Doicin, D., 1976, Quadripole-quadripole arrays for direct current measurements: Geophysics, v. 41, p. 79–95.
Edwards, R. N., 1974, The magnetometric resistivity method and its application to the mapping of a fault.: Can. J. Earth Sci., v. 11, p. 1136–1156.
Eve, A. S., and Keys, D. A., 1929, Applied geophysics, 1st ed.: Cambridge, Cambridge University Press.
Fournier, H. G., Ward, S. H., and Morrison, H. F., 1963, Magnetotelluric evidence for the low velocity layer: Report 76, series #4, Space Sciences Laboratory, University of California, Berkeley.
Fox, R. W., 1830, On the electromagnetic properties of metalliferous veins in the mines of Cornwall: Roy Soc. London, Phil. trans., p. 399–414.
Frank, P., and von Mises, R., 1935, Die differential and integralgleichung der mechanik und physik: Braunschweig, Friedn., Vieweg u. Sohn., v. 2, 1106 p.
Fraser, D. C., 1972, A new multicoil aerial electromagnetic prospecting system: Geophysics, v. 37, p. 518–537.
Gamble, T. D., Goubau, W. M., and Clarke, J., 1979, Magnetotellurics with remote reference: Geophysics, v. 44, p. 53–68.
Ghosh, D. P. ,1971, The application of linear filter theory to the direct interpretation of geoelectrical resistivity sounding measurements: Geophys. Prosp., v. 19, p. 192–217.
Glenn, W. E., Ryu, J., Ward, S. H., Peeples, W. J., and Phillips, R. J., 1973, Inversion of vertical magnetic dipole data over a layered structure: Geophysics, v. 38, p. 1109–1129.
Hallof, P. G., 1957, On the interpretation of resistivity and induced polarization results: Ph.D. thesis, MIT.
Hedstrom, H., 1940, Phase measurements in electrical prospecting: Geophysics, v. 5, p. 456–472; from AIME trans., v. 138.
Hohmann, G. W., 1973, Electromagnetic coupling between grounded wires at the surface of a two-layer earth: Geophysics, v. 38, p. 854–863.
——— 1975, Three-dimensional induced polarization and electromagnetic modeling: Geophysics, v. 40, p. 309–324.
Inman, J. R., Ryu, J., and Ward, S. H., 1973, Resistivity inversion: Geophysics, v. 38, p. 1088–1108.
Jepsen, A. F., 1969, Resistivity and induced polarization modeling: Ph.D. thesis, University of California, Berkeley.
Jupp, D. L. B., and Vozoff, K., 1977, Two-dimensional magnetotelluric inversion: Geophys. J. Roy. Astr. Soc., v. 5, p. 333–352.
Kelly, S. F., 1950, The rise of geophysics: Can. min. manual, p. 1–7.
——— 1957, Spontaneous polarization survey on Noranda mines Quebec, 1924, *in* Methods and case histories in mining geophysics: Sixth Common. Min. and Metal. Cong., Montreal, p. 290–293.
Koefoed, O., 1968, The application of the kernel function in interpreting geoelectrical measurements: Berlin-Stuttgart, Gebruder-Borntraeger, Geoexplor. monograph, series I, no. 2.
Kunetz, G., 1966, Principles of direct current resistivity prospecting: Berlin, Gebruder Borntraeger, 103 p.
Lajoie, J. J., and West, G. F., 1976, The electromagnetic response of a conductive inhomogeneity in a layered earth: Geophysics, v. 41, p. 1133–1156.
Lamontagne, Y., and West., G. F., 1976, A wide-band time-domain, ground EM system, *in* Proc. symp. on electromagnetic exploration methods, Univ. Toronto, p. 2–1 to 2–5.
Langer, R. E., 1933, An inverse problem in differential equations: Am. Soc. Math. J., v. 39, p. 14–28.
Logn, O., 1954, Mapping nearly vertical discontinuities by earth resistivities: Geophysics, v. 19, p. 734–760.
Lundberg, H., and Zuschlag, T., 1931, A new development in electrical prospecting: A.I.M.E. tech. publ. 415, 18 p.
Madden, T. R., 1971, The resolving power of geoelectric measurements for delineating resistive zones within the crust: Geophys. monograph 14, AGU, p. 95–105.
——— 1972, Transmission systems and network analogies to geophysical forward and inverse problems: MIT tech. rep. no. 72–3.
Marshall, D. J., and Madden, T. R., 1959, Induced polarization: A study of its causes: Geophysics, v. 24, p. 790–816.
Mateucci, M. C., 1867, Sur les courants electriques de la terre: Annales. Chim. et Phys., ser. 4, v. 4, p. 148–159.
Millet, F. B., Jr., 1967, Electromagnetic coupling of collinear dipoles on a uniform half-space, *in* Mining geophysics, v. II: Tulsa, SEG.
Mooney, H. M., and Wetzel, W. W., 1956, The potentials about a point electrode and apparent resistivity curves for a two-, three-, and four-layer earth: Minneapolis, Univ. Minnesota Press, 146 p.
Morgan, F. D., Madden, T. R., and Williams, E. R., 1979, On streaming potentials in geophysics: Presented at the 49th Annual International SEG Meeting, November 7, in New Orleans.
Nabighian, M. N., 1971, Quasi-static transient response of a conducting permeable two-layer sphere in a dipolar field: Geophysics, v. 36, p. 25–37.
——— 1977, The Newmont EMP method; *in* Geophysics applied to detection and delineation of non-energy, non-renewable resources: Report on grant AER 76-80802 from the Nat'l Sci. Foun., Dept. Geol. and Geophys., Univ. of Utah.
Nelson, P. H., 1977, Induced-polarization effects from grounded structures: Geophysics, v. 42, p. 1241–1253.
Nourbehecht, B., 1963, Irreversible thermodynamic effects in inhomogeneous media and their application in certain geoelectric problems: Ph.D. thesis, M.I.T.
Paterson, N. R., 1961, Experimental and field data for the dual-frequency, phase-shift method of airborne electromagnetic prospecting: Geophysics, v. 26, p. 601–617.
Pelton, W. H., Rijo, L., and Swift, C. M., Jr., 1978, Inversion of two-dimensional resistivity and induced-polarization data: Geophysics, v. 43, p. 788–803.

Petrick, W. R., Pelton, W. H., and Ward, S. H., 1977, Ridge regression inversion applied to crustal resistivity sounding data from South Africa: Geophysics, v. 42, p. 995–1005.

Petrick, W. R., Sill, W. R., and Ward, S. H., 1979, 3-D dc resistivity inversion using alpha centers: Presented at the 49th Annual International SEG Meeting, November 7, in New Orleans.

Petrowsky, A. A., 1928, The problem of a hidden polarized sphere, part I: Philos. Mag., v. 5, p. 334–353; part II, p. 914–917; part III, p. 927–933.

Pridmore, D. F., 1978, Three-dimensional modelling of electric and electromagnetic data using the finite-element method: Ph.D. thesis, Univ. of Utah.

Roy, A., and Apparao, A., 1971, Depth of investigation in direct current methods: Geophysics, v. 36, p. 943–959.

Ryss, Y. S., Ouchinnikova, T. M., Gaurilov, J. G., Voronin, D. V., and Panteleimanov, V. M., 1967, Method of geophysical prospecting of ore deposits: Can. pat. appl. no. 992–477.

Sato, M., and Mooney, H. M., 1960, The electrochemical mechanism of sulfide self-potentials: Geophysics, v. 25, p. 226–249.

Schlumberger, M., 1939, The application of telluric currents to surface prospecting: AGU trans., p. 271–277.

Schlumberger, C., 1920, Etude sur la prospection electrique du sous-sol: Paris, Gauthier-Villars, 94 p.

Seigel, H. O., 1949, Theoretical and experimental investigations into the applications of the phenomenon of overvoltage to geophysical prospecting: Ph.D. thesis, Univ. of Toronto.

——— 1959, Mathematical formulation and type curves for induced polarization: Geophysics, v. 24, p. 547–565.

——— 1974, The magnetic induced polarization method: Geophysics, v. 39, p. 321–339.

Seigel, H. O., and Pitcher, D. H., 1978, Mapping earth conductivities using a multifrequency airborne electromagnetic system: Geophysics, v. 43, p. 563–575.

Shaub, Y. B., 1965, Use of nonlinear conductivity effect in rocks for electrical prospecting: Bull. U.S.S.R. Acad. Sci., Earth Physics, p. 76–81.

Sims, W. E., Bostick, F. X., Jr., and Smith, H. W., 1971, The investigation of magnetotelluric impedance tensor elements from measured data: Geophysics, v. 36, p. 938–942.

Singh, S. K., 1973, Electromagnetic transient response of a conducting sphere embedded in a conductive medium: Geophysics, v. 38, p. 864–893.

Skal'skaya, I. P., 1948, Pole tochechnogo ishtochnika toka, respolozhennogo na poverkhnosti zemli nad naklonnym plastom: Akad. Nauk SSSR zhur. tekk. Fiz., v. 18, p. 1242–1524.

Slichter, L. B., 1932, Observed and theoretical electromagnetic model response of conducting spheres: Geophys. Prosp., p. 442–459.

——— 1933, The interpretation of the resistivity prospecting method for horizontal structures: Physics, v. 4, p. 307–322.

Snyder, D. D., 1976, A method for modeling the resistivity and IP response of two-dimensional bodies: Geophysics, v. 41, p. 997–1015.

Statham, L., 1936, Electrical earth transients in geophysical prospecting: Geophysics, v. 1, p. 271–277.

Stefanesco, S., 1950, Modeles theoreques de milieux heteirogenes pour les methodes de prospection electrique a courants stationnaires: Comitetul Geologic, Studii technice si economice, seria D., Nr. 2, and Nationola, Bucaresti.

Stefanesco, S., Schlumberger, C., and Schlumberger, M., 1930, Sur la distribution electrique potentielle autour d'une prise de terre ponctuelle dans un terrain a couches horizontales homogenes et isotropes: J. Phys. et Rad., ser. 7, v. 1, p. 132–141.

Stoyer, C. H., and Greenfield, R. J., 1976, Numerical solutions of the response of a two-dimensional earth to an oscillating magnetic dipole source: Geophysics, v. 41, p. 519–520.

Sumner, J. S., 1976, Principles of induced polarization for geophysical exploration: New York, Elsevier Scientific Publ. Co., 277 p.

Sundberg, K., Lundberg, H., and Eklund, J., 1925, Electrical prospecting in Sweden: Stockholm.

Swift, C. M., Jr., 1971, Theoretical magnetotelluric and Turam response from two-dimensional inhomogeneities: Geophysics, v. 36, p. 38–52.

Tagg, G. F., 1930, The earth resistivity method of geophysical prospecting: Some theoretical considerations: Mining Mag., v. 43, p. 150–158.

Tichonov, A. H., 1950, Determination of the electrical characteristics of the deep strata of the earth's crust: Dokladi, Akad. Sci., v. LXXIII, p. 295.

Ting, S. C., and Hohmann, G. W., 1980, Three-dimensional magnetotelluric modelling: Geophysics, submitted for publication.

Tornquist, G., 1958, Some practical results of airborne electromagnetic prospecting in Sweden: Geophys. Prosp., v. 6, p. 112–126.

Tripp, A. C., Hohmann, G. W., and Swift, C. M., Jr., 1979, Two-dimensional resistivity inversion: Presented at the 49th Annual International SEG Meeting, November 6, in New Orleans.

Van Bemmelen, W., 1908, Registration of earth-currents at Batavia for the investigation of the connection between earth-current and force of earth-magnetism: Kon Akad. Van wetens. te Amsterdam, Part I, Proc. v. 10-2, p. 512–523; part II, Proc. v. 10-2, p. 782–789; part III, Proc. v. 11, p. 242–248.

Van Nostrand, R. G., and Cook, K. L., 1966, Interpretation of resistivity data: U.S.G.S. prof. paper 499, 310 p.

Van Voorhis, G. D., Nelson, P. H., and Drake, T. L., 1973, Complex resistivity spectra of porphyry copper mineralization: Geophysics, v. 38, p. 49–60.

Vozoff, K., 1972, The magnetotelluric method in the exploration of sedimentary basins: Geophysics, v. 37, p. 98–141.

Vozoff, K., and Jupp, D. L. B., 1975, Joint inversion of geophysical data: J. Roy Astr. Soc.

Wait, J. R., 1951, A conducting sphere in a time varying magnetic field: Geophysics, v. 16, p. 666–672.

——— 1953, Induction by a horizontal magnetic dipole over a conducting homogeneous earth: AGU trans., v. 34, p. 185–189.

——— 1954, On the relations between telluric currents and the earth's magnetic field: Geophysics, v. 19, p. 281–289.

——— 1955, Mutual electromagnetic coupling of loops over a homogeneous ground: Geophysics, v. 20, p. 630–637.

——— 1958, Induction by an oscillating magnetic dipole over a two layer ground: Appl. Sci. Res., sec. B, v. 7, p. 73–80.

Ward, S. H., 1952, A theoretical and experimental study of the electromagnetic method of geophysical prospecting: Ph.D. thesis, Univ. of Toronto.

——— 1957, Airborne electromagnetic surveying, *in* Methods and case histories in mining geophysics: CIMM special volume, p. 71–78.

——— 1979, Ground electromagnetic methods and base metals, *in* Geophysics and geochemistry in the search for metallic ores: P. J. Hood, Ed., Geol. Surv. Can., econ. geol. rep. 31, p. 45–62.

Ward, S. H., Cartier, W. O., Harvey, H. A., McLaughlin, G. H., and Robinson, W. A., 1958, Prospecting by use

of natural alternating fields of audio- and sub-audio frequencies: CIMM bull. 51, p. 487–494.
Ward, S. H., and Harvey, H. A., 1954, Electromagnetic surveying of diamond drill holes: Can. Min. manual, p. 3–8.
Watson, H. G. I., 1931, The Bieler-Watson method: Mem. Geol. Surv. Can. 165, p. 144–160.
Wenner, F., 1912, The four-terminal conductor and the Thomson bridge: U.S. Bur. Standards Bull., v. 8, p. 559–610.
West, S. S., 1940, Three-layer resistivity curves for the Eltran electrode configurations: Geophysics, v. 5, p. 43–46.
Won, J., 1980, A wide-band electromagnetic exploration method—Some theoretical and experimental results: Geophysics, v. 45, p. 928–940.
Zohdy, A. A. R., 1975, Automatic interpretation of Schlumberger sounding curves, using modified Dar Zarrouk functions: U.S.G.S. Bull., 1313-E, 39 p.

AUTOMATIC INTERPRETATION OF SCHLUMBERGER SOUNDINGS

Keisuke Ushijima

Kyushu University 36
Fukuoka 812, Japan

ABSTRACT

The automatic interpretation of apparent resistivity curves from horizontally layered earth models is carried out by the curve-fitting method in three steps: (1) the observed VES data are interpolated at equidistant points of electrode separations on the logarithmic scale by using the cubic spline function, (2) the layer parameters which are resistivities and depths are predicted from the sampled apparent resistivity values by SALS system program and (3) the theoretical VES curves from the models are calculated by the Ghosh's linear filter method using the Zhody's computer program.

Two soundings taken over Takenoyu geothermal area were chosen to test the procedures of the automatic interpretation.

INTRODUCTION

The interpretation of the field data obtained in a geothermal area is done by the frame works as shown in figure 1.

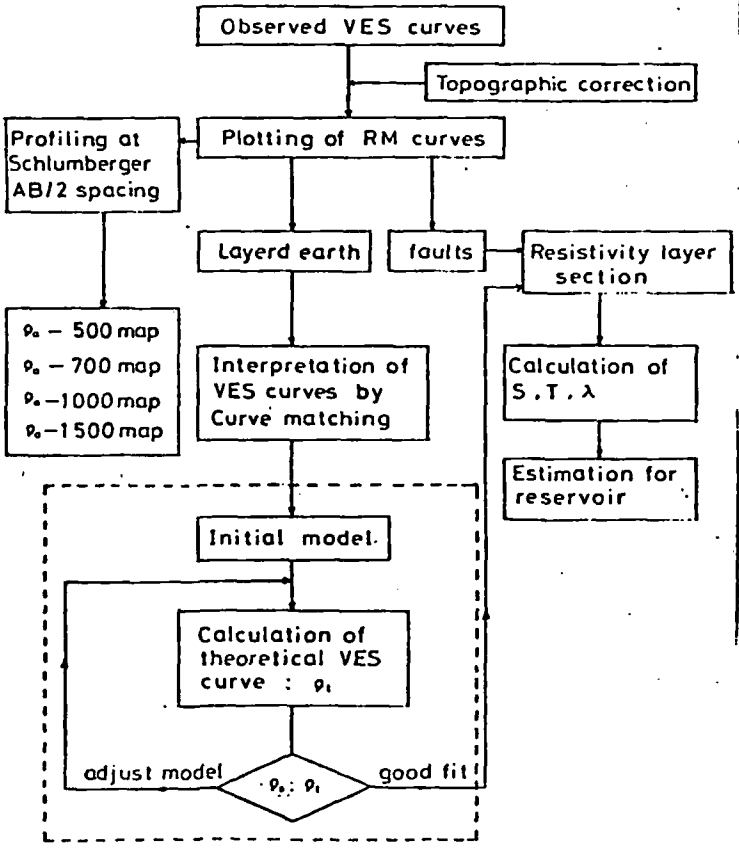

Fig. 1 Flow sheet for interpretation works of VES curves in a geothermal area

For the quantitative interpretation of VES curves, a complete curve matching method may be used on the condition that the subsurface of the surveyed area is a horizontally layered structure. For this purpose, several albums of standard graphs have been published by many authors, CGG (1955) and EAEG (1969).

In case of failure of obtaining a fit by these standard curves, the interpreter can obtain his own curve by using one of the computer programs for calculating theoretical VES curves which have been coded by Argelo (1967), Onodera (1969), Zhody (1974) and the author (1978).

However, a direct interpretation of VES curve is prefered, as a trial and error process is not only time consuming but unreliable. The methods of direct interpretation also have been investigated by many authors, Ghosh (1971), Marsden (1973) , Inman (1973, 1975), Zhody (1975),Koefoed (1976), Bichara (1976) and Johansen(1977).

These investigations are refered to as the direct interpretation, the automatic interpretation and resistivity inversion and will be classified into two groups , that is, the interpretation in the kernel function domain and the apparent resistivity domain.

In the present paper, the automatic interpretation of Schlumberger resistivity soundings is done by the curve-fitting method in three steps: (1) the observed VES data are interpolated at equidistant points of electrode separations (ln(10)/6= 0.38) on the logarithmic scale by the cubic spline function, (2) the layer parameters which are resistivities and depths are estimated from SALS (Statistical Analysis with Least-Squares Fitting) system program developed by Nakagawa and Oyanagi (1980) and (3) the theoretical VES curves from horizontally layered models are calculated by the Ghosh's linear filter method using the Zhody's computer program.

The practical applications to the field data obtained over Takenoyu geothermal area are given.

FUNDAMENTAL RELATION

The apparent resistivity for a horizontally layered earth is given by

Stefanesco (1930) as

$$\rho_a = \rho_1 \left\{ 1 + 2s^2 \int_0^\infty K(\lambda) \cdot J_1(\lambda s) \cdot \lambda \, d\lambda \right\} \quad (1)$$

where $J_1(\lambda s)$ = Bessel function of first kind, $K(\lambda)$ = Kernel function, determined by resistivities and depths of layers.

In a field determination of apparent resistivity(fig. 2), the current, I, flowing between two electrodes, A and B; the difference in potential, V, between two measuring electrodes, M and N, and the distances between the electrodes, L and l are measured.

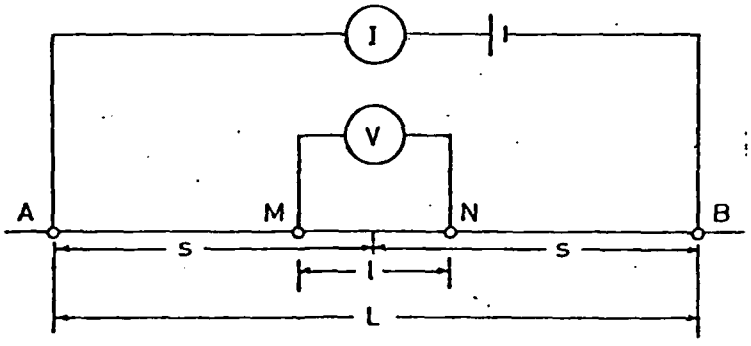

Fig. 2 Schlumberger array

Thus the following equation applies for the Schlumberger array used in measuring earth resistivity:

$$\rho_a = \pi \frac{L^2 - l^2}{4l} \cdot \frac{V}{I} \quad (2)$$

CURVE-FITTING

The least square statement of the problem of automatic interpretation in the apparent resistivity domain is

$$S = \sum_{i=1}^{m} \left\{ \rho_{af}(s_i) - \rho_{at}(s_i) \right\}^2 = \text{minimum} \quad (3)$$

where ρ_{at} = theoretical and ρ_{af} = field apparent resistivities.

On the other hand, the interpretation in the kernel function domain, Ghosh's linear filter method was used to obtain the resistivity transform from the interpolated apparent resistivity curve. According to Ghosh(1971), the statement of the digitized convolution would be

$$T_k = \sum_{j=-3}^{5} a_j \cdot R_{k-j} \quad (k = 0, 1, 2, \cdots) \quad (4)$$

An explicit expression of the resistivity transform is obtained from the relation to the kernel function by

$$T(\lambda) = \rho_1 \left\{ 1 + 2K(\lambda) \right\} \quad (5)$$

Thus the least square statement of the problem in the kernel function domain is

$$S = \sum_{i=1}^{n} \left\{ T_f(\lambda_i) - T_t(\lambda_i) \right\}^2 = \text{minimum} \quad (6)$$

As eq.(6) is the same form as eq.(3), then the problems can be solved in the same way.

Generally, if we wish the least squares solution to the system of equations

$$A x = y \quad (7)$$

where there are more equations than unknowns, we multiply both sides by A^t, and then solve the resulting normal equation

$$(A^t A) x = A^t y \quad (8)$$

and the solution is

$$x = (A^t A)^{-1} (A^t y) \quad (9)$$

where A = Yacobian matrix, A^t = transpose matrix and $(\ )^{-1}$ = inverse matrix.

In the problem of the automatic interpretation of VES curves, it is necessary to fit an expression with a nonlinear formula. The nonlinear equation is solved by a particular iteration scheme.

Starting from the rough estimate for the layer parameters, the solution will be refined. Once layer parameters are determined, we have a new estimate for the layer parameters

$$X_j = X_j^{(0)} + \delta X_j \quad (10)$$

COMPARISON OF THE METHODS

The problem of the automatic interpretation may be solved for both domains of the apparent resistivity and the kernel. For the numerical techniques for solving the non-linear least square problems, Gauss-Newton and Marquardt methods will be used. The numerical values from these four different approaches are shown in table 1. The table 1 indicates that there are no large differences between Gauss-Newton and Marquardt methods in the results. However, a comparison of the apparent resistivity domain with the kernel function domain show that significant differences are in the estimated parameters and the parameter standard deviations. This reason is considered that the error produced in the transformation of the apparent resistivity to the kernel have an influence upon the interpretation process.

Neverthless, the interpretation in the kernel domain should be further studied as it has the following advantages: (1) calculation of theoretical resistivity transform values and the partial derivatives of the kernel with respect to the parameters are not so difficult, (2) estimation of the initial guess is relatively easy because the resistivity transform is a very good reflector of the apparent resistivity curve: $T(0) = \rho_1$, $T(\infty) = \rho_n$; and (3) calculation of VES curve is not necessary during the repeating process.

Table 1. Automatic interpretation for the Schlumberger VES at C-8
***** Model parameters and Standard deviations *****

Initial Guess	Apparent Resistivity Domain		Kernel Function Domain	
	GAUSS-NEWTON	MARQUARDT	GAUSS-NEWTON	MARQUARDT
ρ_1 = 250	228.1 ± 18.7(8.2%)	228.1 ± 18.7(8.2%)	236.3 ± 51.6(21.8%)	236.4 ± 51.9(22.0%)
ρ_2 = 50	67.4 ± 6.1(9.1%)	67.4 ± 6.1(9.1%)	71.7 ± 48.5(67.6%)	71.9 ± 48.6(67.6%)
ρ_3 = 2	1.8 ± 0.3(16.7%)	1.8 ± 0.3(16.7%)	1.9 ± 3.3(173.7%)	1.9 ± 3.3(173.7%)
ρ_4 = 25	32.9 ± 4.5(13.7%)	32.9 ± 4.5(13.7%)	30.2 ± 5.9(19.5%)	30.2 ± 5.8(19.2%)
h_1 = 5	4.4 ± 0.6(13.6%)	4.4 ± 0.6(13.6%)	4.3 ± 4.0(93.0%)	4.3 ± 4.0(93.0%)
h_2 = 30	33.2 ± 1.5(4.5%)	33.2 ± 1.5(4.5%)	29.5 ± 15.7(53.2%)	29.4 ± 15.6(53.1%)
h_3 = 250	293.6 ± 49.9(17.0%)	293.6 ± 49.9(17.0%)	271.2 ± 529.(195.1%)	272.5 ± 527.(193.4%)
RSS	8.3571	8.3570	1.9016	1.9010
S	0.7464	0.7464	0.3561	0.3560
AIC	60.709	60.708	28.139	28.133
BIC	31.768	31.768	9.2385	9.2339
CPT(s)	8.8200	9.2200	5.9700	5.2200

Apparent Resistivity Domain						Kernel Function Domain					
NO.	AB/2	ρa	GAUSS	MARQT	RE	NO.	1/λ	T(λ)	GAUSS	MARQT	RE
1	3.15	240.0	218.9	218.9	-0.088	1	3.3075	219.2	218.6	218.6	-0.003
2	4.62	199.9	205.1	205.1	0.026	2	4.8548	196.0	197.5	197.4	0.008
3	6.79	165.0	176.8	176.8	0.072	3	7.1258	173.8	171.7	171.7	-0.012
4	9.96	135.0	136.8	136.8	0.013	4	10.459	143.1	146.6	146.6	0.024
5	14.62	110.0	99.53	99.53	-0.095	5	15.352	129.7	123.9	123.9	-0.045
6	21.46	71.20	75.75	75.75	0.064	6	22.534	98.06	102.2	102.2	0.042
7	31.50	70.70	61.16	61.16	-0.135	7	33.075	83.99	80.46	80.49	-0.042
8	46.24	43.60	45.23	45.23	0.037	8	48.548	57.93	60.33	60.35	0.041
9	67.86	25.30	25.90	25.90	0.024	9	71.257	45.52	43.69	43.71	-0.040
10	99.61	10.10	10.44	10.44	0.034	10	104.59	29.95	31.12	31.13	0.039
11	146.2	3.70	3.52	3.52	-0.049	11	153.52	22.90	22.14	22.15	-0.033
12	214.6	2.57	2.34	2.34	-0.089	12	225.34	15.73	16.03	16.04	0.019
13	315.0	2.46	2.73	2.72	0.110	13	330.75	12.57	12.11	12.11	-0.037
14	462.4	3.51	3.33	3.33	-0.051	14	485.48	9.61	9.86	9.86	0.026
15	678.6	4.61	4.37	4.37	-0.052	15	712.57	9.14	8.93	8.93	-0.023
16	996.1	5.78	5.98	5.98	0.035	16	1045.9	8.77	9.06	9.06	0.033
17	1462.1	8.22	8.12	8.12	-0.012	17	1535.2	10.17	10.08	10.08	-0.009
18	2146.1	10.50	10.79	10.79	0.028	18	2253.4	11.53	11.83	11.82	0.026
19	3150.0	14.00	13.97	13.97	-0.002	19	3307.5	14.32	14.09	14.09	-0.016
20	4623.6	17.50	17.52	17.52	0.001	20	4854.8	17.32	16.66	16.66	-0.038
21	6786.4	21.00	21.18	21.18	0.009	21	7125.7	19.19	19.26	19.27	0.004
22	9961.1	25.00	24.62	24.62	-0.015	22	10459.2	21.26	21.68	21.70	0.020

FIELD EXAMPLES

Two field curves (C-7 and C-8) will be analyzed. The data were taken at Takenoyu geothermal area, Kumamoto prefecture in Japan. The interpretation results are shown in figures 3 and 4, respectively. Drill hole information is given for the sounding at C-7. The electrical resistivity section at C-7 from the interpretation show a good correlation to the drill hole geologic section GSR-3 as shown in figure 5.

In Takenoyu geothermal field, hot water mixtures is from Hohi volcanics (pyroxene andesite). Therefore, detailed knowledges of the depth to this horizon and its resistivity value are important in determining the location of drill site for a geothermal steam production.

The two soundings will be reinterpreted by using the drill hole data.

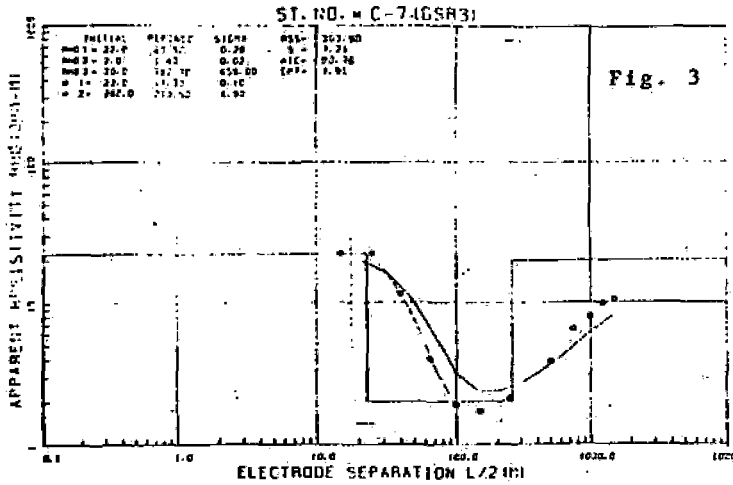

Fig. 3

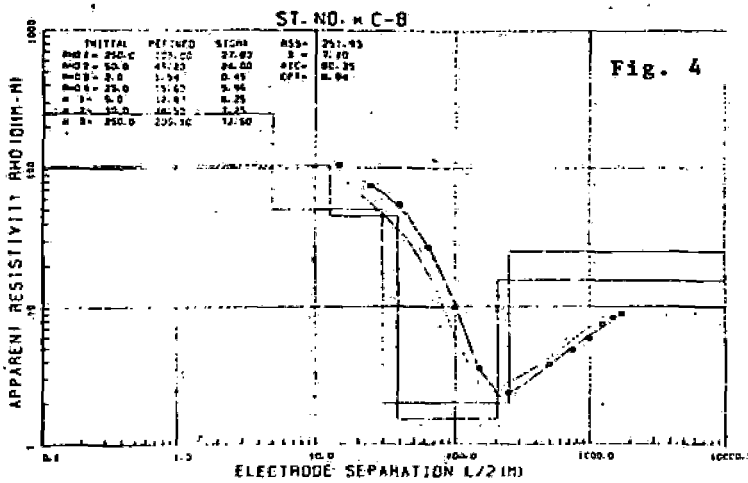

Fig. 4

REFERENCES

Ghosh, D. P., 1971, The application of linear filter theory to the direct interpretation of geoelectrical resistivity sounding measurements: GP, v.19, p.192

Inman, J. R., 1975, Resistivity inversion with ridge regression: GE, v.40, p.798

Johansen, H. K., 1977, A man/computer interpretation system for resistivity soundings over a horizontally stratified earth: GP, v.25, p.667.

Marsden, D., 1973, The automatic fitting of a resistivity sounding by a geometrical progression of depths: GP, v.21, p.266.

Nakagawa, T., and Oyanagi, Y., 1980, Program system SALS for nonlinear least-square fitting: system design; SIAM J. Sci. Statist. Comp.,

Ushijima, K., and Ushijima, K., 1978, Computer program for calculating theoretical curves and its application to VES data in geothermal areas: Geoth. Resouces Council, Transactions, v.2 p.671.

Zhody, A. A. R., 1974, A computer program for the calculation of Schlumberger sounding curves by convolution: U.S. Geol. Survey Rept. USGS-GD-74-010, PB-232056

_____, 1975, Automatic interpretation of Schlumberger sounding curves, using modified Dar Zarrouk functions: U.S. Geol. Survey Bull., 1313-E, 39p.

* GP: Geophysical Prospecting
GE: Geophysics

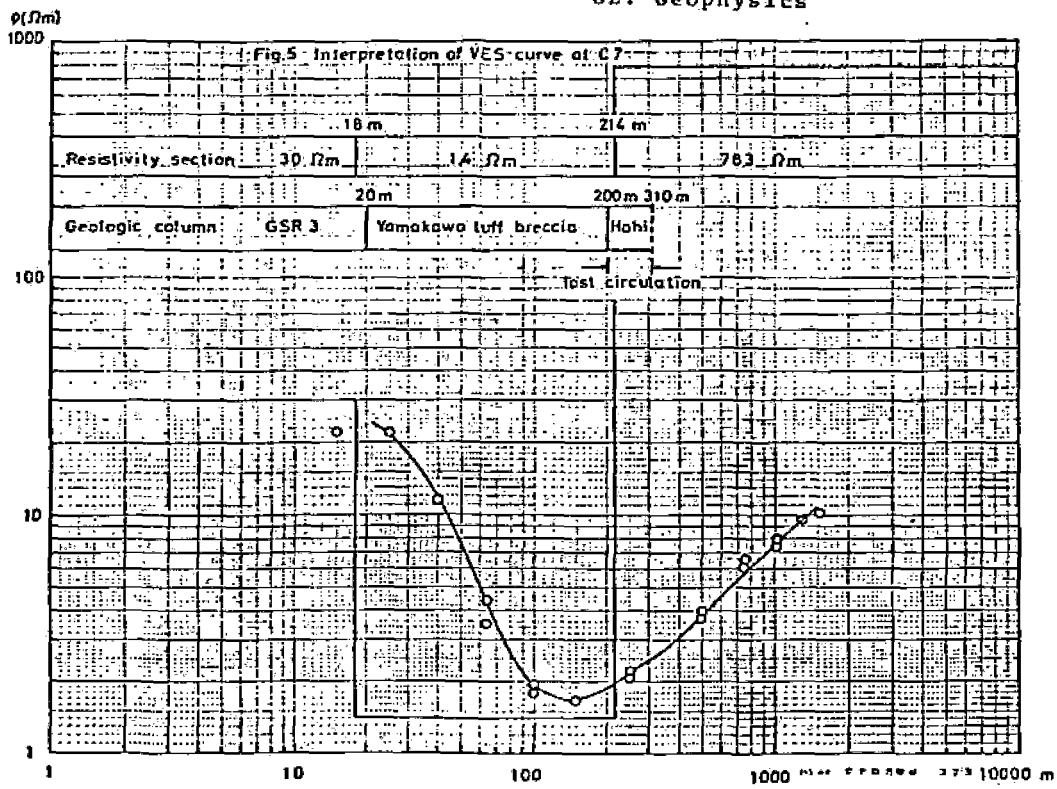

EMA ELECTRO MAGNETIC APPLICATIONS, INC.

CULTURAL NOISE IN EM SURVEYS

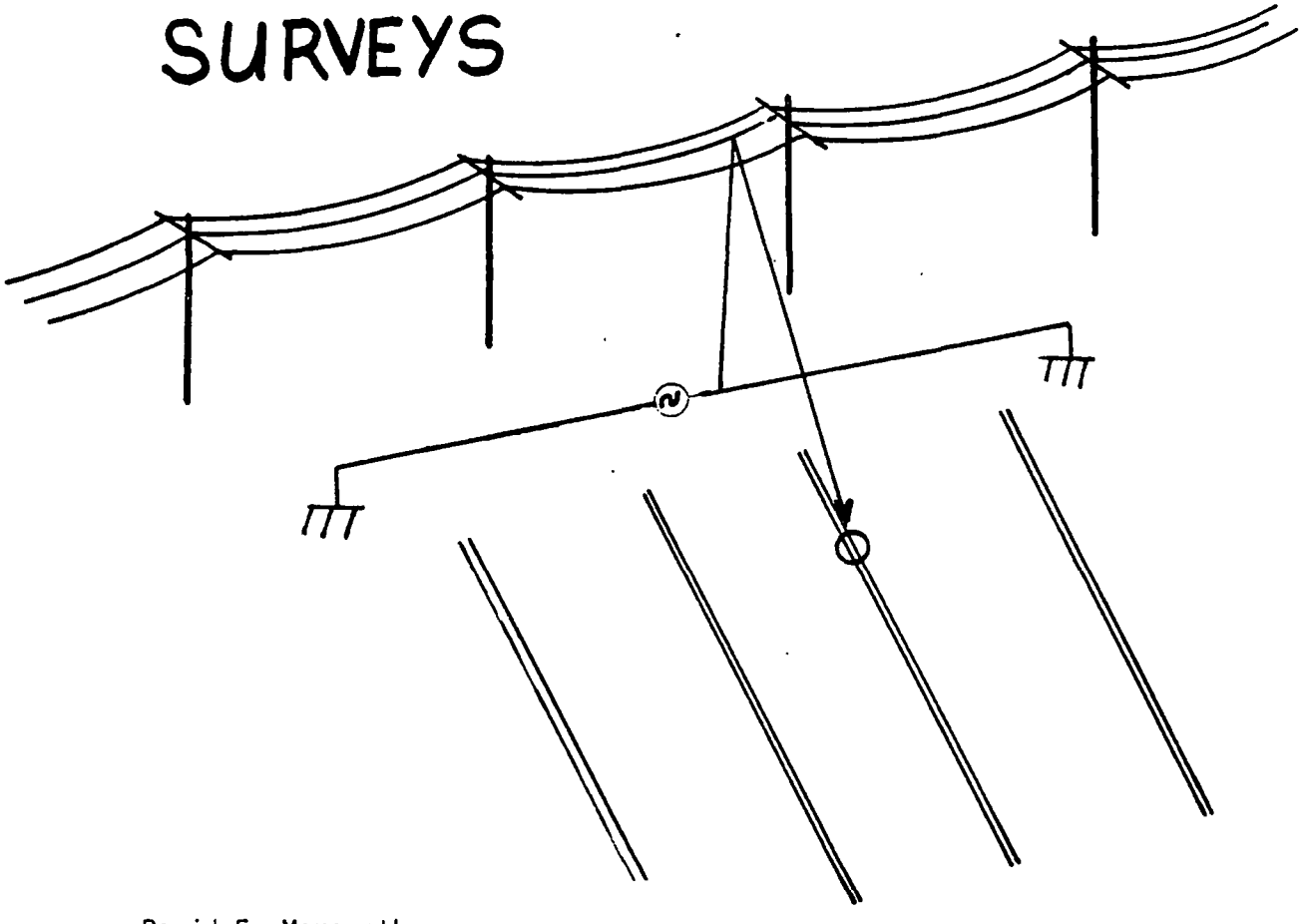

David E. Merewether
Electro Magnetic Applications, Inc.
P. O. Box 8482
Albuquerque, NM 87198
Phone: (505) 265-3538

Abstract

This memo provides a statement of the goals, technical approach and status of "A Study of the Characterization and Elimination of Cultural Noise in EM Surveys", Department of Energy Contract #DE-FC07-791D12041. A final report will be available in January 1981.

I Introduction

To search for deeply buried, geothermal resources by electromagnetic methods, interest must be directed to the very low frequency part of the survey data and surveys must be conducted over larger areas. Small signal amplitudes are to be expected and significant interference from cultural noise sources can be anticipated.

The first part of the work underway at EMA is the characterization of the cultural noise re-radiated by:

1) Overhead lines (power and telephone)
2) Fences
3) Railroad tracks
4) Buried cables (power and telephone)
5) Buried pipelines
6) Well casings

Both transient and CW excitation of these conductors are considered. Predictions are made of both horizontal and vertical components of the re-radiated field at reasonable observer locations on the earth's surface. These noise predictions are then compared to signals expected from deeply buried conductors.

The second part of the work is to examine ways in which the cultural noise could be eliminated from the data, either by data reduction techniques or by additional measurements.

The work is about 40% complete at present. It is to be completed in December 1980 and a final report issued in January 1981.

II Technical Approach

Initially a literature search was undertaken to identify recent publications of related information. Forty-two titles were identified. In this effort we were assisted by Dr. G. V. Keller of the Colorado school of mines.

We selected the time domain EM (TDEM) technique (including EM60 and UTEM) as the most promising approach to finding deeply buried Geothermal targets. Most of our analysis shall be concerned with predicting the cultural noise exhibited in TDEM type measurements. The frequency range of interest was selected to be 0.01 to 10KHz which is consistent with the assumption that we are searching for deeply buried targets.

Five aspects of the problem have to be addressed:

1) predicting the fields produced by transmitting antenna.
2) predicting the currents induced on cultural conductors
3) predicting the fields re-radiated by the cultural conductors
4) determining methods of noise removal by data analysis
5) determining methods of noise removal by additional measurements

We have preliminary results on the first three problem areas and those will be discussed in the following sections.

III Fields Produced by Transmitting Antennas

Three antennas have been chosen for study; a small horizontal loop, which is called a Vertical Magnetic Dipole (VMD). A small horizontal electric dipole (HED) and a horizontal electric dipole of finite length grounded on each end. For each of these antennas we require the electric and magnetic fields above the surface of a homogeneous conducting halfspace and the horizontal electric field below the surface of the conductor. The fields above the surface are needed as reference fields, and they are also needed as the drive fields for the above ground cultural conductors. Below the ground the horizontal electric field is used as the drive field for pipeline and power cable conductors.

To address the expected return from a deeply buried target we are also computing the surface fields for a two layered media where the second layer is more conducting and is located at 5KM below the surface. Figure 1 shows the formulas that we presently use in these predictions. Fields at points on or above the surface are obtained from image theory which have been shown to agree well with exact solutions.[1] Fields below the surface are estimated by attenuating the horizontal components of the field at the surface by skin depth formulas.

IV Excitation of Cultural Scaterers

All of the cultural scatterers of interest are modeled using transmission line theory (Figure 2). In both power lines and fence calculations there is a soil impedance parameter that must be evaluated.[2] This parameter is defined to be

$$Z_{soil} = \frac{-E_z(x=0)}{I} = \left(\frac{\omega\mu_0}{\pi}\right) \int_0^\infty \left(\frac{}{\sqrt{u^2+i} + u}\right) \exp\left(-2h\sqrt{\mu_0\omega\sigma_{soil}}\right) du$$

1 Bannister, Peter P. "Summary of Image Theory Expre-sions for the Quase Station Fields of Antennas at or Above the Earth's Surface". Proceeding of the IEEE Vol. 67, No. 7, July 1979, pp. 1001-1008.

2 Carson, John R. "Wave Propagation on Overhead Wires with Ground Return" Bell System Technical Journal 1926 No. 5, pp. 539 - 554.

Numerical integration of this formula reveals that at low frequencies both the real and imaginary parts are nearly directly proportional to frequency. At high frequencies both the real and imaginary parts are equal and proportional to (frequency)$^{1/2}$. We are using a simple fit to these curves in our calculations.

$$Zsoil = A\left(\frac{\sqrt{\omega_R \omega}}{\sqrt{\omega+\omega_R}}\right) + jB\,\frac{\sqrt{\omega_I \omega}}{\sqrt{\omega+\omega_I}}$$

where A and B are independent of soil conductivity and ω_R and ω_I are inversely proportional to soil conductivity.

Once the currents are computed the re-radiated fields at the observer location are calculated assuming that the cultural scatterer is a line source.

	E_ϕ	H_z
Infinitesimal Loop 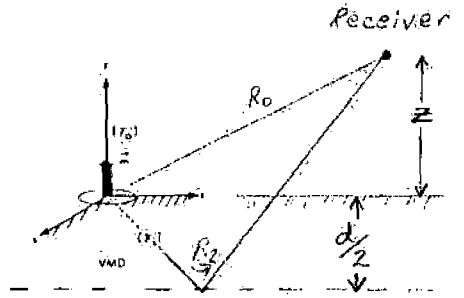	$E_\phi \approx -\frac{i\omega\mu_0 IA\rho}{4\pi}\left(\frac{1}{R_0^3} - \frac{1}{R_2^3}\right)$	$H_z \approx -\frac{IA}{4\pi}\left\{\frac{1}{R_0^3}\left[1 - \frac{3(z-h)^2}{R_0^2}\right] - \frac{1}{R_2^3}\left[1 - \frac{3(z+d+h)^2}{R_2^2}\right]\right\}$
Infinitesimal Dipole 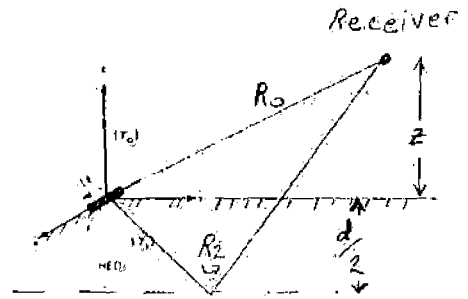	$E_\phi \approx \frac{Il\sin\phi}{4\pi i\omega\epsilon_0}$ * $\left\{\frac{1}{R_0^3} - \frac{1}{R_1^3} + \frac{2\gamma_0^2}{\gamma_1^2 R_1^3} + \gamma_0^2\left(\frac{1}{R_0} - \frac{1}{R_2}\right)\right\}$	$H_z \approx \frac{Il\rho\sin\phi}{4\pi}\left[\frac{1}{R_0^3} - \frac{1}{R_2^3}\right]$
Finite Dipole 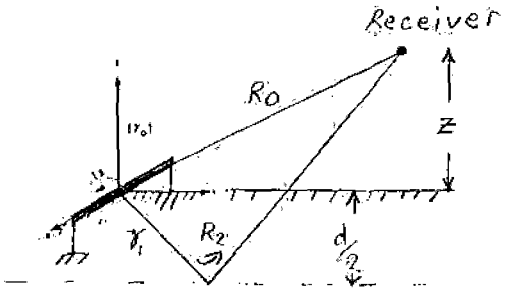	$E_x \approx -\frac{i\omega\mu_0 I}{4\pi}\left\{\ln\left[\frac{R_{11S} - (x+L/2)}{R_{12S} - (x-L/2)}\right] - \ln\left[\frac{R_{21P} - (x+L/2)}{R_{22P} - (x-L/2)}\right] + \frac{1}{\gamma_0^2}\left[\frac{(x+L/2)}{R_{21P}^3} - \frac{(x-L/2)}{R_{22P}^3}\right] - \frac{1}{\gamma_0^2}\left(1 - \frac{2\gamma_0^2}{\gamma_1^2}\right)\left[\frac{(x+L/2)}{R_{21S}^3} - \frac{(x-L/2)}{R_{22S}^3}\right]\right\}$	$H_z \approx -\frac{Iy}{4\pi}\left\{\frac{1}{[y^2 + (d+z+h)^2]}\right.$ * $\left[\frac{(x+L/2)}{R_{11S}} - \frac{(x-L/2)}{R_{12S}}\right] - \frac{1}{[y^2 + (z-h)^2]}$ * $\left.\left[\frac{(x+L/2)}{R_{21P}} - \frac{(x-L/2)}{R_{22P}}\right]\right\}$

Figure 1. Models for Transmitting Antennas.

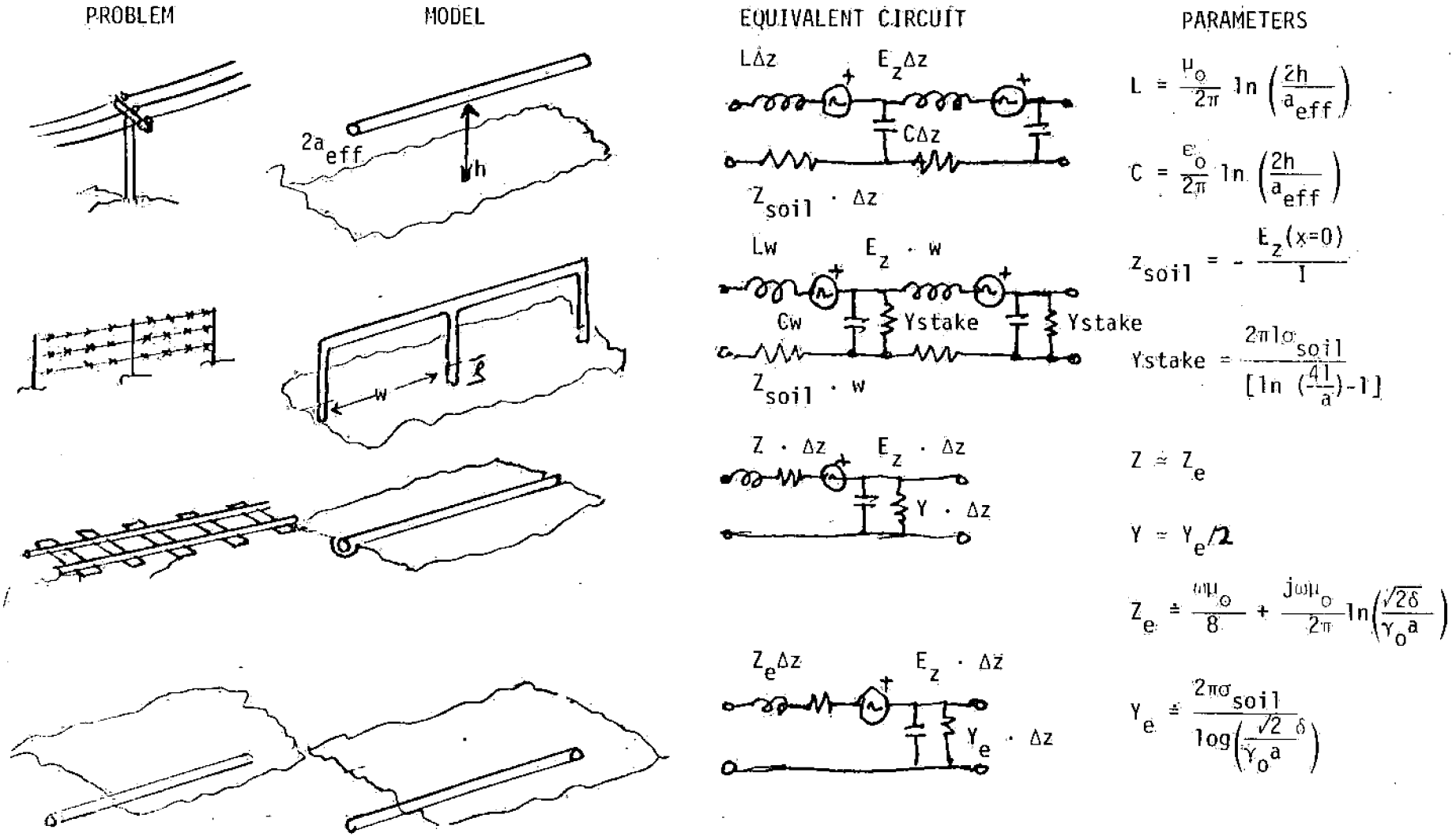

Figure 2. Models Used to Predict Currents on Cultural Conductors.

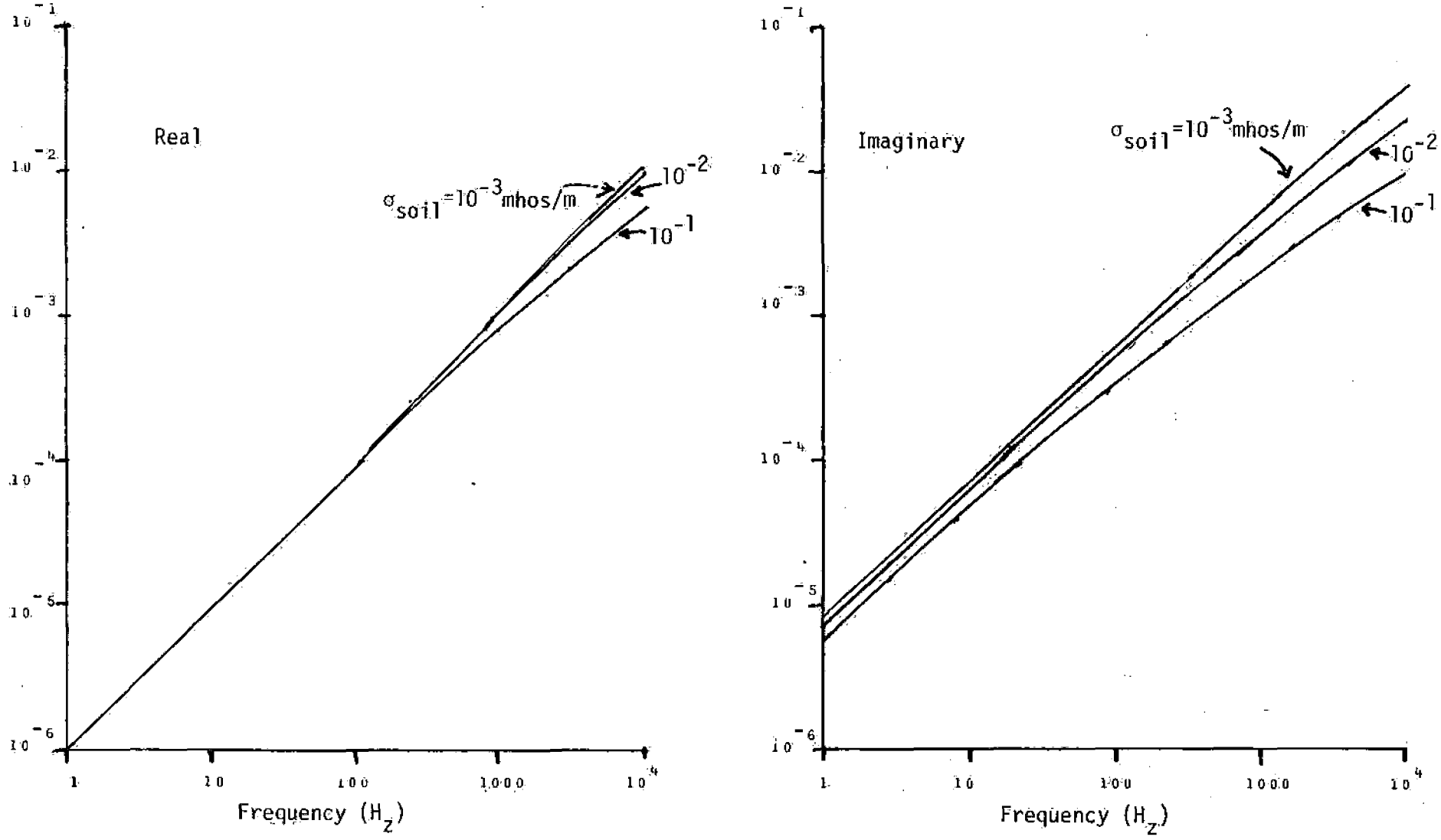

Figure 3. Real and Imaginary Parts of the Soil Impedance Evaluated for a Power Line 10 meters high.

GEONOMICS, INC.

191 Main Street, P.O.Box 382
Hempstead, New York 11550
(516) 481-6695

EXPLORATION, EVALUATION, AND DEVELOPMENT OF NATURAL RESOURCES

ELECTRICAL RESISTIVITY TECHNIQUES IN GEOTHERMAL EXPLORATION

1972

INTRODUCTION

Analysis of geothermal exploration case histories from about a dozen countries shows that electrical resistivity is a most powerful geophysical exploration technique for geothermal resources (Meidav and Banwell, 1972, in press).

Electrical resistivity techniques measure the specific resistance of rocks of any depth to the flow of electricity. The resistivity of water-saturated rocks depends upon the rock temperature, salinity of the saturating fluid, clay content, formation factor, and steam or gas content.

The resistivity in geothermal areas is usually lower than the resistivity in the surrounding non-thermal areas, because most of the above factors tend to work together to reduce the resistivity of geothermal reservoirs. The resistivity contrast between hot, water-saturated rocks within the geothermal area and the colder surrounding rocks may be as great as 1:100 but is often of the order of 1:5 (Meidav and Banwell, 1972). Because of that great contrast in electrical properties between hot rocks and the colder surrounding area, electrical resistivity techniques have proven invaluable in geothermal exploration (cf. for example Banwell and MacDonald, 1965; Meidav, 1970; Keller, 1970).

The resistivity of vapor-dominated reservoirs can be higher than that of surrounding rocks, thus creating an important exception to the above rule.

In liquid-dominated systems, the relationship between the resistivity of the rock, the salinity of the saturating fluid, the formation factor and the temperature are graphically shown in Figure 1. It is seen that by measuring the resistivity on the earth's surface (labelled "Rock Resistivity"), by estimating the formation factor of the rocks it is possible to either estimate the temperature of the reservoir fluids (if the salinity is known) or to estimate the salinity, if the temperature at depth can be approximated.

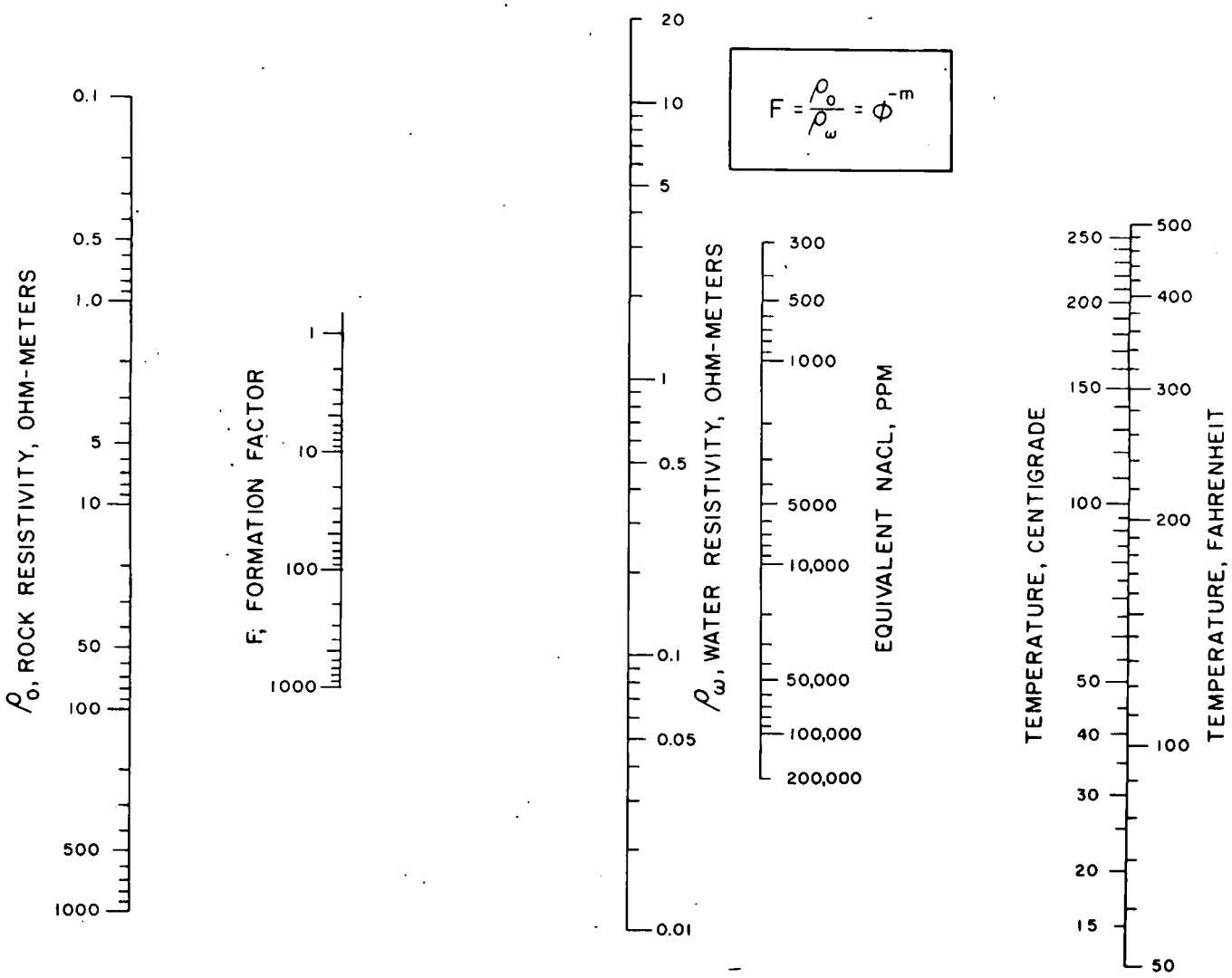

Figure 1. A nomogram for relating resistivity, which is measurable on the earth's surface, to temperature or salinity of the rocks at depth.

1. RECONNAISSANCE RESISTIVITY TECHNIQUES

A. THE ROVING DIPOLE TECHNIQUE

The roving dipole technique is designed to facilitate rapid reconnaissance of large areas, in order to select specific targets for detailed investigation. The advantage of this technique is that it is lower in cost per unit area, is faster than other methods, and does not require straight survey lines, making it especially useful in rugged terrain. The shortcoming of the method is that it only provides a general evaluation of the areas surveyed

Figure 2 is a map showing the resistivity contours derived from illuminating a geothermal area in Indonesia from two different locations. Although in agreement generally, the difference between the two sets of contours reflects the difference in effective probing depth at each receiver station relative to sources A and B.

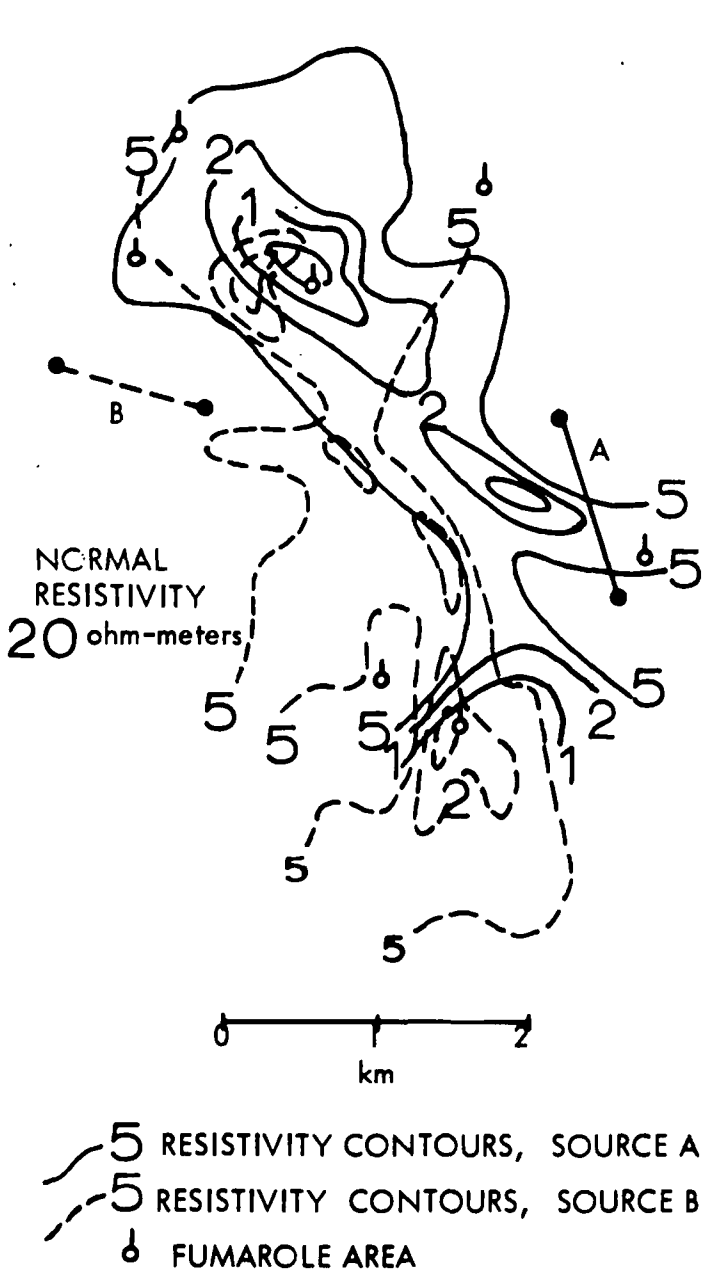

Figure 2. Roving dipole survey, Indonesia, using two different transmitter locations (A and B). The low resistivity areas coincide with the location of surface thermal features (fumaroles).

The interpretation of roving dipole data is facilitated through the preparation of electrical conductance maps. At large transmitter-receiver distances, in areas underlain by a very resistive basement, conductance maps are not affected as much by the distance factor as are the resistivity maps. Figure 3 schematically shows the electrical conductance profiles that would be obatined over two common geological situations. It should be noted that at short distances the apparent conductance C_a is not equal to the true conductance because at short transmitter-receiver distances, the physical condition for establishing conductance (i.e., a large distance from the source compared with depth to the basement) is not fulfilled. However, by multiple-illumination, i.e. by roving across the area in more than one direction, it is possible to establish the correct conductance value of the area. Moreover, multiple coverage permits some preliminary three-dimensional determination of conductivity and thickness components of the area under investigation.

Roving dipole techniques also permit the execution of detailed depth soundings in the vicinity of each of the widely separated current electrodes. Such soundings may be referred to as monopole soundings. They provide very smooth data, when no lateral discontinuities exist.

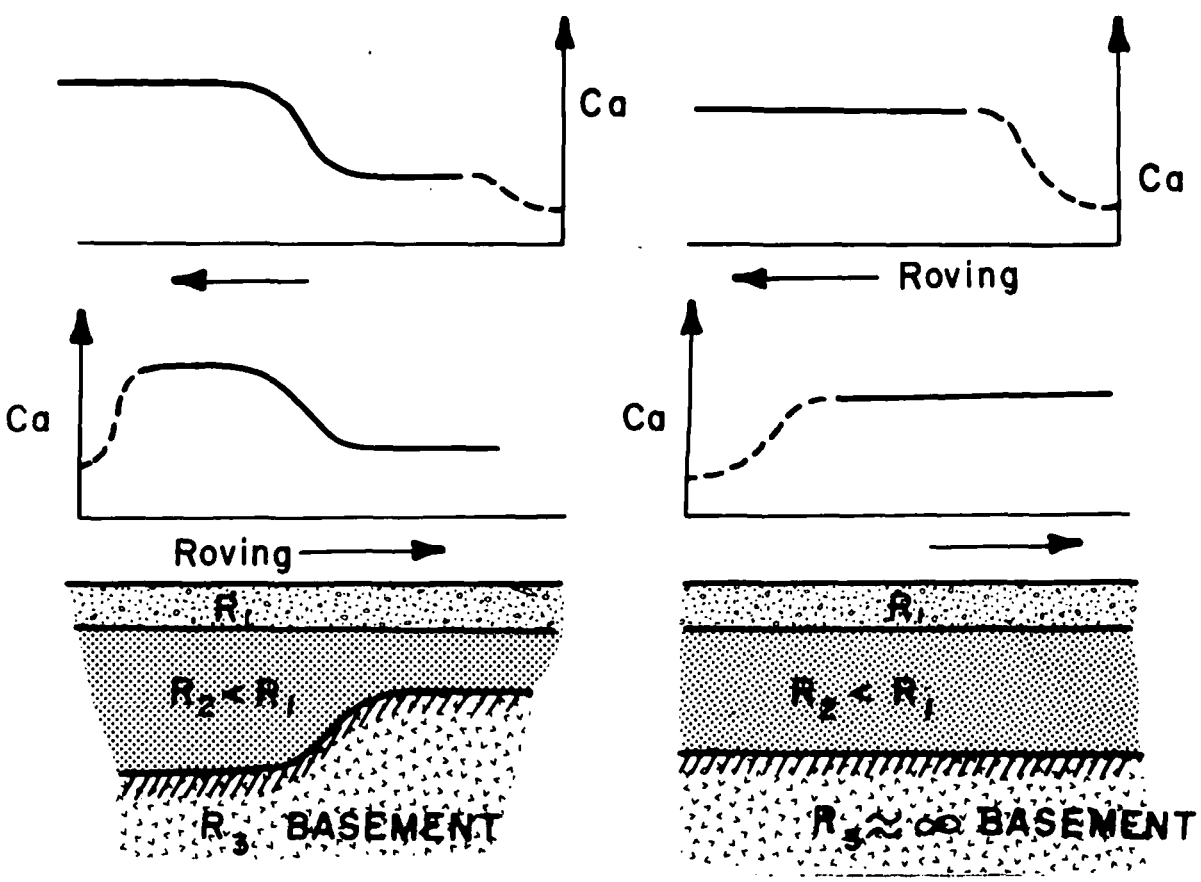

Figure 3. Synthetic apparent electrical conductance (C_a) profiles over a three-layered earth, where the middle layer is the most conductive one. Note that at short distances, the apparent conductance (broken line) is different from the true conductance (solid line)

B. CONSTANT DEPTH PROFILING

This technique also provides a rapid reconnaissance of large areas. Its advantage, as with the roving dipole method, lies in speed. Its major disadvantage lies in the need to carry the transmitter to the center of the station to be explored, which might be logistically difficult in some cases.

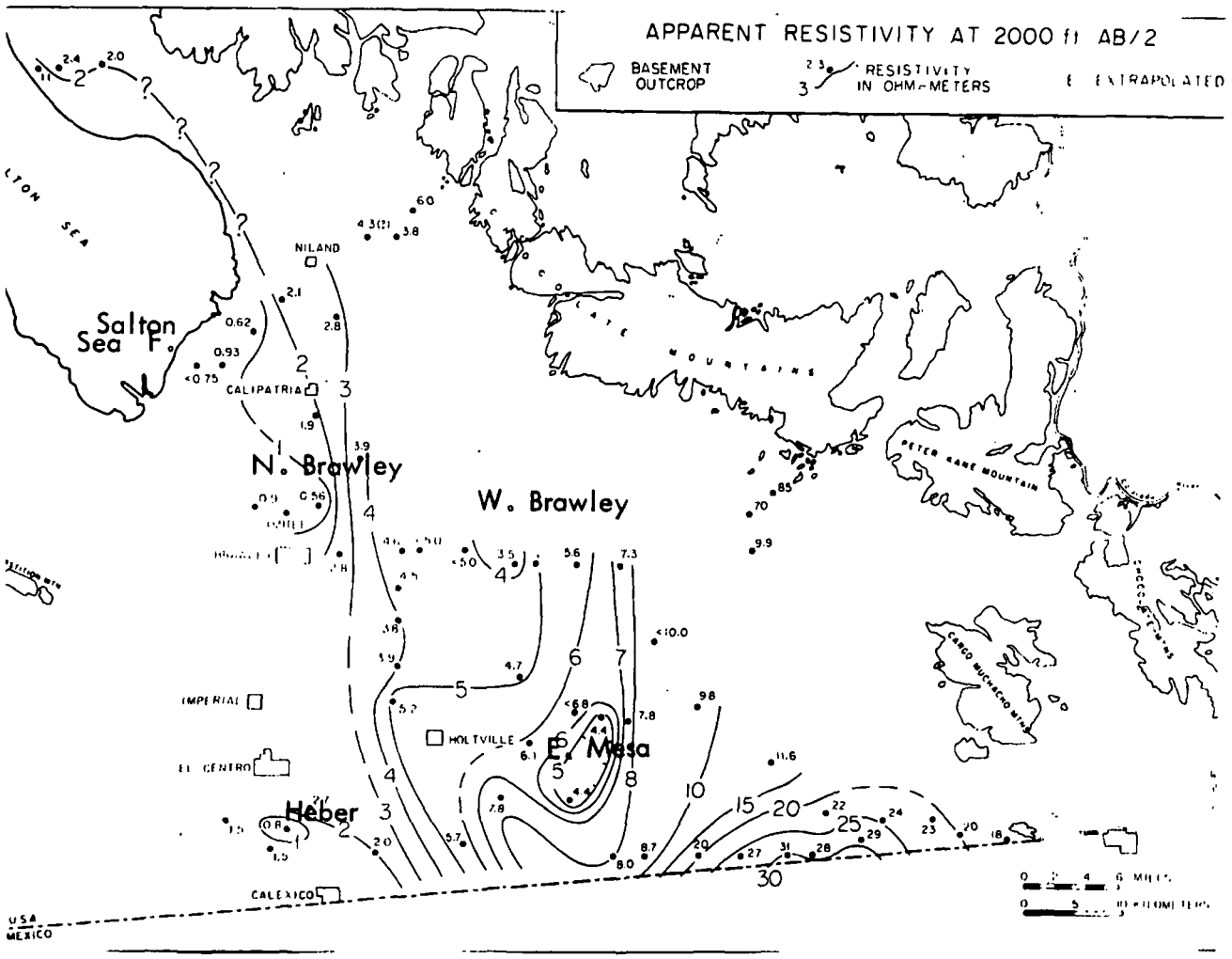

Figure 4. Apparent resistivity map for a 2,000' constant depth profiling of the Imperial Valley, California. Note the regional resistivity gradient upon which the various geothermal fields, partly discovered through this resistivity survey, are superimposed.

2. SEMI-DETAILING TECHNIQUES

DIPOLE-DIPOLE PROFILING

The dipole-dipole technique has been extensively utilized in mineral exploration, and recently in geothermal exploration. The advantage of the dipole-dipole technique is that it provides a resistivity cross-section in line of the dipole-dipole profile. It has been successfully employed by the U. N. in Kenya in delimiting the boundaries of a geothermal field, as well as the location of a major fault running through that field.

The dipole-dipole technique may be regarded as a semi-detailing technique. It is slower than the roving dipole technique, but provides greater detail along the profile. This technique requires reasonably straight lines to be run. It may be used to advantage to obtain finer details of anomalies detected by any of the reconnaissance techniques, or, if funds permit, as both the reconnaissance as well as detailing technique. However, depth computations from dipole-dipole data must be evaluated with some caution, because the very shallow resistivity distributions (at depths less than 1.4n), which greatly affect the rest of the deeper data are not normally available.

3. DETAILING TECHNIQUES

SCHLUMBERGER DEPTH SOUNDINGS

The Schlumberger depth sounding technique has been employed successfully for detailed determination of layering in terms of electrical resistivity of earth strata to a great depth (cf. for example, Meidav and Furgerson, 1972). This technique is the most proven of the various depth sounding techniques, with a very large repertoire of experience for interpretation of the data. The technique is used to resolve some of the finer details of the geologic structure of the area. A survey utilizing the Schlumberger depth soundings exclusively has been conducted across the Imperial Valley of California (Meidav, 1970). Three of the residual resistivity lows have been drilled after the conclusion of that survey, confirming the relationship between resistivity lows and temperature highs. Figure 5 shows the resistivity cross-section which was derived from the Schlumberger depth soundings. We predict that the Brawley resistivity low will prove the existence of a significant geothermal reservoir when drilled eventually.

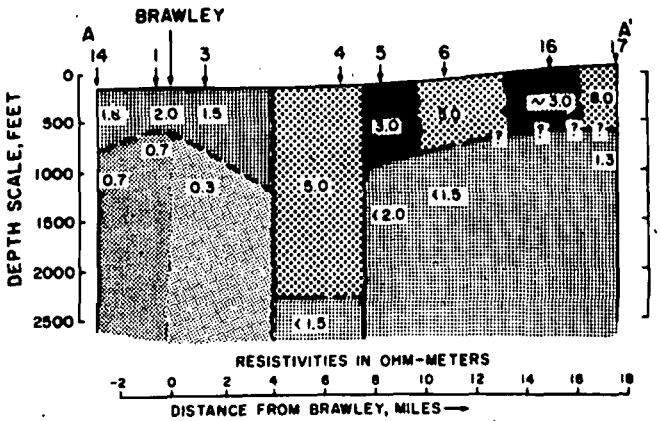

Figure 5. A resistivity cross-section across the North Brawley anomaly in the Imperial Valley, showing the location of suspected faults, and the very low resistivity associated with the Brawley geothermal field. The cross-sections were constructed from resistivity depth sounding data.

REFERENCES CITED

1. Banwell, J. and W.J.P. MacDonald, 1965 Resistivity surveying in New Zealand geothermal areas, Eighth Commonwealth Mining and Metallurgical Congress, Australia and New Zealand.

2. Keller, G.V., 1966, Dipole method for deep resistivity studies, Geophysics V. 31:1088-1104.

3. Meidav, T., 1970, Application of electrical resistivity and gravimetry in deep geothermal exploration, United Nations Symposium on the Development and Utilization of Geothermal Resources, Pisa 1970; Vol.2, Part 1:303-310.

4. Meidav, T., 1970, Arrays and nomograms for electrical resistivity exploration Geophysical Prospecting, V. 18:550-563.

5. Meidav, T., and R. Furgerson, 1972, Resistivity studies of the Imperial Valley Geothermal Area, California, Vol. 1, No. 2:47-62.

McPHAR

McPHAR GEOPHYSICS LIMITED

LOOP-LOOP EM-RESISTIVITY SYSTEM - INTRODUCTORY PAPER

BY

PHILIP G. HALLOF AND MRINAL K. GHOSH

Presented at the
Symposium on Electromagnetic Exploration Methods (SEEM)
at the
University of Toronto
May 2nd to May 5th, 1973

Loop-Loop EM-Resistivity System - Introductory Paper

By

Philip G. Hallof and Mrinal K. Ghosh

Introduction

The resistivity method was among the first of those used by early geophysicists. Electrical current could be made to flow through the ground, and the earth-forming materials had varying specific resistivity values. Initially, the potential equations could be solved for only a few simple geometries; as mathematical physics became more sophisticated, the forward problem was solved for more complex earth geometries. In recent years, iterative techniques using high-speed digital computers, with large storage capabilities, have given approximate solutions to even more problems.

Except for a few experimental programs, quantitative interpretations for resistivity field surveys are still obtained only by "curve-matching" techniques. These solutions are largely limited to field surveys in which the earth can be approximated by a layered geometry with relatively few layers.

The development of equipment to make the resistivity measurements has largely outdistanced the theoretical aspects of the problem and the interpretation of the data. Reliable, light-weight equipment is now available to make measurements at frequencies from d.c. to 0.5 Hz, using battery sources or motor-generators.

It has been recognized for sometime, that apparent resistivities could be determined from the analysis of electromagnetic fields from various types of sources (Frischknecht, Keller and Frischknecht, Ward). Since solutions of Maxwell's equation are even more difficult than those of Poisson's equations, theoretical solutions are available for only a few earth geometries and sources. Much of the available theoretical data has appeared in print, but very little field data has been published.

In this short paper we would like to discuss two exploration problems in which conventional dipole-dipole resistivity survey data has been of some help. However, our experience has led us to believe that resistivity measurements using electromagnetic sources may be preferable to the more usual grounded resistivity techniques. The geometries encountered in these two exploration problems are simple enough that a successful application of the electromagnetic resistivity determination is anticipated. Electronic equipment is available to make the necessary measurements.

Application of the Resistivity Technique

The resistivity method has been used in several areas of exploration in addition to exploration for conductive sulphide mineralization. These include depth of overburden determinations and groundwater exploration in several types of environments. In recent years, the McPhar Group of Companies have used the resistivity method in two additional types of exploration problems.

1) Exploration for Geothermal Sources

The terms "Energy Shortage" and "Energy Crisis" have become widely used, particularly in North America, in recent years. The implied problems have been compounded by various real, or imagined, dangers to the environment. This combined situation has given rise to a greatly renewed interest in geothermal energy sources. Heat (in the form of steam or hot water) is currently used as an energy source in the U.S.A., New Zealand, Mexico, Italy and Iceland. Exploration for suitable sources is now underway in many areas.

Not much is known about the detailed properties of these high-temperature zones within the very uppermost portion of the earth's crust. One recognized characteristic of all of the known geothermal zones is their low resistivity. This is due to the high temperature and salinity of the fluids and the high porosity of the enclosing rocks. (Meidav).

The high temperature zones have been found in all types of rocks; the undisturbed resistivities are in the range from 3.0 to 3000 ohm-meters. The

true resistivity within the geothermal source itself is always in the range from 0.50 to 5.0 ohm-meters.(Meidav).

Various types of resistivity techniques have been successfully employed to locate, and outline, geothermal sources. McPhar has successfully applied the dipole-dipole survey technique in several areas around the "Pacific Rim". For a reconnaissance survey of this type we have used the dipole-dipole electrode configuration with X = 2000' to X = 4000' and n = 1,2,3,4,5. The results, when plotted in "pseudo-section" form, have been found to be very helpful in the detection of low resistivity zones that could be related to high temperature zones.

The resistivity data shown in Figure I and Figure II are typical of those from surveys in which the country rocks were a thick section of volcanic flows and fragmental rocks. Zones of low resistivity were located, at depth, on both of the lines shown; the lines are positioned one mile apart.

The results shown in Figure I have outlined a relatively narrow zone of lower resistivities, at considerable depth. One mile to the west (Figure II), the low resistivity zone has a much greater width. At about 100S, the apparent resistivities were relatively uniform, with a magnitude about equal to those at the southern end of Figure I.

If the anomalous patterns indicated by the contoured "pseudo-section" data plots are simple enough, an attempt can be made at quantitative interpretation using curve-matching techniques. This has been done for the results shown on Figure I and Figure II, assuming a horizontally layered geometry. The interpreted parameters are shown on the data plots.

In the examples shown, the interpretation of the reconnaissance resistivity results is quite satisfactory. In field surveys in which the results are more variable, these quantitative interpretations will be less accurate. However, the extensive zones of low resistivity can usually be detected, even at considerable depth.

Many areas of potential geothermal interest are very large in areal extent. This will continue to be true as long as the geological and geochemical tools being used for primary exploration are still in the development

RESISTIVITY SURVEY IN WESTERN U.S.A.

LINE – ONE MILE WEST

DIPOLE – DIPOLE ELECTRODE CONFIGURATION

X = 2000 FT., – N = 1, 2, 3, 4, – FREQUENCY – 0·05 Hz.

$\rho a/2\pi$ IN OHM FEET (0·52 X ρa – OHM METRES)

(GEOTHERMAL)

Theoretical fit for
One-layer earth.

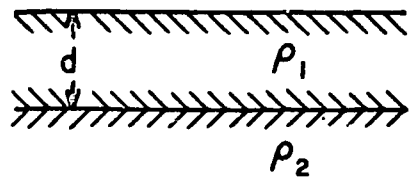

ZONE I C
d = infinity
ρ_1 = 100 – 110 ohm metres

ZONE I B
d = 2000 feet = 600 metres
ρ_1 = 105 – 115 ohm metres
ρ_2 = 10 – 11 ohm metres

ZONE I A
d = infinity
ρ_1 = 105 – 115 ohm metres

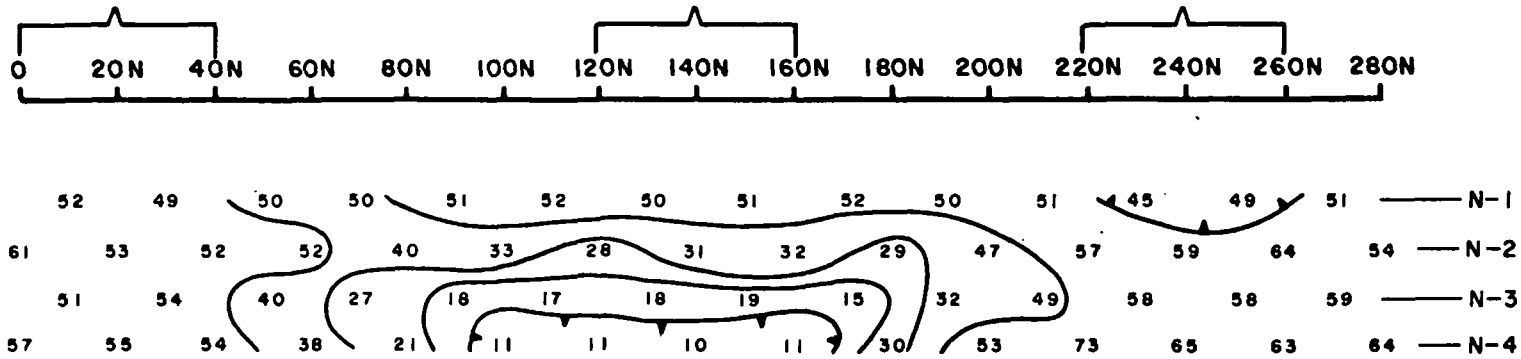

FIG. 1

RESISTIVITY SURVEY IN WESTERN U.S.A.

LINE – TWO MILES WEST

DIPOLE–DIPOLE ELECTRODE CONFIGURATION

X = 2000 FT., – N = 1, 2, 3, 4, – FREQUENCY – 0·05 Hz.

$\rho a/2\pi$ IN OHM FEET (0·52 X ρa – OHM METRES)

(GEOTHERMAL)

Theoretical fit for
One-layer earth.

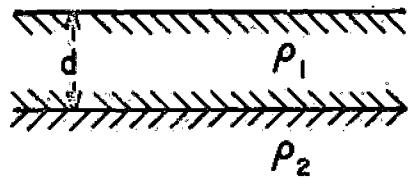

ZONE II C
d = 1000 feet = 300 metres
ρ_1 = 100–110 ohm metres
ρ_2 = 5·0–5·5 ohm metres

ZONE II B
d = 2000 feet = 600 metres
ρ_1 = 100–110 ohm metres
ρ_2 = 5·0–5·5 ohm metres

ZONE II A
d = infinity
ρ_1 = 100–110 ohm metres

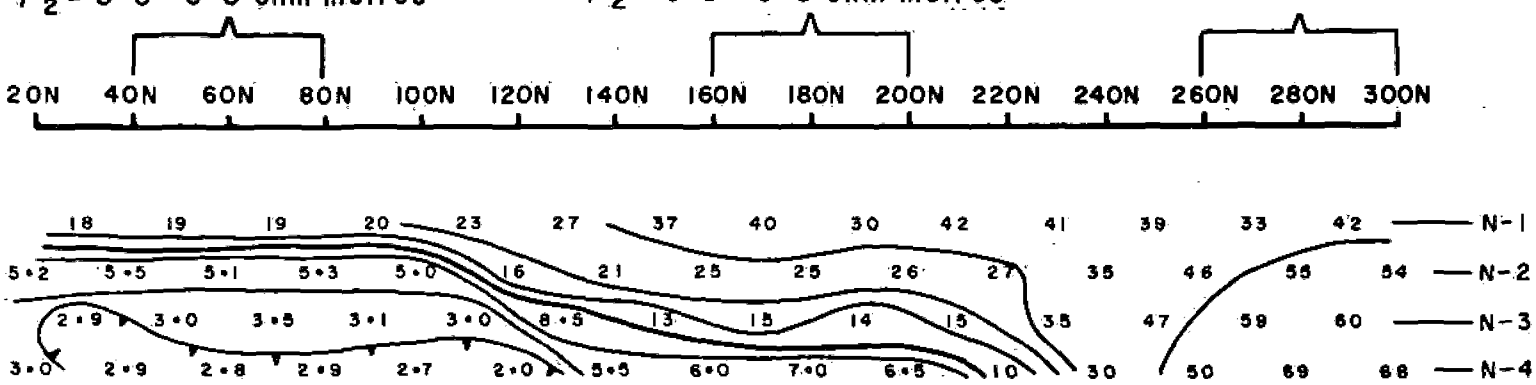

FIG. 2

stage. Further, many of the areas of interest occur in regions of rugged topography. Under these conditions, it would be desirable to be able to make the reconnaissance resistivity determinations without having to move along regularly surveyed lines. Therefore, some type of "spot-to-spot" resistivity determination using an electromagnetic source would be very useful.

2) Depth of permafrost determinations in the Arctic

The energy shortage has also spurred the search for oil and gas within North America. Much of this work has taken place within the Canadian Arctic. The initial targets were structures of very great size and extent. In this work, sophisticated corrections to the reflection seismic data were not necessary. Recently, more detailed analysis has revealed that in order to do accurate interpretation of the seismic data it is necessary to correct from the velocity change that is present at the base of the permafrost. Further, it has become clear that the depth of the permafrost is much more variable than was previously supposed.

The frozen sediments within the permafrost layer of the basins have complex properties. It is known that they have a higher seismic velocity than the unfrozen sediments. The resistivity value within the permafrost layer is also higher than at depth. In some areas, the results of dipole-dipole resistivity surveys have successfully indicated changes in the depth of permafrost and permitted corrections to be made to seismic data.

The dipole-dipole resistivity results shown in Figure III ($X = 1000'$, $n = 1,2,3,4$) are fairly typical of those from the Canadian Arctic. The layering is quite evident to the north and south. Near 90N to 100N, the lower resistivity rocks extend quite close to the surface. This feature, which extends across several parallel lines, suggests a sudden and dramatic change in the permafrost depth.

Again if the geometry of the earth is simple enough so that a layering approximation can be made, some quantitative interpretation can be done, as was done from the data shown in Figure III. Even these approximate solutions are useful in the interpretation of the seismic data.

RESISTIVITY SURVEY IN CANADIAN ARCTIC

LINE "A"

DIPOLE-DIPOLE ELECTRODE CONFIGURATION

X = 2000 FT., – N = 1,2,3,4,– FREQUENCY – 0·05 Hz.

$\rho a/2\pi$ IN OHM FEET (0·52 X ρa – OHM METRES)

(PERMAFROST)

Theoretical fit for
One-layer earth.

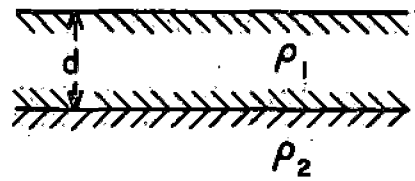

ZONE A III
d = 900 feet = 275 metres
ρ_1 = 4000 ohm metres
ρ_2 = 50–55 ohm metres

ZONE A II
ρ_1 = 35–45 ohm metres

ZONE A I
d = 400 feet = 125 metres
ρ_1 = 4000 ohm metres
ρ_2 = 200 ohm metres

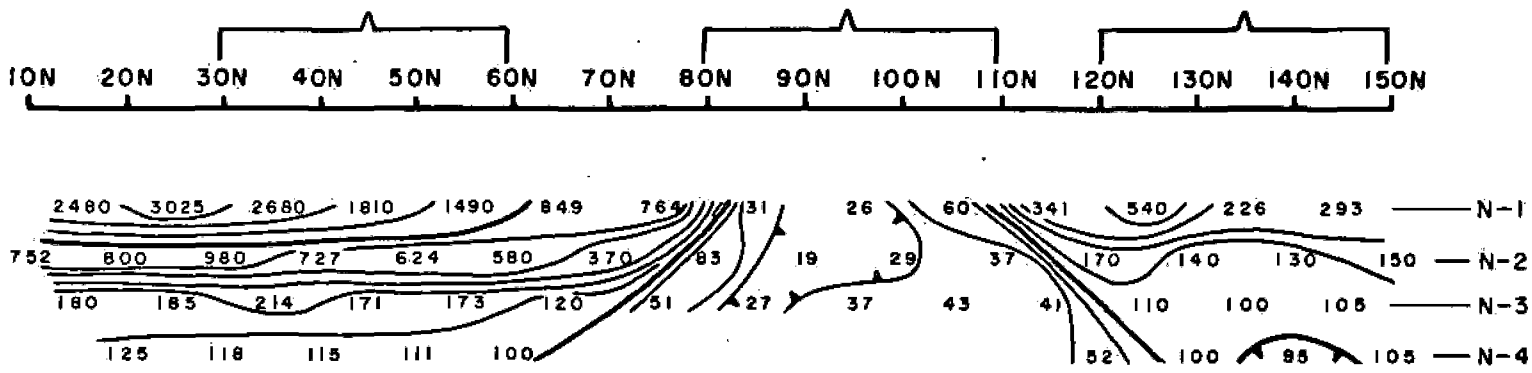

FIG. 3

The dipole-dipole resistivity data is quite satisfactory for the acquisition of the necessary data. The difficulty is in the timing. In order to get practical survey production the resistivity survey must be done in the summer when current electrodes can be easily prepared. The seismic work is done in the winter, when transport over the frozen surface is easiest. In order to keep the support costs down, the resistivity survey must be done at the same time as the seismic survey. Therefore, a resistivity measurement using an electromagnetic source would be desirable.

System for Resistivity Measurements Using Electromagnetic Fields

The two exploration problems described above are of the same nature. A resistive layer overlies a conductive substructure, and we desire to know the thickness of the upper layer and the resistivity of the two layers. This particular problem is one of the easiest to solve using electromagnetic techniques (Ghosh, Ward).

An electromagnetic system has been designed and built to permit measurements to attack this problem.

The transmitter is a variable frequency oscillator powered by a motor-generator. The system operates at twelve frequencies between 15.0 Hz and 45,000 Hz. The magnetic dipole is created by using a multi-turn, air-cored coil; any one of several coils can be attached to the transmitter console. (Figure IVa).

The largest dipole moments of about 3,000,000 ampere-turn-meters^2 can be achieved with the coil horizontal (i.e. a vertical dipole). For instance, a 10 turn coil, 200 feet in diameter, with a maximum of 10 amperes of current has a dipole moment of 3,140,000 ampere-turn-meter^2. (Figure IVb).

For a horizontal dipole the coil must be suspended in a vertical plane; this is more difficult to achieve. A loop with a 30 foot diameter and 36 turns, also carrying 10 amperes, has a moment of 286,000 ampere-turn-meter^2. (Figure IVc).

The motor-generator weighs about 55 lbs; the transmitter console has a total weight of about 125 lbs. The coils have a weight of 100 lbs. to 200 lbs.

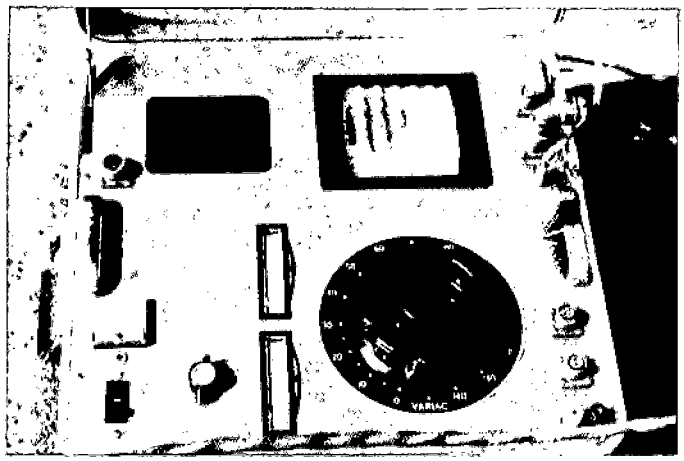

Fig. IV A - Tx

Fig. IV A - Tx with tuning box

Fig. IV B - Vertical dipole Tx Loop

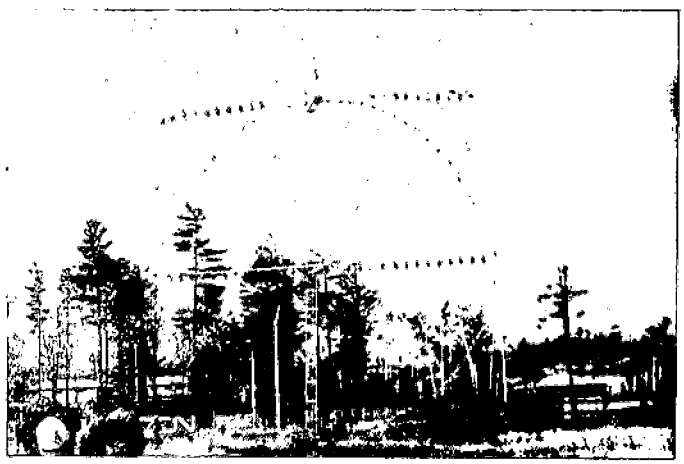

Fig. IV C - Horizontal dipole Tx Loop

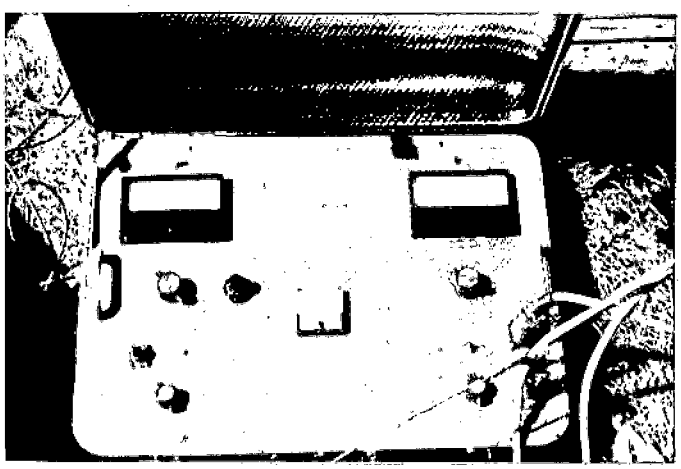

Fig. IV D - Rx Console

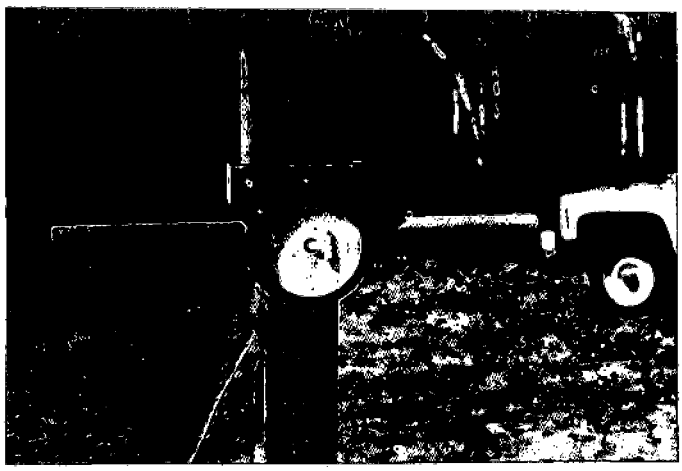

Fig. IV D - Rx Coil

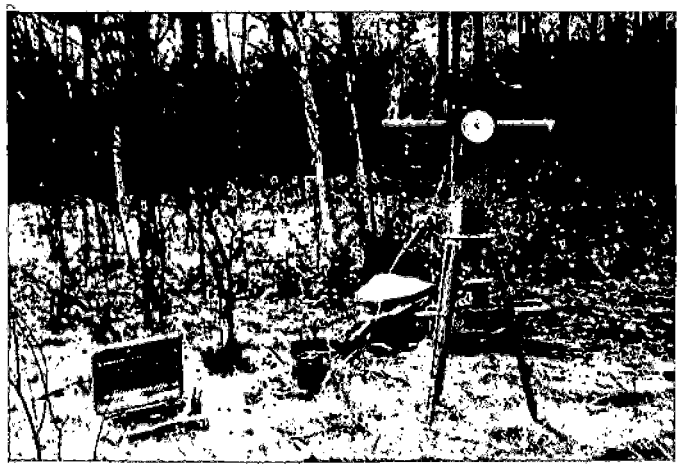

Fig. IV D - Rx Coil oriented for horizontal field

Fig. IV D - Rx Coil oriented for vertical field

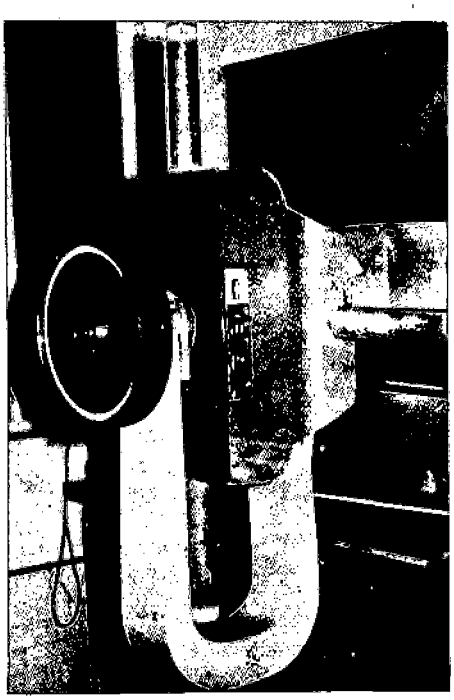

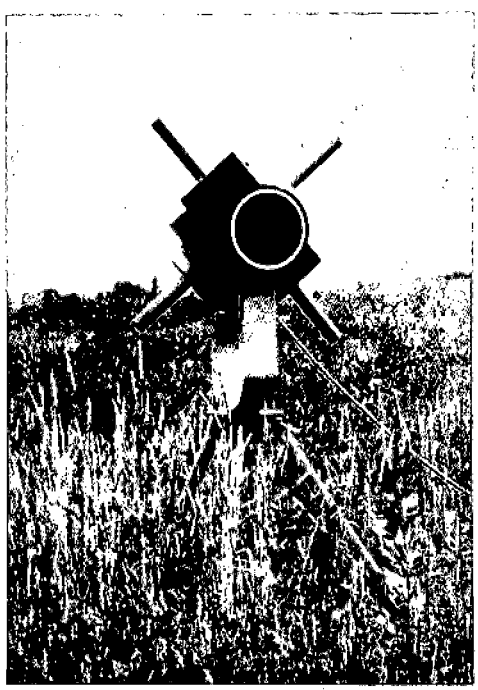

Fig. IV E - Cross Coil System

depending upon the diameter, number of turns, etc.

The receiver-detector can be of any one of three types:

1) With a reference cable, a single coil detector can be used to measure the IN-PHASE and OUT-OF-PHASE magnitude of the total field (Figure IVd). The detector coil is orientable so that the field in any direction can be measured. The field components are measured as a percent of the maximum-coupled primary field; the accuracy is $\pm$ 2.5%.

2) With a crossed-coil system, and an internal frequency reference, no reference cable is needed. The system measures the tilt angle and ellipticity of the ellipse-of-polarization of the total field (Figure IVe). The tilt-angle can be measured with an accuracy of 0.25 degrees; the ellipticity can be measured with an accuracy of $\pm$ 1%. This is the system previously described by Ward, et al.

3) Using the two-channel system from the dip-angle measurement described above (without a reference cable) with a length of wire and two non-polarizing electrodes, it is possible to measure the ratio $\left|\frac{E\phi}{Hr}\right|^2$ with an accuracy of $\pm$ 5%. Since $E\phi$ and Hr are orthogonal this is equivalent to an "applied field" magneto-telluric measurement.

The measurement accuracy that can be attained with the system described above depends upon the dipole source chosen by the geophysicist, the ambient electrical noise, the conductivities of the earth, the measurement chosen and the accuracy required. Under "normal" conditions measurements can be made at a maximum distance of 1.0 Km to 3.0 Km from the source.

Calculation of Field Components

The calculation of the field components on a one-layer earth has been previously reported (see Reference) and the mathematical development will not be repeated here. The coordinate system we will use is shown in Figure V. The possible magnetic field components calculated by Wait (1955) for a homogeneous earth are shown in Figure VI. Notice that for the vertical, co-planar coils the coupling ratio increases uniformly and that the variations occur at relatively low values of $R\sqrt{f\sigma_1}$

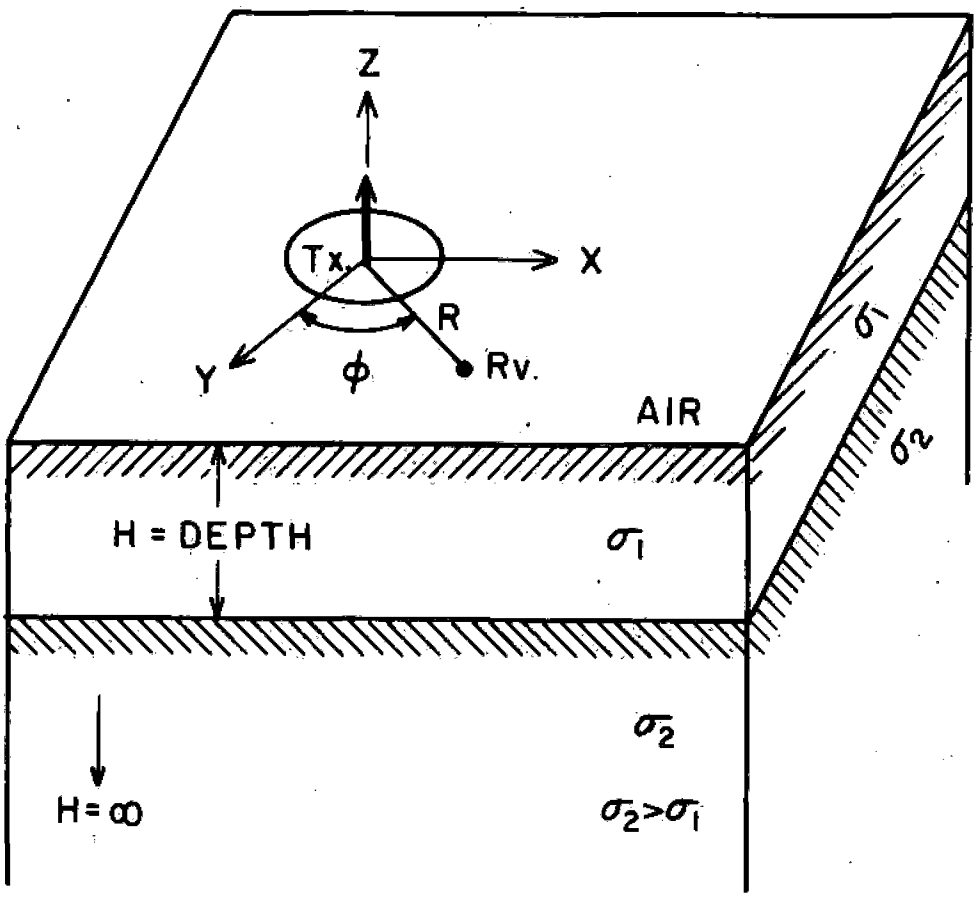

FIG. 5 Co-ordinate System

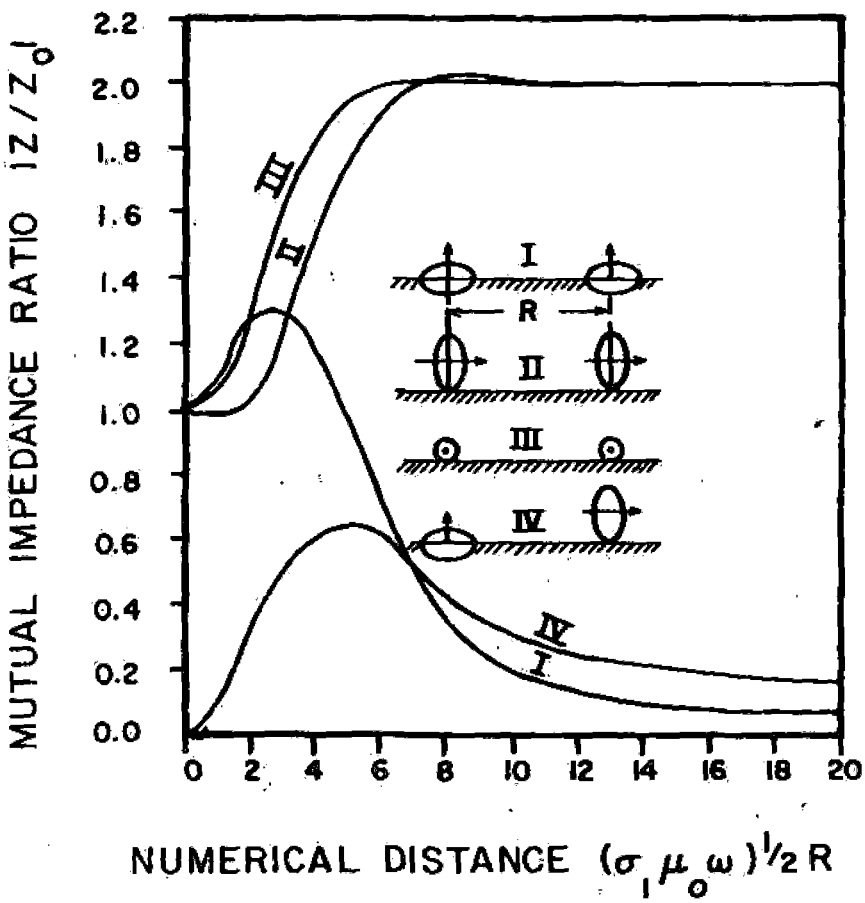

FIG. 6 Mutual impedance ratio for homogeneous half-space (after Wait, 1955)

For a one-layer earth, the same coupling ratios can be theoretically calculated, if the ratio of the conductivities is specified as well as the ratio of the thickness of the upper layer (H) to the distance between the source and detector (R). In Figure VIIa we have shown the curve for variables σ_2/σ_1 for constant R/H. In Figure VIIb the results are planned for constant σ_2/σ_1 with various values for R/H. As was the case for the uniform earth, it can be seen that the curves for the vertical, co-planar coils are the most diagnostic of all those for parallel magnetic field components. The most diagnostic curves of all are for the minimum coupled magnetic field (Hr) for the vertical dipole source.

In a field system to investigate the resistivity of a one-layer earth, it is obviously desirable to obtain as much information as possible from measurements from a single placement of the coils, as the frequency is varied. Since there is a limit to the dipole moment that can be used for the source and a further limitation on the sensitivity that we can reasonably expect to achieve in the receiver-detector, it is also obviously desirable to be able to make diagnostic measurements with as small a coil separation as possible.

These practical considerations suggest that for a horizontal dipole the apparent conductivity determinations should be made for vertical, co-planar coils. For a vertical dipole source measurements utilizing Hr should be diagnostic. Ward and his group have reported that measurements of the tilt-angle and ellipticity of the ellipse-of-polarization of the total field are quite diagnostic. This is true because these measurements utilize the Hr component of the field.

We will report here on the use of $\left|\frac{E\phi}{Hr}\right|^2$ to determine an apparent resistivity curve for a one-layer earth. This is essentially a magneto-telluric measurement using an applied field.

Apparent Conductivity Curves Using Vertical Co-Planar Coils

To introduce the concept of apparent conductivity in E.M. depth-sounding let us consider the vertical co-planar configuration. By comparing the theoretically computed response curves on the surface of a one-layer earth with those on a

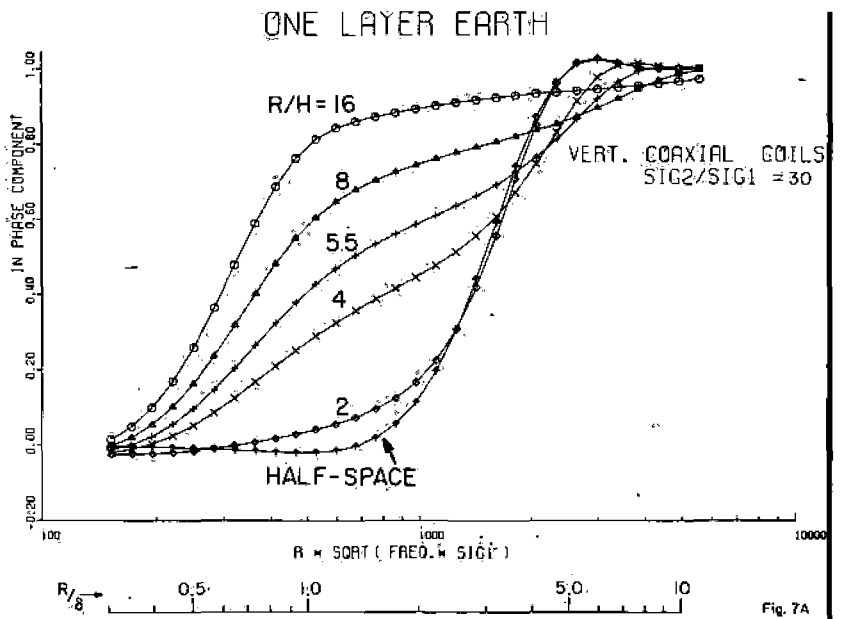

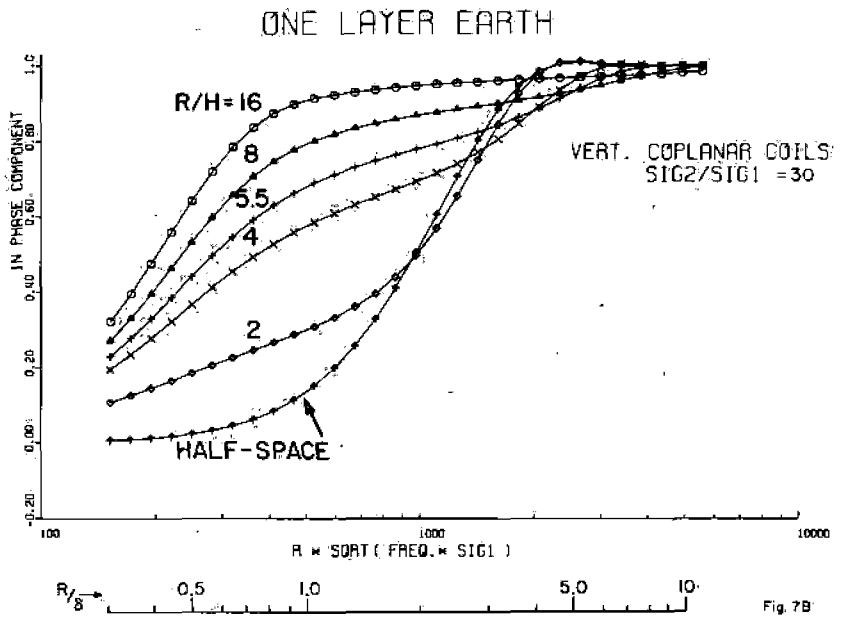

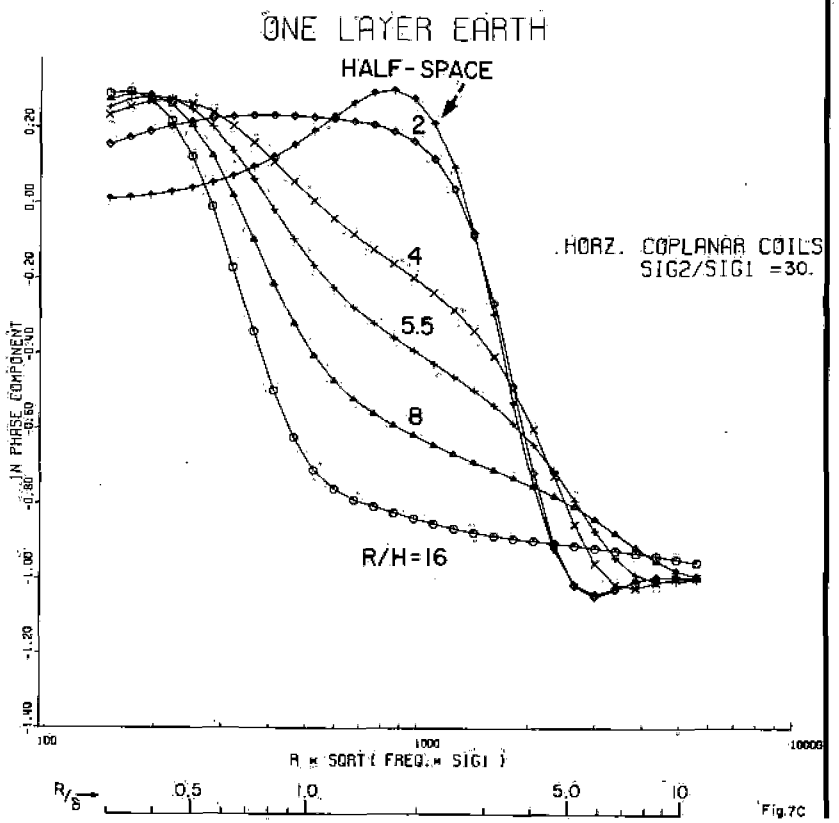

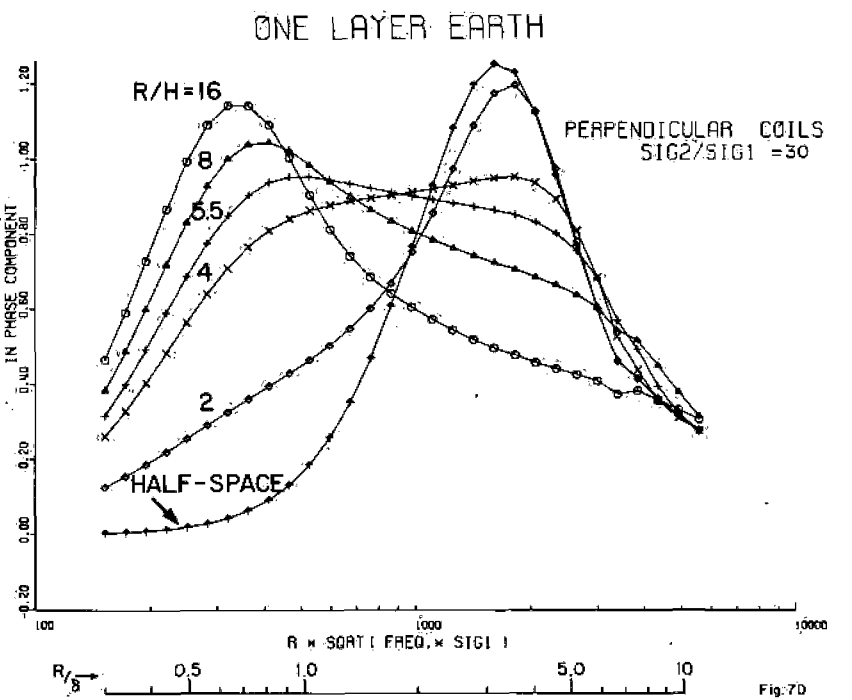

FIG. 7 In-phase responses over one-layer model for different coil-configurations.

uniform earth, it is possible to define an "apparent conductivity" that is similar to that used for the grounded-current resistivity method. A few of these apparent conductivity curves using secondary in-phase response for four values of R/H are shown in Figure VIII. These curves are quite resolved for different values of σ_2 / σ_1. As expected, the apparent conductivity values are closer to the real conductivities for small thickness of layers. This is quite noticeable in low frequencies. The general behavior of the apparent conductivity curves are similar to those in dipole d.c. resistivity sounding.

Field measurements of responses may be converted to the apparent conductivity values using a theoretically computed master chart for the homogeneous half-space. These apparent conductivity values may be plotted against $R\sqrt{f}$ on a similar log-log tracing paper. This field curve can then be matched with the appropriate set of apparent conductivity curves for the one-layer model by shifting along the 'X' and 'Y' axes. The 'X' and 'Y' offsets in the origin would indicate $\sqrt{\sigma_1}$ and σ_1. The values of σ_1 from both the axes should be consistent. The depth of the layer is obtained from the set of curves with which a match has been obtained.

Cagniard Resistivity Curves from $\left|\frac{E\phi}{Hr}\right|^2$

(AFMT Method)

For a magnetic dipole source, different components of the magnetic field and the electric field may be measured in the field. We have already seen that the most useful magnetic field component is the perpendicular component Hr (Figure VII). In this section, we shall make use of the amplitudes of Hr and $E\phi$ components (Figure V) for a vertical magnetic dipole source. We shall call this "Applied Field Magneto-Telluric" measurements (AFMT).

In the classical magneto-telluric problem, apparent resistivities are obtained from $\left|\frac{E\phi}{Hr}\right|$ measurements according to (Cagniard, 1953).

$$\rho_{\text{apparent}} = \frac{1}{\omega\mu} \left|\frac{E\phi}{Hr}\right|^2$$

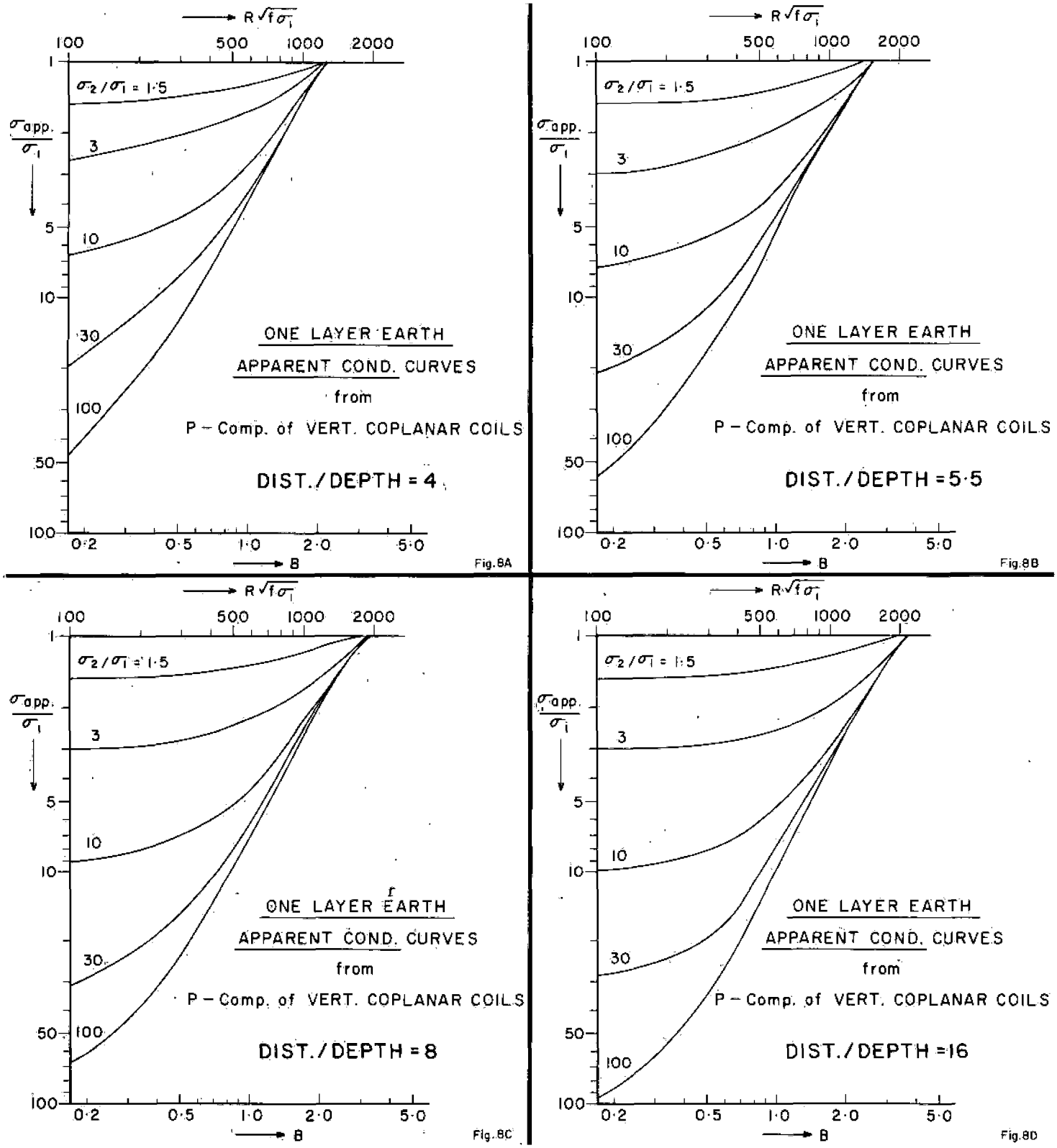

FIG. 8 Apparent conductivity curves for one-layer model derived from the in-phase component of the vertical coplanar coil-configuration.

In our problem, the measurements are made in the audio frequency range at finite distances from the transmitter. Hence, the apparent resistivity determination according to the above equation is not correct. However, it is possible to define a "Cagniard Resistivity" in a similar way; i.e.

$$\text{Cagniard} = \frac{1}{\omega\mu} \left| \frac{E\phi}{Hr} \right|^2$$

It should be noted at this point that the Cagniard resistivity is not a constant for a homogeneous half-space. Theoretical computations have shown that, for a homogeneous half-space, the Cagniard resistivity is a function of the parameter $R\sqrt{f\sigma_1}$. Cagniard resistivity has been found to be equal to the true resistivity when $R\sqrt{f\sigma_1}$ is larger than 5000. This corresponds to a 'skin-depth' (δ) equal to 10 (Figure X). Cagniard resistivity increases logarithmically with decrease in $R\sqrt{f\sigma_1}$. It changes by about four decades with only one decade of change in $R\sqrt{f\sigma_1}$. We have used this phenomenon in the problem of depth-sounding.

We have theoretically computed Cagniard resistivity curves for the one-layer earth model. Some typical curves for σ_2/σ_1 equal to 30 and 100 have been shown in Figures Xa and Xb, respectively. Each figure contains a range of values of R/H.

It is clear that, at a fixed distance from the transmitter, the actual values of σ_1, can be obtained from field measurements of $\left| \frac{E\phi}{Hr} \right|$ at a very high frequency. The depth of the layer (H) may be determined by curve matching.

Both the Figures Xa and Xb show that a ratio of R/H which is greater than four does not make the Cagniard resistivity curve significantly different excepting that the trough in the curve (around $R\sqrt{f\sigma_1} = 1500$) increases in magnitude. Even for R/H equal to two, the difference in Cagniard resistivity from the one-layer model to the half-space model is more than two decades when $R\sqrt{f\sigma_1}$ is equal to 100 (Figure Xc). Another interesting feature to note is that this difference in Cagniard resistivity increases as $R\sqrt{f\sigma_1}$ decreases.

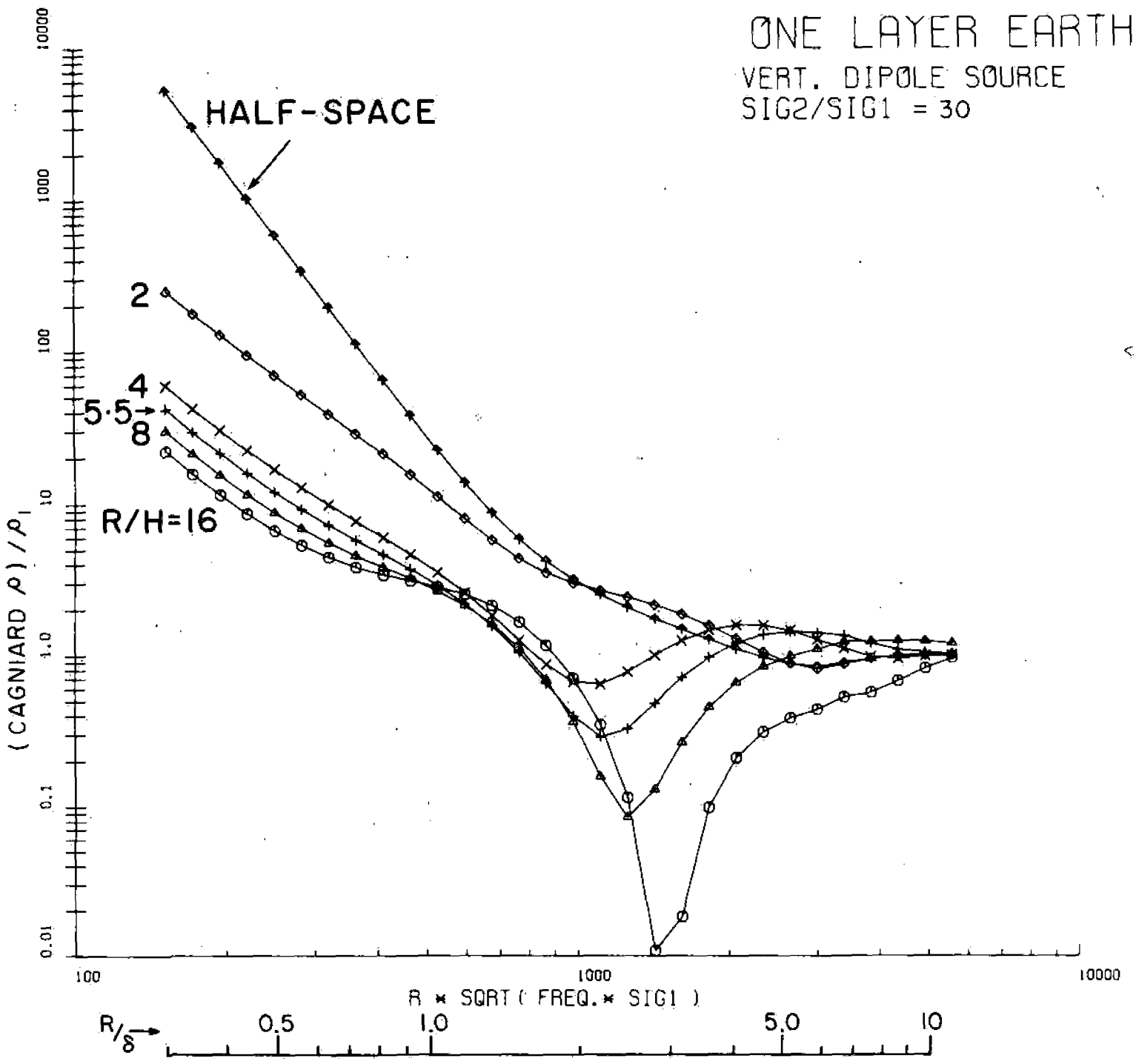

FIG. 10A Theoretically computed Cagniard resistivity curves for the one-layer model derived from $\left| \frac{E\phi}{H_R} \right|$ ratios.

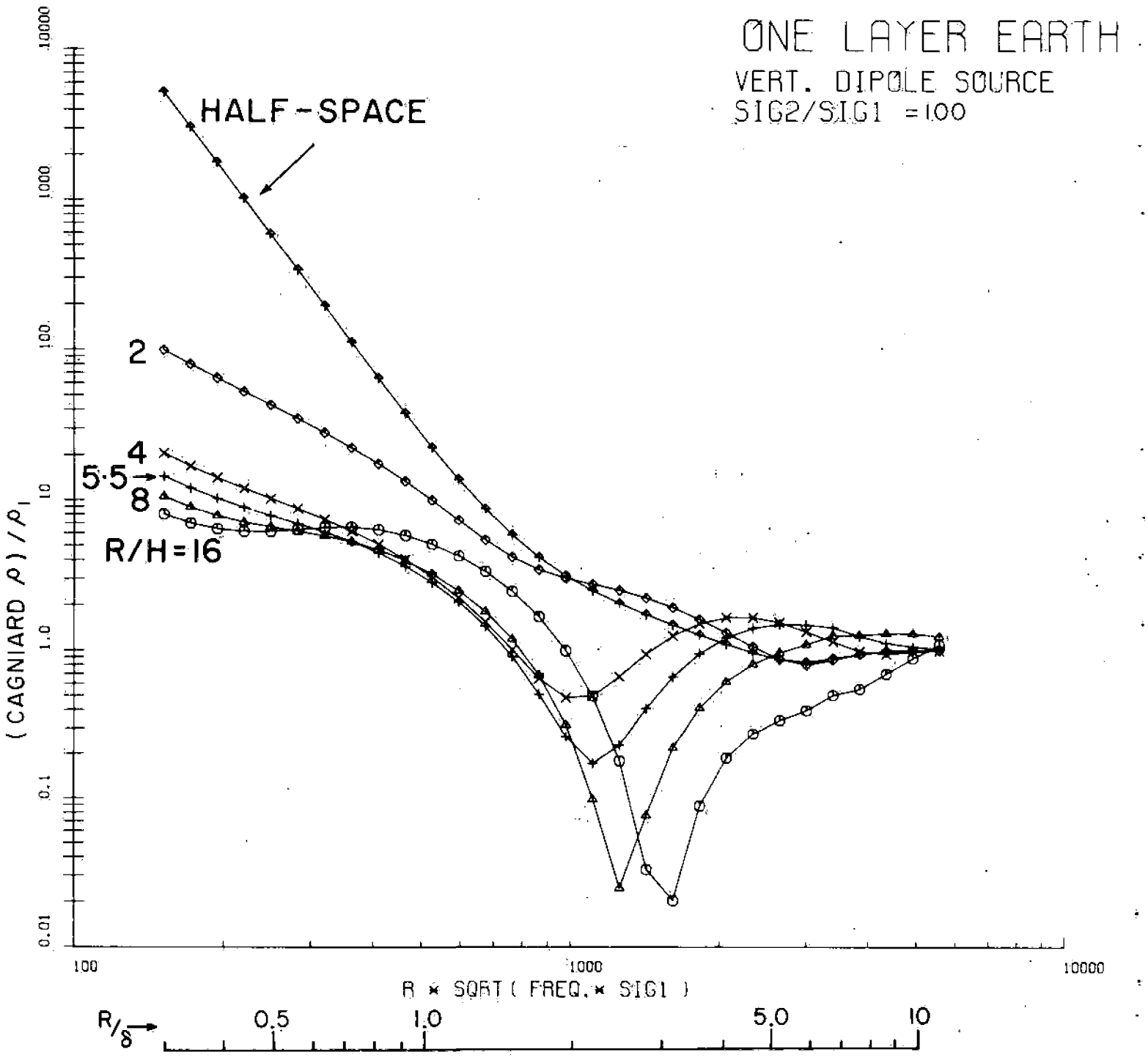

FIG. 10B Theoretically computed Cagniard resistivity curves for the one-layer model derived from $\left| \frac{E_\phi}{H_R} \right|$ ratios.

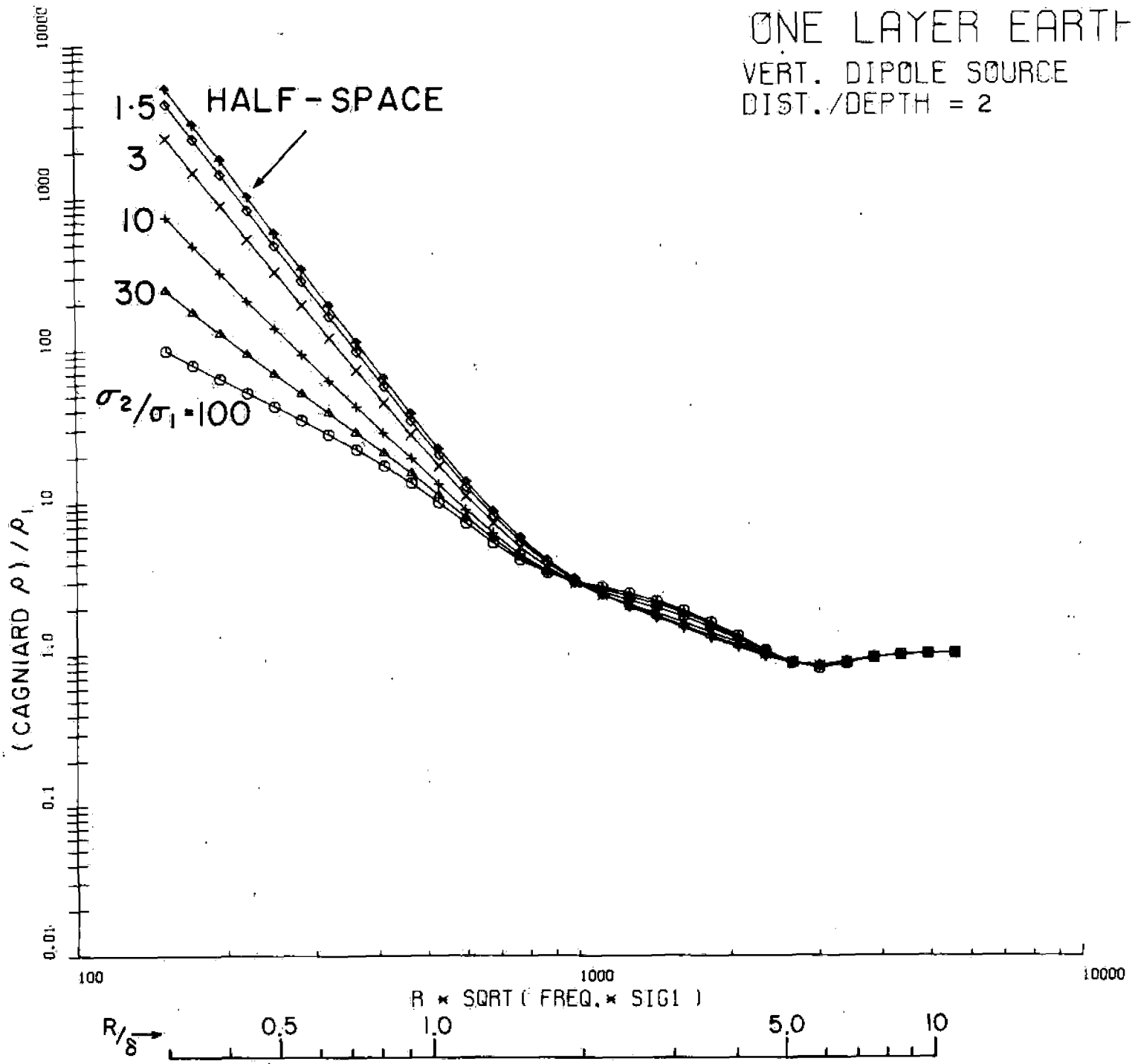

FIG. 10C Cagniard resistivity curves of different conductivity ratios for $'R/H'$ equal to two.

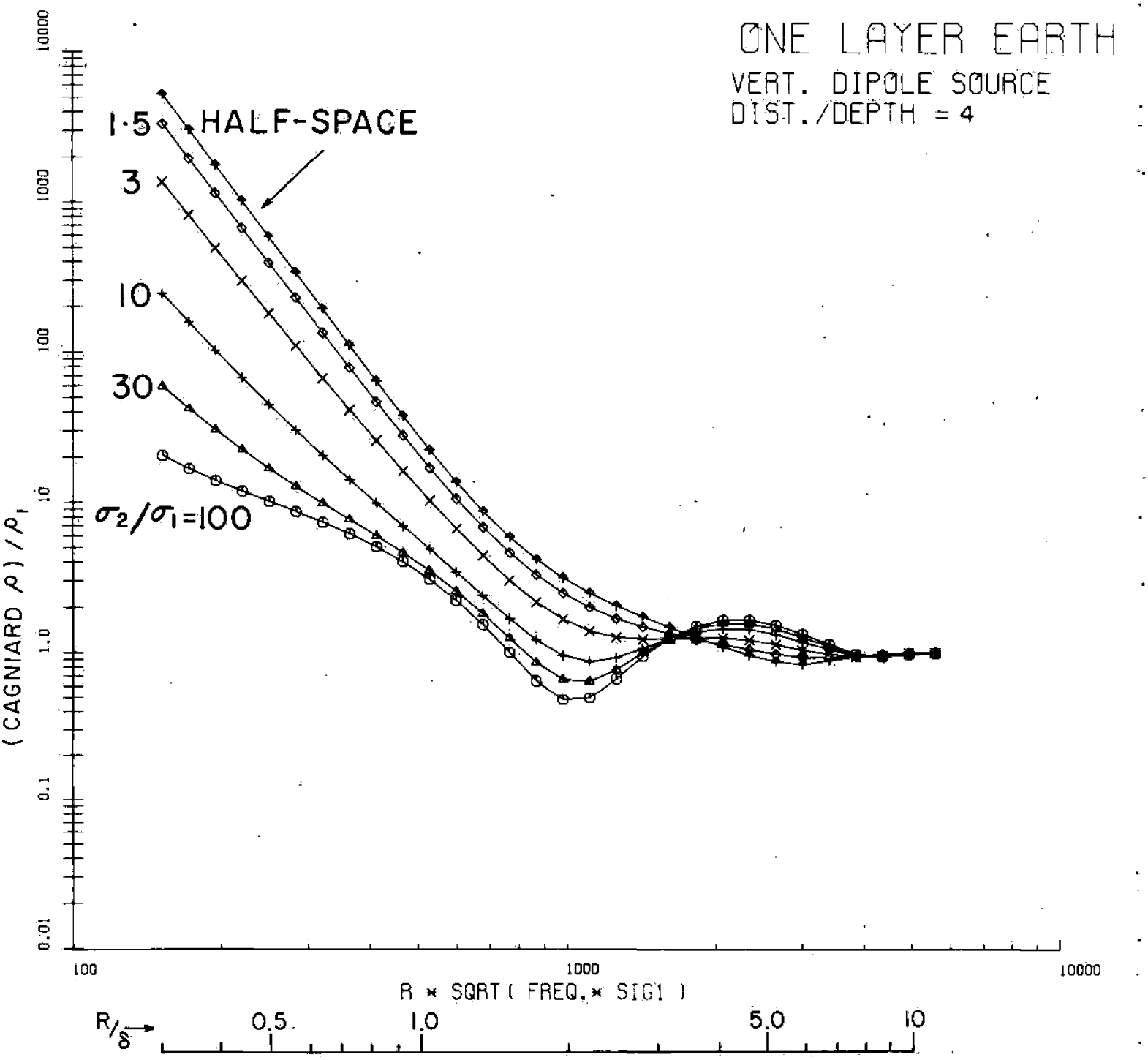

FIG. 10D Cagniard resistivity curves of different σ_2/σ_1 ratios for $|R/H|$ equal to four.

This shows that if measurements are made in low values of , the distance from the transmitter to the point of measurement need not be greater than two times the depth of investigation. With our present equipment, it is possible to make measurements at a maximum distance of 3 K meters. Therefore, the maximum depth that can be investigated is more than 1 K meter.

We are in a process of computing the apparent resistivity curves from Cagniard resistivity in a way similar to the one described for the vertical co-planar configuration (Figure VIII). This should simplify the interpretation of the field curves.

Using Loop-Loop EM Resistivity Determinations

In the above description we have outlined two different ways in which electromagnetic measurements could be used to carry out resistivity determinations in the geothermal and permafrost problems shown in Figure I, Figure II and Figure III. As yet, no field data is available for AFMT measurements, but we can use the theoretical curves to examine the expected behaviour of the Cagniard resistivity from electromagnetic sources. We have shown the curves only for the apparent resistivity determinations using $\left|\frac{E\phi}{Hr}\right|$.

The expected Cagniard resistivity curves for the two geothermal problems described in Figures I and II are shown in Figures XI and XII. Figure XI shows that the low resistivity of Line 1 Mile West between 120N to 160N at a depth of 600 meters can very well be recognized from the surrounding homogeneous medium.

Figure XII shows that the step like variation in resistivity of Line 2 Mile West can be detected by AFMT method.

In both the above examples, the frequencies to be used are too low for the equipment because the resistivity of the top layer is quite low (100 ohm. meters). A different kind of measurements employing higher frequencies are to be made in these cases.

Figure XIII shows the Cagniard resistivity curves for the permafrost problem described in Figure XII. The curves A_1, A_2 and A_3 are quite well

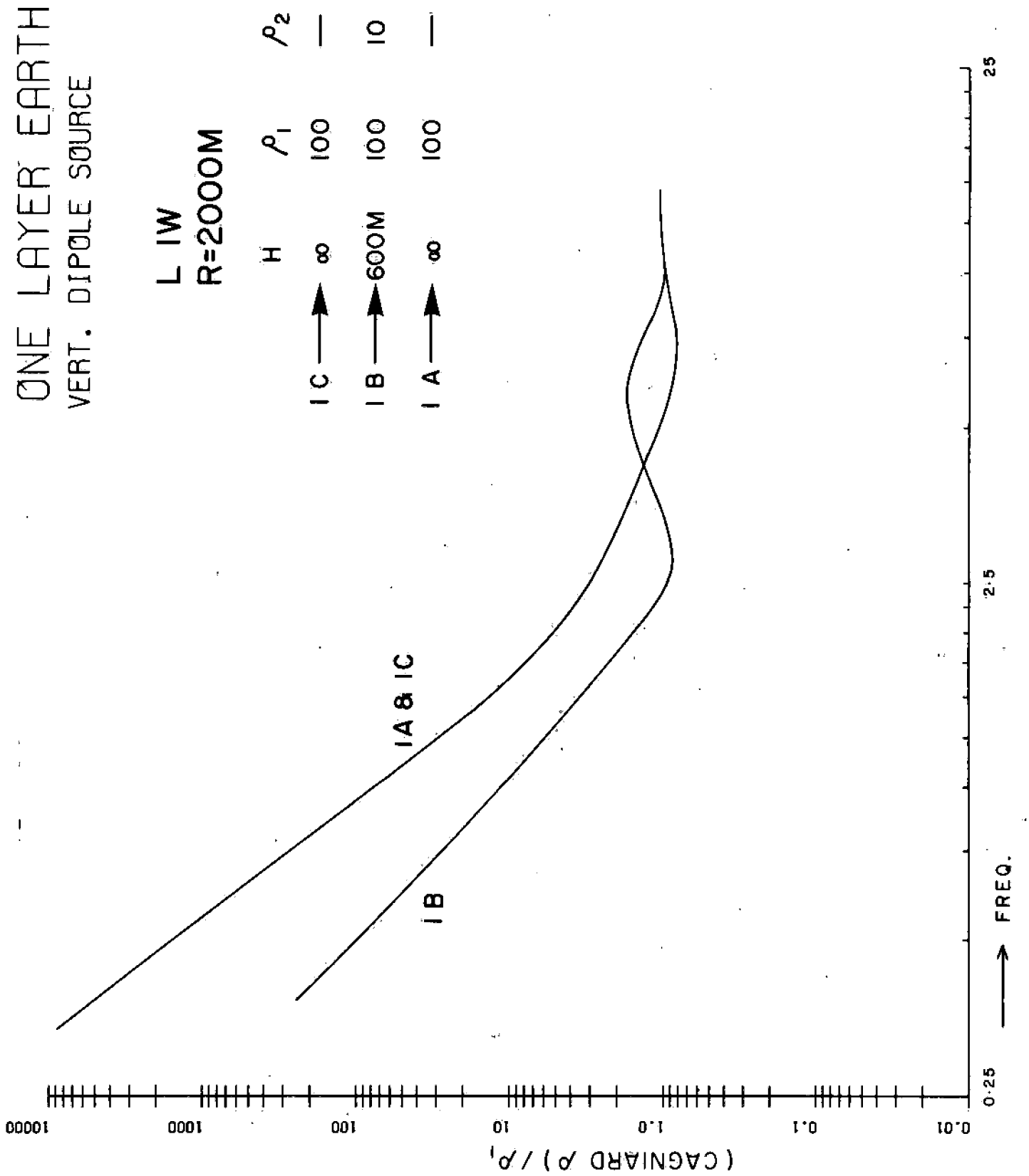

FIG. 11 Expected Cagniard resistivity curves for Line 1 Mile West

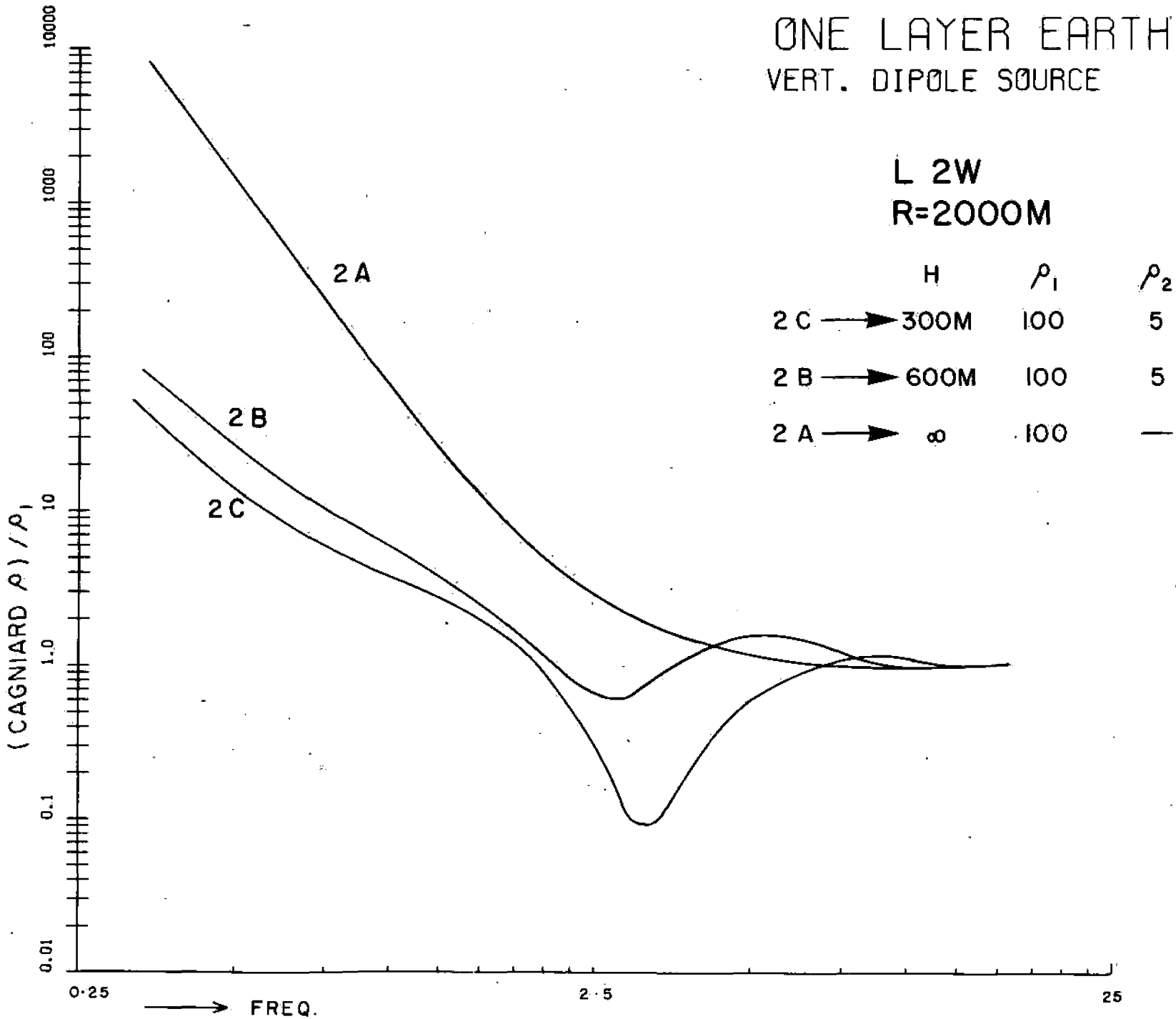

FIG. 12 Expected Cagniard resistivity curves for Line 2 Mile West

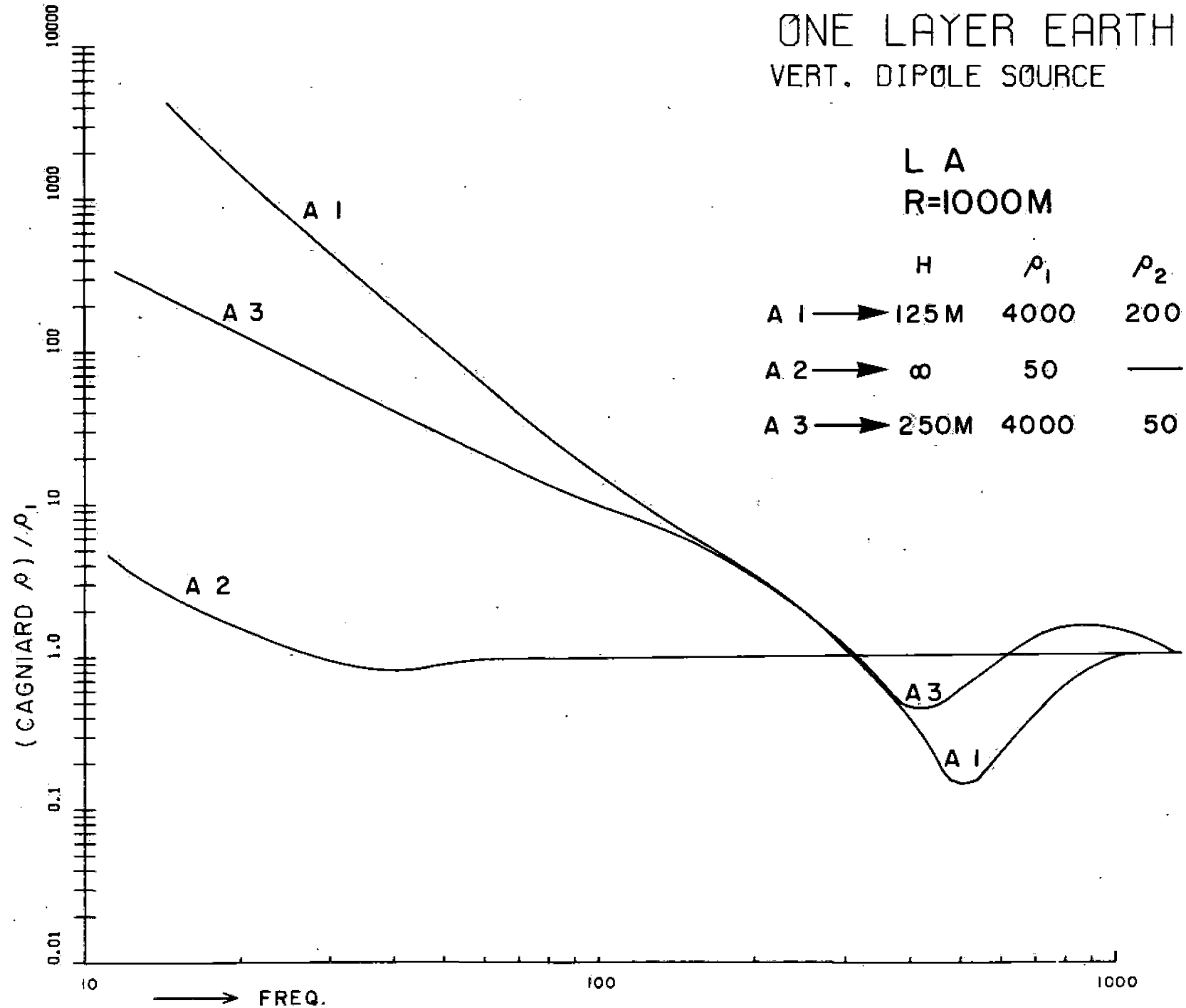

FIG. 13 Expected Cagniard resistivity curves for Line A.

separated. This shows the different resistivity zones can be mapped. Notice the variation in the Cagniard resistivity occurring in the frequency range 10 - 1,000 Hertz.

Conclusions

We have presented an analysis of the depth-sounding problem using a magnetic dipole source. Any component of the magnetic field may be measured in depth investigation, and interpretation may be made using the apparent resistivity curves for the one-layer model. Interpretation is easier to make if the parameter which is measured changes monotonously with frequency. The vertical co-planar coil-configuration seems to be the best for parallel component measurements. In this case, either the amplitude of the field or the in-phase component should be measured.

The measurement of the perpendicular magnetic field Hr seems to be even better than the vertical co-planar measurement. The parameters of the ellipse of polarization measurements as described by Ward, et al. are also quite diagnostic as they contain the Hr component.

AFMT method described here seems to be the best. In this method, the measurements are to be made in low values of $R\sqrt{f\sigma_1}$. The point of measurements does not have to be greater than two times the depth of investigation. AFMT method contains the simplest form of field measurements (the amplitudes of $E\phi$ and Hr). No reference link is needed. Instrumentation is also simple as the amplitudes of the fields are measured.

We are also investigating the possibilities of H_z measurements for the vertical dipole source.

References

Cagniard, L., (1953): Basic Theory of the Magneto-Telluric Method of Prospecting, Geophysics, Vol.18, No.3, pp 605-635.

Dey, A., and Ward, S.H., (1970): Inductive Sounding of a Layered Earth with a Horizontal Magnetic Dipole, Geophysics, Vol.35, No.4, pp 660-703.

Ghosh, M.K., (1969): Electromagnetic Dipole Induction Methods for Exploring Shallow Horizontal Layers, M.Sc. thesis, Dept. of Physics, University of Toronto.

Ghosh, M.K., Grant, F.S., and West, G.F., (1969): Electromagnetic Depth-Sounding, 39th Annual International Meeting, Society of Exploration Geophysicists, Calgary.

Ryu, J., Morrison, H.F., and Ward, S.H., (1970): Electromagnetic Fields about a Loop Source of Current, Geophysics, Vol.35, No.5, pp 862-896.

Wait, J.R., (1955): Mutual Coupling of Loops Lying on the Ground, Geophysics, Vol.20, No.3, pp 630-637.

Vanyan, L.L., (1967): Electromagnetic Depth Soundings, Consultants Bureau, New York.

AFOSR 69-0189 TR

Methods of Magnetotelluric Analysis

By
William E. Sims and F. X. Bostick, Jr.
Department of Electrical Engineering

Technical Report No. 58
January 7, 1969

ELECTRICAL GEOPHYSICS RESEARCH LABORATORY

prepared under
Grant GA-1236
National Science Foundation
and
Contract N00014-67-A-0216-0004
Office of Naval Research
Washington, D.C.

ELECTRONICS RESEARCH CENTER
THE UNIVERSITY OF TEXAS AT AUSTIN
AUSTIN, TEXAS 78712

The Electronics Research Center at The University of Texas at Austin constitutes interdisciplinary laboratories in which graduate faculty members and graduate candidates from numerous academic disciplines conduct research.

Research conducted for this technical report was supported in part by the Department of Defense's JOINT SERVICES ELECTRONICS PROGRAM (U.S. Army, U.S. Navy, and U.S. Air Force) through the Research Grant AF-AFOSR-67-766E. This program is monitored by the Department of Defense's JSEP Technical Advisory Committee consisting of representatives from the U.S. Army Electronics Command, U.S. Army Research Office, Office of Naval Research and the U.S. Air Force Office of Scientific Research.

Additional support of specific projects by other Federal Agencies, Foundations, and The University of Texas is acknowledged in footnotes to the appropriate sections.

UNCLASSIFIED
Security Classification

AD-685-130

DOCUMENT CONTROL DATA - R & D

(Security classification of title, body of abstract and indexing annotation must be entered when the overall report is classified)

1. ORIGINATING ACTIVITY *(Corporate author)*
The University of Texas at Austin
Electronics Research Center
Austin, Texas 78712

2a. REPORT SECURITY CLASSIFICATION
UNCLASSIFIED

2b. GROUP

3. REPORT TITLE

METHODS OF MAGNETOTELLURIC ANALYSIS

4. DESCRIPTIVE NOTES *(Type of report and inclusive dates)*
Scientific Interim

5. AUTHOR(S) *(First name, middle initial, last name)*

William E. Sims F. X. Bostick, Jr.

6. REPORT DATE	7a. TOTAL NO. OF PAGES	7b. NO. OF REFS
7 January 1969	94	41

8a. CONTRACT OR GRANT NO.
AF-AFOSR-67-766E

b. PROJECT NO.
4751

c.
6144501F

d. 681305

9a. ORIGINATOR'S REPORT NUMBER(S)
JSEP, Technical Report No. 58

9b. OTHER REPORT NO(S) *(Any other numbers that may be assigned this report)*
AFOSR 69-0189 TR

10. DISTRIBUTION STATEMENT

1. This document has been approved for public release and sale; its distribution is unlimited.

11. SUPPLEMENTARY NOTES TECH, OTHER
Research sponsored by NSF Grant GA-1236 and ONR Contract N00014-A-0126-0004

12. SPONSORING MILITARY ACTIVITY JSEP through
AF Office of Scientific Research (SREE)
1400 Wilson Boulevard
Arlington, Virginia 22209

13. ABSTRACT

Magnetotelluric prospecting is a method of geophysical exploration that makes use of the fluctuations in the natural electric and magnetic fields that surround the earth. These fields can be measured at the surface of the earth and they are related to each other by a surface impedance that is a function of the conductivity structure of the earth's substrata.

This report describes some new methods for analyzing and interpreting magnetotelluric data. A discussion is given of the forms of the surface impedance for various classes of models, including one, two and three dimensional models. Here, an n dimensional model is one in which the parameters describing the model are functions of at most n space coordinates. Methods are discussed for estimating the strike direction for data that is at least approximately two dimensional. A new linearized approach to the one dimensional problem is discussed. Subject to the approximations of the linearization, it is shown that under appropriate transformations of the frequency and depth scales, the reciprocal of the surface impedance as a function of frequency is equal to the square root of the conductivity as a function of depth convolved with a linear response function that is somewhat like a low pass filter.

Included in this report is a comparison of several methods of estimating the auto and cross power density spectra of measured field data, and of several methods for estimating the surface impedance from these spectra. The effects of noise upon these estimates are considered in some detail. Special emphasis is given to several types of artificial noise including aliasing, round off or digitizer noise, and truncation effects. Truncation effects are of the most interest since they depend upon the particular window used in the spectral analysis.

DD FORM 1 NOV 65 1473

UNCLASSIFIED
Security Classification

14. KEY WORDS	LINK A		LINK B		LINK C	
	ROLE	WT	ROLE	WT	ROLE	WT
MAGNETOTELLURICS						
DATA ANALYSIS						

METHODS OF MAGNETOTELLURIC ANALYSIS*

By

William E. Sims and F. X. Bostick, Jr.
Department of Electrical Engineering

Technical Report No. 58
January 7, 1969

ELECTRICAL GEOPHYSICS RESEARCH LABORATORY

prepared under

Grant GA-1236

National Science Foundation

and

Contract N00014-67-A-0216-0004

Office of Naval Research

Washington, D. C.

ELECTRONICS RESEARCH CENTER

THE UNIVERSITY OF TEXAS AT AUSTIN

Austin, Texas 78712

*Research sponsored in part by the Joint Services Electronics Program under the Research Grant AF-AFOSR-67-766E

ABSTRACT

Magnetotelluric prospecting is a method of geophysical exploration that makes use of the fluctuations in the natural electric and magnetic fields that surround the earth. These fields can be measured at the surface of the earth and they are related to each other by a surface impedance that is a function of the conductivity structure of the earth's substrata.

This report describes some new methods for analyzing and interpreting magnetotelluric data. A discussion is given of the forms of the surface impedance for various classes of models, including one, two and three dimensional models. Here, an n dimensional model is one in which the parameters describing the model are functions of at most n space coordinates. Methods are discussed for estimating the strike direction for data that is at least approximately two dimensional. A new linearized approach to the one dimensional problem is discussed. Subject to the approximations of the linearization, it is shown that under the appropriate transformations of the frequency and depth scales, the reciprocal of the surface impedance as a function of frequency is equal to the square root of the conductivity as a function of depth convolved with a linear response function that is somewhat like a low pass filter.

Included in this report is a comparison of several methods of estimating the auto and cross power density spectra of measured field data, and of several methods for estimating the surface impedance from these spectra. The effects of noise upon these estimates are considered in some detail. Special emphasis is given to several types of artificial noise including aliasing, round off or digitizer noise, and truncation effects. Truncation effects are of the most interest since they depend upon the particular window used in the spectral analysis.

TABLE OF CONTENTS

LIST OF FIGURES

I. INTRODUCTION

Magnetotelluric prospecting is a relatively new method of geophysical exploration, although the electric and magnetic fields that it employs have long been observed. More than a century ago it was recognized by several investigators that a correlation existed between the variations in the telluric currents and the geomagnetic field. In 1940 Chapman and Bartels reviewed the various theories on the relationship between these fields. In the late 1940's and early 1950's several investigators such as Tikhonov in the USSR; Kato, Kikuchi, Rikitake, and Yokoto in Japan; and Cagniard in France began to recognize the electromagnetic nature of these fields.

In 1953 Cagniard published a paper in which he gave a quantitative description of the relationship between the electric and magnetic fields at the surface of a horizontally layered earth. Soon thereafter many people began making theoretical and experimental contributions to the field of magnetotellurics. By the late 1950's, it was recognized by several investigators that the scalar impedance described by Cagniard was not sufficient to describe many of the frequently encountered geologic situations. For an anisotropic or laterally inhomogeneous earth, the impedance becomes a tensor quantity (Neves, 1957), (Rankin, 1960), (Cantwell, 1960),(Kovtun, 1961), (Rokityanskii, 1961), (d'Erceville and Kunetz, 1962), (Bostick and Smith, 1962), (Srivastava, 1963). Principal contributors to the growing body of literature on magnetotellurics, in addition to those previously mentioned, include Berdichevskii, Vladimirov, and Kolmakov in the USSR, Porstendorfer in Germany, Adam and Vero of the Hungarian Academy of Sciences, Fournier in France, and many people in the U.S.A. and Canada. Hugo Fournier (1966) has a comprehensive history and bibliography of the science of magnetotellurics.

The tensor relationship between the E (electric) and H (magnetic) fields at any given frequency can be expressed as

$$\begin{bmatrix} E_x \\ E_y \end{bmatrix} = \begin{bmatrix} Z_{xx} & Z_{xy} \\ Z_{yx} & Z_{yy} \end{bmatrix} \begin{bmatrix} H_x \\ H_y \end{bmatrix} \qquad (1.1)$$

where rectangular cartesian coordinates have been indicated. This tensor impedance Z, a function of frequency and space coordinates, depends upon the conductivity of the earth in the surrounding area, and if the horizontal wavelengths of the incident fields are sufficiently long, Z will be independent of time and source polarization. Therefore, Z can be a useful measure of the conductivity structure of the earth, and in fact it can sometimes be interpreted almost completely in terms of a simplified earth model.

The magnetotelluric problem can conveniently be divided into three parts: data acquisition, analysis, and modeling. Data acquisition includes the instrumentation and all of the field work involved with recording the electric and magnetic field variations. Analysis includes processing the field measurements to determine estimates of the Z tensor and other related parameters. Modeling consists of interpreting this impedance tensor in terms of a particular earth model.

The research that went into this thesis was aimed at developing better methods of magnetotelluric analysis and interpretation. The thesis itself provides for the first time a unified treatment of the techniques developed as a result of this research. The treatment is facilitated by first considering the forms of theoretical impedance tensors for several classes of models. Next, various methods are presented for estimating actual impedance tensors from measured field data. Finally, the effects that various types of noise have upon the impedance estimates are considered.

II. ONE DIMENSIONAL MODELS

In this chapter several one dimensional models, that is, models which have medium parameters that are functions of only one space coordinate will be considered.

A. Homogeneous Half Space Model

The simplest of all possible models is one in which the earth is considered to be a homogeneous, isotropic half space of conductivity σ, permittivity ϵ, permeability μ. Within any medium of constant σ, ϵ, and μ, if we assume time variations of the form $e^{j\omega t}$, Maxwell's equations

$$\text{Curl} \quad \nabla \times \vec{E} = - j\omega\mu \vec{H} \tag{2.1}$$

$$\text{Curl} \quad \nabla \times \vec{H} = (\sigma + j\omega\epsilon) \vec{E} \tag{2.2}$$

$$\nabla \cdot \vec{H} = 0 \tag{2.3}$$

$$\nabla \cdot \vec{E} = 0 \tag{2.4}$$

combine to give the vector Helmholtz equations

$$\nabla^2 \vec{E} = - \gamma^2 \vec{E}$$

$$\nabla^2 \vec{H} = - \gamma^2 \vec{H}$$

where

$$\gamma^2 = j\omega\mu\sigma - \omega^2\mu\epsilon \tag{2.5}$$

In rectangular cartesian coordinates, this vector equation separates, so that each of the components of the E and H fields satisfies the scalar Helmholtz equation. Elementary solutions to this equation are of the form

$$Ae^{-(\gamma_x x + \gamma_y y + \gamma_z z)}$$

where

$$\gamma_x^2 + \gamma_y^2 + \gamma_z^2 = \gamma^2 = j\omega\mu\sigma - \omega^2\mu\epsilon \tag{2.6}$$

The general solution is obtained by summing various elementary solutions with different values of A, γ_x, γ_y, and γ_z, subject to the constraints of equation (2.6). Returning for the moment to an elementary solution, if the coordinate axes are aligned such that positive z is down, and the direction of propagation is in the x-z plane, then the elementary solution is of the form

$$Ae^{-\gamma_x x - \gamma_z z}\ ;\ \gamma_x^2 + \gamma_z^2 = \gamma^2 \tag{2.7}$$

Thus, for a homogeneous plane electromagnetic wave with its direction of propagation in the x-z plane, each of the components of E and H will be of the form shown in (2.7).

Since any homogeneous plane wave can be separated into TE (horizontal E field only) and TM (horizontal H field only) modes, and since the equations are linear with respect to the fields, one can consider the two modes separately.

For the TE mode,

$$E_x = E_z = 0$$

and equation (2.1) becomes

$$-\bar{i}\frac{\partial E_y}{\partial z} + \bar{k}\frac{\partial E_y}{\partial x} = -j\omega\mu(\bar{i}H_x + \bar{j}H_y + \bar{k}H_z)$$

Thus

$$\gamma_z E_y = -j\omega\mu H_x$$

$$-\gamma_x E_y = -j\omega\mu H_z$$

$$H_y = 0$$

In particular,

$$Z_{TE} = -\frac{E_y}{H_x} = \frac{j\omega\mu}{\gamma_z} \tag{2.8}$$

For the TM mode,

$$H_x = H_z = 0$$

and equation (2.2) becomes

$$-\bar{i}\frac{\partial H_y}{\partial z} + \bar{k}\frac{\partial H_y}{\partial x} = (\sigma + j\omega\epsilon)(\bar{i}E_x + \bar{j}E_y + \bar{k}E_z)$$

Thus

$$\gamma_z H_y = (\sigma + j\omega\epsilon) E_x$$

$$-\gamma_x H_y = (\sigma + j\omega\epsilon) E_z$$

$$E_y = 0$$

and

$$Z_{TM} = \frac{E_x}{H_y} = \frac{\gamma_z}{(\sigma + j\omega\epsilon)} = \frac{j\omega\mu\gamma_z}{\gamma^2} \tag{2.9}$$

For the range of parameters normally encountered in magnetotelluric work, displacement currents in the earth can be neglected. That is to say

$$\omega\epsilon << \sigma \tag{2.10}$$

so that

$$\gamma^2 = j\omega\mu\sigma \tag{2.11}$$

Continuity of the tangential fields at the surface z = 0 requires that

$$\gamma_{x\ air} = \gamma_{x\ earth} \tag{2.12}$$

For a plane wave striking the earth at a real angle θ measured from normal incidence,

$$\gamma_{x\ air} = j\omega\sqrt{\mu\epsilon}\ \sin\ \theta \tag{2.13}$$

Equation (2.10), (2.12) and (2.13) together imply that $|\gamma_x|^2 << |\gamma|^2$. Therefore one may take

$$\gamma_z = \gamma = \sqrt{j\omega\mu\sigma} \tag{2.14}$$

Under these conditions, equations (2.8) and (2.9) give

$$Z_{TE} = Z_{TM} = \sqrt{\frac{j\omega\mu}{\sigma}} \tag{2.15}$$

This implies that the impedance is independent of the polarization of the elementary solution. Thus, any general solution made up of elementary solutions satisfying the conditions of equation (2.14) will give a scalar impedance

$$Z = \sqrt{\frac{j\omega\mu}{\sigma}} \tag{2.16}$$

which will relate any horizontal component of the total H field to the orthogonal horizontal component of the E field.

Actually it is not necessary to restrict the general solution for the incident fields to modes corresponding to real angles of incidence, as

indicated by equation (2.13). Elementary solutions for which $|\gamma_x|^2 > \omega^2\mu\varepsilon$ will still give rise to total fields which satisfy equation (2.16) provided

$$|\gamma_x|^2 << \omega\mu\sigma \tag{2.17}$$

It is convenient to define a parameter δ, called skin depth, for conductive materials by

$$\delta = \sqrt{2/\omega\mu\sigma} \tag{2.18}$$

Then

$$e^{-\gamma_z z} = e^{-(1+j)z/\delta} \tag{2.19}$$

Thus δ is a measure of the depth that an electromagnetic field will penetrate into a conductive medium. It is the depth at which the field will have been attenuated to 1/e of its surface value.

If one then defines the horizontal wavelength λ of an elementary solution by

$$\lambda = \frac{2\pi}{k_x}; \quad jk_x = \gamma_x$$

then a statement that is equivalent to equation (2.17) is that

$$\lambda >> \delta \tag{2.20}$$

In other words, the horizontal wavelength is long compared to the skin depth.

In summary then, for an earth model consisting of a homogeneous half space of conductivity σ, with incident fields having horizontal wavelengths long compared to a skin depth, the surface impedance will be given by equation (2.16).

B. Horizontally Layered Model

The next model that might be considered is one in which the earth is represented by a set of horizontal layers, each with a different conductivity. This is usually known as the Cagniard model since it is the one that he considered in his classic paper. One assumes N layers, as shown in figure 1, and assumes elementary solutions in each layer of the form

$$(A_i e^{-\gamma_{zi} z} + B_i e^{\gamma_{zi} z}) e^{-\gamma_{xi} x}$$

where

$$\gamma_{xi}^2 + \gamma_{zi}^2 = \gamma_i^2 = j\omega\mu\sigma_i \tag{2.21}$$

By requiring that the tangential fields be continuous at each boundary, and noting that $B_N = 0$ since the fields must vanish for large z, one finds that the impedance Z_i looking down from the top of the ith layer is given by

$$Z_i = Z_{oi} \frac{1 - R_i e^{-2\gamma_{zi} d_i}}{1 + R_i e^{-2\gamma_{zi} d_i}} \; ; \; i = 1, 2, \ldots N-1$$

$$Z_N = Z_{oN} \tag{2.22}$$

where d_i is the thickness of the ith layer, R_i is a reflection coefficient defined by

$$R_i = \frac{Z_{oi} - Z_{i+1}}{Z_{oi} + Z_{i+1}} \qquad i = 1, 2, \ldots N-1 \tag{2.23}$$

and Z_{oi} is the characteristic impedance of the ith layer. As with the homogeneous half space, the characteristic impedance for the TE mode is

$$Z_{oi}^{TE} = j\omega\mu/\gamma_{zi} \tag{2.24}$$

and for the TM mode is

$$Z_{oi}^{TM} = j\omega\mu\,\gamma_{zi}/\gamma_i^2 \tag{2.25}$$

Again if one assumes that the horizontal wavelengths of the incident fields are long compared to a skin depth in each layer, the two modes become equivalent and

$$Z_{oi} = \sqrt{j\omega\mu/\sigma_i} \tag{2.26}$$

In either case, one may start at the bottom layer and work up, computing R_i and Z_i using the recursion equations (2.23) and (2.22) until Z_1, the surface impedance, is obtained.

Recall from equation (2.16) that for a homogeneous half space

$$\sigma = \frac{\omega\mu}{|Z|^2}$$

Correspondingly, for a layered model, it is customary to define an apparent conductivity $\sigma_a(\omega)$ or apparent resistivity $\rho_a(\omega)$ by

$$\sigma_a(\omega) = \frac{\omega\mu}{|Z_1(\omega)|^2} = \frac{1}{\rho_a(\omega)} \tag{2.27}$$

Some sample curves of apparent resistivity versus frequency for several models are plotted in figures 2 and 3. For high frequencies, $\sigma_a = \sigma_1$, and for low frequencies, $\sigma_a = \sigma_N$. Qualitatively it appears that $\sigma_a(\omega)$ is a "smoothed out" version of $\sigma(z)$ with frequency ω being inversely related to depth z.

Although it is a simple matter to obtain the surface impedance $Z_1(\omega)$ in terms of $\sigma(z)$ for any layered model, the inverse problem of finding $\sigma(z)$ for a specified $Z_1(\omega)$ is not so simple. It is a nonlinear problem that in general can be solved only by using iterative techniques. Computer programs are available for least squares fitting $Z(\omega)$ curves to N layer models (Patrick, 1969).

Since $\sigma_a(\omega)$ is a smooth curve, one might suspect that fine details in $\sigma(z)$ cannot be determined from $\sigma_a(\omega)$. This in fact turns out to be the case; only gross trends in $\sigma(z)$ can successfully be determined from $\sigma_a(\omega)$.

C. General One Dimensional Model

Consider the case where $\sigma(z)$ is a continuously varying function of z rather than being restricted to a finite number of homogeneour layers. In this case, the recursion equations (2.22) and (2.23) are replaced by a differential equation for Z. There are several ways to obtain the differential equation. One way is to combine the recursion equations (2.22) and (2.23), and let Δz replace d_i, and consider the limit as Δz approaches zero. Another simpler method pointed out by Swift (1967) uses Maxwell's equations directly. Consider the TE mode with $E_x = E_z = 0$. Equations (2.1) and (2.2) give

$$\frac{\partial E_y}{\partial z} = j\omega\mu H_x$$

$$\frac{\partial E_y}{\partial x} = -j\omega\mu H_z$$

$$\sigma E_y = -\frac{\partial H_z}{\partial x} + \frac{\partial H_x}{\partial z}$$

Now

$$Z_{TE} = - \frac{E_y}{H_x}$$

$$\frac{\partial Z_{TE}}{\partial z} = - \frac{1}{H_x} \frac{\partial E_y}{\partial z} + \frac{E_y}{H_x^2} \frac{\partial H_x}{\partial z}$$

$$= - \frac{1}{H_x} \left[j\omega\mu \, H_x \right] + \frac{E_y}{H_x^2} \left[\sigma E_y + \frac{\partial H_z}{\partial x} \right]$$

$$= - j\omega\mu + \frac{E_y}{H_x^2} \left[\sigma E_y - \frac{1}{j\omega\mu} \frac{\partial^2 E_y}{\partial x^2} \right]$$

$$= - j\omega\mu + \sigma Z_{TE}^2 - \frac{\gamma_x^2}{j\omega\mu} Z_{TE}^2$$

$$\frac{\partial Z_{TE}}{\partial z} = - j\omega\mu + (1 - \frac{\gamma_x^2}{\gamma^2}) \sigma Z_{TE}^2 \qquad (2.28)$$

Similarly for the TM mode one obtains

$$\frac{\partial Z_{TM}}{\partial z} = - j\omega\mu \, (1 - \frac{\gamma_x^2}{\gamma^2}) + \sigma Z_{TM}^2 \qquad (2.29)$$

Again when the incident fields have horizontal wavelengths large compared to a skin depth, the TE and TM modes become equivalent and

$$\frac{\partial Z}{\partial z} = - j\omega\mu + \sigma Z^2 \qquad (2.30)$$

This differential equation is of course nonlinear in Z; however, if one assumes a $\sigma(z)$ profile such that $\sigma(z) = \sigma_1$, a constant for $z > z_1$, then $Z(z_1) = \sqrt{j\omega\mu/\sigma_1}$ and equation (2.30) can be numerically integrated from $z = z_1$ to $z = 0$ to obtain an expression for the surface impedance in terms of the conductivity profile.

Thus, as with the layered model, the forward going problem of finding the surface impedance in terms of a specified conductivity profile is relatively simple. Again, the inverse problem of finding the $\sigma(z)$ profile which produces a specified surface impedance must be worked iteratively.

D. Linearized One Dimensional Model

Consider the following simplification of the one dimensional problem. Assume that the E field as a function of depth z has the form

$$E_x(z) = Ae^{-\int_0^z \gamma(z')\,dz'} \tag{2.31}$$

where A is independent of z and

$$\gamma(z) = \sqrt{j\omega\mu\,\sigma(z)} \tag{2.32}$$

From Maxwell's equations

$$\frac{dH_y}{dz} = -\sigma E_x$$

Integrating with respect to z and noting that H_y must vanish as $z \to \infty$, one has

$$\int_0^\infty \frac{dH_y}{dz}\,dz = -\int_0^\infty \sigma\, E_x\, dz$$

or

$$H_y(\infty) - H_y(o) = -\int_o^\infty \sigma(z)\, Ae^{-\int_o^z \gamma(z')\, dz'}\, dz$$

Thus, if one defines the surface admittance $Y(\omega)$ as being the reciprocal of the surface impedance, then

$$Y(\omega) = \frac{H_y(z=o)}{E_x(z=o)} = \int_o^\infty \sigma(z)\, e^{-\int_o^z \gamma(z')\, dz'}\, dz \tag{2.33}$$

or, from equation (2.32)

$$Y(\omega) = \int_o^\infty \sigma(z)\, e^{-\sqrt{j\omega\mu}\int_o^z \sqrt{\sigma(z')}\, dz'}\, dz \tag{2.34}$$

Now consider the following transformation. Let

$$e^{\alpha_1} = \int_o^z \sqrt{\sigma(z')}\, dz' \tag{2.35}$$

and

$$e^{-\alpha_2} = \sqrt{\omega\mu/2} \tag{2.36}$$

Noting that

$$e^{\alpha_1}\, d\alpha_1 = \sqrt{\sigma(z)}\, dz \tag{2.37}$$

and

$$z = o \rightarrow \alpha_1 = -\infty$$

$$z = \infty \rightarrow \alpha_1 = \infty$$

equation (2.34) becomes

$$Y(\alpha_2) = \int_{-\infty}^{\infty} \sqrt{\sigma(\alpha_1)}\ e^{-(1+j)\, e^{(\alpha_1 - \alpha_2)}}\ e^{\alpha_1}\, d\alpha_1$$

or

$$Y(\alpha_2)\, e^{-\alpha_2} = \int_{-\infty}^{\infty} \sqrt{\sigma(\alpha_1)}\ e^{-(1+j)\, e^{-(\alpha_2 - \alpha_1)}}\ e^{-(\alpha_2 - \alpha_1)}\, d\alpha_1 \qquad (2.38)$$

Noting from equation (2.27) that

$$\sqrt{\sigma_a(\omega)} = \sqrt{\omega\mu}\ |\, Y(\omega)\,|$$

equation (2.38) gives

$$\sqrt{\sigma_a(\alpha)} = |\sqrt{\sigma(\alpha)} * g(\alpha)| \qquad (2.39)$$

where

$$g(\alpha) = \sqrt{2}\ e^{-(1+j)\, e^{-\alpha}}\ e^{-\alpha} \qquad (2.40)$$

Thus, under this simplified model, which in effect neglects internal reflections in the E field, the apparent conductivity can be obtained by convolving the actual conductivity profile with a complex linear response

function in α-space. A plot of the magnitude of $g(\alpha)$ versus α is shown in figure 4. The magnitude of $g(\alpha)$ peaks up at $\alpha = 0$ and decays as $|\alpha|$ increases. Also

$$\left| \int_{-\infty}^{\infty} g(\alpha)\, d\alpha \right| = 1$$

So $g(\alpha)$, although it is complex, is somewhat like the response of a low pass filter with unity DC gain. This is consistent with the earlier observation that $\sigma_a(\omega)$ is a "smoothed out" version of $\sigma(z)$ with ω inversely related to z.

In practice, this simplified approach is probably not very useful by itself since the assumed form of the E field in equation (2.31) is not too realistic. Strictly speaking it is valid only if

$$\left| \frac{d\sigma(z)}{dz} \right| << \gamma(z)\, \sigma(z) \tag{2.41}$$

for all z. On the other hand this approach could be quite useful for obtaining a first guess to be used in an iterative inversion scheme. In particular if one simply assumes that

$$\sigma(\alpha) \cong \sigma_a(\alpha) \tag{2.42}$$

then frequency and depth may be related through equations (2.35) and (2.36) to give

$$\sigma(z) \cong \sigma_a(z_a(\omega)) \tag{2.43}$$

where

$$z_a(\omega) = \int_{\omega}^{\infty} \frac{d\omega_o}{\sqrt{2\omega_o^3 \mu \sigma_a(\omega_o)}} \tag{2.44}$$

Thus, an approximate depth scale may be attached to the frequency scale for an apparent conductivity curve. Notice that for $\sigma_a(\omega) = \sigma$, a constant, equation (2.44) reduces to the standard skin depth, so one may think of $z_a(\omega)$ as sort of an integrated skin depth. In fact, for cases where equation (2.41) is satisfied, $z_a(\omega)$ will be the depth at which the fields have decayed to 1/e of their surface value.

E. Generalized Skin Depth

As suggested by the preceding paragraph, it will be useful to generalize the idea of skin depth for an inhomogeneous model. For a homogeneous medium, the skin depth was defined to be the depth at which the fields are attenuated to 1/e of their surface values. For an inhomogeneous model, the fields of course do not have a simple exponential decay; however, if one defines $\delta(\omega)$ to be the depth at which

$$\mathrm{Re}\left[\int_0^{\delta(\omega)} \sqrt{j\omega\mu\sigma(z)}\, dz\right] = 1 \tag{2.45}$$

then δ will be a good measure of the depth of penetration of the fields and as such it may be taken as the skin depth.

In the discussion of the horizontally layered model, the statement was made that the incident fields could be treated as normally incident plane waves if the actual horizontal wavelengths were long compared to a skin depth in each layer since for that case

$$\gamma_{zi} \cong \gamma_i$$

A less restrictive yet adequate requirement is that

$$\int_0^{\delta} \gamma_z\, dz \cong \int_0^{\delta} \gamma\, dz \tag{2.46}$$

where δ is defined by equation (2.45). Clearly this condition will exist provided

$$\left| \int_0^{\delta} \gamma_x \, dz \right| << \left| \int_0^{\delta} \gamma \, dz \right| \tag{2.47}$$

where $\gamma_x^2 + \gamma_z^2 = \gamma^2 = j\omega\mu\sigma$. But $\gamma_x = jk_x = j2\pi/\lambda$. Thus

$$\left| \int_0^{\delta} \gamma_x \, dz \right| = \frac{2\pi\delta}{\lambda} \tag{2.48}$$

Also, from equation (2.45), the definition of δ,

$$\left| \int_0^{\delta} \gamma \, dz \right| = \sqrt{2}$$

Thus, the condition (2.47) will exist provided

$$\frac{2\pi\delta}{\lambda} << \sqrt{2}$$

or

$$\delta << \lambda/\sqrt{2\pi}$$

So, if the horizontal wavelengths are long compared to the skin depth defined by equation (2.45), the incident fields may in effect be treated as normally incident plane waves.

In conclusion then, the forward going one dimensional problem is reasonably simple. If the incident fields are assumed to have horizontal wavelengths long compared to a skin depth, then any horizontal component of the H field is related to the orthogonal horizontal component of the E

field by a scalar impedance which is related to the conductivity profile. The inverse problem of estimating the conductivity profile from a measured surface impedance, while it is nonlinear has been worked with some success using iterative techniques. The simple linearized model discussed here should be useful for providing a first guess for such iterative solutions.

III. TWO AND THREE DIMENSIONAL MODELS

The scalar surface impedance discussed in the previous chapter is not sufficient to describe the relationship between the horizontal E and H fields for a model that has lateral variations in conductivity. In this chaper some general relationships will be developed for two dimensional models (models for which σ is a function of two space coordinates, the vertical or z coordinate and one horizontal coordinate, say x) and for three dimensional models (models for which σ is a function of all three space coordinates). It will be shown that for these models the impedance must be expressed as a rank two tensor as was indicated in equation (1.1).

A. Z_{TE} and Z_{TM} for Two Dimensional Models

Consider again Maxwell's equations as stated in equations (2.1) through (2.4). If one assumes that the conductivity σ is a function of x and z, equations (2.1) through (2.3) are still applicable; however, equation (2.4) must be replaced by

$$\nabla \cdot (\sigma E) = 0 \tag{3.1}$$

where once again it is assumed that displacement currents in the earth are negligible. If one also assumes once again that the horizontal wavelengths of the incident fields are long compared to a skin depth, then in the earth, everything is essentially uniform in the y direction so that equations (2.1) through (2.3) together with equation (3.1) in component form become

$$-\frac{\partial E_y}{\partial z} = -j\omega\mu H_x \tag{3.2}$$

$$\frac{\partial E_x}{\partial z} - \frac{\partial E_z}{\partial x} = -j\omega\mu H_y \tag{3.3}$$

$$\frac{\partial E_y}{\partial x} = j\omega\mu H_z \tag{3.4}$$

$$-\frac{\partial H_y}{\partial z} = \sigma E_x \tag{3.5}$$

$$\frac{\partial H_x}{\partial z} - \frac{\partial H_z}{\partial x} = \sigma E_y \tag{3.6}$$

$$\frac{\partial H_y}{\partial x} = \sigma E_z \tag{3.7}$$

$$\frac{\partial H_x}{\partial x} + \frac{\partial H_z}{\partial z} = 0 \tag{3.8}$$

$$\frac{\partial(\sigma E_x)}{\partial x} + \frac{\partial(\sigma E_z)}{\partial z} = 0 \tag{3.9}$$

Observe that the only field components involved in equations (3.2), (3.4), (3.6), and (3.8) are E_y, H_x, and H_z. Also, the only components entering equations (3.3), (3.5), (3.7), and (3.9) are E_x, E_z, and H_y. Thus it is apparent that the two modes are decoupled and may be considered separately. The mode involving E_y, H_x, and H_z is usually called the TE or E parallel mode since the E field is horizontal and parallel to the strike. The mode involving E_x, E_z, and H_y is called the TM or E perpendicular mode since the magnetic field is horizontal and the electric field is perpendicular to the strike. The strike is the direction along which there are no variations in the model parameters, in this case, the y direction.

Thus, for a two-dimensional model two impedances are required to define the relationship between the horizontal components of the E and H fields: $Z_{TE} = -E_y/H_x$ and $Z_{TM} = E_x/H_y$. Exact solutions for $Z_{TE}(\omega,x)$ and $Z_{TM}(\omega,x)$ in terms of $\sigma(x,z)$ are not tractable analytically although a few approximate cases have been worked out. In general, solutions are obtainable only by using numerical methods such as finite differencing over a two dimensional grid. Computer programs are available which implement these

techniques (Patrick, 1969). It would appear that the inverse problem of finding $\sigma(x,z)$ in terms of $Z_{TE}(\omega,x)$ and $Z_{TM}(\omega,x)$ could in principle be solved using iterative techniques similar to those used for the one dimensional inverse problem. It is believed that such a solution would be unique, although no proof is known. On the other hand, the number of calculations involved for grids large enough to be of interest is so great that the problem seems to be out of the range of present day computers. Nevertheless, useful and instructive information about two dimensional modeling can be obtained from solutions of the forward going problem.

B. Z in a General Coordinate System for Two Dimensional Models

As was shown above, for a two dimensional model the TE and TM modes decouple when one of the horizontal coordinates is aligned with the strike. It will now be useful to obtain the relationship between the tangential fields in a coordinate system in which the horizontal axes are arbitrarily oriented.

Suppose that the x' - y' coordinate system as shown in figure 5 is aligned with the strike, so that

$$E'_x = Z_{TM} H'_y \tag{3.10}$$

and

$$E'_y = -Z_{TE} H'_x \tag{3.11}$$

Suppose that the x-y coordinate system is oriented at an angle θ with respect to the x' - y' system as shown in figure 5. Then

$$E_x = E'_x \cos\theta + E'_y \sin\theta \tag{3.12}$$

$$E_y = -E'_x \sin\theta + E'_y \cos\theta \tag{3.13}$$

and

$$H_x = H'_x \cos\theta + H'_y \sin\theta \tag{3.14}$$

$$H_y = -H'_x \sin\theta + H'_y \cos\theta \tag{3.15}$$

or alternately

$$H'_x = H_x \cos\theta - H_y \sin\theta \tag{3.16}$$

$$H'_y = H_x \sin\theta + H_y \cos\theta \tag{3.17}$$

Combining these equations gives

$$\begin{aligned} E_x &= E'_x \cos\theta + E'_y \sin\theta \\ &= (Z_{TM} H'_y) \cos\theta + (-Z_{TE} H'_x) \sin\theta \\ &= Z_{TM}(H_x \sin\theta + H_y \cos\theta)\cos\theta - Z_{TE}(H_x \cos\theta - \\ &\qquad - H_y \sin\theta) \sin\theta \\ &= H_x[(Z_{TM} - Z_{TE}) \sin\theta\cos\theta] + H_y[Z_{TM} \cos^2\theta + \\ &\qquad + Z_{TE} \sin^2\theta] \end{aligned}$$

Thus if one defines

$$E_x = Z_{xx} H_x + Z_{xy} H_y$$

then

$$\begin{aligned} Z_{xx} &= (Z_{TM} - Z_{TE}) \sin\theta\cos\theta \\ &= \left(\frac{Z_{TM} - Z_{TE}}{2}\right) \sin 2\theta \end{aligned}$$

and

$$\begin{aligned} Z_{xy} &= Z_{TM} \cos^2\theta + Z_{TE} \sin^2\theta \\ &= \left(\frac{Z_{TM} + Z_{TE}}{2}\right) + \left(\frac{Z_{TM} - Z_{TE}}{2}\right) \cos 2\theta \end{aligned}$$

Similarly for the other components, one obtains

$$Z_{yx} = -\left(\frac{Z_{TM} + Z_{TE}}{2}\right) + \left(\frac{Z_{TM} - Z_{TE}}{2}\right) \cos 2\theta$$

and

$$Z_{yy} = \left(\frac{Z_{TE} - Z_{TM}}{2}\right) \sin 2\theta$$

In summary

$$\begin{bmatrix} E_x \\ E_y \end{bmatrix} = \begin{bmatrix} Z_1 \sin 2\theta & Z_2 + Z_1 \cos 2\theta \\ -Z_2 + Z_1 \cos 2\theta & -Z_1 \sin 2\theta \end{bmatrix} \begin{bmatrix} H_x \\ H_y \end{bmatrix} \tag{3.18}$$

where

$$Z_1 = (Z_{TM} - Z_{TE})/2 \tag{3.19}$$

$$Z_2 = (Z_{TM} + Z_{TE})/2 \tag{3.20}$$

In general, then, for a two dimensional model, the tangential components of E and H are related by a rank two tensor impedance. The diagonal terms of the Z matrix are in general negatives of each other and they reduce to zero when the axes are aligned with the strike.

C. General Form of Z for Three Dimensional Models

For three dimensional models where σ is a function of all three space coordinates, the six field components are in general all coupled to each other, so it is not possible to separate the analysis into two distinct modes as was done for the two dimensional case. Nevertheless, it is possible to make some general statements about the relationship between the tangential components of the E and H fields.

It will now be shown that a rank two tensor impedance of the form shown in equation (1.1) is unique and stable, subject once again of course to the assumption that the horizontal wavelengths of the incident fields are long compared to a skin depth in the earth. Also it will be useful for later purposes to establish that in general the vertical magnetic field can be expressed as a linear combination of the two horizontal H field components. That is,

$$H_z = r_{zx} H_x + r_{zy} H_y \tag{3.21}$$

where r_{zx} and r_{zy} are dimensionless constants, subject also of course to the assumption that the incident fields have horizontal wavelengths long compared to a skin depth. This assumption implies that the incident fields may be treated as normally incident plane waves. This being the case, the incident fields can be separated into two orthogonal linearly polarized plane waves. Clearly, for a linearly polarized normally incident plane wave, each of the components of the total E and H fields will be proportional to the amplitude of the incident wave. Thus, if the incident E is linearly polarized in the x direction then

$$E_x = a_1 E_{xi}$$

$$E_y = a_2 E_{xi}$$

$$H_x = b_1 E_{xi}$$

$$H_y = b_2 E_{xi}$$

$$H_z = c_1 E_{xi}$$

where E_{xi} is the incident field. Similarly, if the incident E is linearly polarized in the y direction

$$E_x = a_3 E_{yi}$$

$$E_y = a_4 E_{yi}$$

$$H_x = b_3 E_{yi}$$

$$H_y = b_4 E_{yi}$$

$$H_z = c_2 E_{yi}$$

Since all of the field equations are linear with respect to E and H, superposition must hold. Thus for a general normally incident plane wave

$$E_x = a_1 E_{xi} + a_3 E_{yi}$$

$$E_y = a_2 E_{xi} + a_4 E_{yi}$$

$$H_x = b_1 E_{xi} + b_3 E_{yi}$$

$$H_y = b_2 E_{xi} + b_4 E_{yi}$$

$$H_z = c_1 E_{xi} + c_2 E_{yi}$$

or in matrix notation

$$\begin{bmatrix} E_x \\ E_y \end{bmatrix} = [A] \begin{bmatrix} E_{xi} \\ E_{yi} \end{bmatrix}$$

$$\begin{bmatrix} H_x \\ H_y \end{bmatrix} = [B] \begin{bmatrix} E_{xi} \\ E_{yi} \end{bmatrix}$$

and

$$H_z = [C] \begin{bmatrix} E_{xi} \\ E_{yi} \end{bmatrix}$$

If [B] is nonsingular, then

$$\begin{bmatrix} E_{xi} \\ E_{yi} \end{bmatrix} = [B]^{-1} \begin{bmatrix} H_x \\ H_y \end{bmatrix}$$

so that

$$\begin{bmatrix} E_x \\ E_y \end{bmatrix} = [A][B]^{-1} \begin{bmatrix} H_x \\ H_y \end{bmatrix}$$

and

$$H_z = [C][B]^{-1} \begin{bmatrix} H_x \\ H_y \end{bmatrix} \tag{3.22}$$

Thus

$$[Z] = [A][B]^{-1} \tag{3.23}$$

and

$$[r] = [r_{zx}, r_{zy}] = [C][B]^{-1} \tag{3.24}$$

So [Z] and [r] are defined, and E_x, E_y and H_z can be expressed as linear combinations of H_x and H_y. The only problem that might arise would be if [B] were singular. Singularity of [B] implies that

$$b_1 b_4 = b_2 b_3 \tag{3.25}$$

Now for any reasonable earth model, the reflection coefficient for the magnetic field at the surface is almost unity so that the total H field is close to twice the incident field. Thus, a normally incident plane wave with E linearly polarized in the x direction (and hence H linearly polarized in the y direction) will give rise to total fields such that H_y will be considerably greater than H_x. Thus

$$|b_2| >> |b_1|$$

Similarly, for a normally incident plane wave with E linearly polarized in the y direction, H_x will be somewhat greater than H_y. Thus

$$|b_3| >> |b_4|$$

So clearly

$$|b_2 b_3| >> |b_1 b_4|$$

Comparing this with equation (3.25) indicates that for any reasonable earth model, [B] will not be singular, and hence Z is defined by equation (3.23).

Next it will be useful to observe the behavior of the elements of Z as the coordinate system is rotated. As with the two dimensional model,

the elements of Z in the x-y coordinate system will be expressed in terms of the elements of Z in the x'-y' coordinate system as shown in figure 5. The derivation is the same as for the two dimensional case except that equations (3.10) and (3.11) are replaced by

$$E'_x = Z'_{xx} H'_x + Z'_{xy} H'_y \tag{3.26}$$

and

$$E'_y = Z'_{yx} H'_x + Z'_{yy} H'_y \tag{3.27}$$

Thus

$$\begin{aligned} E_x &= E'_x \cos\theta + E'_y \sin\theta \\ &= (Z'_{xx} H'_x + Z'_{xy} H'_y) \cos\theta + (Z'_{yx} H'_x + Z'_{yy} H'_y) \sin\theta \\ &= (Z'_{xx} \cos\theta + Z'_{yx} \sin\theta) H'_x + (Z'_{xy} \cos\theta + Z'_{yy} \sin\theta) H'_y \\ &= (Z'_{xx} \cos\theta + Z'_{yx} \sin\theta)(H_x \cos\theta - H_y \sin\theta) \\ &\quad + (Z'_{xy} \cos\theta + Z'_{yy} \sin\theta)(H_x \sin\theta + H_y \cos\theta) \\ &= [Z'_{xx} \cos^2\theta + Z'_{yy} \sin^2\theta + (Z'_{yx} + Z'_{xy}) \sin\theta \cos\theta] H_x \\ &\quad + [Z'_{xy} \cos^2\theta - Z'_{yx} \sin^2\theta + (Z'_{yy} - Z'_{xx}) \sin\theta \cos\theta] H_y \end{aligned}$$

So that

$$Z_{xx} = Z'_{xx} \cos^2\theta + Z'_{yy} \sin^2\theta + (Z'_{xy} + Z'_{yx}) \sin\theta \cos\theta$$

$$\left(\frac{Z'_{xx} + Z'_{yy}}{2}\right) + \left(\frac{Z'_{xx} - Z'_{yy}}{2}\right) \cos 2\theta + \left(\frac{Z'_{xy} + Z'_{yx}}{2}\right) \sin 2\theta$$

Similar expressions for Z_{xy}, Z_{yx}, and Z_{yy} are obtained. The results are

$$Z_{xx} = Z_1 + Z_2 \cos 2\theta + Z_3 \sin 2\theta \tag{3.28}$$

$$Z_{xy} = Z_4 + Z_3 \cos 2\theta - Z_2 \sin 2\theta \tag{3.29}$$

$$Z_{yx} = -Z_4 + Z_3 \cos 2\theta - Z_2 \sin 2\theta \tag{3.30}$$

$$Z_{yy} = Z_1 - Z_2 \cos 2\theta - Z_3 \sin 2\theta \tag{3.31}$$

where

$$Z_1 = \frac{Z'_{xx} + Z'_{yy}}{2} \tag{3.32}$$

$$Z_2 = \frac{Z'_{xx} - Z'_{yy}}{2} \tag{3.33}$$

$$Z_3 = \frac{Z'_{xy} + Z'_{yx}}{2} \tag{3.34}$$

$$Z_4 = \frac{Z'_{xy} - Z'_{yx}}{2} \tag{3.35}$$

If one further defines

$$Z_o(\theta) = Z_3 \cos 2\theta - Z_2 \sin 2\theta \tag{3.36}$$

Then equations (3.28) through (3.31) become

$$Z_{xx} = Z_1 - Z_o(\theta + 45^\circ) \tag{3.37}$$

$$Z_{xy} = Z_4 + Z_o(\theta) \tag{3.38}$$

$$Z_{yx} = -Z_4 + Z_o(\theta) \tag{3.39}$$

$$Z_{yy} = Z_1 + Z_o(\theta + 45^\circ) \tag{3.40}$$

The function $Z_o(\theta)$ traces an ellipse in the complex plane centered on the origin as θ varies from zero to 180°. To show that this is true take

$$Z_o(\theta) = x + jy$$

where x and y are real. From equation (3.36)

$$x = \mathrm{Re}[Z_3]\cos 2\theta - \mathrm{Re}[Z_2]\sin 2\theta$$

$$= A\cos(2\theta - \alpha)$$

$$y = \mathrm{Im}[Z_3]\cos 2\theta - \mathrm{Im}[Z_2]\sin 2\theta$$

$$= B\cos(2\theta - \beta)$$

Letting

$$2\theta - \alpha = \varphi$$

$$\beta - \alpha = \varphi_o$$

gives

$$x = A\cos\varphi$$

and

$$y = B\cos(\varphi - \varphi_o) = C\cos\varphi + D\sin\varphi$$

Thus

$$\cos\varphi = \frac{x}{A}$$

and

$$\sin\varphi = \pm\sqrt{1 - (x/A)^2}$$

So that

$$y = C\left[\frac{x}{A}\right] + D\left[\pm\sqrt{1 - (x/A)^2}\right]$$

or

$$y^2 - \frac{2C}{A}xy + \frac{C^2}{A^2}x^2 = D^2\left(1 - \frac{x^2}{A^2}\right)$$

or

$$A^2y^2 + (C^2 + D^2)x^2 - 2ACxy - D^2A^2 = 0$$

This is the standard form for an ellipse centered on the origin. Thus $Z_o(\theta)$ traces an ellipse in the complex plane as θ varies. Referring to equations (3.37) through (3.40) one observes that each of the elements of Z then traces an ellipse in the complex plane as the measuring axes are rotated.

D. Comparison of Z Matrix for Two and Three Dimensional Models

As was shown in the previous section, for a three dimensional model, the elements of Z trace ellipses in the complex plane as the measuring axes are rotated. From equation (3.18) one observes that for two dimensional models, the theta dependent parts of the elements of Z have fixed phases. Thus the ellipses degenerate to straight lines for the two dimensional case. Also one observes from equation (3.18) that the diagonal terms of the Z matrix for the two dimensional case have no constant term. Thus the straight line representing the locii of Z_{xx} and Z_{yy} in the complex plane passes through the origin. Figure 6 illustrates the general form of the locii of the elements of Z in the complex plane for the two and three dimensional cases.

At the present time solutions for the general three dimensional problem are not available. For this reason, it is usually desirable to find one dimensional or two dimensional models that approximately fit measured data which in general is of course three dimensional. It frequently happens that, over some limited frequency range, measured data looks almost two dimensional; that is, the Z ellipses almost collapse to straight lines and the diagonal terms of the Z matrix are almost negatives of each other. This situation will occur whenever there exists a horizontal direction along which the conductivity cross section is nearly constant for a distance of several skin depths. Whenever this situation exists, it is desirable to determine the approximate strike direction and to estimate the corresponding Z_{TE} and Z_{TM} for comparison with theoretical Z's from two dimensional models.

Several methods have been proposed for estimating the principal impedance axes [Swift, 1967] all of which converge to the correct result when the data is actually two dimensional. From the point of view of the impedance ellipses, the most reasonable way seems to be to take

$$Z_{TE}\ ,\ Z_{TM} = Z_4 \pm Z'_o \tag{3.41}$$

where Z'_o is the semi-major axis of the ellipse $Z_o(\theta)$ as defined in equation (3.36).

This method yields the principal directions as the values of θ which maximize $|Z_o(\theta)|$. A little algebra will show that these values of θ are given by the equation

$$\tan 4\theta = \frac{2(x_2x_3 + y_2y_3)}{(x_2^2 + y_2^2) - (x_3^2 + y_3^2)} \qquad (3.42)$$

where x_i and y_i are the real and imaginary parts of Z_i respectively, with Z_i being defined by equations (3.33) and (3.34). Incidentally, this method gives the same result as Swift's method of finding the angle θ which maximizes $\{|Z_{xy}|^2 + |Z_{yx}|^2\}$ or minimizes $\{|Z_{xx}|^2 + |Z_{yy}|^2\}$.

Having thus obtained estimates of the principal axes of the impedance matrix and the corresponding principal impedance values, it is desirable to have some measure of how two dimensional the data actually is. To accomplish this, there are two parameters that should be considered. First, there is the ratio of the constant terms in the diagonal and off diagonal elements of the Z matrix. In other words, the ratio Z_1/Z_4 where Z_1 and Z_4 are defined in equations (3.32) and (3.35). Second, there is the ratio of the minor axis to the major axis of the $Z_o(\theta)$ ellipse. The magnitudes of both of these ratios should be small compared to unity in order for the data to fit a two dimensional model.

E. Use of H_z for Determining the Strike Direction

In the previous section, an indication was given as to how one might estimate the principal axes of a measured impedance matrix which is approximately two dimensional. However, no method was given for determining which axis represents the strike direction. This matter can be easily resolved in terms of H_z, the vertical magnetic field. Recall from equations (3.2) through (3.9) that H_z appears only in the equations for the TE mode. Thus, with the x'-y' axes aligned with the strike, as in section B of this chapter,

$$E'_y = -Z_{TE} H'_x$$

and

$$H'_z = r'_{TE} H'_x$$

In the x-y coordinate system, at an angle θ from the x'-y' system

$$H_z = H'_z = r'_{TE} H'_x = r'_{TE} (H_x \cos\theta - H_y \sin\theta)$$

$$H_z = H_x r'_{TE} \cos\theta - H_y r'_{TE} \sin\theta \qquad (3.43)$$

Recall from equation (3.21) that for the general three dimensional model

$$H'_z = r'_{zx} H'_x + r'_{zy} H'_y$$

so that

$$\begin{aligned} H_z = H'_z &= r'_{zx} H'_x + r'_{zy} H'_y \\ &= r'_{zx} (H_x \cos\theta - H_y \sin\theta) + r'_{zy} (H_x \sin\theta + H_y \cos\theta) \\ &= H_x (r'_{zx} \cos\theta + r'_{zy} \sin\theta) + H_y (r'_{zy} \cos\theta - r'_{zx} \sin\theta) \end{aligned}$$

Thus

$$r_{zx} = r'_{zx} \cos\theta + r'_{zy} \sin\theta \qquad (3.44)$$

and

$$r_{zy} = r'_{zy} \cos\theta - r'_{zx} \sin\theta \qquad (3.45)$$

Comparison of equations (3.44) and (3.45) with equation (3.36) indicates that r_{zx} and r_{zy} like $Z_o(\theta)$ trace ellipses in the complex plane as θ varies. However, the important difference is that the magnitudes of r_{zx} and r_{zy} have only one peak every 180° instead of every 90° like $Z_o(\theta)$. Furthermore, one observes from equation (3.43) that in the two dimensional limit, the angle θ that maximizes r_{zx} is the strike direction.

Thus, when measured data is approximately two dimensional, the angle that maximizes $|r_{zx}|$ should correspond to one of the principal axes of

the Z matrix, and so it is possible to estimate the approximate strike direction and the corresponding Z_{TE} and Z_{TM}.

IV. METHODS FOR ESTIMATING THE Z MATRIX FROM MEASURED DATA

Now that a considerable amount of attention has been given to the forms of the Z matrix for various classes of models and to possible interpretations of Z, it is time to consider some methods for estimating Z from measured E and H field data.

A. The General Problem

Consider the equation

$$E_x = Z_{xx}H_x + Z_{xy}H_y$$

where E_x, H_x, and H_y may be considered to be Fourier transforms of measured electric and magnetic field data. If one has two independent measurements of E_x, H_x, and H_y at a given frequency, denoted by E_{x1}, H_{x1}, H_{y1}, E_{x2}, H_{x2} and H_{y2} respectively, then

$$Z_{xx} = \frac{\begin{vmatrix} E_{x1} & H_{y1} \\ E_{x2} & H_{y2} \end{vmatrix}}{\begin{vmatrix} H_{x1} & H_{y1} \\ H_{x2} & H_{y2} \end{vmatrix}}$$

and

$$Z_{xy} = \frac{\begin{vmatrix} H_{x1} & E_{x1} \\ H_{x2} & E_{x2} \end{vmatrix}}{\begin{vmatrix} H_{x1} & H_{y1} \\ H_{x2} & H_{y2} \end{vmatrix}}$$

provided

$$H_{x1}H_{y2} - H_{x2}H_{y1} \neq 0 \qquad (4.1)$$

Equation (4.1) simply states the fact that the two field measurements must have different source polarizations. If the two have the same polarization, they are not independent.

Since any physical measurement of E or H will include some noise, it is usually desirable to make more than two independent measurements, and then to use some type of averaging that will reduce the effects of the noise. Suppose one has n measurements of E_x, H_x, and H_y at a given frequency. One can then estimate Z_{xx} and Z_{xy} in the mean square sense. That is, define

$$\Psi = \sum_{i=1}^{n} (E_{xi} - Z_{xx}H_{xi} - Z_{xy}H_{yi})(E^*_{xi} - Z^*_{xx}H^*_{xi} - Z^*_{xy}H^*_{yi})$$

where E^*_{xi} is the complex conjugate of E_{xi}, etc., and then find the values of Z_{xx} and Z_{xy} that minimize Ψ. Setting the derivatives of Ψ with respect to the real and imaginary parts of Z_{xx} to zero yields

$$\sum_{i=1}^{n} E_{xi}H^*_{xi} = Z_{xx}\sum_{i=1}^{n} H_{xi}H^*_{xi} + Z_{xy}\sum_{i=1}^{n} H_{yi}H^*_{xi} \qquad (4.2)$$

Similarly, setting the derivatives of Ψ with respect to the real and imaginary parts of Z_{xy} to zero yields

$$\sum_{i=1}^{n} E_{xi}H^*_{yi} = Z_{xx}\sum_{i=1}^{n} H_{xi}H^*_{yi} + Z_{xy}\sum_{i=1}^{n} H_{yi}H^*_{yi} \qquad (4.3)$$

Notice that the summations represent auto and cross power density spectra. Equations (4.2) and (4.3) may then be solved simultaneously for Z_{xx} and Z_{xy}. This solution will minimize the error caused by noise on E_x. It is possible to define other mean square estimates that minimize other types of noise. For example, if one takes

$$\Psi = \sum_{i=1}^{n} \left(\frac{E_{xi}}{Z_{xx}} - H_{xi} - \frac{Z_{xy}}{Z_{xx}} H_{yi}\right)\left(\frac{E^*_{xi}}{Z^*_{xx}} - H^*_{xi} - \frac{Z^*_{xy}}{Z^*_{xx}} H^*_{yi}\right)$$

the resulting solution will minimize the error introduced by noise on H_x.

There are four distinct equations that arise from the various mean square estimates. In terms of the auto and cross power density spectra, they are

$$\overline{E_x E^*_x} = Z_{xx}\overline{H_x E^*_x} + Z_{xy}\overline{H_y E^*_x} \tag{4.4}$$

$$\overline{E_x E^*_y} = Z_{xx}\overline{H_x E^*_y} + Z_{xy}\overline{H_y E^*_y} \tag{4.5}$$

$$\overline{E_x H^*_x} = Z_{xx}\overline{H_x H^*_x} + Z_{xy}\overline{H_y H^*_x} \tag{4.6}$$

and

$$\overline{E_x H^*_y} = Z_{xx}\overline{H_x H^*_y} + Z_{xy}\overline{H_y H^*_y} \tag{4.7}$$

Strictly speaking, equations (4.4) through (4.7) are valid only if $\overline{E_x E^*_x}$, $\overline{E_x E^*_y}$, etc. represent the power density spectra at a discrete frequency ω. In practice however, Z_{ij} are slowly varying functions of frequency, and as such, $\overline{E_x E^*_x}$, etc. may be taken as averages over some finite bandwidth. This is fortunate since it facilitates the estimation of the power density spectra.

B. Estimation of Power Density Spectra

There are a variety of standard techniques available for estimating $\overline{E_x E^*_x}$, $\overline{E_x E^*_y}$, etc., the auto and cross power density spectra, several of which will be considered here. In all the cases, it will be assumed that the field components are given as sampled time sequences.

1. One method that was frequently used in the past was that of using the auto and cross correlation functions of the field components. This method makes use of the fact that the Fourier transform of the auto correlation function of a given signal is equal to the power density spectrum of that signal. Also the Fourier transform of the cross correlation function between two signals is equal to the cross power density spectrum of the two signals. Blackman and Tukey (1958) have considered in detail the various aspects of estimating correlation functions and the corresponding power-density spectra for sampled time sequences. They have given careful attention to the spectral windows that result from truncating the time sequences and the correlation functions. Hopkins (1966) and others have used this method for obtaining estimates of $\overline{E_x E_x^*}$, $\overline{E_x E_y^*}$, etc. in magnetotelluric work. This method, when compared with the ones that will be considered next, has several disadvantages. First it is more time consuming on the computer when many cross spectra are needed. Second, it gives statistically correct results only when the signals are stationary. Finally, it is more susceptible to error from the side lobes of the spectral window when the spectra are not reasonably flat. Blackman and Tukey suggest that this third disadvantage can be circumvented to some extent by digitally prewhitening the time sequences prior to computing the correlation functions.

2. Another method for estimating the power density spectra of the field components begins by subdividing each of the time sequences into several blocks. For each data block one computes the Fourier transformation to obtain estimates of $E_x(\omega)$, $E_y(\omega)$, etc. Then one forms the products $E_x E_x^*$, $E_x E_y^*$, etc. Finally, for each frequency, one averages the products over the several time blocks, thus obtaining time averaged estimates of $\overline{E_x E_x^*}$, $\overline{E_x E_y^*}$, $\overline{E_x H_x^*}$, etc. This method is particularly well suited to small digital computers since only one time block of data needs to be stored in memory at any given time, and the blocks may be quite small compared to the

total time sequences. Also this method is especially useful for situations where the signals contain noise bursts that are isolated in time. Such noise bursts may arise from tape drop-out, system saturation caused by large amplitude signals, or many other sources. Such noise bursts are often readily detectable so that data blocks containing them may simply be omitted from the time average.

3. Another method for estimating the power spectra that is very similar to the previous one consists of feeding the original time sequences into a bank of narrow band digital recursive filters spanning the desired frequency range. The outputs of these filters are then treated the same as the outputs of the block Fourier transforms of the previous method. This recursive filter method has essentially the same advantages as the previous method together with the additional advantage that it lends itself quite readily to obtaining spectral estimates equally spaced on a log frequency scale. This is because the recursive filters may be designed such that they all have the same Q and have the appropriate spacing on the frequency scale. Swift (1967) has used this technique.

4. For the final method to be considered here, one begins by Fourier transforming each of the entire time sequences. The products $E_x E_x^*$, $E_x E_y^*$, etc. are then formed for each harmonic. Finally the products are averaged over several neighboring harmonics to obtain the desired bandwidth. As far as computation time is concerned, this method is quite efficient if one uses the Cooley-Tukey algorithm for fast Fourier transforms. In fact, for a given number of multiplications, the spectral windows obtainable by this method are better than those obtainable by any of the other methods considered here. (A detailed discussion of spectral windows is included in Chapter V.) This method, like the last one, lends itself readily to constant Q estimates of the spectral density since the number of harmonics averaged in each band may be made approximately proportional to the center

frequency of the band. The primary disadvantage of this method is that, compared to the two previous methods, it requires a fairly large number of storage locations; in general it requires a large computer. Actually, in a modified form which is not quite as efficient computationally, the Cooley-Tukey algorithm is applicable to small computers. For a detailed consideration of this algorithm, see Cooley (1965).

If then, by one means or another, estimates of the auto and cross power density spectra are obtained, one can proceed to estimate the elements of the Z matrix.

C. Estimation of Z from Auto and Cross Power Density Spectra

Consider equations (4.4) through (4.7). Under certain conditions, these equations are independent so that any two of them may be solved simultaneously for Z_{xx} and Z_{xy}. Since there are six possible distinct pairs of equations, there are six ways to estimate Z_{xx} and Z_{xy}. For example, the six estimates for Z_{xy} are

$$\bar{Z}_{xy} = \frac{(\overline{H_x E_x^*})(\overline{E_x E_y^*}) - (\overline{H_x E_y^*})(\overline{E_x E_x^*})}{(\overline{H_x E_x^*})(\overline{H_y E_y^*}) - (\overline{H_x E_y^*})(\overline{H_y E_x^*})} \tag{4.8}$$

$$\bar{Z}_{xy} = \frac{(\overline{H_x E_x^*})(\overline{E_x H_x^*}) - (\overline{H_x H_x^*})(\overline{E_x E_x^*})}{(\overline{H_x E_x^*})(\overline{H_y H_x^*}) - (\overline{H_x H_x^*})(\overline{H_y E_x^*})} \tag{4.9}$$

$$\bar{Z}_{xy} = \frac{(\overline{H_x E_x^*})(\overline{E_x H_y^*}) - (\overline{H_x H_y^*})(\overline{E_x E_x^*})}{(\overline{H_x E_x^*})(\overline{H_y H_y^*}) - (\overline{H_x H_y^*})(\overline{H_y E_x^*})} \tag{4.10}$$

$$\bar{Z}_{xy} = \frac{(\overline{H_x E_y^*})(\overline{E_x H_x^*}) - (\overline{H_x H_x^*})(\overline{E_x E_y^*})}{(\overline{H_x E_y^*})(\overline{H_y H_x^*}) - (\overline{H_x H_x^*})(\overline{H_y E_y^*})} \tag{4.11}$$

$$\bar{Z}_{xy} = \frac{(\overline{H_x E_y^*})(\overline{E_x H_y^*}) - (\overline{H_x H_y^*})(\overline{E_x E_y^*})}{(\overline{H_x E_y^*})(\overline{H_y H_y^*}) - (\overline{H_x H_y^*})(\overline{H_y E_y^*})} \tag{4.12}$$

and

$$\bar{Z}_{xy} = \frac{(\overline{H_x H_x^*})(\overline{E_x H_y^*}) - (\overline{H_x H_y^*})(\overline{E_x H_x^*})}{(\overline{H_x H_x^*})(\overline{H_y H_y^*}) - (\overline{H_x H_y^*})(\overline{H_y H_x^*})} \tag{4.13}$$

where $\bar{Z}_{xy}$ denotes a measured estimate of Z_{xy}.

It turns out that two of these expressions tend to be relatively unstable for the one dimensional case, particularly when the incident fields are unpolarized. For this case $\overline{E_x E_y^*}$, $\overline{E_x H_x^*}$, $\overline{E_y H_y^*}$, and $\overline{H_x H_y^*}$ tend toward zero, so that equations (4.10) and (4.11) become indeterminant. The other four expressions are quite stable and correctly predict $Z_{xy} = E_x/H_y$ for the one dimensional case, provided the incident fields are not highly polarized.

This same thing is true of the other three impedance elements Z_{xx}, Z_{yx}, and Z_{yy}. In each case there are six ways to estimate Z_{ij}, two of which are unstable for one dimensional models with unpolarized incident fields. Also in each case the other four estimates are quite stable for any reasonable earth model provided the incident fields are not highly polarized.

As was mentioned earlier, any physical measurement of E or H will necessarily contain some noise. It is desirable now to consider how such noise will affect the Z estimates defined above. Suppose that

$$E_x = E_{xs} + E_{xn} \tag{4.14}$$

$$E_y = E_{ys} + E_{yn} \tag{4.15}$$

$$H_x = H_{xs} + H_{xn} \tag{4.16}$$

$$H_y = H_{ys} + H_{yn} \tag{4.17}$$

where

$$\begin{bmatrix} E_{xs} \\ E_{ys} \end{bmatrix} = \begin{bmatrix} Z_{xx} & Z_{xy} \\ Z_{yx} & Z_{yy} \end{bmatrix} \begin{bmatrix} H_{xs} \\ H_{ys} \end{bmatrix}$$

and E_{xn}, E_{yn}, H_{xn} and H_{yn} are noise terms. If the noise terms are all zero, then the four stable estimates of each of the elements of Z are the same, and

$$\bar{Z}_{ij} = Z_{ij}$$

On the other hand, when the noise terms are nonzero, the four estimates are in general different.

Equation (4.13) for Z_{xy} corresponds to the one that Swift (1967) used. He showed that his estimates of Z_{ij} were biased down by random noise on the H signal, but were not affected by random noise on the E signal. Similar arguments for the four stable estimates defined above indicate that in each case, two of them are biased down by random noise on H and are not biased by random noise on E (for example, equations (4.12) and (4.13) for $\bar{Z}_{xy}$) while the other two are biased up by random noise on E and are not biased by random noise on H (for example, equations (4.8) and (4.9) for $\bar{Z}_{xy}$). The effects of the noise are most easily seen for the one dimensional model. For this model, if the incident fields are depolarized so that $\overline{E_x E_y^*}$, $\overline{E_x H_x^*}$, $\overline{E_y H_y^*}$, and $\overline{H_x H_y^*}$ tend to zero, then equations (4.8) and (4.9) for $\bar{Z}_{xy}$ reduce to

$$\bar{Z}_{xy} = \overline{E_x E_x^*} \,/\, \overline{H_y E_x^*} \tag{4.18}$$

Equations (4.12) and (4.13) reduce to

$$\bar{Z}_{xy} = \overline{E_x H_y^*} \,/\, \overline{H_y H_y^*} \tag{4.19}$$

If one assumes that E_x and H_y are given by equations (4.14) and (4.17) and the E_{yn} and H_{xn} are random and independent of the signals and of each other, then the expected values of the power density spectra are

$$\langle \overline{E_x E_x^*} \rangle = \langle \overline{E_{xs} E_{xs}^*} \rangle + \langle \overline{E_{xn} E_{xn}^*} \rangle$$

$$\langle \overline{H_y H_y^*} \rangle = \langle \overline{H_{ys} H_{ys}^*} \rangle + \langle \overline{H_{yn} H_{yn}^*} \rangle$$

$$\langle \overline{E_x H_y^*} \rangle = \langle \overline{H_y E_x^*} \rangle^* = \langle \overline{E_{xs} H_{ys}^*} \rangle$$

Thus, if the spectral estimates contain enough terms in the average so that the cross terms may be neglected (i.e. $\overline{E_{xs} E_{xn}^*}$, etc. are negligible), then equation (4.18) gives

$$\bar{Z}_{xy} = \frac{\overline{E_{xs} E_{xs}^*} + \overline{E_{xn} E_{xn}^*}}{\overline{H_{ys} E_{xs}^*}} = Z_{xy} \left(1 + \frac{\text{E noise power}}{\text{E signal power}}\right) \qquad (4.20)$$

and equation (4.19) gives

$$\bar{Z}_{xy} = \frac{\overline{E_{xs} H_{ys}^*}}{\overline{H_{ys} H_{ys}^*} + \overline{H_{yn} H_{yn}^*}} = Z_{xy} / \left(1 + \frac{\text{H noise power}}{\text{H signal power}}\right) \qquad (4.21)$$

Thus the estimate shown in equation (4.20) is biased to the high side by random noise on E while the one in equation (4.21) is biased to the low side by random noise on H. For similar percentages of random noise on E and H, an average of the various estimates hopefully will be better than any one estimate by itself. Also the scatter between the various estimates should be a good measure of the amount of random noise present.

In practice of course things are not quite this neat because the assumption that the cross terms in the average power estimates are negigible may not be valid. For example, terms of the form $\overline{E_{xn} H_{yn}^*}$ will not be

negligible if the two noises are coherent. Such might be the case for certain types of instrumentation noise or local industrial noise or 60 cps power line noise. Also terms of the form $\overline{E_{xs} E^*_{xn}}$ will not be negligible if the noise is coherent with the signal source. Even if all of the noise terms are random and independent of the signals and of each other, the cross terms may not be negligible if the average power estimates do not have enough degrees of freedom.

V. NOISE PROBLEMS

As was mentioned in the previous chapter, any physical measurement of E or H will include some noise. This noise may be in the form of a constant bias caused by inaccurate calibration of the measuring system, or it may be a nonlinear effect such as would result from drift in the sensitivity of the measuring system. On the other hand many types of noise are independent of the signal. These include such things as amplifier noise, 60 cps power line noise, digitizer round off noise, and, if the signals are recorded in analog form, tape recorder noise. Also, there is always the possibility of having source generated noise. For example, if the incident fields include some plane waves with horizontal wavelengths short compared to a skin depth in the earth, the resulting surface fields may be represented as containing noise.

In any event one can always represent the measured field components as sums of signals and noises as indicated in equations (4.14) through (4.17). The degree to which the noise terms are independent of the signal terms depends entirely upon the source of the noise. In the cases where the noise terms are dependent upon each other or upon the signal terms, the effects of the noise upon the Z estimates vary according to which estimates are used, and according to which signal and noise terms are coherent. No attempt has been made to catalogue all of the various possible combinations of signals and coherent noises.

For the situation where the noise terms are independent of each other and independent of the signals, some interesting results can be shown.

A. General Incoherent Noise

As was mentioned in the previous chapter, the various estimates of the elements of the Z matrix are biased either up by random noise on E or down by random noise on H. This is caused by the fact that the auto power

density spectra are in general biased up by random noise, while the cross power density spectra are not biased. For example, suppose that

$$E_x = E_{xs} + E_{xn} \tag{5.1}$$

and

$$H_y = H_{ys} + H_{yn} \tag{5.2}$$

where

$$\langle E_{xs} E^*_{xn} \rangle = 0 \tag{5.3}$$

$$\langle H_{ys} H^*_{yn} \rangle = 0 \tag{5.4}$$

$$\langle E_{xn} H^*_{yn} \rangle = 0 \tag{5.5}$$

and where the brackets < > denote "expected value of." Clearly, for this situation

$$\langle E_x E^*_x \rangle = \langle E_{xs} E^*_{xs} \rangle + \langle E_{xn} E^*_{xn} \rangle \tag{5.6}$$

$$\langle H_y H^*_y \rangle = \langle H_{ys} H^*_{ys} \rangle + \langle H_{yn} H^*_{yn} \rangle \tag{5.7}$$

and

$$\langle E_x H^*_y \rangle = \langle E_{xs} H^*_{ys} \rangle \tag{5.8}$$

Equation (5.8) implies that the cross power can be estimated to any arbitrary degree of accuracy by measuring the fields for a long enough period of time. On the other hand, equations (5.6) and (5.7) imply that the estimates of the auto powers will be biased regardless of the length of time that the fields are measured.

These ideas lead one to consider an alternate approach to the problem. Suppose that one performs two simultaneous independent measurements of one of the field components, say E_x. If the results are

$$E_{x1} = E_{xs} + E_{xn1} \tag{5.9}$$

and

$$E_{x2} = E_{xs} + E_{xn2} \tag{5.10}$$

where

$$\langle E_{xs} E^*_{xn1} \rangle = 0 \tag{5.11}$$

$$\langle E_{xs} E^*_{xn2} \rangle = 0 \tag{5.12}$$

and

$$\langle E_{xn1} E^*_{xn2} \rangle = 0 \tag{5.13}$$

then

$$\langle E_{x1} E^*_{x2} \rangle = \langle E_{xs} E^*_{xs} \rangle \tag{5.14}$$

Equation (5.14) implies that the E_x auto power density spectrum can be estimated to any arbitrary degree of accuracy from two simultaneous noisy measurements of E_x if the measurements are taken for a long enough period of time and if the noises on the two measurements are independent.

In general, if one has double measurements of either the two tangential components of E or the two tangential components of H, one can obtain estimates of the four elements of the Z matrix that are not biased by random noise.

B. Numerical Noise

At this time consideration will be given to several specific types of numerical noise. The term numerical noise as used here refers to any noise that is artificially injected into the signal when the latter is sampled for numerical processing.

1. Perhaps the most commonly recognized form of numerical noise is that which is usually referred to as aliasing. In accordance with the sampling theorem, if a continuous function which is sampled at a rate f_o has any frequency components greater than the Nyquist or folding frequency (equal to $f_o/2$), these components will be lost from the sampled version of the function.

If any spectral analysis is performed on the sampled function, the lost frequency components will appear folded down into the desired spectrum, and will of course represent noise. Since aliasing is a well documented and well understood phenomenon, nothing more will be said about it here except to note that anyone who deals with magnetotelluric data or any other form of sampled data should be aware of it.

2. The next type of noise that will be considered here is round off error on the analog-to-digital converter. This type of noise arises from the fact that the A-D converter has only a finite number of discrete levels. Typically the signal passes through many levels between sample points. For this reason, the noise can be characterized quite well as a sequence of independent random variables with amplitudes ranging from $\epsilon/2$ to $-\epsilon/2$ with a flat distribution where ϵ is the distance between adjacent levels on the A-D converter. Thus the noise spectrum will be flat. The total noise power for 2m data points will be

$$\text{Total Noise Power} = \frac{1}{\epsilon} \int_{-\epsilon/2}^{\epsilon/2} x^2 dx = \epsilon^2/12 \tag{5.15}$$

Since the spectrum is flat, the average noise power per harmonic would be $\epsilon^2/12m$ for m harmonics. If the signal spectrum were also flat, the average signal power associated with each harmonic would be about $(M\epsilon)^2/12m$ where M is the number of digitizer levels that corresponds to the maximum peak to peak amplitude of the signal. Thus, the signal to noise ratio would be on the order of M^2. In practice, it frequently happens that the signal spectrum is not flat. In this case the expected signal to noise level for a given harmonic is about

$$M^2 \frac{\text{Signal power in harmonic}}{\text{Average signal power per harmonic}}$$

$$= M^2 m \frac{\text{Signal power in harmonic}}{\text{Total signal power}} \tag{5.16}$$

if there is a total of m harmonics.

As an experimental check of the digitizer noise, the following was done. A typical set of actual magnetic field data was selected. It was Fourier transformed, and each harmonic was multiplied by a theoretical Z computed from a typical layered model. The resulting theoretical E was Fourier transformed back to the time domain and digitized; that is, rounded off to a given number of significant bits. The resulting E together with the original H were used to compute an apparent resistivity versus frequency curve. Figure 7 shows the individual harmonics of the true E power density spectrum along with the expected digitizer noise levels for eight and twelve bit digitizing. Figures 8 and 9 show apparent resistivity versus frequency for the individual harmonics for eight and twelve bit digitizing together with the true ρ_a computed from the assumed model. Figures 10 through 12 give the corresponding results when the power density spectra are first averaged in bands of constant Q. From these figures, it is seen that, as expected, the apparent resistivities computed from the individual harmonics have random scatter when the signal power is not sufficiently large compared to the noise. Also as expected, the apparent resistivities computed from the averaged power estimates are biased to the high side by random digitizer noise on E. These experimental results are consistent with the theoretical discussion of digitizer noise.

3. The next type of numerical noise that will be considered is that which results from truncating the time series to a finite length T. Suppose that one of the field components has an amplitude that is described by f(t) for all time. The Fourier transform $F(\omega)$ is then given by

$$F(\omega) = \int_{-\infty}^{\infty} f(t)\ e^{-j\omega t}\ dt \qquad (5.17)$$

It is then desired to approximate $F(\omega)$ by $\overline{F}(n\omega_o)$, a Fourier series representation

of f(t) over some time interval T. Thus

$$\bar{F}(n\omega_o) = \int_{-T/2}^{T/2} f(t)\, e^{-jn\omega_o t}\, dt; \quad n = 0 \pm 1, \pm 2, \ldots \tag{5.18}$$

where $\omega_o = 2\pi/T$.

Notice that

$$\bar{F}(\omega) = \int_{-\infty}^{\infty} f(t)\, d(t)\, e^{-j\omega t}\, dt \tag{5.19}$$

where $d(t) = 1$ for $|t| < T/2$ and $d(t) = 0$ for $|t| > T/2$. Thus, from the convolution theorem

$$\bar{F}(n\omega_o) = \int_{-\infty}^{\infty} F(\omega)\, D(n\omega_o - \omega)\, d\omega \tag{5.20}$$

where

$$D(\omega) = \int_{-\infty}^{\infty} d(t)\, e^{-j\omega t}\, dt$$

$$= \int_{-T/2}^{T/2} e^{-j\omega t}\, dt$$

$$= \frac{2\pi}{\omega_o} \frac{\sin(\pi\omega/\omega_o)}{(\pi\omega/\omega_o)} \tag{5.21}$$

$D(\omega)$ is usually called the spectral window since the observed spectrum $\bar{F}(\omega)$ is equal to the true spectrum $F(\omega)$ convolved with $D(\omega)$.

The spectral window defined by equation (5.21) is actually not very desirable since the side lobes go off only as $1/\omega$. A better window, usually known as the Hanning window is obtained by letting

$$d(t) = \begin{cases} .5 + .5 \cos \omega_o t & ; \quad |t| < T/2 \\ 0 & ; \quad |t| > T/2 \end{cases} \tag{5.22}$$

Then

$$D(\omega) = \int_{-T/2}^{T/2} (.5 + .5 \cos \omega_o t)\ e^{-j\omega t}\ dt$$

$$= \frac{\omega_o^2 \sin(\pi\omega/\omega_o)}{\omega(\omega_o^2 - \omega^2)} \qquad (5.23)$$

The main lobe of this spectral window is twice as wide as the main lobe of the previous one; however, the side lobes go off as $1/\omega^3$. The two windows are compared in figure 13.

One could define windows that have even smaller side lobes; however, they would necessarily have wider main lobes, and as will be seen later, this is not desirable. The Hanning window seems to be an adequate compromise between main lobe width and side lobe height.

One is then faced with the fact that any physical estimate of the power density at a particular frequency ω is necessarily a weighted average of the true power density over a band of frequencies, the weighting function being the spectral window $D(\omega)$. If the impedance function that one is attempting to estimate does not change significantly over the bandwidth defined by $D(\omega)$, then the estimate will not be corrupted by the truncation effects. In practice, however, the impedance does change some so that there will be some truncation noise. The problem is particularly severe if the power density spectra have resonant peaks or other steep slopes. If one is attempting to estimate the power density near the bottom of a steep slope, the contributions from the side lobes of the spectral window may be significant compared to the contribution from the main lobe. This effectively broadens the bandwidth over which the impedance function must not change.

These considerations lead one to inquire into the spectral behavior of the E and H fields used in magnetotelluric surveying. One would hope that the general shape of the spectra of the incident E and H fields might be more

or less independent of time and space coordinates. If this were the case, then the measured total H field, which is close to twice the incident H field, would also be reasonably stationary with respect to time and space coordinates, and hence it could be prewhitened. On the other hand, the total E field is a strong function of the local conductivity structure and hence, although it would be stationary with respect to time, the shape of the spectrum would change from one location to the next as the conductivity structure changes. But still, the surface impedance Z is a well behaved function of frequency and as such one would expect that if the E signals were passed through the same filters as were designed to prewhiten the H signals, the resulting filtered E signals would have a reasonably well behaved spectrum. This, in general, turns out to be the case. Actually, as is indicated by equations (2.16) and (2.27), Z tends on the average to be proportional to the square root of frequency so that an optimum filter for E would differ from the H filter by a factor of $1/\sqrt{\omega}$.

With these ideas in mind, a study was made of the spectra of some actual H field data recorded in central Texas. Figures 14 and 15 give composite plots of H_x and H_y power density spectra obtained from 104 different data samples recorded at five different sites in central Texas. This data was recorded by D. R. Word, and a magnetotelluric interpretation of the data is given by him (Word, 1969). From these figures it is apparent that at least for the locations and times involved here, the general shape of the H power density spectra is fairly well defined. However, there are some definite resonant peaks (for example, around .07 cps and around 2.5 cps) that appear in some of the spectra but are absent from others. These results are consistent with those obtained by other investigators (Hopkins, 1966), (Bleil, 1964). It is believed that if the analog H signals are prewhitened according to the general trends shown in figures 14 and 15, the Hanning window can be used without encountering any side lobe difficulties except perhaps immediately adjacent to the observed resonances.

In order to get an estimate of the effects of truncation upon the individual harmonics of the Fourier spectra, consider the following problem. Assume a one dimensional case with

$$E(\omega) = Z(\omega)\ H(\omega) .$$

Suppose that the H signal is prewhitened with a filter that has a response $F_H(\omega)$, and the the E signal is passed through a filter whose response is $F_E(\omega)$ which may or may not be the same as $F_H(\omega)$. Assume that the outputs of these filters are $H_o(\omega)$ and $E_o(\omega)$ respectively, so that

$$Z(\omega) = \frac{E(\omega)}{H(\omega)} = \frac{E_o(\omega)}{H_o(\omega)} \cdot \frac{F_H(\omega)}{F_E(\omega)} \qquad (5.24)$$

Then define

$$G(\omega) = \frac{E_o(\omega)}{H_o(\omega)} = \frac{Z(\omega)\, F_E(\omega)}{F_H(\omega)} \qquad (5.25)$$

Thus $G(\omega)$ is the ratio of the prewhitened electric and magnetic field signals and will be equal to $Z(\omega)$ if the two prewhitening filters are the same. If the prewhitened signals are then sampled and a Fourier series analysis is performed on each, the results will be

$$\overline{H}(n\omega_o) = \int_{-\infty}^{\infty} H_o(n\omega_o - \omega)\ D(\omega)\ d\omega \qquad (5.26)$$

and

$$\overline{E}(n\omega_o) = \int_{-\infty}^{\infty} E_o(n\omega_o - \omega)\ D(\omega)\ d\omega$$

$$= \int_{-\infty}^{\infty} H_o(n\omega_o - \omega)\ G(n\omega_o - \omega)\ D(\omega)\ d\omega \qquad (5.27)$$

where $D(\omega)$ is again the spectral window used. If G were constant over the

width of the window, then one would have

$$\overline{E}(n\omega_o) = G(n\omega_o) \int_{-\infty}^{\infty} H_o(n\omega_o - \omega)\, D(\omega)\, d\omega$$

$$= G(n\omega_o)\, \overline{H}(n\omega_o) \tag{5.28}$$

the desired result. In practice, however, G usually varies some. Suppose that in the neighborhood of $n\omega_o$, G can be represented by the first two terms of a Taylor series expansion. Thus

$$G(\lambda) = G(n\omega_o) + (\lambda - n\omega_o)\, G'(n\omega_o) \tag{5.29}$$

where

$$G'(\omega) = \frac{dG(\omega)}{d\omega} \tag{5.30}$$

If one lets $\lambda = n\omega_o - \omega$, equation (5.29) gives

$$G(n\omega_o - \omega) = G(n\omega_o) - \omega G'(n\omega_o) \tag{5.31}$$

Putting this into equation (5.27) gives

$$\overline{E}(n\omega_o) = \int_{-\infty}^{\infty} H_o(n\omega_o - \omega)\, [G(n\omega_o) - \omega G'(n\omega_o)]\, D(\omega)\, d\omega$$

$$= G(n\omega_o)\, \overline{H}(n\omega_o) - G'(n\omega_o) \int_{-\infty}^{\infty} H_o(n\omega_o - \omega)\, D(\omega)\, \omega d\omega \tag{5.32}$$

If one then defines

$$\overline{G}(n\omega_o) = \overline{E}(n\omega_o) / \overline{H}(n\omega_o) \tag{5.33}$$

and

$$\text{error} = [\overline{G}(n\omega_o) - G(n\omega_o)] / G(n\omega_o) \tag{5.34}$$

then from equation (5.32)

$$\bar{G}(n\omega_o) = G(n\omega_o) - G'(n\omega_o) \frac{\int_{-\infty}^{\infty} H_o(n\omega_o - \omega)\, D(\omega)\, \omega d\omega}{\int_{-\infty}^{\infty} H_o(n\omega_o - \omega)\, D(\omega)\, d\omega} \tag{5.35}$$

and

$$\text{error} = -\frac{G'(n\omega_o)}{G(n\omega_o)} \frac{\int_{-\infty}^{\infty} H_o(n\omega_o - \omega)\, D(\omega)\, \omega d\omega}{\int_{-\infty}^{\infty} H_o(n\omega_o - \omega)\, D(\omega)\, d\omega} \tag{5.36}$$

Assume now that the integrals in equation (5.36) can be approximated by summations of the form

$$\overline{H(n\omega_o)} = \int_{-\infty}^{\infty} H_o(n\omega_o - \omega)\, D(\omega)\, d\omega$$

$$= \sum_{i=-m}^{m} H_{on,i} D_i \tag{5.37}$$

where

$$H_{on,i} = H_o(n\omega_o - i\Delta\omega) \tag{5.38}$$

and

$$\sum_{i=-m}^{m} D_i = 1 \tag{5.39}$$

Then

$$\bar{W}(n\omega_o) = \int_{-\infty}^{\infty} H_o(n\omega_o - \omega)\, D(\omega)\, \omega d\omega$$

$$= \sum_{i=-m}^{m} H_{on,i} D_i \frac{i\Omega}{m} \tag{5.40}$$

where Ω is the maximum value of ω contributing to the integral. That is, $\omega = \Omega$ corresponds to $i = m$.

Assume that for any fixed n, $H_{on,i}$ are a sequence of $2m+1$ independent complex random variables whose components have normal distributions and zero means. Also assume that the original H signal was prewhitened enough so that over any given band, the expected value of the power density is constant. That is,

$$<H_{on,i} H^*_{on,i}> = \sigma_n^2 \; ; \; i = 0, \pm 1, \pm 2, \ldots \pm m \tag{5.41}$$

Since $H_{on,i}$ are assumed to be independent and have zero means,

$$<H_{on,i}> = 0 \tag{5.42}$$

and

$$<H_{on,i} H^*_{on,j}> = 0 \; ; \; i \neq j \tag{5.43}$$

Since $H_{on,i}$ are complex normal random variables, $\bar{H}(n\omega_o)$ and $\bar{W}(n\omega_o)$, which are linear combinations of $H_{on,i}$, must also be complex normal random variables. Consider the statistics of $\bar{H}(n\omega_o)$ and $\bar{W}(n\omega_o)$.

$$<\bar{H}(n\omega_o)> = <\sum_{i=-m}^{m} H_{on,i} D_i>$$

$$= \sum_{i=-m}^{m} <H_{on,i}> D_i$$

$$= 0 \tag{5.44}$$

$$<\bar{H}(n\omega_o)\bar{H}^*(n\omega_o)> = <\left(\sum_{i=-m}^{m} H_{on,i} D_i\right)\left(\sum_{j=-m}^{m} H^*_{on,j} D_j\right)>$$

(Eq. cont'd on next page)

$$= \sum_{i=-m}^{m} \sum_{j=-m}^{m} D_i D_j \langle H_{on,i} H^*_{on,j} \rangle$$

$$= \sum_{i=-m}^{m} D_i^2 \langle H_{on,i} H^*_{on,i} \rangle$$

$$= \sigma_n^2 \sum_{i=-m}^{m} D_i^2 \qquad (5.45)$$

$$\langle \overline{W}(n\omega_o) \rangle = \langle \sum_{i=-m}^{m} H_{on,i} D_i \frac{i\Omega}{m} \rangle$$

$$= \frac{\Omega}{m} \sum_{i=-m}^{m} \langle H_{on,i} \rangle D_i \; i$$

$$= 0 \qquad (5.46)$$

$$\langle \overline{W}(n\omega_o) \overline{W}^*(n\omega_o) \rangle = \langle \left(\sum_{i=-m}^{m} H_{on,i} D_i \frac{i\Omega}{m} \right) \left(\sum_{j=-m}^{m} H^*_{on,j} D_j \frac{j\Omega}{m} \right) \rangle$$

$$= \left(\frac{\Omega}{m} \right)^2 \sum_{i=-m}^{m} \sum_{j=-m}^{m} D_i D_j \; ij \langle H_{on,i} H^*_{on,j} \rangle$$

$$= \left(\frac{\Omega}{m} \right)^2 \sigma_n^2 \sum_{i=-m}^{m} i^2 D_i^2 \qquad (5.47)$$

$$\langle \overline{H}(n\omega_o) \overline{W}^*(n\omega_o) \rangle = \langle \left(\sum_{i=-m}^{m} H_{on,i} D_i \right) \left(\sum_{j=-m}^{m} H^*_{on,j} D_j \frac{j\Omega}{m} \right) \rangle$$

(Eq. cont'd.)

$$= \frac{\Omega}{m} \sum_{i=-m}^{m} \sum_{j=-m}^{m} D_i D_j \langle H_{on,i} H^*_{on,j} \rangle$$

$$= \frac{\Omega}{m} \sigma_n^2 \sum_{i=-m}^{m} i D_i^2 \qquad (5.48)$$

If the spectral window $D(\omega)$ is an even function of ω, then $D_i^2 = D_{-i}^2$ and

$$\sum_{i=-m}^{m} i D_i^2 = 0 \qquad (5.49)$$

so that

$$\langle \bar{H}(n\omega_o) \overline{W^*}(n\omega_o) \rangle = 0 \qquad (5.50)$$

Thus, $\bar{H}(n\omega_o)$ and $\overline{W}(n\omega_o)$ are independent complex normal random variables with zero means and with variances defined by equations (5.45) and (5.47).

A standard exercise in random variable theory indicates that if two random variables X and Y are normal and independent with zero means and equal variances, then the function

$$V = \sqrt{X^2 + Y^2}$$

has a Rayleigh distribution (see for example, Papoulis, 1965). Since $\bar{H}(n\omega_o)$ and $\overline{W}(n\omega_o)$ are complex normal random variables with zero means, their real and imaginary parts satisfy the conditions of the above exercise. Thus $|\bar{H}(n\omega_o)|$ and $|\overline{W}(n\omega_o)|$ must have Rayleigh distributions.

Another standard exercise in random variable theory indicates that if

$$V = X/Y$$

then the distribution of V is given by

$$F_V(v) = \int_0^{\infty} \int_{-\infty}^{yv} f_{XY}(x,y)\, dx\, dy + \int_{-\infty}^{0} \int_{yv}^{\infty} f_{XY}(x,y)\, dx\, dy \qquad (5.51)$$

where $f_{XY}(x,y)$ is the joint density of X and Y (see Papoulis, 1965). If X and Y are independent and have Rayleigh distributions then equation (5.51) becomes

$$F_V(v) = \int_0^\infty \int_0^{yv} f_X(x)\, f_Y(y)\, dx\, dy$$

$$= \int_0^\infty f_Y(y)\, F_X(yv)\, dy$$

$$= \int_0^\infty \frac{y}{\alpha_y^2}\, e^{-y^2/2\alpha_y^2} \left[1 - e^{-(yv)^2/2\alpha_x^2}\right] dy$$

$$= 1 - \frac{1}{1 + \left(\frac{v\alpha_y}{\alpha_x}\right)^2} \qquad (5.52)$$

where $\alpha_x^2 = \langle X^2 \rangle$ and $\alpha_y^2 = \langle Y^2 \rangle$.

Now recall that $|\overline{H}(n\omega_o)|$ and $|\overline{W}(n\omega_o)|$ have Rayleigh distributions. From equations (5.45) and (5.47)

$$\langle |\overline{H}(n\omega_o)|^2 \rangle = \sigma_n^2 \sum_{i=-m}^{m} D_i^2 \qquad (5.53)$$

and

$$\langle |\overline{W}(n\omega_o)|^2 \rangle = \left(\frac{\Omega}{m}\right)^2 \sigma_n^2 \sum_{i=-m}^{m} i^2 D_i^2 \qquad (5.54)$$

Also, from equations (5.36), (5.37), and (5.40),

$$|\text{error}| = \left| \frac{G(n\omega_o)\, \overline{W}(n\omega_o)}{G'(n\omega_o)\, \overline{H}(n\omega_o)} \right| \qquad (5.55)$$

Recall that $F_V(v)$ is by definition the probability that $V \leq v$. Thus, equations

(5.52) through (5.55) combine to give

$$P\{|\text{error}| \le \epsilon\} = 1 - \frac{1}{1 + (\epsilon \left| \frac{G(n\omega_o)}{G'(n\omega_o)} \right| K)^2} \tag{5.56}$$

where

$$K^2 = \frac{\sum_{i=-m}^{m} D_i^2}{(\frac{\Omega}{m})^2 \sum_{i=-m}^{m} i^2 D_i^2} \tag{5.57}$$

and where $P\{X\}$ denotes the probability, then X occurs. Recall from equations (5.37) through (5.40) that the summations arose as approximations to integrals. If one now lets $m \to \infty$ and passes back to the integral formulation, equation (5.57) becomes

$$K^2 = \frac{\int_{-\infty}^{\infty} D^2(\omega)\, d\omega}{\int_{-\infty}^{\infty} \omega^2 D^2(\omega)\, d\omega} \tag{5.58}$$

Since $D(\omega)$ has been assumed to be an even function of ω, and since

$$P\{|\text{error}| > \epsilon\} = 1 - P\{|\text{error}| \le \epsilon\}$$

one has from equation (5.56)

$$P\{|\text{error}| > \epsilon\} = \frac{1}{1 + \epsilon^2 \left| \frac{G(n\omega_o)}{G'(n\omega_o)} \right|^2 \frac{\int_0^{\infty} D(\omega)^2\, d\omega}{\int_0^{\infty} \omega^2 D(\omega)^2 d\omega}} \tag{5.59}$$

If $D(\omega)$ is a block window of width BW, equation (5.59) becomes

$$P\{|\text{error}| > \epsilon\} = \frac{1}{1 + \frac{12\epsilon^2}{(BW)^2}\left|\frac{G(n\omega_o)}{G'(n\omega_o)}\right|^2}$$

or

$$P\{|\text{error}| > \epsilon\} = \frac{1}{1 + 12\epsilon^2\left|\frac{G(n\omega_o)}{\Delta G(n\omega_o)}\right|^2} \tag{5.60}$$

where $\Delta G(n\omega_o) = G'(n\omega_o) \cdot BW$ = change in $G(\omega)$ over a band of width BW around $n\omega_o$. Similarly, for the Hanning window with

$$D(\omega) = \text{Sin}\,\frac{\pi\omega}{\omega_o}\left(\frac{\omega_o^2}{\omega(\omega_o^2 - \omega^2)}\right) \tag{5.61}$$

one obtains

$$P\{|\text{error}| > \epsilon\} = \frac{1}{1 + \frac{3\epsilon^2}{\omega_o^2}\left|\frac{G(n\omega_o)}{G'(n\omega_o)}\right|^2} \tag{5.62}$$

It has been observed that for one dimensional models

$$-\frac{1}{2} \le \frac{d\log\sigma_a(\omega)}{d\log\omega} \le \frac{1}{2} \tag{5.63}$$

Now if one uses the same prewhitening filters on E and H

$$|G(\omega)| = |Z(\omega)| = \sqrt{\omega\mu/\sigma_a(\omega)} \tag{5.64}$$

and it follows that

$$\frac{1}{4} \le \frac{d\log|G(\omega)|}{d\log\omega} \le \frac{3}{4} \tag{5.65}$$

or

$$\frac{d\log|G(\omega)|}{d\log\omega} = \frac{\omega}{|G(\omega)|}\frac{d|G(\omega)|}{d\omega} \le \frac{3}{4} \tag{5.66}$$

or, for the worst case

$$\left| \frac{G(n\omega_o)}{G'(n\omega_o)} \right| = \frac{4n\omega_o}{3} \tag{5.67}$$

Thus, for this case equation (5.62) becomes

$$P\{|\text{error}| > \epsilon\} = \frac{1}{1 + \frac{16}{3} n^2 \epsilon^2} \tag{5.68}$$

Equation (5.68) indicates that, as expected, the probability of the error being greater than ϵ goes down as ϵ increases. Also, as expected, the probable error decreases as n, the harmonic number, increases. The latter result is expected since $|\Delta G(\omega)/G(\omega)|$ should be proportional to the percentage bandwidth of the window, which in turn is inversely proportional to the harmonic number. The results of equation (5.68) are summarized in figure 16.

It is doubtful that the results shown in figure 16 are useful quantitatively because of the assumptions made about the form of $H_o(\omega)$, the prewhitened magnetic field signal. In particular, it was assumed that $\sigma^2_{H_o} = \langle H_o(\omega)\, H_o(\omega)^* \rangle$ is independent of frequency. In practice this is not attainable since, as noted earlier, magnetotelluric signals are not really stationary.

In order to get some type of estimate of the effects of truncation upon realistic data, the following experiment was performed. A typical set of actual magnetic field data was selected. It was Fourier transformed using the Hanning window, and each harmonic was multiplied by a theoretical Z computed from a typical layered model. The resulting theoretical E was Fourier transformed back to the time domain. This E, together with the original H, were truncated to some fraction of the original length. The resulting truncated E and H signals were Fourier transformed, and apparent resistivities were computed from each harmonic. These apparent resistivities were then compared with the true apparent resistivities for the assumed model. This experiment

was repeated for several different models with several different original data lengths and several different truncated data lengths. The results showed a very definite trend. In each case, the apparent resistivities computed from the first eight to ten harmonics were significantly in error. The higher harmonics showed very little error. The amount of error on the first few harmonics depended significantly upon how white the spectra were; the whiter spectra had less error. Figures 17 and 18 show the results of a typical run. Figure 17 shows the individual harmonics of the spectrum of a truncated H signal. Figure 18 shows the corresponding apparent resistivities along with the true apparent resistivity curve for the assumed model.

These considerations lead one to believe that the first few harmonics of a Fourier spectrum of typical magnetotelluric data are likely to be corrupted considerably by truncation error.

VI. CONCLUSION

The methods of analysis discussed in the foregoing chapters have been implemented in a digital computer program constructed by the author for use on the CDC 6600 computer at The University of Texas Computation Center. This program estimates the power density spectra of sampled E and H signals by computing the Fourier transforms of the sampled data using the Cooley-Tukey algorithm, and averaging the resulting auto and cross powers in frequency bands of constant percentage bandwidth as discussed in Chapter IV, Section B.4. The Hanning window discussed in Chapter V, Section B.3 is used for the Fourier transforms. The elements of the Z matrix are then estimated from the power density spectra using the techniques described in Chapter IV, Section C. The principal axes are then determined in accordance with the discussion in Chapter III, Sections C and D. Also the approximate strike direction is determined from the vertical magnetic field as discussed in Chapter III, Section E. As diagnostics, the tensor coherency mentioned in Chapter IV, Section C, and the two-dimensionality parameters mentioned in Chapter III, Section D, are determined.

This program has been used extensively for analysis of magnetotelluric data recorded in central Texas by Darrell Word. Samples of the results are given by Word (1969). For most of the data analyzed using this program, the resulting surface impedance estimates have been consistent and repeatable. In areas where the geology is reasonably one dimensional, these surface impedances have been successfully interpreted in terms of horizontally layered models. The resulting resistivity profiles have agreed quite well with independent observations such as resistivity well logs in cases where the latter have been available.

In areas where the geology is more complex, particularly where it is highly three dimensional, interpretation has not been so successful. However, even here the surface impedance estimates have been fairly repeatable. Thus,

it is believed that now, perhaps for the first time, the surface impedances have been measured more accurately than they can at present be interpreted. For this reason, it is believed that future contributions to the science of magnetotellurics must come in the area of interpretation.

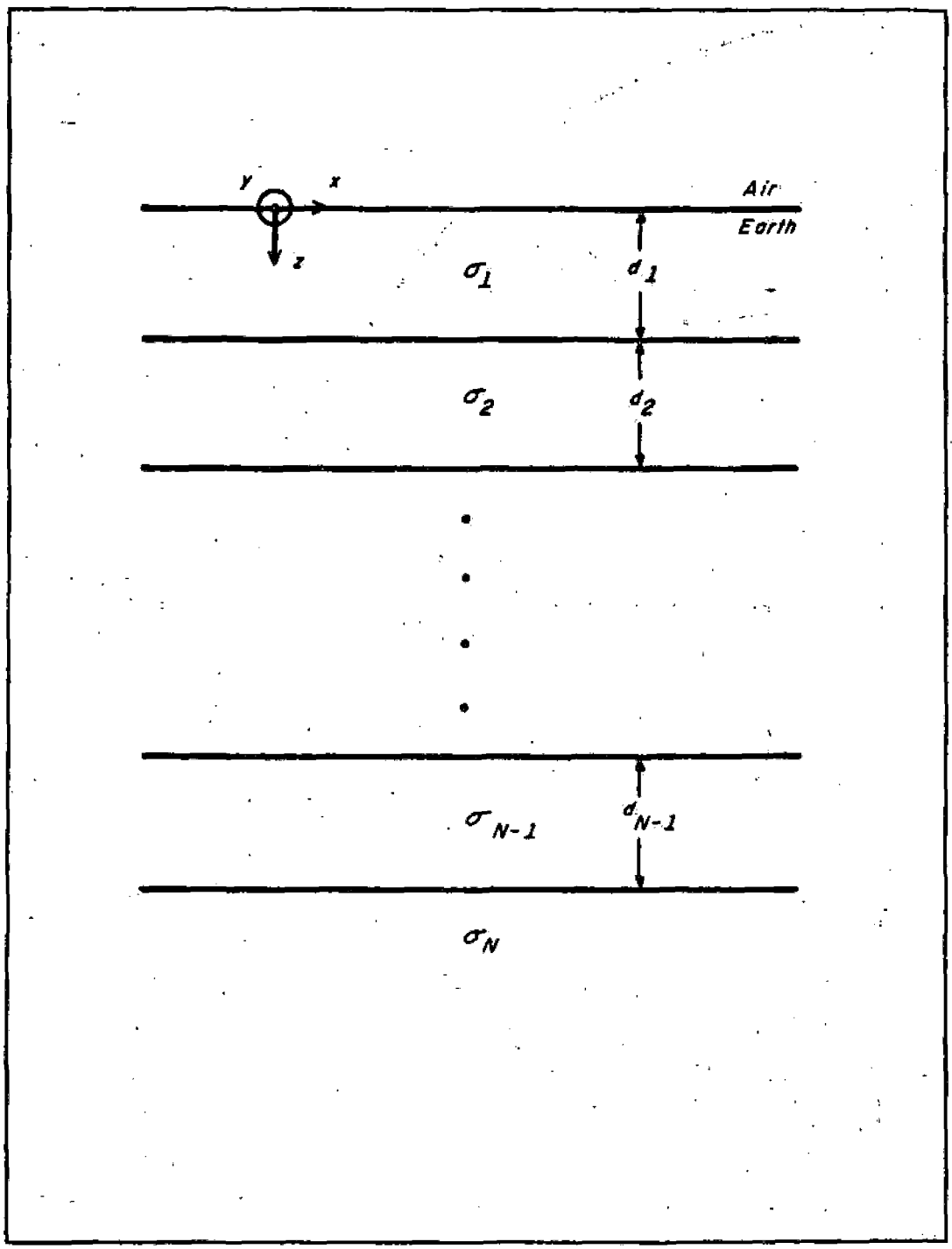

Fig. 1 Description of N Layer Model

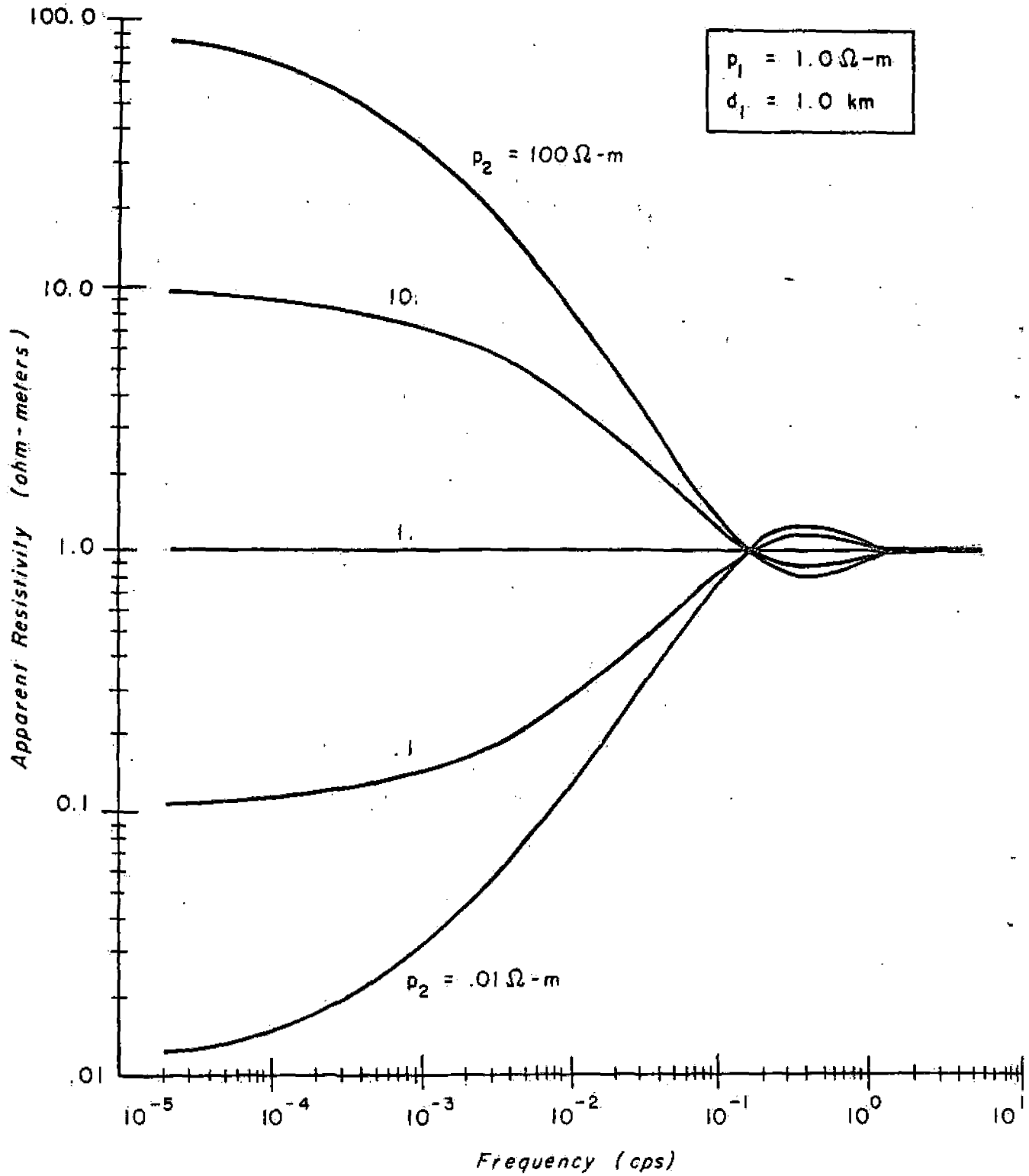

Fig. 2 Sample Two Layer Apparent Resistivity Curves

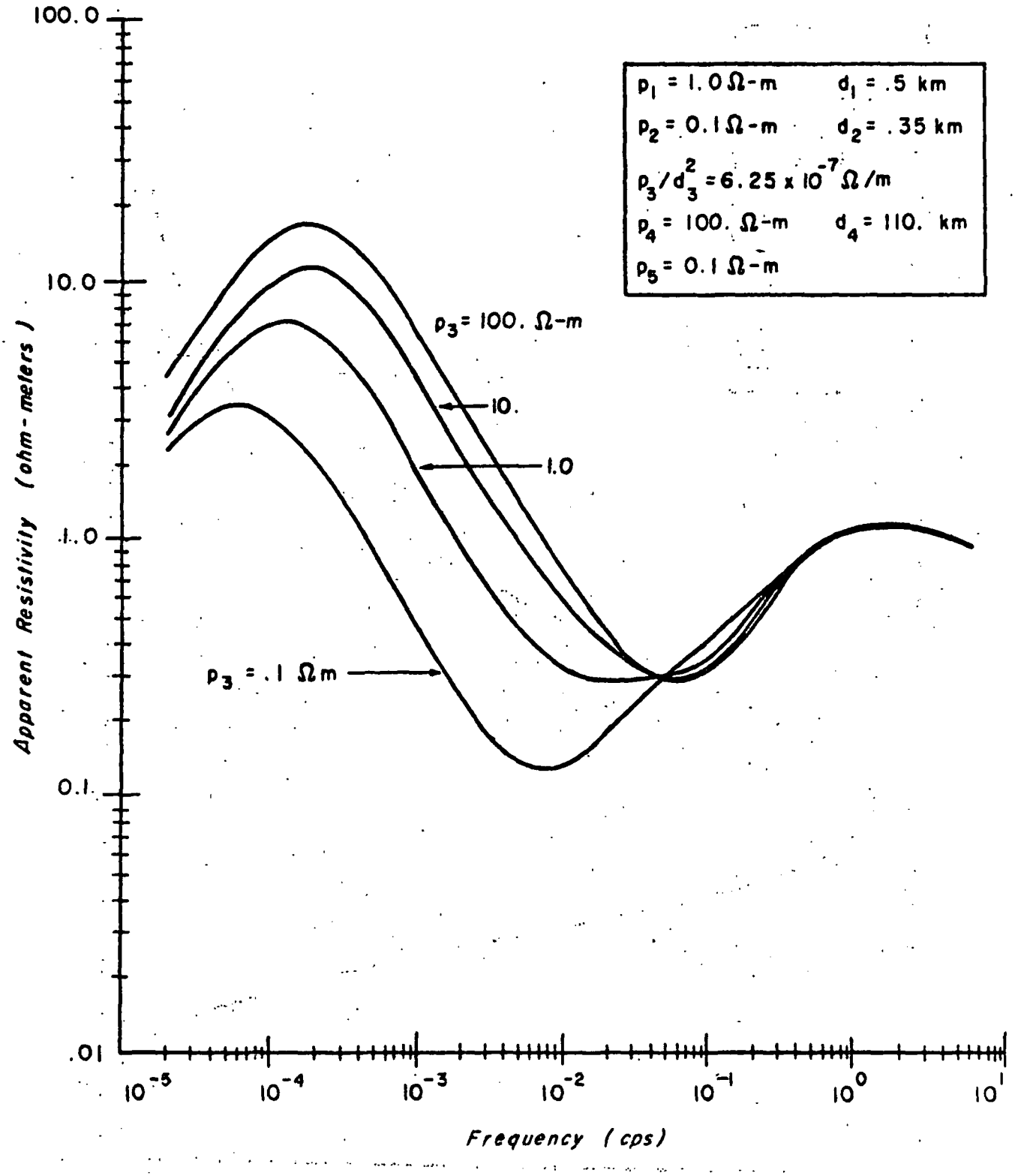

Fig. 3 Sample Five Layer Apparent Resistivity Curves

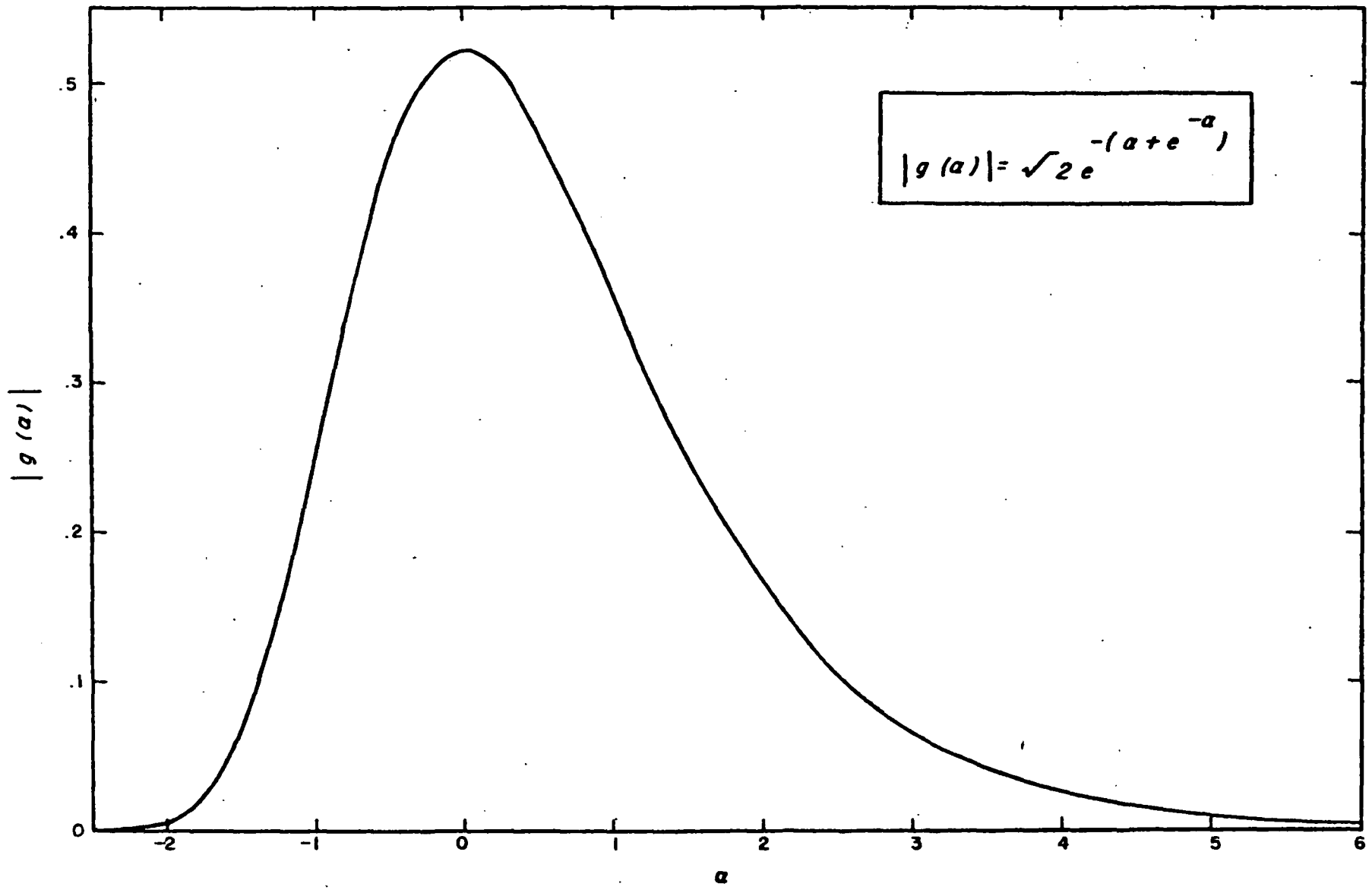

Fig. 4. Convolver for Linearized One Dimensional Problem

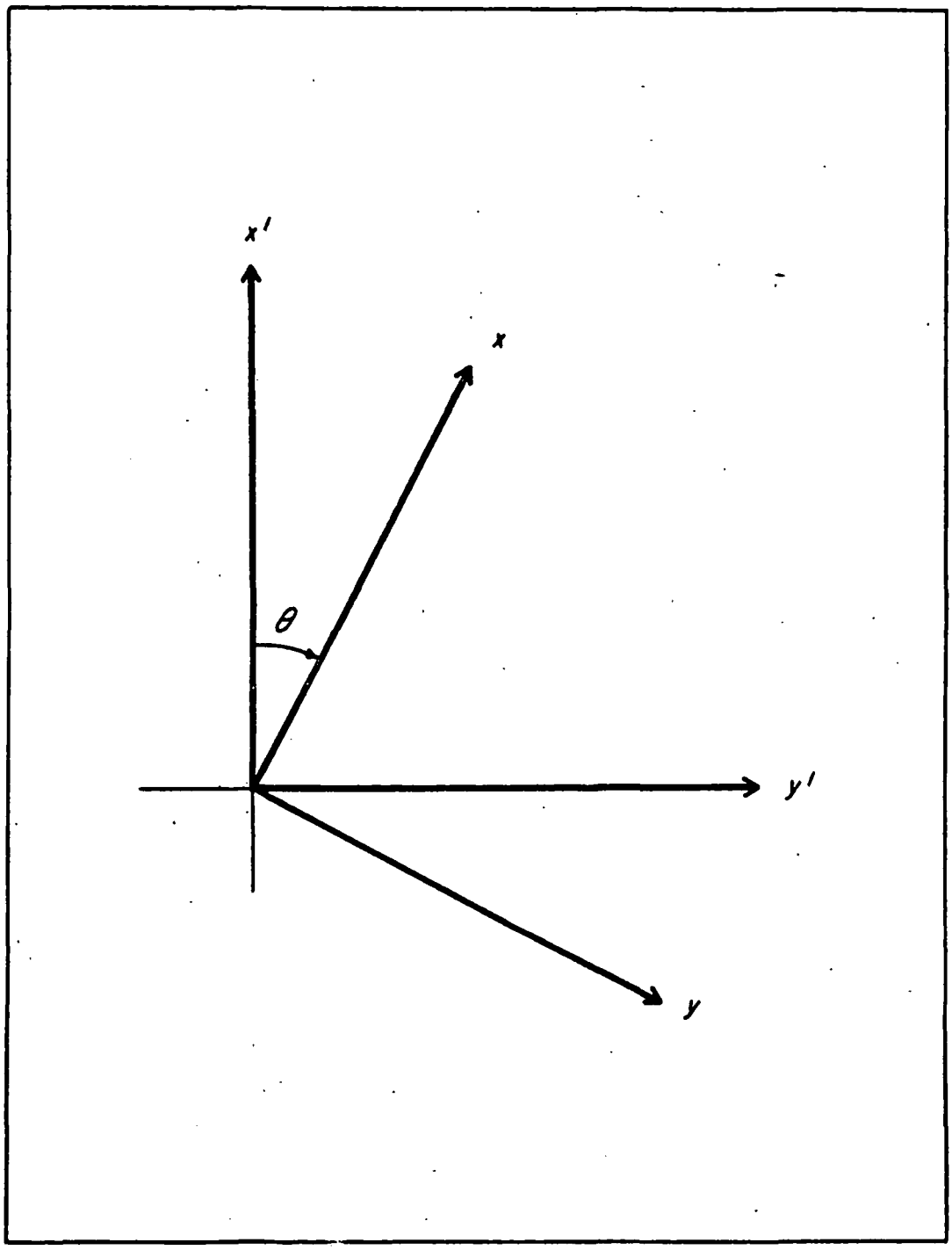

Fig. 5 Relative Orientation of x'-y' and x-y Coordinate Systems

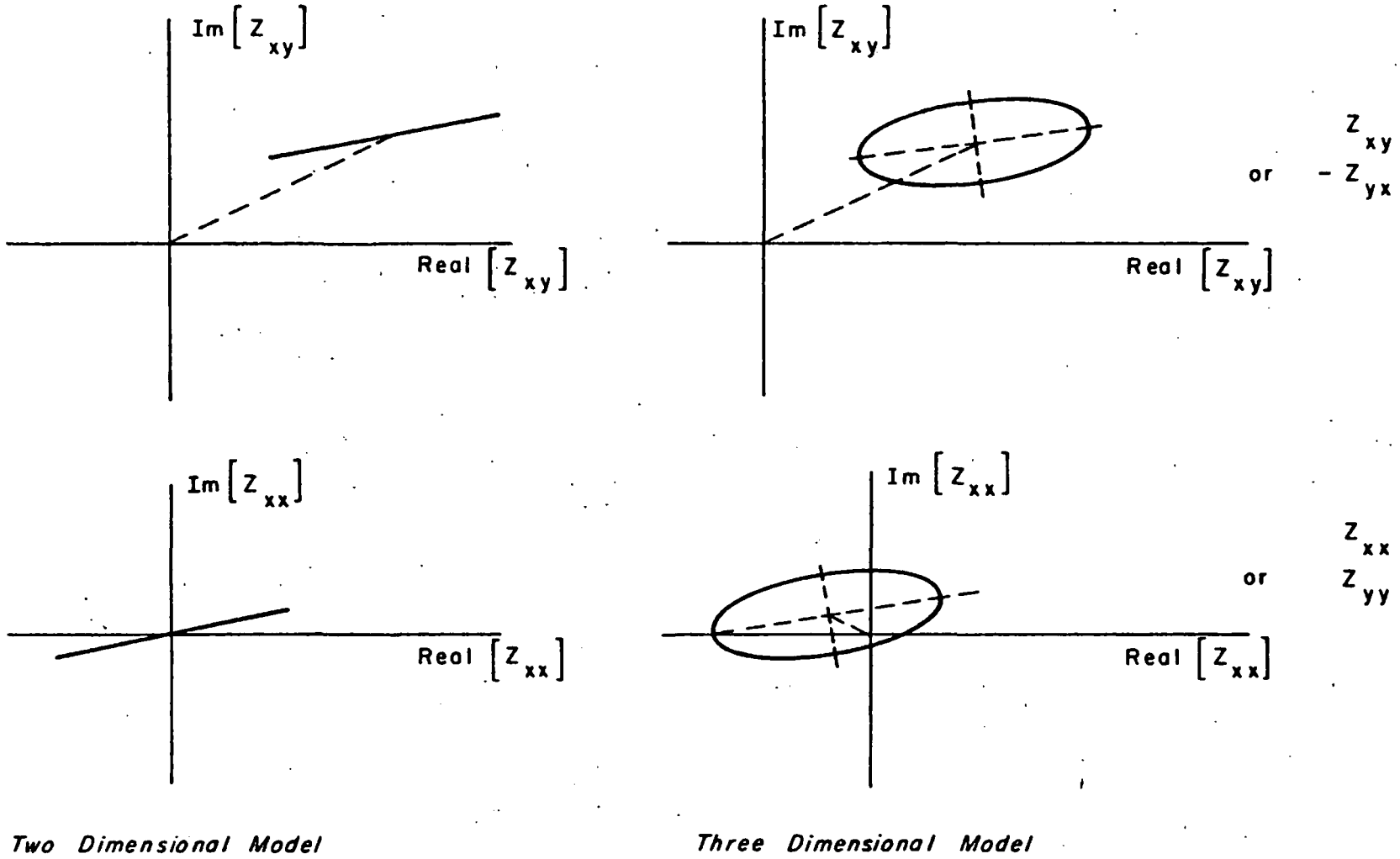

Fig. 6 Locii of Z_{ij} in the Complex Plane as the Measuring Axes are Rotated

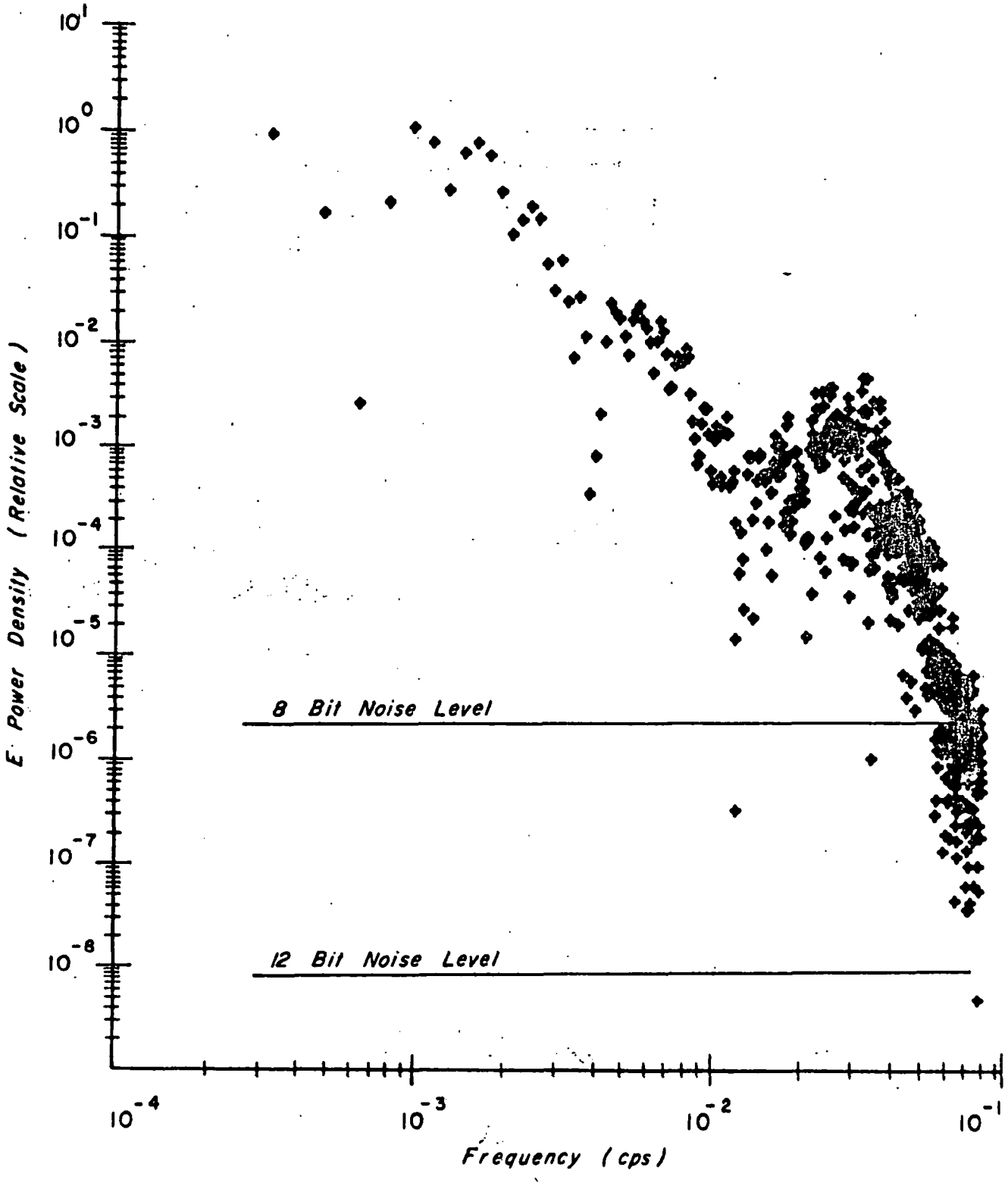

Fig. 7 Individual Harmonics of E Power Density Spectrum for Digitizer Noise Test with Expected Noise Levels for Eight and Twelve Bit Digitizing

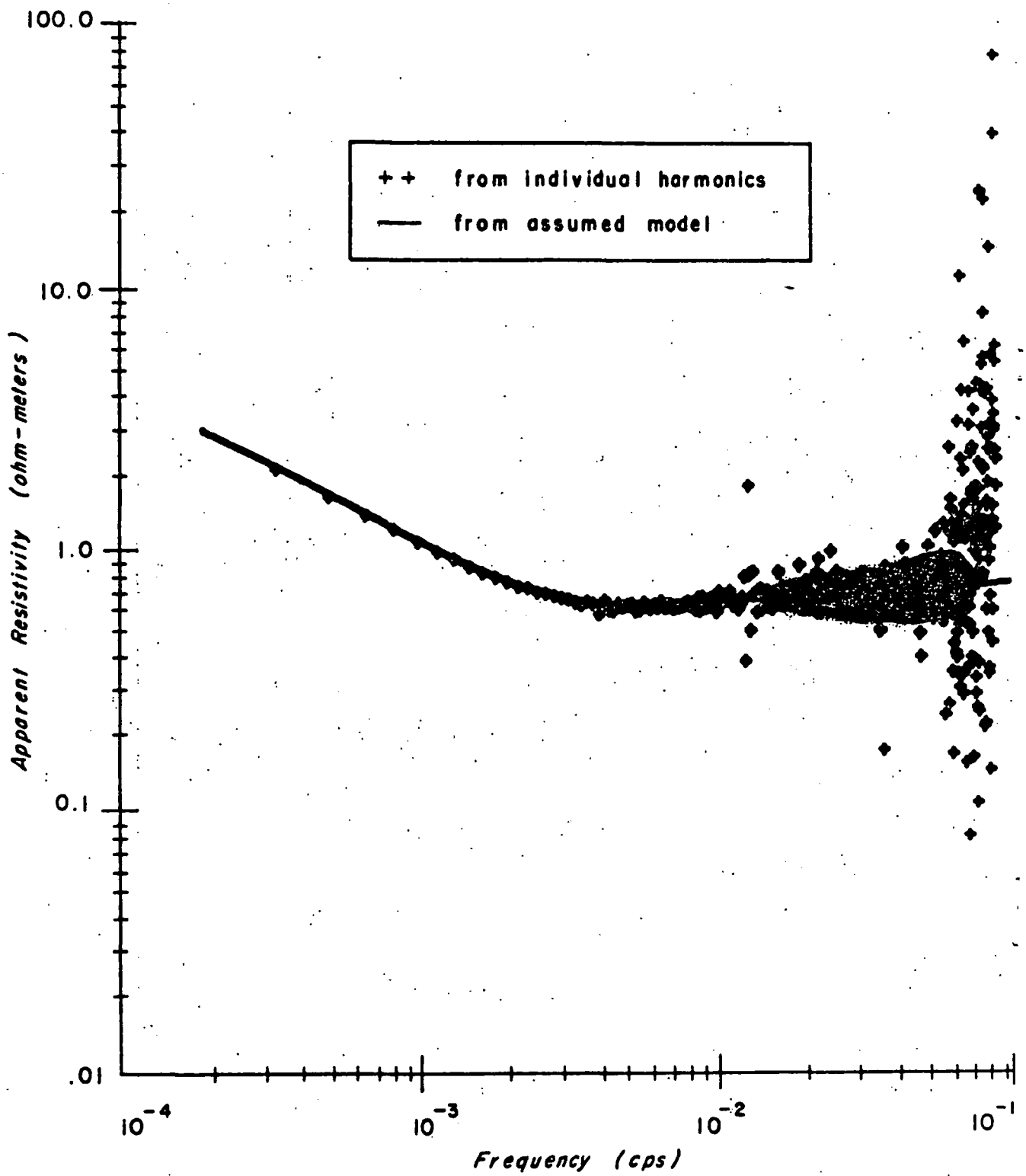

Fig. 8 Apparent Resistivity versus Frequency for Individual Harmonics for Eight Bit Digitizing

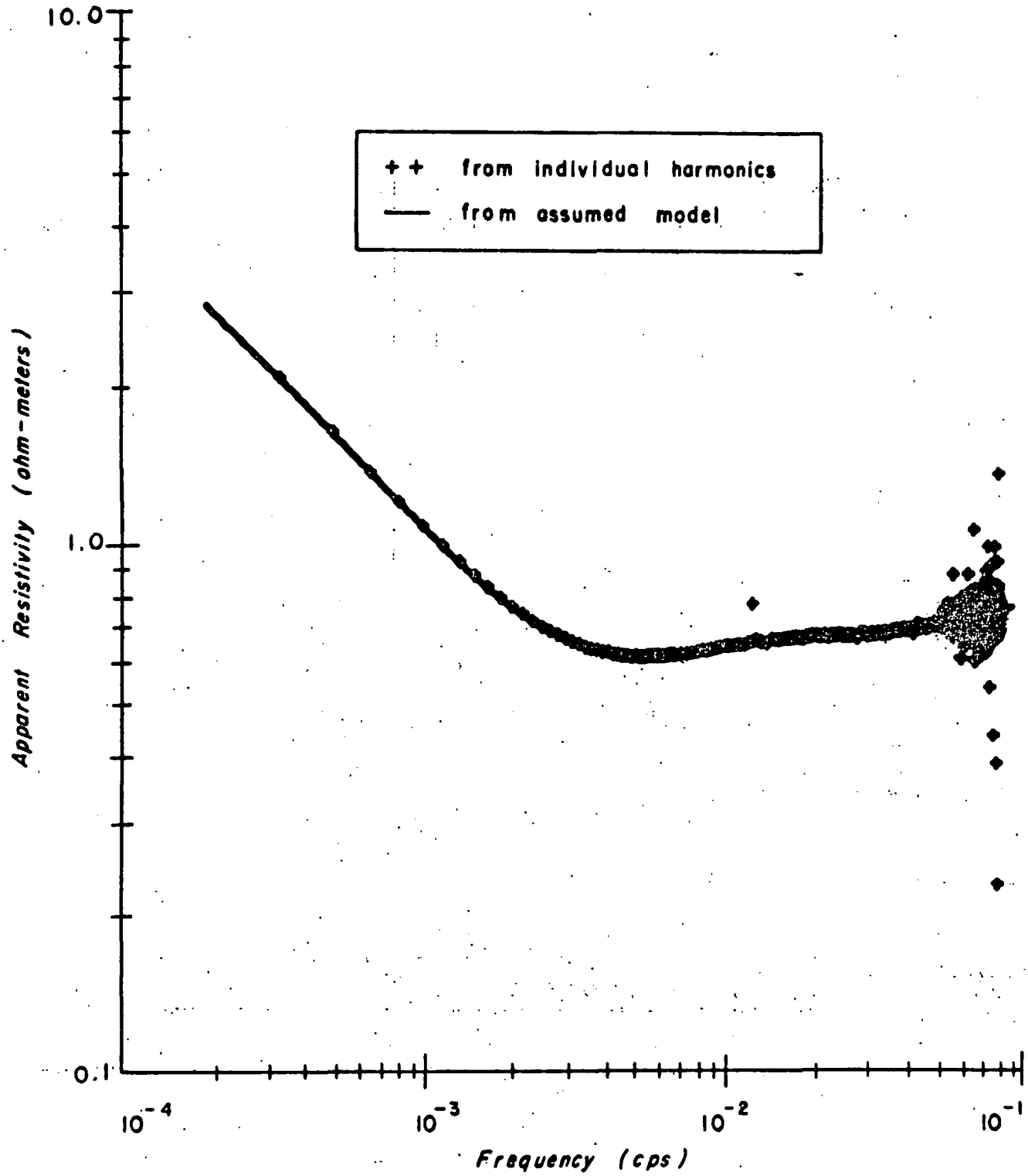

Fig. 9 Apparent Resistivity versus Frequency for Individual Harmonics for Twelve Bit Digitizing

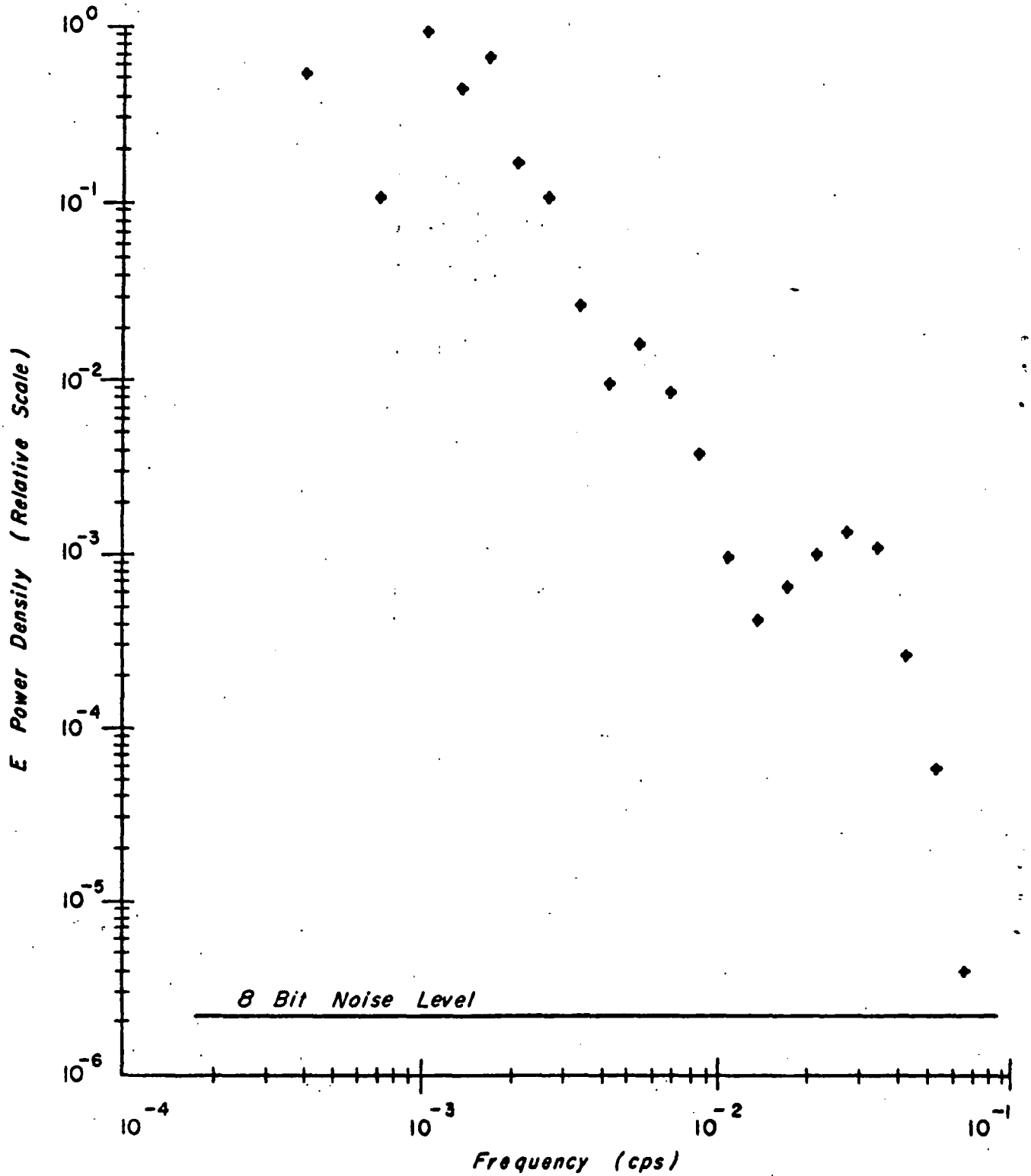

Fig. 10 Average E Power Density Spectrum for Digitizer Noise Test with Expected Noise Level for Eight Bit Digitizing

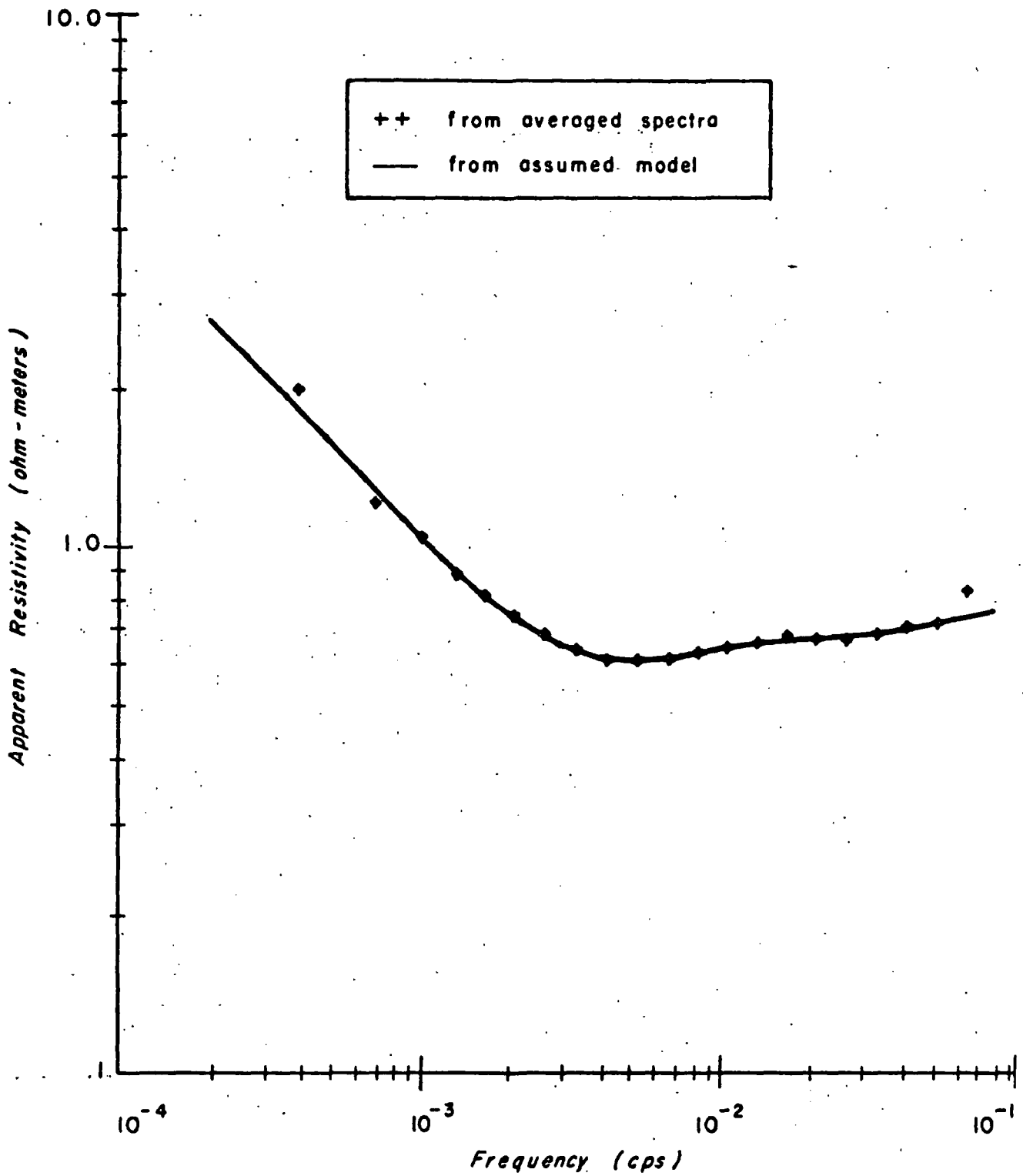

Fig. 11 Apparent Resistivity versus Frequency for Average Power Density Spectra with Eight Bit Digitizing

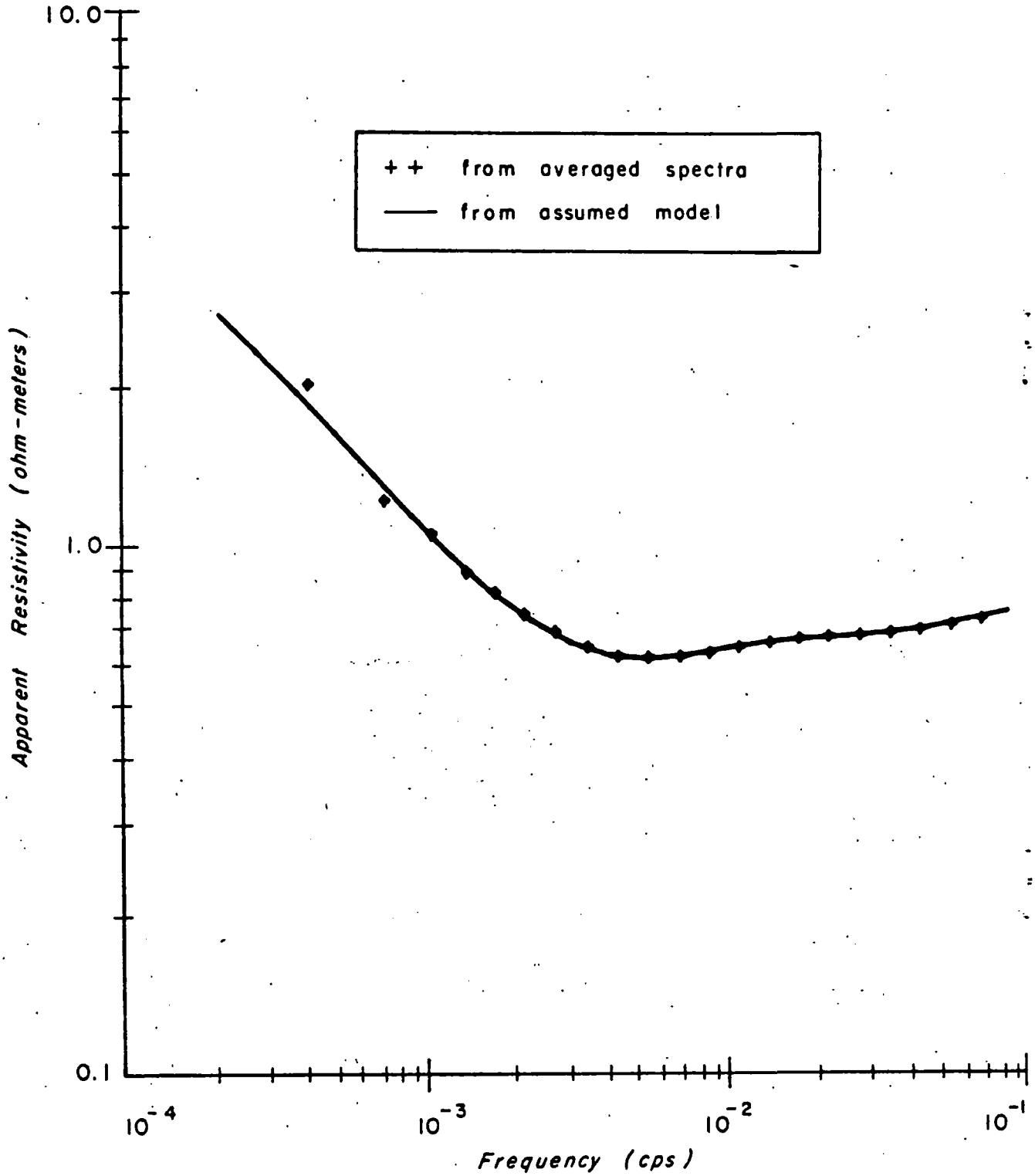

Fig. 12 Apparent Resistivity versus Frequency for Average Power Density Spectra with Twelve Bit Digitizing

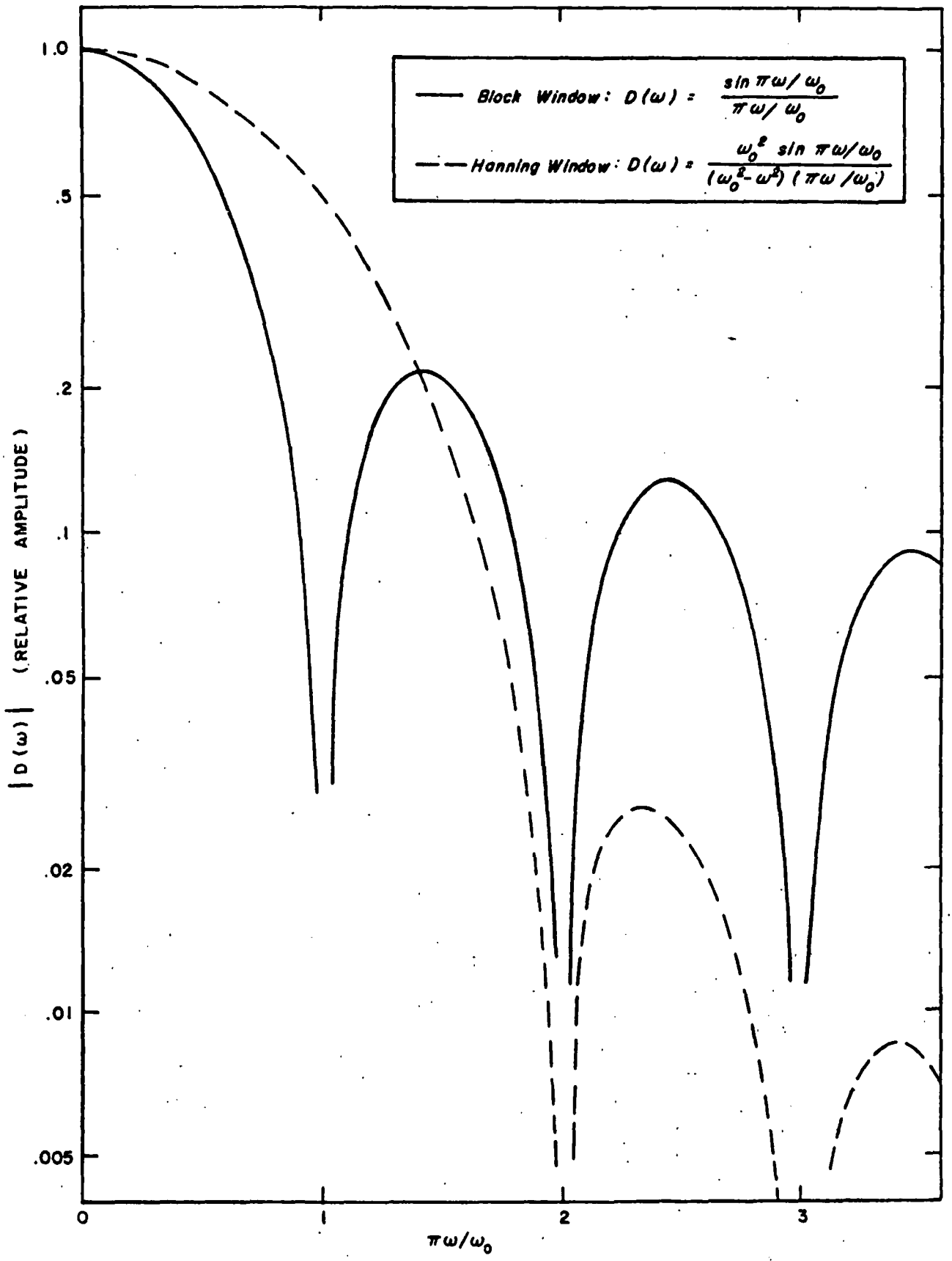

Fig. 13 Comparison of the Block and Hanning Spectral Windows

Fig. 14 H_x Power Density Spectra for 104 Different Data Samples Recorded in Central Texas

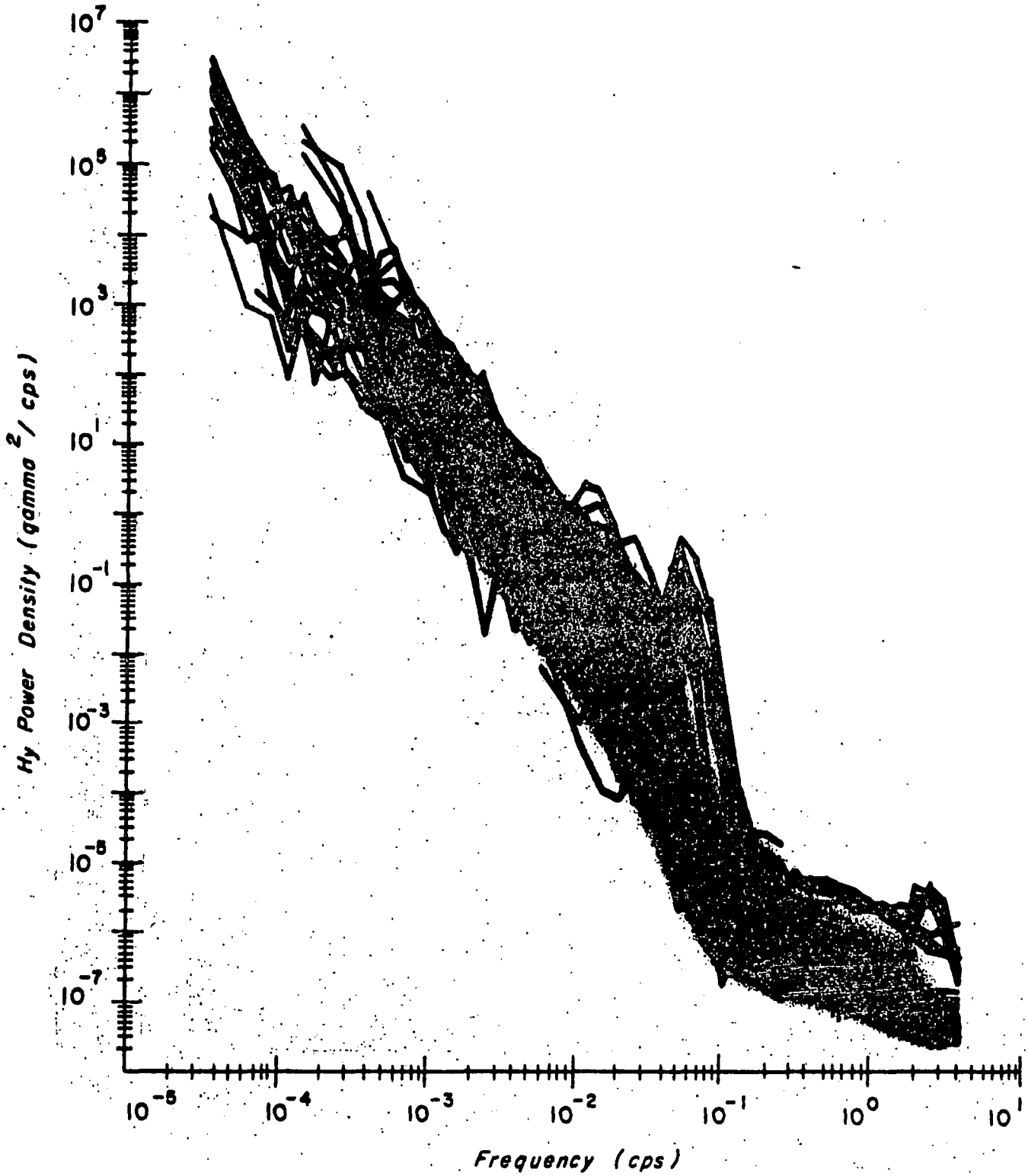

Fig. 15 H_y Power Density Spectra for 104 Different Data Samples Recorded in Central Texas

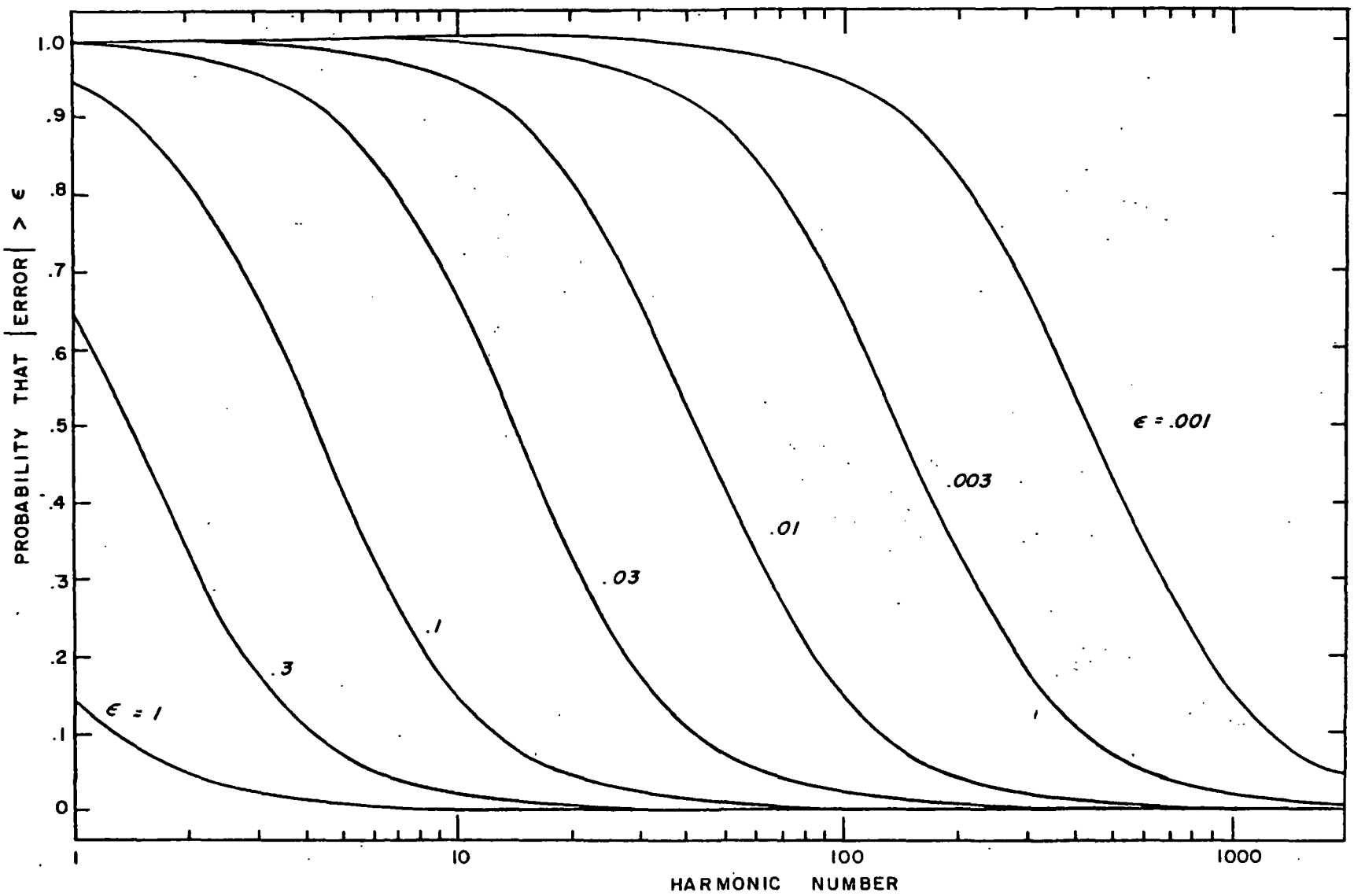

Fig. 16 Probability of Truncation Error on Impedance Estimates from Individual Harmonics

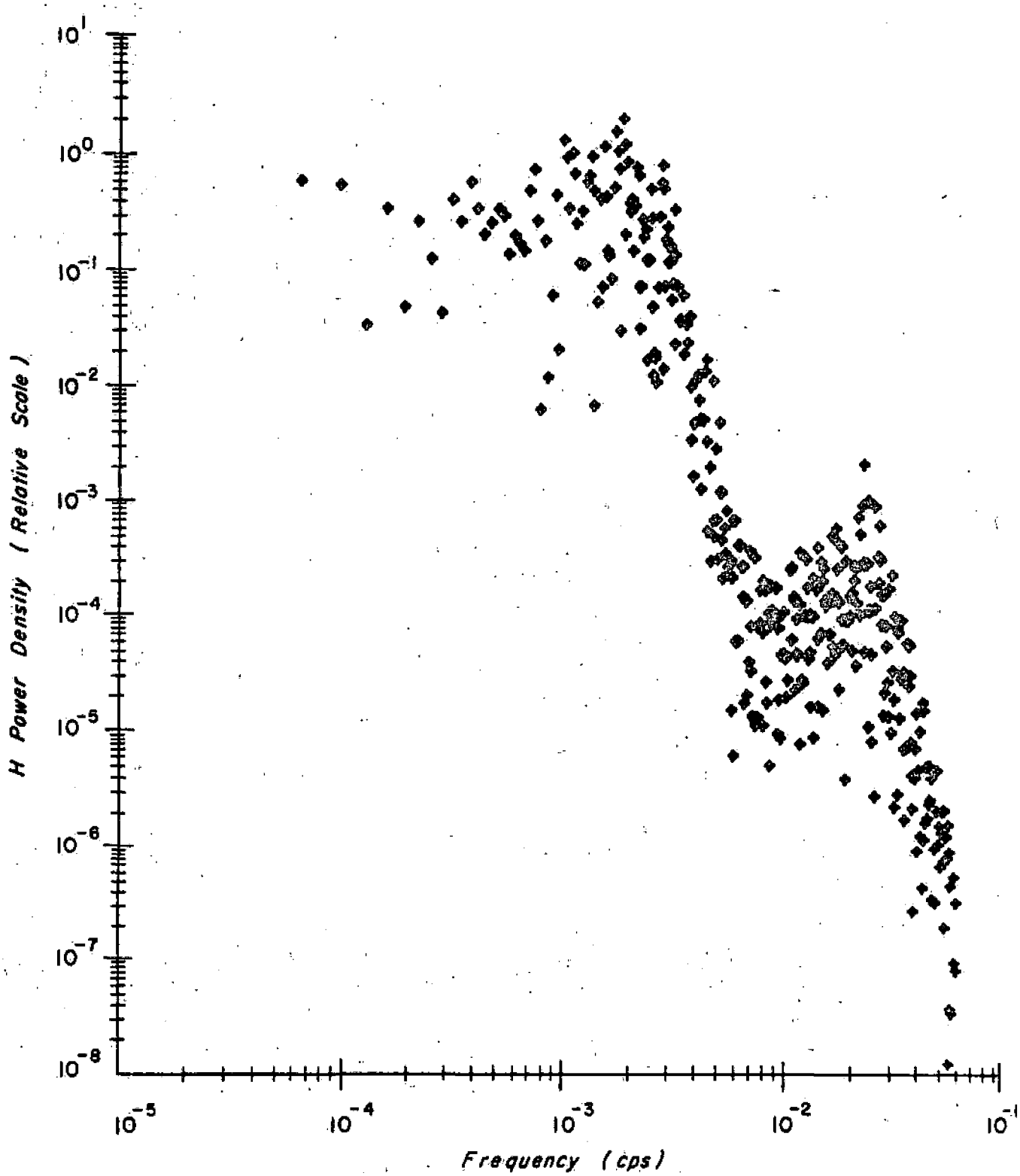

Fig. 17 Individual Harmonics of the Spectrum of a Truncated H Signal

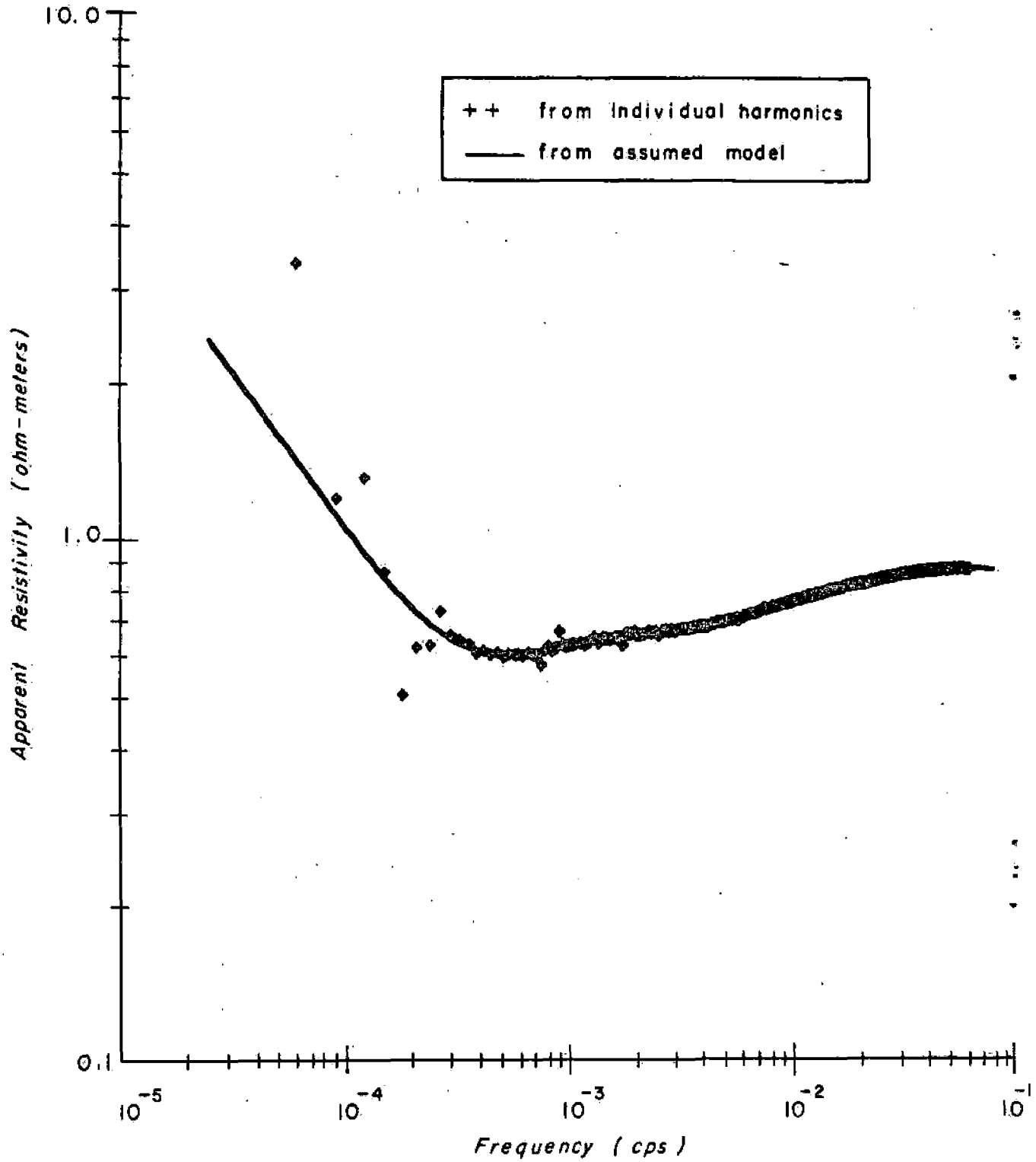

Fig. 18 Apparent Resistivity Estimates from Individual Harmonics of Truncated E and H Signals

BIBLIOGRAPHY

1. Blackman, R. B., Linear Data Smoothing and Prediction in Theory and Practice, Addison-Wesley, 1965.

2. Blackman, R. B., and J. W. Tukey, The Measurement of Power Spectra, Dover Publications, Inc., New York, 1959.

3. Bleil, D. F., Natural Electromagnetic Phenomena Below 30 kc/s, Plenum Press, New York, 1964.

4. Born, M., and E. Wolf, Principles of Optics, Pergamon Press, Inc., New York, 1965.

5. Bostick, F. X., Jr., and H. W. Smith, "An Analysis of the Magnetotelluric Method for Determining Subsurface Resistivities," Electrical Engineering Research Laboratory Report No. 120, The University of Texas at Austin, 1961.

6. Bostick, F. X., Jr., and H. W. Smith, "Investigation of Large-Scale Inhomogeneities in the Earth by the Magnetotelluric Method," Proceedings of the IRE, Vol. 50, No. 11, pp. 2339-2346, 1962.

7. Cagniard, L., "Basic Theory of the Magneto-Telluric Method of Geophysical Prospecting," Geophysics, Vol. 18, pp. 605-635, 1953.

8. Cantwell, T., "Detection and Analysis of Low Frequency Magnetotelluric Signals," Ph.D. thesis, Massachusetts Institute of Technology, 1960.

9. Cantwell, T., P. Nelson, J. Webb, and A.S. Orange, "Deep Resistivity Measurements in the Pacific Northwest," Journal of Geophysical Research, Vol. 70, No. 8, pp. 1931-1937, 1965.

10. Chapman, S., and J. Bartels, Geomagnetism, Oxford University Press, London, 1940.

11. Cooley, J. W., and J. W. Tukey, "An Algorithm for the Machine Calculation of Complex Fourier Series," Mathematics of Computation, Vol. 19, No. 90, pp. 297-301, 1965.

12. Eckhardt, D. H., "Theory and Interpretation of the Electromagnetic Impedance of the Earth," Journal of Geophysical Research, Vol. 73, No. 16, pp. 5317-5326, 1968.

13. d'Erceville, I., and G. Kunetz, "The Effect of a Fault on the Earth's Natural Electromagnetic Field," Geophysics, Vol. 27, No. 5, pp. 651-665, 1962.

14. Fournier, H. G., "Essai d'un Historique des Connaissances Magneto-Telluriques," Note 17, Institut de Physique du Globe, Universite de Paris, 1966.

15. Hancock, J. C., An Introduction to the Principles of Communication Theory, McGraw-Hill Book Company, Inc., New York, 1961.

16. Hopkins, G. H., Jr., and H. W. Smith, "An Investigation of the Magneto-telluric Method for Determining Subsurface Resistivities," Electrical Engineering Research Laboratory Report No. 140, The University of Texas at Austin, 1966.

17. Kovtun, A. A., "The Magnetotelluric Investigation of Structures ... Inhomogeneous in Layers," Bulletin, Academy of Sciences, USSR, Geophys. Series, English Translation, pp. 1085-1087, 1961.

18. Madden, T. R., "Spectral, Cross-Spectral, and Bispectral Analysis of Low Frequency Electromagnetic Data," Natural Electromagnetic Phenomena Below 30 kc/s, Ed., D. F. Bleil, pp. 429-450, Plenum Press, New York, 1964.

19. Mann, J. E., "Magnetotelluric Theory of the Sinusoidal Interface," Journal of Geophysical Research, Vol. 69, No. 16, pp. 3517-3524, 1964.

20. Mann, J. E., "The Importance of Anisotropic Conductivity in Magneto-telluric Interpretation," Journal of Geophysical Research, Vol. 70, No. 12, pp. 2940-2942, 1965.

21. Morse, P. M., and H. Feshback, Methods of Theoretical Physics, McGraw-Hill Book Company, Inc., New York, 1953.

22. Neves, A. S., "The Magnetotelluric Method in Two Dimensional Structures," Ph.D. thesis, Massachusetts Institute of Technology, 1957.

23. Niblett, E. R., and C. Sayn-Wittgenstein, "Variation of Electrical Conductivity with Depth by the Magneto-Telluric Method," Geophysics, Vol. 25, pp. 998-1008, 1960.

24. Papoulis, A., Probability, Random Variables, and Stochastic Processes, McGraw-Hill Book Company, Inc., New York, 1965.

25. Patrick, F. W., "Magnetotelluric Modeling Techniques," Ph.D. thesis, The University of Texas at Austin, 1969.

26. Price, A. T., "The Theory of Magnetotelluric Methods when the Source Field is Considered," Journal of Geophysical Research, Vol. 67, No. 5, pp. 1907-1918, 1962.

27. Rankin, D., "A Theoretical and Experimental Study of Structure in the Magnetotelluric Field," Ph.D. thesis, University of Alberta, 1960.

28. Rankin, D., "The Magneto Telluric Effect on a Dike," Geophysics, Vol. 27, No. 5, pp. 666-676, 1962.

29. Rankin, D., G. D. Garland, and K. Vozoff, "An Analog Model for the Magnetotelluric Effect," Journal of Geophysical Research, Vol. 70, No. 8, pp. 1939-1945, 1965.

30. Rokityanski, I. I., "On the Application of the Magnetotelluric Method to Anisotropic and Inhomogeneous Masses," Bulletin, Academy of Sciences, USSR, Geophys. Series, English Translation, pp. 1050-1053, 1961.

31. Scholte, J. G., and J. Veldkamp, "Geomagnetic and Geoelectric Variations," Journal of Atmospheric and Terrestrial Physics, Vol. 6, No. 1, pp. 33-45, 1955.

32. Shanks, J. L., "Recursion Filters for Digital Processing," Geophysics, Vol. 32, No. 1, pp. 33-51, 1967.

33. Spitznogle, F. R., "Some Characteristics of Magnetotelluric Fields in the Soviet Arctic," Ph.D. thesis, The University of Texas at Austin, 1966.

34. Srivastava, S. P., "An Investigation of the Magnetotelluric Method for Determining Subsurface Resistivities," Ph.D. thesis, The University of British Columbia, 1962.

35. Srivastava, S. P., "Application of the Magnetotelluric Method to Anisotropic and Inhomogeneous Bodies," Journal of Geophysical Research, Vol. 68, No. 20, pp. 5857-5868, 1963.

36. Swift, C. M., Jr., "A Magnetotelluric Investigation of an Electrical Conductivity Anomaly in the Southwestern United States," Ph.D. thesis, Massachusetts Institute of Technology, 1967.

37. Tikhonov, A. N., N. V. Lipskaya, and B. M. Yanovsky, "Some Results of the Deep Magneto-Telluric Investigations in the USSR," Journal of Geomagnetism and Geoelectricity, Vol. 15, No. 4, pp. 275-279, 1964.

38. Vozoff, K., H. Hasegawa, and R. M. Ellis, "Results and Limitations of Magnetotelluric Surveys in Simple Geologic Situations," Geophysics, Vol. 28, No. 5, pp. 778-792, 1963.

39. Wait, J. R., "On the Relation Between Telluric Currents and the Earth's Magnetic Field," Geophysics, Vol. 19, pp. 281-289, 1954.

40. Wait, J. R., Electromagnetic Waves in Stratified Media, MacMillan Company, New York, 1962.

41. Word, D. R., "An Investigation of the Magnetotelluric Tensor Impedance Method," Ph.D. thesis, The University of Texas at Austin, 1969.

SUBJ
GPHYS
Elec
NEP

Nonlinear Electrical Properties

Gary R. Olhoeft
U.S. Geological Survey

1979

Presented to 1979 Symposium on Oilfield & Geothermal Chemistry, 22-24 January, 1979 at Houston, TX (under auspices of SPE)

to appear in: Proceedings of: Comportements non-lineaires des molecules, atomes et ions dans les champs electriques, magnetiques ou electromagnetiques, 31st International Meeting of the Societe de Chimie Physique, Associazone Italiana di Chimic Fisica, Deutsche Bunsengesellschaft fur Physikalische Chemie, and the Faraday Division of the Chemical Society, Abbaye de Fontevraud, 25-28 September, 1978, Fontevraud, France

NONLINEAR ELECTRICAL PROPERTIES

G.R. OLHOEFT
U.S. Geological Survey MS964, Box 25046 Federal Center, Denver, CO 80225 USA

ABSTRACT

Electrical properties become nonlinear in several different ways due to a variety of mechanisms and processes. In naturally occurring materials, nonlinear behavior is dominantly caused by the charge transfer reactions accompanying either oxidation-reduction processes or ion-exchange processes. Since most nonlinearities are directly caused by specific chemical phenomena, nonlinear electrical properties may be used in the remote measurement of geochemical activity within the earth. Applications through borehole geophysics include the determination of geochemical information during solution mining of minerals, monitoring ground water chemistry for leaks around nuclear waste repositories, and measuring the buildup of clays and similar alteration products that may clog pores in geothermal systems.

INTRODUCTION

Electrical properties are useful in the earth sciences in a wide variety of ways as they are one of the easiest of all physical properties to measure and they are one of the most sensitive to changes in material or environmental parameters (Keller and Frischknecht, 1966; Olhoeft, 1976). The extreme sensitivity of some electrical properties to small changes in a wide variety of parameters is sometimes a problem. As an example, a volcanic material like basalt may exhibit an electrical resistivity at a frequency of 10^{-3} Hz which is 10^{12} ohm-m when vacuum dry at room temperature. That same material will have a resistivity of 10^{3} ohm-m if it is saturated with a few weight percent water or if it is raised to a temperature of 700°C or if it is measured at a frequency of 10^{5} Hz. A few weight percent clay or a single monolayer of adsorbed water can alter the low frequency resistivity by an order of magnitude while not altering the high frequency resistivities at all.

To address the ambiguous and multiple nature of electrical properties, investigators measure the widest possible number of electrical parameters as functions of variables that are easily controlled by the experimenter. Typically this involves the use of frequency of measurement as a variable.

In the frequency domain, the electrical properties describing a system response

relate the input (or stimulus or excitation) to the output (or response) of the system by a multiplicative factor, the transfer function of the system. If the input to the system is an electrical field and the output is current density, then the transfer function is the complex electrical conductivity. If the input is current density and the output is electrical field, then the transfer function is the complex electrical resistivity. The complex electrical resistivity and complex electrical conductivity are reciprocals of each other and are further discussed in the appendix.

The equation relating the input and output of a system is called the system equation. If all the derivatives of the input and output in the system equation are raised to the first power only and there are no products of derivatives, then the system is said to be linear. Mathematical properties of linear systems include additivity and homogeneity (together called superposition) which are discussed in detail in Cooper and McGillem (1967). These mathematical properties of linearity result in two measurable properties of linear systems: 1) the transfer function of a linear system is independent of the amplitude of the input to the system, and 2) the output of a linear system contains no new harmonic content that did not appear in the input to the system. In the latter case, if the input to the linear system is a pure sine wave, then the output contains no harmonics.

In addition to linearity, systems are described as being causal or acausal and by being integrably transformable or not. Causal systems have outputs which are independent of future values of the input. All physically realizable systems are causal (they cannot predict the future). A system which is linear may be integrably transformable. The integral transforms of the input, output, or system transfer function do not exist unless the integrals are convergent (Sneddon, 1972). Most physically realizable waveforms are convergent in this sense, and it is always possible to choose the input to a system such that the input and the output are both convergent.

The integral transform of a causal function has a time function that is completely specified by either the real or the imaginary part of the transform (see derivation in Landau and Lifshitz, 1960). Thus, the real and imaginary parts and the amplitude and phase spectra of the transfer function are related to each other. The relation between the real and imaginary parts is called the Hilbert transform or the Kramers-Kronig relations (Landau and Lifshitz, 1960). If the real and imaginary parts of the transfer function do not obey the Hilbert transform and the input was chosen to give a convergent input and output, then the system is either acausal or nonlinear. As all physically realizable systems must be causal, such a system must then be nonlinear.

As a consequence, there are two additional measures of nonlinearity: 3) the transfer function of a system in the frequency domain is the Laplace transform of the impulse response of the system in the time domain (see Cooper and McGillem,

1967), and 4) the real and imaginary parts of the transfer function are a Hilbert transform pair. In practice the third measure of linearity is very difficult to obtain as the impulse response is difficult to measure directly. However, a similar test may be performed using the step response or by measuring and comparing the transfer functions of a system measured by using two very different waveforms of input (such as a sine-wave versus a triangular-wave). In linear systems, the transfer function is independent of the form of the input.

Thus, there are four methods of measuring nonlinearity in an electrical system:

1) Measure the electrical transfer function at two or more different values of input signal amplitude. A measure of the nonlinearity is the derivative of the transfer function with respect to amplitude of input. Note that the transfer function is a complex quantity and that amplitude and phase spectra may be independently nonlinear.

2) Measure the harmonic content of the input and output of the system. The root-mean-square (RMS) difference between the harmonics in input and output is the total-harmonic-distortion (THD) and is a measure of nonlinearity.

3) Measure the transfer function using a sine-wave and a triangular-wave input. The difference between the resultant transfer functions is a measure of nonlinearity.

4) Measure the frequency dependence of the transfer function. Use the Hilbert transform to generate new real and imaginary parts of a synthetic transfer function from the imaginary and real parts of the measured transfer function. The differences between the derived synthetic and the original measured transfer functions are measures of nonlinearity versus frequency.

Further, these four generalized measures of nonlinearity may appear in different ways. It is possible to have a complex transfer function with an amplitude nonlinearity (the amplitude or magnitude of the transfer function varies with the amplitude of the input) but without a phase nonlinearity (for example, if the nonlinearities in the real and imaginary parts of the transfer function cancel). It is also possible to have a system which exhibits the first two types of nonlinearity (amplitude and harmonic), but does not exhibit the last type of nonlinearity (Hilbert). The reverse is also possible and has been found to be common in clay minerals.

EXAMPLES

Nonlinear electrical properties have been studied for a number of years by electrochemists through a variety of techniques, including polarography, cyclic voltammetry, and others. These techniques are discussed in textbooks such as Bockris and Reddy (1970), Fleet and Jee (1973), Nurnberg (1974), Galus (1976), Antropov (1977), and others. The best known of the nonlinear processes is that accompanying charge transfer during oxidation-reduction reactions (for a general discussion of charge transfer, see Mathews and Bockris, 1971).

The linear equation describing electrical properties is Ohm's law, given by

$$J = \sigma E \quad \text{(see appendix)}$$

where J = current density

E = electric field strength

and σ = electrical conductivity (transfer function between E and J).

The oxidation-reduction reaction carrying charge across an interface between a solution and an electrode is given by the nonlinear Butler-Volmer absolute rate equation

$$J = C_1 e^{\beta C_2 E} + C_3 e^{-(1-\beta)C_4 E}$$

where C_i = various constants involving chemical parameters such as diffusion coefficients, concentrations, kinetics, and so forth

and β = anodic transfer coefficient.

The details of the coefficients are unimportant for the purposes of describing how nonlinear behavior appears (for further discussions see Sluyters-Rehbach and Sluyters, 1970, or the electrochemistry textbooks referenced above).

The Butler-Volmer type of equation yields electrical properties which are not only nonlinear, but are also complex, frequency dependent, and asymmetrical with respect to the polarity of the input. The properties may become linear for very small perturbations of E, for frequencies of input that are higher than the speed of reaction, and for conditions which may be diffusion or otherwise limited. The properties may be asymmetrical if the constants in the equation are not equal for the anodic and cathodic terms, or if the anodic (reduction) process is not completely reversible during the cathodic (oxidation) process, or if the system stores energy and exhibits memory (a dynamic system) differently for the anodic process than for the cathodic process.

Figure 1 illustrates the plot of current versus electric potential across a pyrite/water interface. In both parts of the figure, the sample is in a three-terminal sample holder similar to the corrosion cell of Peters (1977) with 0.1 molar NaCl aqueous solution at a pH of 7. The driving waveform is a sinewave with the illustrated Lissajous patterns proceeding in a clockwise direction. The dotted lines are the actual waveforms recorded by a digital oscilloscope while the solid line in Figure 1b is a model fit based upon the Butler-Volmer equation (offset for clarity).

Figure 1a illustrates the pyrite with a freshly polished surface at a frequency of 0.1 Hz and a current density of 0.085 A/m^2. Each change in slope or distortion of the pattern relative to an ellipse is indicative of a specific chemical reaction. Reactions occur at specific potentials across the interface (Milazzo and Caroli, 1978), and if the current density is not high enough to generate the required potential then the reaction will not occur. Similarly, reactions proceed at specific rates (determined by either the reaction kinetics or the speeds of diffusion, see Arvia and Marchiano, 1971, and Bernasconi, 1976), and if the

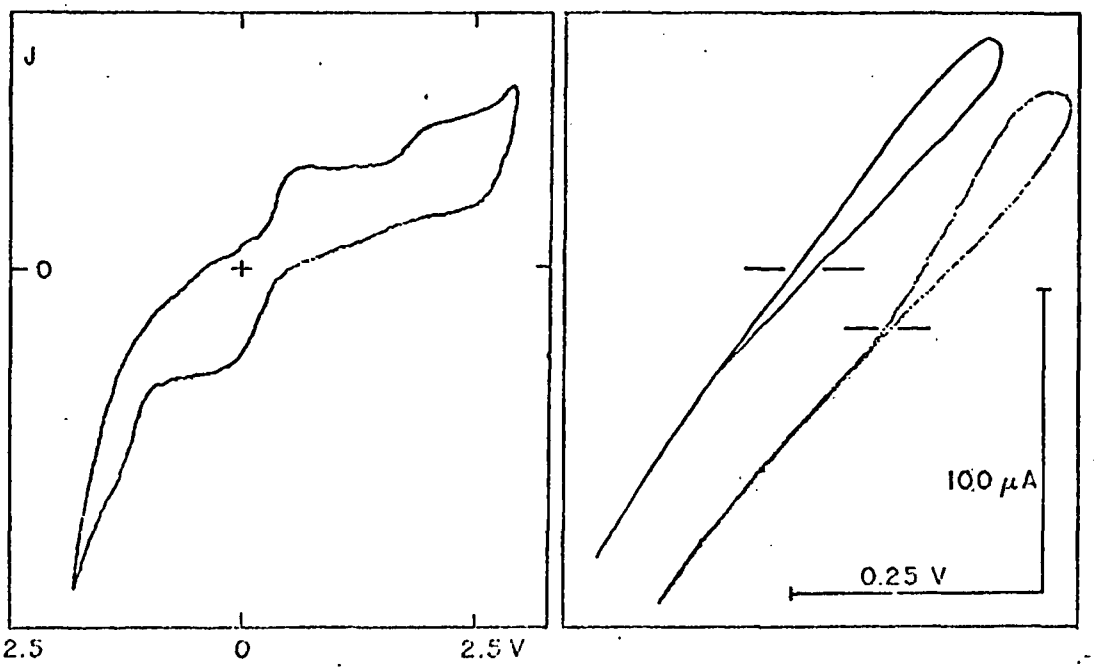

FIGURE 1: Figure 1a (left) illustrates the Lissajous pattern of current density (vertical axis) versus electrical potential (horizontal axis) across the pyrite-water interface with a 0.1 molar NaCl aqueous solution. The cross marks zero current and zero potential. The frequency is 0.1 Hz at a maximum current density of 0.085 A/m^2. Figure 1b (right) illustrates the same sample and conditions as part 1a except a frequency of 0.01 Hz and a current density of 0.008 A/m^2. At this current density, only one oxidation-reduction couple is present. The dotted curve is the actual digitized data while the solid line is a model fit based upon the Butler-Volmer equation. The two curves are offset for clarity with broken horizontal bars through each indicating zero current.

frequency of excitation is too high, the reaction will not occur. In either case of too low a current density or too high a frequency, the system becomes linear.

Figure 1a illustrates several reactions occurring with the lower left quadrant (anodic) of the plot reducing the sample and generating hydrogen gas while the upper right quadrant (cathodic) is where the sample is oxidized and oxygen may be evolved. Figure 1b illustrates the same sample at a lower current density and a lower frequency where only one reaction couple is activated. The opening of the loop in the oxidizing quadrant indicates that the sample either resists being oxidized or the oxidizing reaction is diffusion limited. As the plot does not change upon stirring the solution, the sample must be resistant to oxidation. The lower left reducing quadrant illustrates that the sample is not diffusion limited nor resistant to being reduced. For further discussion of the detailed electrochemistry of pyrite, see Peter (1977), Hall (1975), Biegler and others (1977), Scott and Nicol (1977), and Klein and Shuey (1978a, b).

Figure 2 illustrates the dependence of highly altered pyrite upon current density at 0.1 Hz in a four-terminal sample holder. The sample holder has a symmetrical arrangement with a current electrode in solution, a potential electrode near but not touching the pyrite sample, the pyrite sample potted in silicone,

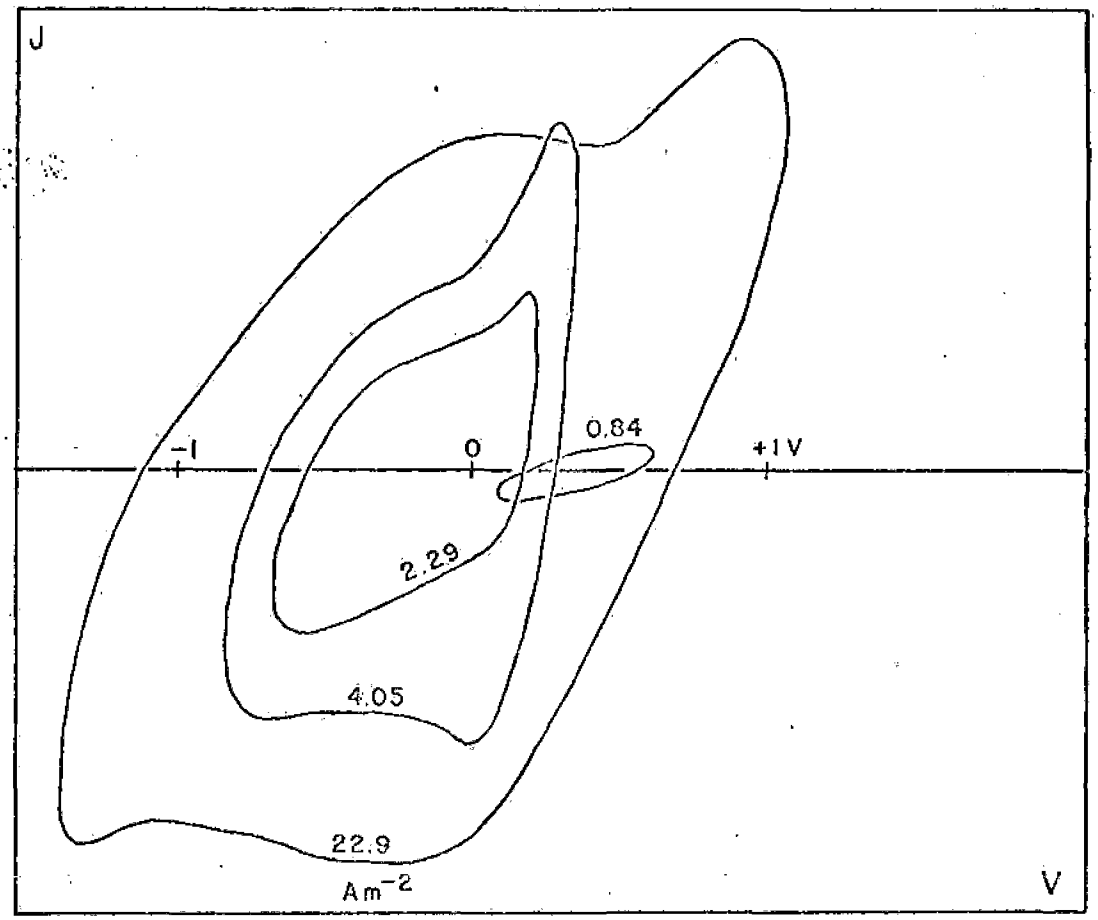

FIGURE 2: An altered pyrite-electrolyte interface under similar conditions as for Figure 1 with a frequency of 0.1 Hz and various current densities as indicated on each curve. This is a four-terminal sample holder as described in the text.

another potential electrode, and another current electrode in solution. The electrodes are all constructed of platinum mesh (bright platinum as the platinized electrodes introduce impurities and do not stay platinized over long periods of time). High input impedance ($>>10^{11}$ ohms) electrometer amplifiers are used in the measurement of the potential electrodes so as to not draw enough current to generate significant charge transfer impedances in the potential measuring circuit. The electrode arrangement is identical with common practice for geophysical and borehole instrumentation (Keller and Frischknecht, 1966). This electrode arrangement will not produce the characteristic and asymmetrical plots of Figure 1 unless the oxidation-reduction reactions are incompletely reversible or are dynamically different at anode and cathode. In the latter case, dynamically different means the anode stores energy and exhibits memory (phase lag) in a manner different than the cathode.

Figure 2 illustrates the pyrite-electrolyte reactions as a function of current density showing the distinct asymmetry for one of the above reasons. In addition, the 0.84 A/m^2 current density pattern is nearly a perfect ellipse and therefore

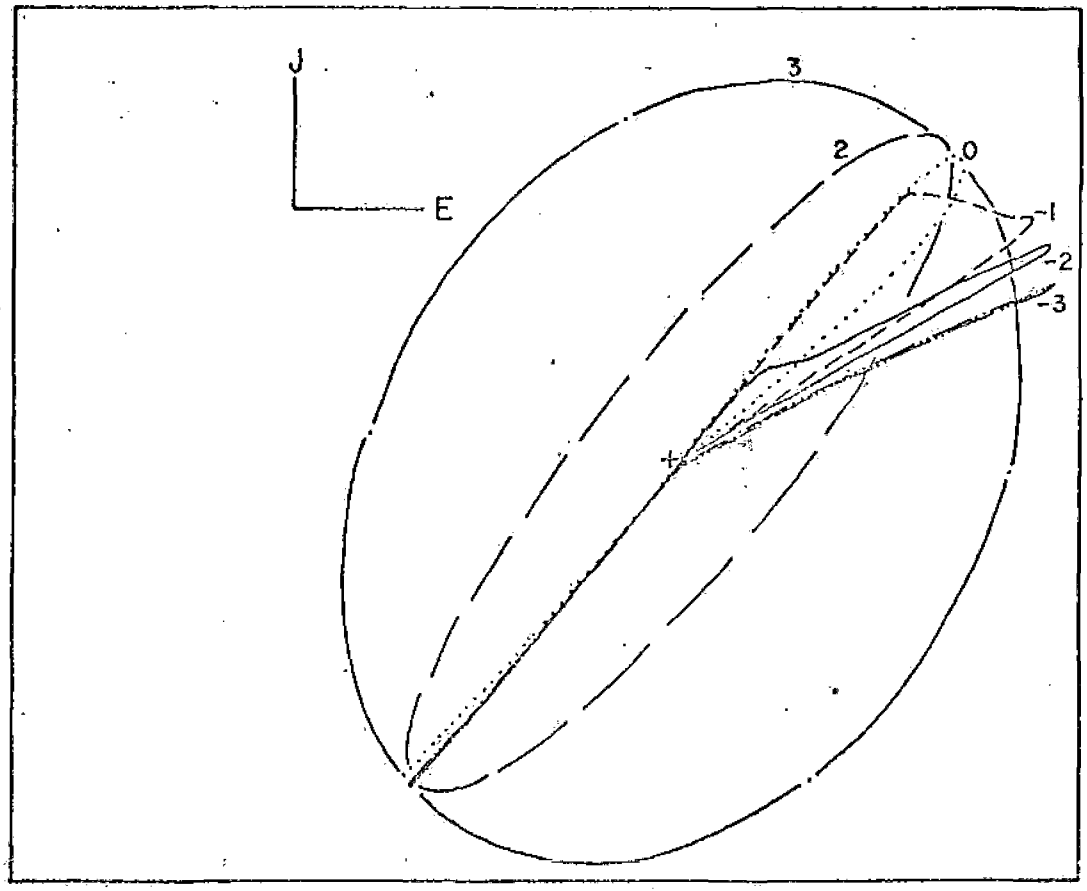

FIGURE 3: The frequency dependence of the Lissajous patterns for a cation exchange resin as a function of frequency. The numbers next to each curve are the logarithm of the frequency to base ten. The 1 Hz and 10 Hz patterns overlap and are nearly identical. The patterns are essentialy linear above 10 Hz.

approaching a linear system response. The specimen in Figure 2 has a highly altered surface and requires higher current densities for nonlinear behavior than the highly polished specimen of Figure 1.

The second important charge transfer process in natural materials that causes measurable nonlinear electrical behavior is due to ion exchange. Unfortunately, the process of ion exchange is itself very little understood and the electrochemistry of ion exchange is even less well known. The best discussions occur in Carroll (1959), Payne (1972), Dukhin and Shilov (1974), Dukhin (1974), Dukhin and Derjaguin (1974), Derjaguin and Dukhin (1974), Adamson (1976) and van Olphen (1977). Some attempts at models of the electrochemistry have been made by Armstrong (1959), Timmer and others (1970), and others.

The following examples illustrate the type of behavior that has been observed in a variety of clays and zeolites. For simplicity, the examples will be drawn from investigations performed on ion exchange resins. Essentially similar results have been obtained with a variety of clay minerals. Figure 3 illustrates the

electrical behavior of a cation exchange resin (Table 1) in a four-terminal sample holder as a function of frequency. The resins are very dynamic and exhibit considerable memory. The cations easily adsorb onto the surface, but reluctantly desorb. This causes the distinct nonlinear asymmetry shown in the figure. Also, at the higher frequencies the cations cannot respond to the driving force and the process becomes linear as it is diffusion limited. Due to the memory and diffusion coefficients, the frequency dependence of the transfer function is measurably different depending upon whether it is measured from low to high frequencies or from high to low frequencies.

TABLE 1

Both exchange resins are styrene divinylbenzene copolymer matrix beads, 16-50 mesh size, laboratory grade, with a working range of 0-14 pH, and are manufactured by J.T. Baker Company.

Designation	C-267 cation	ANGA-542 anion
Type	strong acid	strong base
Form (ionic form)	H	OH
Group	sulfonic functional	alkyl quaterbary amine
Total dry exchange capacity (meq/g)	4.0	3.2
Moisture content	45-55	60-70 percent
Working density (g/l)	400-500	300-500

Figure 4 illustrates the frequency dependence of the cation resin and an equivilant anion resin (Table 1) measured from low to high frequency. Note that the cation resin has a much higher total-hermonic-distortion (THD) that the anion resin, has a larger phase angle, and has a stronger frequency dependence. Also, the three resistivities plotted represent the asymmetry of the system with the resistivity determined from the whole waveform (W), from just the positive half (P), and from just the negative half (N). The cation resin is considerably more asymmetrical than the anion resin.

Due to the generally smaller size of the cation, it is not surprising that it is more important than the anion in adsorption processes (see discussions in van Olphen, 1977). Also, most materials tend to have negative surface charges in excess and thus prefer to attract cations over anions. Thus, all other things being equal, it is fortunate that the cation exchange process is more nonlinear than the anion process as this allows the nonlinear effects to be used to acquire additional information about the material surface with which the ions are interacting.

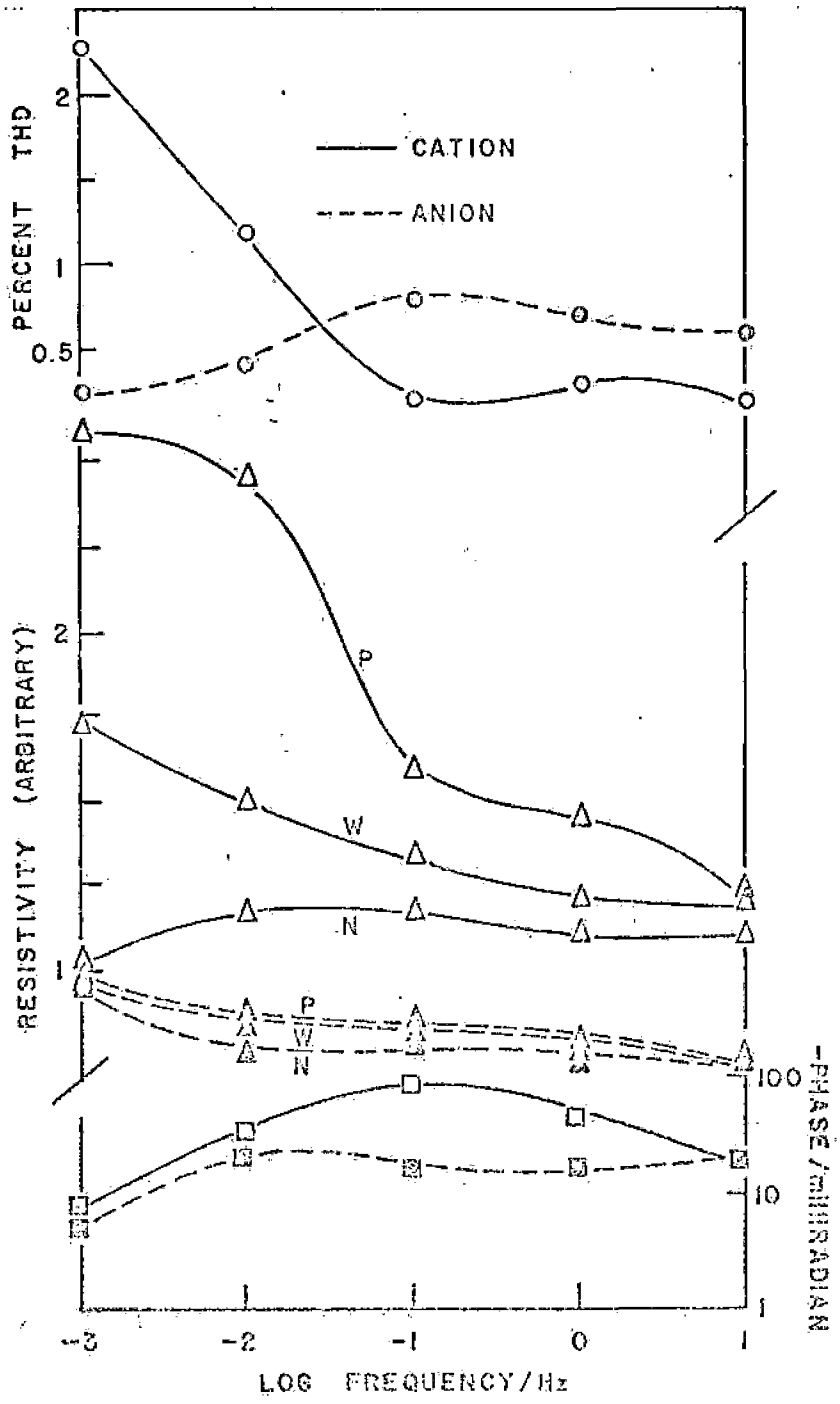

FIGURE 4: The frequency dependence of the total-harmonic-distortion (THD), the real part of the complex resistivity, and the phase angle of the cation exchange (solid lines with open symbols) and the anion exchange (dashed lines with closed symbols) resins of Table 1. P, W, and N on the resistivity plots indicate the use of only the positive half, the whole, or only the negative half of the waveforms (as in Figure 3) for the construction of the resistivity.

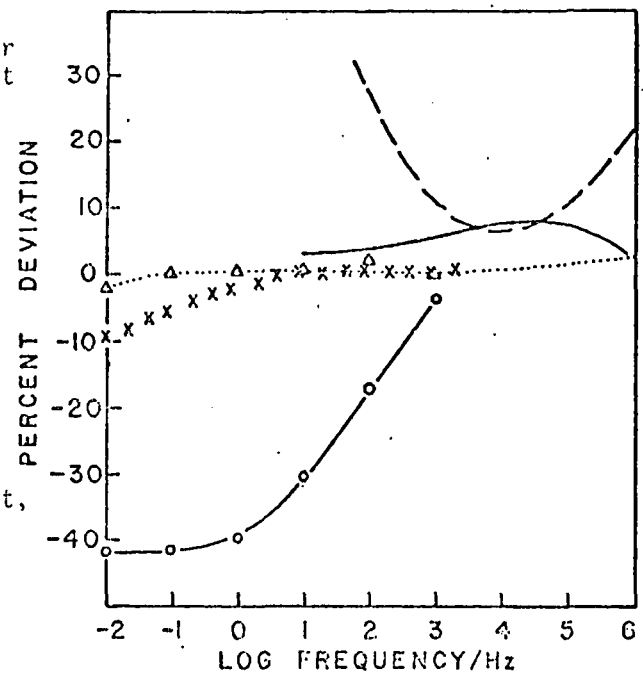

FIGURE 5: The Hilbert nonlinear effect as the deviation in percent of the real resistivity actually measured from that derived by the Hilbert transform from the actually measured imaginary resistivity. The dashed, solid, and dotted curves are the deviations for the following instrumentation: General Radio 1615 and Wayne-Kerr B-201 bridges together (dashed), General Radio 1621 and Wayne-Kerr B-201 bridges together (solid), and the U.S.G.S. Petrophysics Laboratory transfer function analyzer (dotted, Olhoeft, 1978). The triangles, crosses, and circles are data from real materials, respectively: an unaltered juvite in distilled water, very pure water (greater than 150,000 ohm-m), and a highly altered juvite in distilled water.

Figure 5 illustrates the final nonlinear example. This figure shows the percent deviation of a resistivity transfer function when the real and imaginary parts are tested with a Hilbert transform. A problem with the measurement of this type of nonlinearity lies in its occurrence in common laboratory measurement apparatus. Several examples are shown for commercial instruments as well as the instrument used to acquire the sample data illustrated (see Olhoeft, 1978).

The data in Figure 5 illustrating the nonlinear Hilbert response for real materials includes a juvite specimen saturated with distilled water (triangles), very pure water (crosses), and a highly altered specimen of juvite saturated with distilled water. This type of nonlinearity has been commonly observed in clays, zeolites, and other highly altered materials such as the altered juvite shown. The reason for the nonlinearity is not known, but it may be related to the cation exchange process as it is usually not observed in the materials where oxidation-reduction reactions dominate.

The Hilbert nonlinearity in water (crosses in Figure 5) has only been observed in water with DC resistivities above 150,000 ohm-m. There are other dielectric nonlinearities in water (Jones, 1975), but neither this nor the others are well understood.

There are many other examples of nonlinear electrical behavior than these given here, but these should suffice as an introduction. Other examples which may be found in the literature include nonlinear electrokinetic phenomena (Dukhin and Derjaguin, 1974), nonlinear dielectric phenomena (Kielich, 1972; Jones, 1975), ferroelectrics (Jona and Shirane, 1962; Burfoot, 1967), and others.

APPLICATIONS

Several applications of nonlinear electrical properties are already in use as standard electroanalytical techniques (see texts referenced above), but several other interesting applications are worth mentioning. The first is the study of reactions versus frequency as a way to measure and study the kinetics of reactions. This has been done in the past, but very infrequently. Second is the study of chemical processes under high temperature and pressure conditions in which it is difficult to access the reaction products for analysis but it is relatively easy to insert wires and electrodes to monitor electrical properties. Third, through the use of borehole logging, it should be possible to exploit the electrical nonlinearities to measure ground water and mineral chemistry in situ.

There are other applications, but the first two are primarily laboratory tools to expand the general knowledge of chemistry, particularly of kinetics (Bernasconi, 1976). The last application is of the greatest interest, however, in a variety of current problems. Among these are the problem of determining geochemical parameters to design solution mining procedures for uranium and other scarce minerals, the problem of monitoring ground water chemistry for leaks around nuclear waste repositories, the problem of measuring the buildup of clays and other alteration products which may clog pore structures in geothermal systems, and a variety of problems in the study of permafrost.

Permafrost is particularly interesting because the colloidal clay particles have electrochemical double layers which may be thicker than the average dimension of the clay particle. Such thick double layers help depress the freezing point of water and harbor large amounts of unfrozen water in the permafrost. Electrical measurement techniques may exploit the current channeling capacity of this unfrozen water to utilize the nonlinear response of the cation exchange process to map and detect the presence of clay minerals. This is particularly important in the exploration for sulfide minerals in permafrost where the clay response may be very similar to various standard geophysical instruments, but easily distinguishable between the clays and sulfides through the nonlinear techniques.

In general, the more information upon which to base a decision or course of action, the better. Nonlinear electrical properties provide a considerable amount of information that may not be otherwise available. Rather than being limited to traditional measurements of electrical properties which provide only amplitude and phase versus frequency, nonlinear electrical measurements can also provide amplitude, phase, asymmetry, total harmonic distortion, Hilbert distortion, and a variety of other parameters versus frequency and current density.

ACKNOWLEDGEMENTS

In addition to U.S.G.S. Geothermal and Uranium Program funding, this research has been partly funded by support from the Department of Energy Division of Geothermal Energy and the National Aeronautics and Space Administration Planetary Geology Program.

The use of trade or manufacturer's names in this report does not imply recommendation or endorsement by the U.S. Geological Survey.

REFERENCES

Adamson, A.W., 1976, Physical Chemistry of Surfaces, 3rd ed., New York: Wiley, 698p.

Antropov, L.I., 1977, Theoretical Electrochemistry, Moscow: Mir Publishers, 596p.

Armstrong, R.D., 1969, Relaxation times for adsorption coupled with a homogeneous reaction in solution, J.Electroanal.Chem., 22, 49-53.

Arvia, A.J. and Marchiano, S.L., 1971, Transport phenomena in electrochemical kinetics, pp. 159-241 in Modern Aspects of Electrochemistry, no. 6, J.O'M. Bockris and B.E.Conway, eds., New York: Plenum.

Bernasconi, C.F., 1976, Relaxation Kinetics, New York: Academic Press, 288p.

Biegler, T., Rand, D.A.J., and Woods, R., 1977, Oxygen reduction on sulfide minerals, pp. 291-302 in Trends in Electrochemistry, J.O'M. Bockris, D.A.J.Rand, and B.J. Welch, eds., New York: Plenum.

Bockris, J.O'M. and Reddy, A.K.N., 1970, Modern Electrochemistry, 2 vols. New York: Plenum, 1432p.

Burfoot, J.C., 1967, Ferroelectrics: An Introduction to the Physical Principles, London: Van Nostrand, 261p.

Carroll, D., 1959, Ion exchange in clays and other minerals, Bull. Geol. Soc. Am., 70, 749-780.

Cooper, G.R. and McGillem, C.D., 1967, Methods of Signal and System Analysis, New York: Holt Rinehart and Winston, 432p.

Derjaguin, B.V. and Dukhin, S.S., 1974, Nonequilibrium double layer and electrokinetic phenomena, pp. 273-336 in Surface and Colloid Science, vol.7, E. Matijevic, ed., New York: Wiley.

Dukhin, S.S., 1974, Development of notions as to the mechanism of electrokinetic phenomena and the structure of the colloid micelle, pp. 1-48 in Surface and Colloid Science, vol. 7, E.Matijevic, ed., New York: Wiley.

Dukhin, S.S. and Derjaguin, B.V., 1974, Equilibrium double layer and electrokinetic phenomena, pp. 49-272 in Surface and Colloid Science, vol.7, E.Matijevic, ed., New York: Wiley.

Dukhin, S.S. and Shilov, V.N., 1974, Dielectric Phenomena and the Double Layer in Disperse Systems and Polyelectrolytes, New York: Halsted, 192p.

Fleet, B. and Joe, R.D., 1973, Electroanalytical chemistry: voltammetry, pp. 210-237 in Electrochemistry, vol.3, Specialist Periodical Report, G.J.Hills, Sr. Rptr., London: The Chemical Society.

Fuller, B.D. and Ward, S.H., 1970, Linear system description of the electrical parameters of rocks, IEEE Trans. Geosci. Electronics, GE-8, pp.7-18.

Galus, Z., 1976, Fundamentals of Electrochemical Analysis, Chichester: Ellis Horwood, 520p.

Hall, S.H., 1975, A method of measuring rock electrode kinetics, J.Electroanal. Chem., 59, 323-333.

Jona, F. and Shirane, G., 1962, Ferroelectric Crystals, Oxford: Pergamon, 402p.

Jones, G.P., 1975, Nonlinear dielectric effects, pp.198-248 in Dielectric and Related Molecular Processes, vol.2, Specialist Periodical Reports, M.Davies, Sr. Rptr., London: The Chemical Society.

Keller, G.V., 1959, Analysis of some electrical transient measurements on igneous, sedimentary, and metamorphic rocks, in Overvoltage Research and Applications, J.R.Wait, ed., London: Pergamon.

Keller, G.V. and Frischknecht, F.C., 1966, Electrical Methods in Geophysical Prospecting, New York: Pergamon, 517p.

Kielich, S., 1972, General molecular theory and electric field effects in isotropic dielectrics, pp. 192-387 in Dielectric and Related Molecular Processes, vol.1, Specialist Periodical Reports, M.Davies, Sr.Rptr., London: The Chemical Society.

Klein, J.D. and Shuey, R.T., 1978a, Nonlinear impedance of mineral-electrolyte interfaces, Part I: pyrite, Geophysics, 43, 1222-1234.

Klein, J.D. and Shuey, R.T., 1978b, Nonlinear impedance of mineral-electrolyte interfaces, Part II: galena, chalcopyrite, and graphite, Geophysics, 43, 1235-1249.

Landau, L.D. and Lifshitz, E.M., 1960, Electrodynamics of Continuous Media, London: Pergamon, 417p.

Mathews, D.B. and Bockris, J.O'M., 1971, The mechanism of charge transfer from metal electrodes to ions in solution, pp. 242-328 in Modern Aspects of Electrochemistry, no. 6, J.O'M. Bockris and B.E. Conway, eds., New York: Plenum.

Milazzo, G. and Caroli, S., 1978, Tables of Standard Electrode Potentials, New York: Wiley, 421p.

Nurnberg, H.W., ed., 1974, Electroanalytical Chemistry, New York: Wiley, 609p.

Olhoeft, G.R., 1976, Electrical properties of rocks, pp. 261-278 in The Physics and Chemistry of Minerals and Rocks, R.G.J. Strens, ed., New York: Wiley.

Olhoeft, G.R., 1978, Electrical properties, a chapter in Initial Report of the Petrophysics Laboratory, K.Watson, ed., U.S.Geological Survey Circular, in press.

Olhoeft, G.R., Elliot, C., Fuller, B.D., Keller, G.V., Scott, W.J., and Strangway, D.W., 1978, Proposed Standards for the Presentation of Electrical and Electromagnetic Data, Interim Report of the Electrical Standards Subcommittee of the Mining Committee, Tulsa: Society of Exploration Geophysicists, 14p.

Payne, R., 1972, The study of the ionic double layer and adsorption phenomena, pp. 43-140 in Techniques of Electrochemistry, vol.1, E.Yeager and A.J. Salkind, eds., New York: Wiley-Interscience.

Peters, E., 1977, Electrochemistry of sulfide minerals, pp.267-290 in Trends in Electrochemistry, J.O'M.Bockris, D.A.J.Rand, and B.J.Welch, eds., New York: Plenum.

Scott, P.D. and Nicol, M.J., 1977, The kinetics and mechanisms of the non-oxidative dissolution of metal sulfides, pp. 291-302 in Trends in Electrochemistry, J.O'M. Bockris, D.A.J.Rand, and B.J.Welch, eds., New York: Plenum.

Shuey, R.T. and Johnson, M., 1973, On the phenomenology of electrical relaxation in rocks, Geophysics, 38, 37-48.

Sneddon, I.N., 1972, The Use of Integral Transforms, New York: McGraw-Hill, 539p.

Sluyters-Rehbach, M. and Sluyters, J.H., 1970, Sine wave methods in the study of electrode processes, pp.1-128 in Electroanalytical Chemistry, vol.4, A.J.Bard, ed., New York: Marcel Dekker.

Timmer, B., Sluyters-Rehbach, M., and Sluyters, J.H., 1970, Influence of non-specific adsorption of reactants on the electrode interface, J.Electroanal. Chem., 24, 287-303.

van Olphen, H., 1977, An Introduction to Clay Colloid Chemistry, New York: Wiley,318p

APPENDIX

This appendix is included to introduce the terminology of electrical properties as used by the exploration geophysicist based upon Olhoeft and others (1978). Unless otherwise specified, these terms are defined for systems which are causal, linear, time-invariant, dynamic, and isotropic. The systems may be either lumped-parameter (ordinary differential equation) or distributed-parameter (partial differential equation), and they may be either discrete time (difference equation) or continuous time (differential equation). For definitions of these specifying terms, see Cooper and McGillem (1967). Included with the definitions are the units in the SI system (shown in brackets).

Definitions of electrical properties logically begin with Ohm's Law

$$J = \sigma E \tag{1}$$

where J = free charge current density [Amp/m^2]

E = electrical field strength [Volt/m]

and σ = electrical conductivity [Siemen/m].

This is equivalently presented as

$$E = \rho J \tag{2}$$

where $\rho = \sigma^{-1}$ = electrical conductivity [Ohm-m]. Up to this point, resistivity and conductivity are defined including only free charge transport.

In the general case, the following linear relationship also applies

$$D = \varepsilon E \tag{3}$$

where ε = dielectric permittivity [Farad/m]

and D = dielectric displacement = electric flux density [Coulomb/m].

Combining equations (1) and (3) through Maxwell's equation

$$\nabla \times H = J + \partial D/\partial t = J_T \tag{4}$$

where H = magnetic field strength [Amp/m],

yields a total current density, J_T, which includes both free carrier conduction and dielectric displacement terms

$$J_T = \sigma E + \varepsilon \partial E/\partial t. \tag{5}$$

Since, in the general case, both the conductivity and the dielectric permittivity may be independently complex (Fuller and Ward, 1970), the total resistivity and the total conductivity may be defined through the relation

$$(\rho_T' - i\rho_T'')^{-1} = \sigma_T' + i\sigma_T'' = (\sigma' + i\sigma'') + i\omega\,(\varepsilon' - i\varepsilon'') \tag{6}$$

with a loss tangent, tanδ, and a phase angle, ϕ, defined

$$\tan\delta = \cot\phi = \rho_T'/\rho_T'' = \sigma_T'/\sigma_T'' \tag{7}$$

with the unsubscripted σ and ε from equation (5).

Most instruments fall into two classes: they either measure electrical parameters by measuring voltage and current (related to E and J by the geometry of the system), or they measure equilalent series or parallel admittance or impedance by substitution against standards. In the latter case, the effective capacitance and conductance measured become the effective dielectric permittivity of $(\varepsilon' + \sigma''/\omega)$ from equation (6), and the loss tangent of equation (7).

Those instruments that measure voltage and current usually measure the total current, yielding a typical measurement of the form

$$E = E_o \sin(\omega t + \phi_e) \qquad (8)$$
$$J_T = J_o \sin(\omega t + \phi_j)$$

where E_o = amplitude of E

J_o = amplitude of J_T

t = time [sec]

ω = circular frequency [rad/sec] = $2\pi f$ (where f is frequency in Hertz)

ϕ_e = arbitrary phase offset relative to some time zero for E

and ϕ_j = arbitrary phase offset relative to the same timebase as for E.

In terms of these equations (8), the total resistivity is given as

$$|\rho_T| = (\rho_T'^2 + \rho_T''^2)^{1/2} = E_o/J_o = \text{resistivity magnitude [Ohm-m]} \qquad (9)$$

$$\angle\rho_T = \phi = \operatorname{arccot}(\rho_T'/\rho_T'') = \phi_e - \phi_j = \text{phase angle [radians]} \qquad (10)$$

$$\rho_T' = (E_o/J_o)\cos\phi \quad \text{and} \quad \rho_T'' = (E_o/J_o)\sin\phi \,. \qquad (11)$$

The complex total conductivity may be obtained from equation (6). The loss tangent and phase angle of equation (7) are identical with the definition in equation (10).

The definitions up to this point have been formulated for steady state sinusoidal excitations. However, the definitions are equally valid whatever the form of the excitation and response, provided that only the fundamental frequency is employed in determining the resistivity and phase angle at that frequency from the measured E and J_T. Harmonics may be similarly used only if the system is demonstratably linear.

Further introduction and discussion of these parameters may be found in Keller (1959), Fuller and Ward (1970), Shuey and Johnson (1973), Cooper and McGillem (1967), and Olhoeft and others (1978).

LuTech, Inc.
Phone: (415) 843-1504
P.O. Box 1263, 127 University Avenue, Berkeley, California 94701

3-D Modeling of Electromagnetic Response of Geothermal Reservoirs

Presented by:

Kenneth K. Mei
LuTech, Inc.
P.O. Box 1263
Berkeley, CA 94701

for

Department of Energy
Idaho Falls, Idaho

Under contract No. DE-FC07-79ID12066

September 9, 1980

Objective: To compute and map scattered surface fields of a geothermal reservoir, induced by an incident plane wave

Method: Use Unimoment Method to solve electromagnetic scattering by buried inhomogenities.

Description of Method:

The Unimoment Method separates the scattering configuration into two independent parts. The region inside a Unimoment surface (e.g., a sphere) may be inhomogenous. The region outside the Unimoment surface is assumed to be homogenous or layered earth (Figure 1).

Inside the Unimoment Sphere, the finite element method is used to generate a sequence of solutions of Maxwell's equations consistent with the inhomogeneity.

Outside the Unimoment sphere, multipole expansion of fields satisfying the layered earth boundary conditions are used.

Assuming the solutions inside and outside the Unimoment sphere are numerically complete, the solution may be uniquely determined by enforcing the continuities of the tangential electric and magnetic fields.

Accomplishments to Date:

(1) Derived the variational formulation of Maxwell's Equation's specifically for an axially symmetrical scatterer, for use in finite element applications.

(2) Completed an automatic triangular mesh generator program, for use in finite element applications. Sample plot is shown in Figure 2.

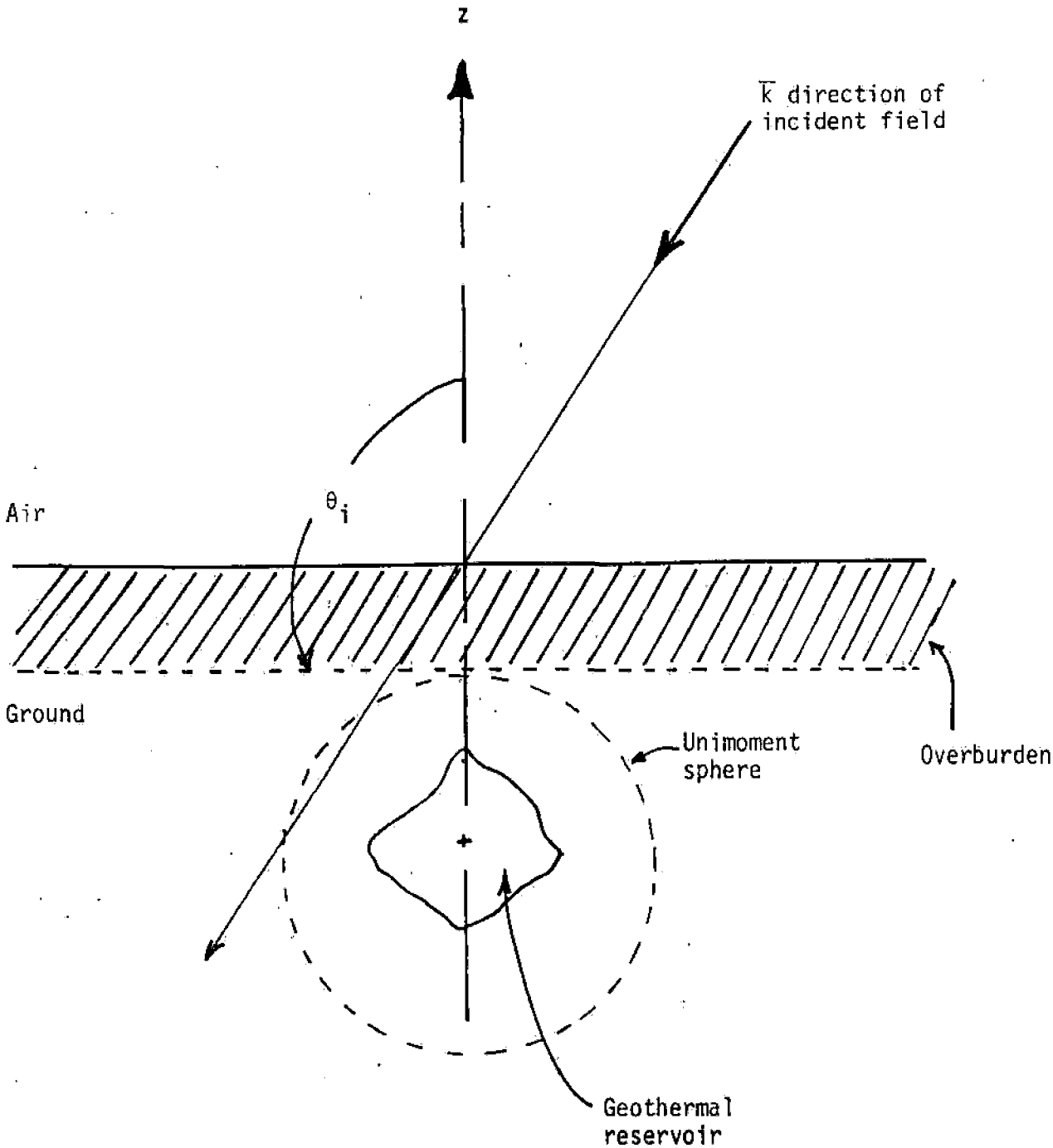

Figure 1. Configuration of EM Scattering by a Geothermal Reservoir

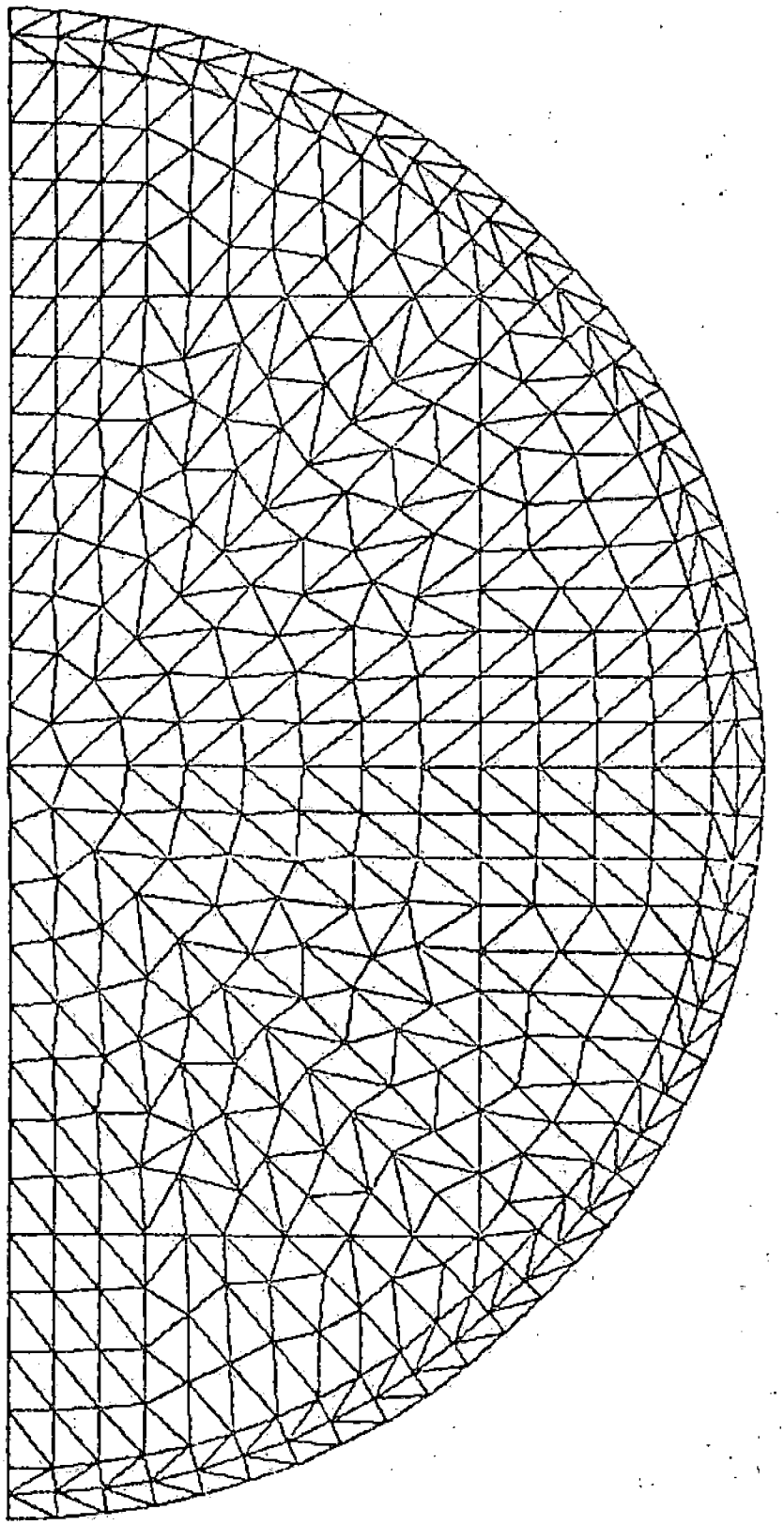

Figure 2. Triangular Element of a Finite Cylinder

Accomplishments to Date (cont.):

(3) Completed finite element program to generate solutions of Maxwell's Equations inside a Unimoment Surface.

(4) Derived the multiple solutions involving air-ground interface boundary conditions, the Generalized Sommerfeld Integrals.

(5) Programmed the computation of Generalized Sommerfeld Integrals.

(6) Programmed the boundary field matchings on the Unimoment surface.

(7) Computed and mapped the scattered surface field due to a finite dielectric cylinder at high frequencies. Scattering configuration and plots are shown in Figure 3.

(8) Defined the low frequency region where approximation of the Generalized Sommerfeld's Integrals exist.

(9) Reprogrammed (5) for medium low frequencies for fast convergence.

Objectives Yet to be Reached:

(1) To compute and map the scattered surface field at low frequencies used in geothermal exploration.

(2) To compare results obtained by other research groups using different approaches.

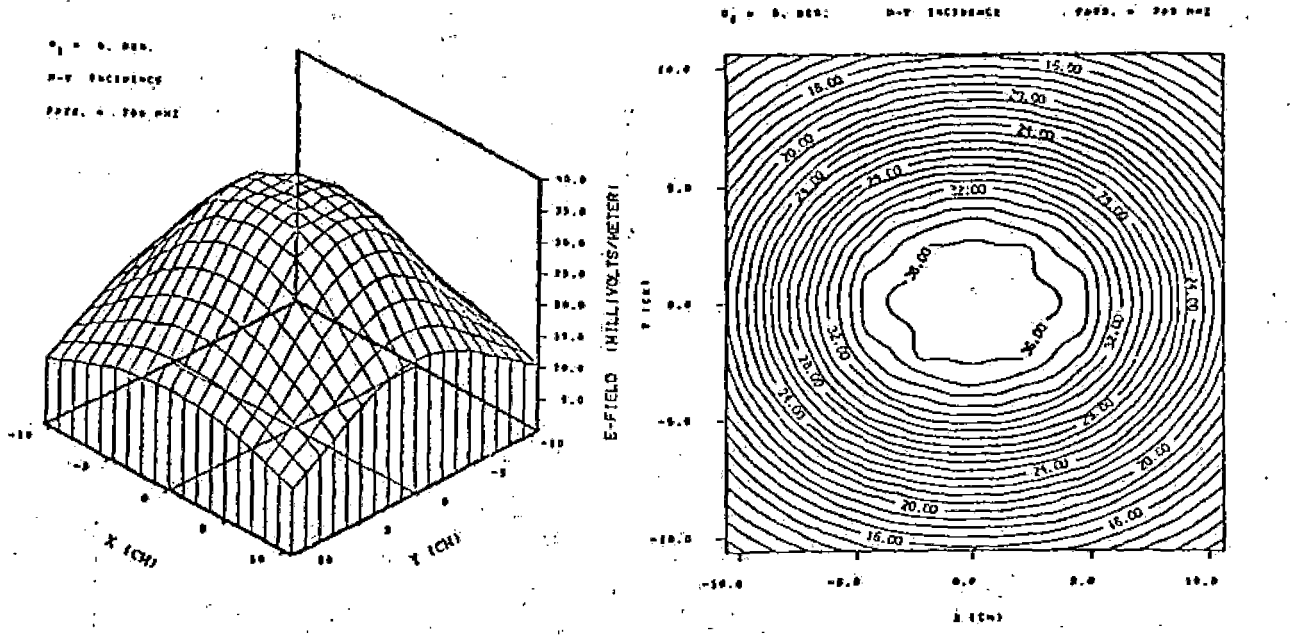

(a) 3-D plot for H-Y incidence (b) Contour plot for H-Y incidence

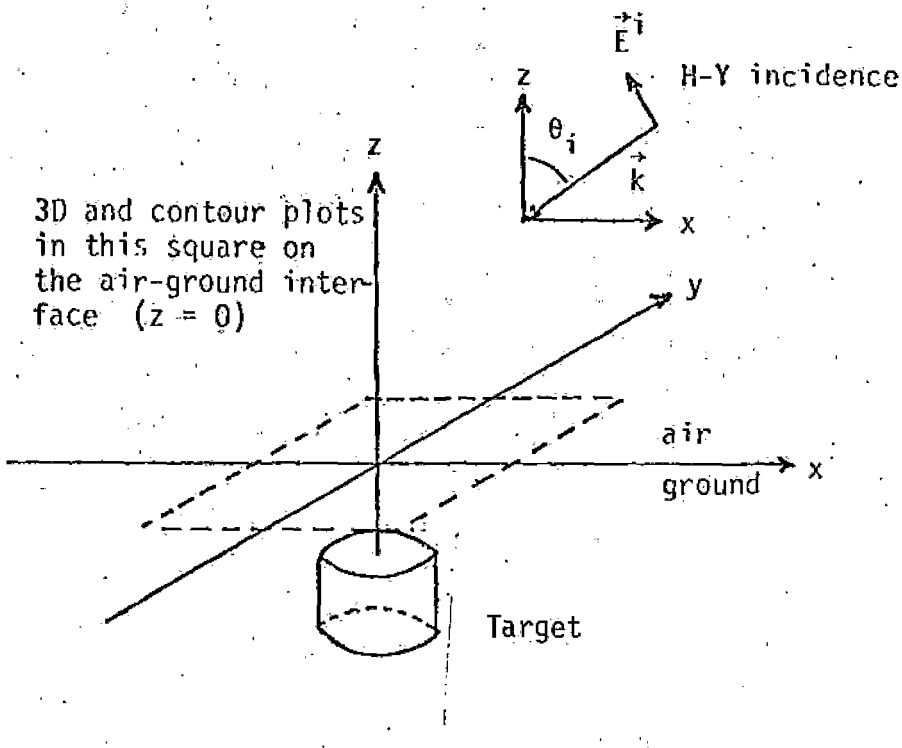

Figure 3. 3-D and Contour Plots of Scattered E-Field Amplitude on the Earth Surface (θ_i = 0°, frequency = 700 MHz)

REFERENCES

[1] K.K. Mei, "Unimoment Method of Solving Antennas and Scattering Problems", IEEE Trans. on Antennas and Propagation, AP-22, 760-766, Nov. 1974. (Received the Honorable Mention to the Best Paper Award of Antennas and Propagation Society of 1974.)

[2] S.K. Chang and K.K. Mei, "Applications of the Unimoment Method to Electromagnetic Scattering of Dielectric Cylinders", IEEE Trans. on Antennas and Propagation, AP-24, 35-41, Jan 1976.

[3] M.A. Morgan, S.K. Chang and K.K. Mei, "Coupled Azimuthal Potentials for Electromagnetic Field Problems in Inhomogenous Axially-Symmetric Media", IEEE Trans. on Antennas & Propagation, AP-25, 413-417, May 1977.

[4] M.A. Margan and K.K. Mei, "Finite Element Computation of Scattering by Inhomogenous Penetrable Bodies of Revolution", IEEE Trans. on Antennas and Propagation, vol. AP-27, No. 2, pp. 202-214, March 1979.

[5] K.K. Mei and M.A. Morgan, "Finite Methods in Electromagnetic Scattering", Conference on Electromagnetic Scattering, Chicago, ILL, June 1976.

[6] S.K. Chang, "On Electromagnetic Wave Scatterings by Buried Objects", Ph.D. Dissertation, University of California, Berkeley, 1976.

TERRAIN EFFECTS IN RESISTIVITY

AND

MAGNETOTELLURIC SURVEYS

Department of Energy Cooperative Agreement

No. DE-FC07-79ID12038

H. T. Holcombe
Department of Geology
University of New Mexico
Albuquerque, New Mexico 87131

G. R. Jiracek
Department of Geosciences
San Diego State University
San Diego, California 92182

Progress summary prepared for Geothermal Resources Council 1980,
Salt Lake City, Utah, September 9-11.

I. INTRODUCTION

The DOE agreement to study "Terrain Effects in Resistivity and Magnetotelluric Surveys" has the following objectives:

1. Development of computer algorithms which calculate the electrical resistivity response (using various electrode arrays) of earth models with arbitrary three-dimensional topography.
2. Development of computer algorithms which calculate the telluric and magnetotelluric (MT) response of earth models with arbitrary two- and three-dimensional topography.
3. Provide validity and accuracy checks for the resistivity and magnetotelluric algorithms.
4. Provide suites of topographic models with calculated responses for resistivity and magnetotelluric surveys.
5. Provide case studies of the application of the algorithms in interpreting existing resistivity and MT field data.

Practical techniques have been developed for modeling the resistivity response in three-dimensions and the magnetotelluric response in two-dimensions. Development of three-dimensional techniques for magnetotellurics is in progress.

II. RESISTIVITY MODELING

The technique used is an adaptation of the solution of the boundary value problem for the electric potential. The solution domain is a hexahedral section of the earth with an arbitrarily irregular upper surface. A standard finite element approach using the variational method is employed. The surface is incorporated into the near surface elements with an isoparametric transformation.

Two programs have been developed and tested. One calculates the bipole-quadrupole total field apparent resistivity response over an arbitrary three-dimensional topography and subsurface resistivity structure, and the other calculates the dipole-dipole response. The programs were verified by comparing results with existing scale model data and results calculated analytically over a hemispherical sink.

As an example, Figure 1 shows the calculated bipole-quadrupole response over a 100 ohm-meter half space with a topographic sink.

III. MAGNETOTELLURIC MODELING

Two independent techniques are being used to calculate the MT response over arbitrary topography. One applies the fast Fourier transform (FFT) numerical technique to the scattering theory proposed by Lord Rayleigh. The other applies the isoparametric finite element technique.

A. Rayleigh-FFT

This technique was first applied to radio frequency scattering but has been successfully extended to magnetotelluric frequencies. Two programs which calculate the MT response over two-dimensional

topography have been successfully tested. One calculates the tranverse electric (TE) responses over a rough homogeneous half space. The other calculates the TE responses over a rough layered half space. Transverse magnetic (TM) responses are obtained using the principle of duality. A program which calculates the response over a three-dimensional rough half space is being developed.

As an example, Figure 2 shows the TE mode response over a two-dimensional asymmetric valley at periods of 100 and one seconds.

B. Finite Element

Two programs using finite element techniques are being tested. One is an adaptation of a program developed by Rijo (1977). It is a two-dimensional program using triangular finite elements, and has been adapted to include topography. The other is a three-dimensional isoparametric finite element program similar to that used for the resistivity problem.

C. Validity Checks

Since there are no known calculated or scale model results for MT response over topography, the two independent methods described are being used to test one another. There are self-consistency checks included in both techniques.

IV. CASE STUDIES

A resistivity case study is being done on data collected by the University of New Mexico surrounding the LASL Hot Dry Rock Geothermal Site in New Mexico. The data include total field mapping from several source locations, intersecting dipole-dipole soundings, and deep Schlumberger soundings. LASL drilling results give local deep well control.

A magnetotelluric case study is being performed on remote reference data collected in the Rio Grande rift. It has both deep well and extensive CDP reflection seismic control.

V. FORTRAN COMPUTER ALGORITHMS

It is anticipated that documented copies of the seven computer programs listed in Table 1 will be included in the final project report which will be released after December 31, 1980. All programs have been developed on a CDC 7600 computer. However, they may be adapted for use on other systems, including mini-computers with a virtual memory capability. Specific details may be obtained by contacting the authors.

TABLE 1. FORTRAN computer programs available upon project completion.

Program Name	Function	System	Approximate Cost Per Run at Sandia Laboratories Computer Center
1. RES3TF †	Calculate bipole-quadrapole total field apparent resistivity over arbitrary 3-D topography and subsurface.	CDC 7600	$15-20
2. RES3DD †	Calculates dipole-dipole apparent resistivity over arbitrary 3-D topography and subsurface	CDC 7600	$70-100
3. MTF2RS †	Calculates TE or TM mode MT apparent resistivity over rough 2-D homogeneous half space	CDC 7600	$3-5
4. MTF2RL †	Calculates TE or TM mode MT apparent resistivity over 2-D rough layered half space	CDC 7600	$10-15
5. MTF2FE *	Calculates TE or TM mode MT apparent resistivity over arbitrary 2-D topography and subsurface	CDC 7600	$20-30
6. MTF3RS *	Calculates MT apparent resistivity over rough homogeneous half space	CDC 7600	$50-100
7. MTF3FE *	Calculates MT response over arbitrary 3-D topography and subsurface	CDC 7600	$500-1000

† Program previously confirmed.

* Program under development.

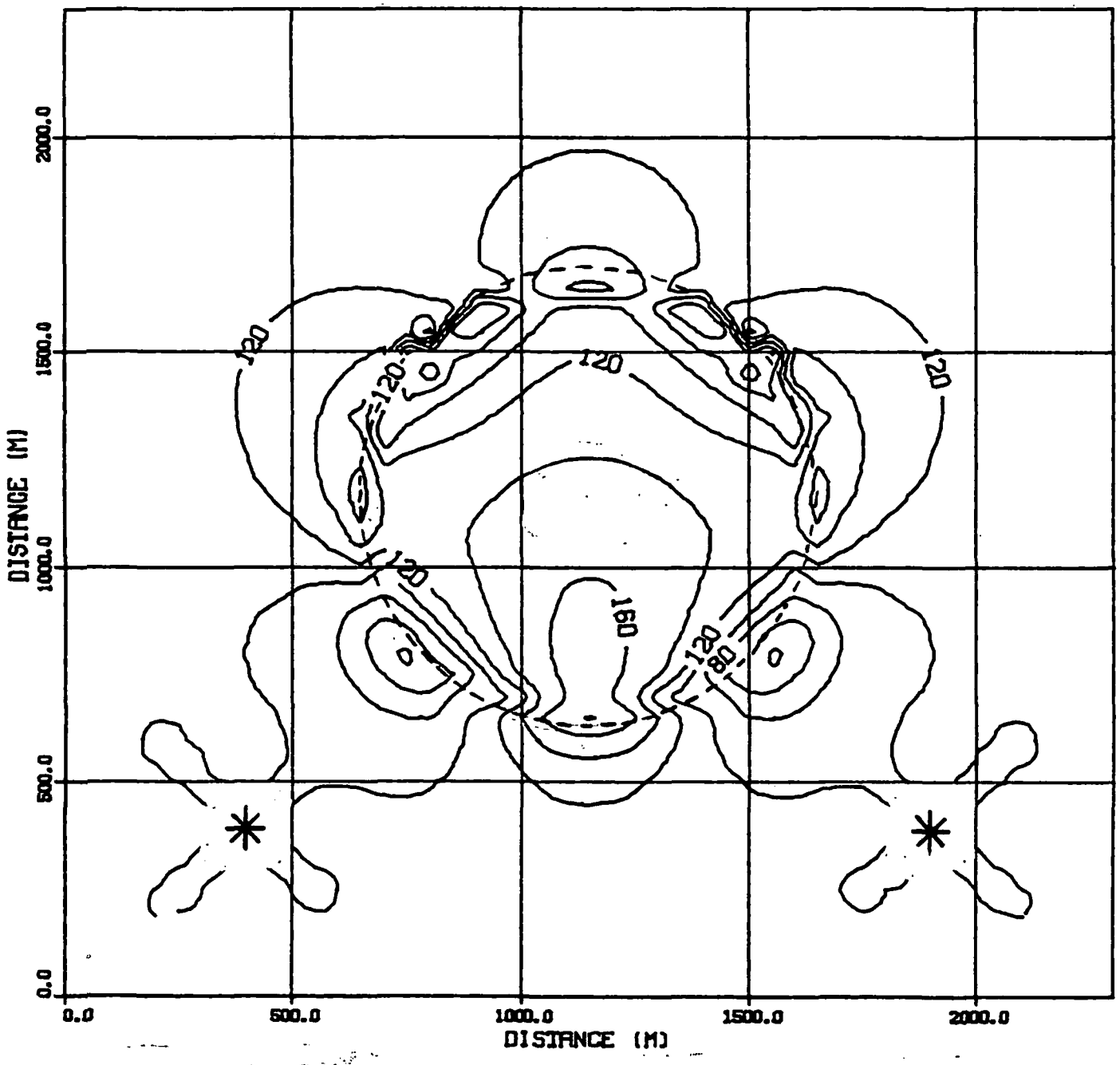

Figure 1. Bipole-quadrupole total field apparent resistivity response over a hemispherical topographic sink in a homogeneous half space. Half space resistivity is 100 ohm-meters. Contour interval is 20 ohm-meters. Asterisks (*) indicate the location of sources. The dotted circle is the edge of the topographic sink.

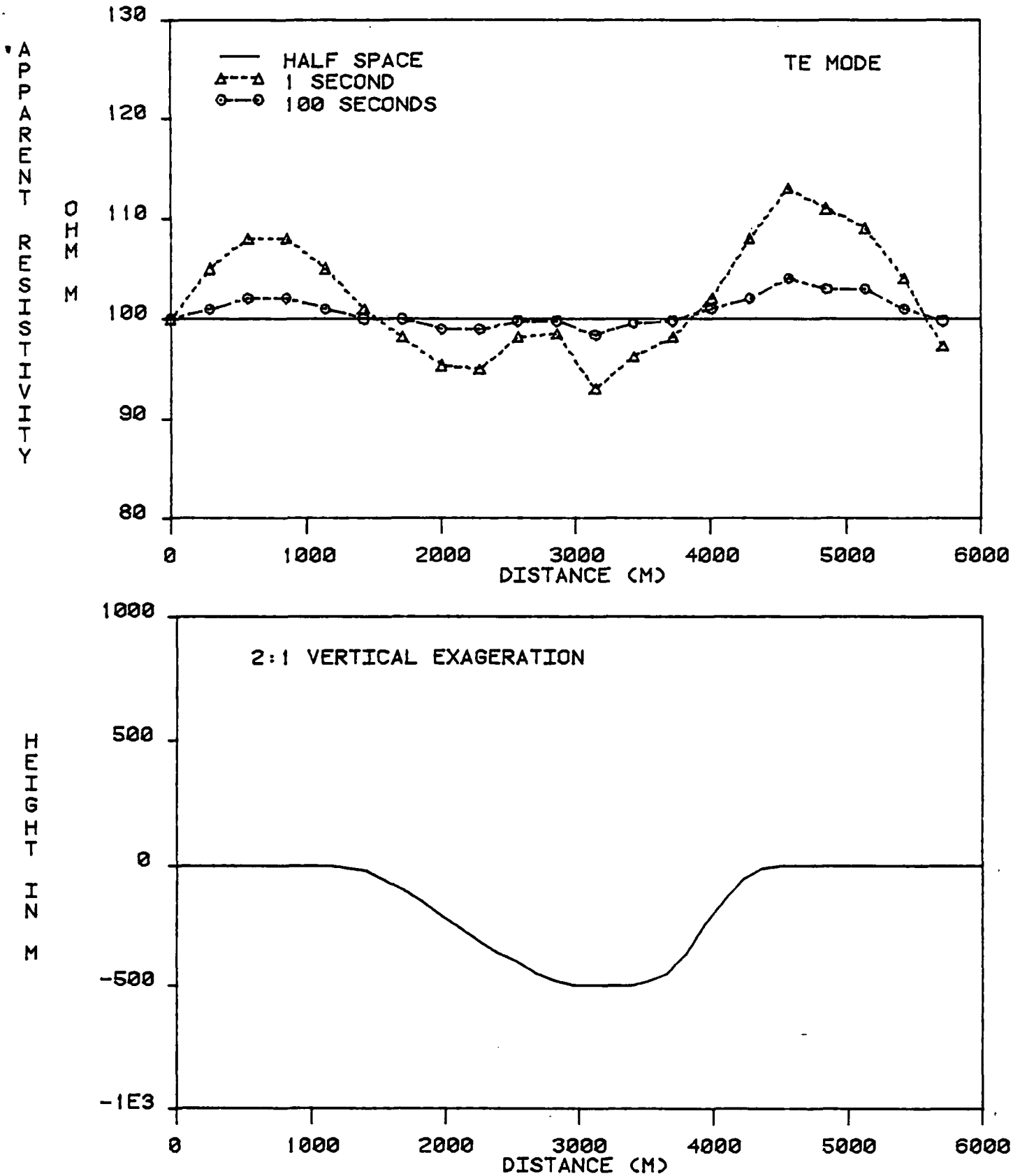

Figure 2. Transverse electric (TE) mode magnetotelluric response over an asymmetric two-dimensional valley in a homogeneous half space . Half space resistivity is]00 ohm-meters.

Geoexploration, 15 (1977) 207—238

© Elsevier Scientific Publishing Company, Amsterdam — Printed in The Netherlands

THE TELLURIC METHODS IN THE STUDY OF SEDIMENTARY STRUCTURES — A SURVEY

SULHI H. YUNGUL

*Chevron Oil Field Research Company, La Habra, California (U.S.A.)**

(Revised version received June 24, 1977)

ABSTRACT

Yungul, S.H., 1977. The telluric methods in the study of sedimentary structures — a survey. Geoexploration, 15: 207—238.

Telluric and magnetotelluric methods are compared from principle and application standpoints, particularly as applied to the study of sedimentary basins, as two distinct methods: magnetotelluric by its completeness, and telluric by its simplicity and economy.

Theory and practice of the relative, intrinsic, and absolute ellipse methods, single-station methods, and hybrid magnetotelluric methods are described, emphasizing physical understanding, with a view to assisting prospective users. Qualitative and quantitative interpretation methods for two- and three-dimensional structures are discussed, with the aid of case histories.

Telluric methods are suited primarily to low-cost reconnaissance in not-too-deep sedimentary structures associated with lateral changes in electrical resistivity that are frequently encountered in petroleum and geothermal exploration.

This paper is primarily a literature survey, but includes some original material. Some procedures that are explained only in patents have also been included.

INTRODUCTION

The four major branches of electrical methods suitable for the exploration of sedimentary basins are: controlled-source dc (resistivity), controlled-source ac (electromagnetic), telluric, and magnetotelluric. Among these, perhaps the telluric method has been covered the least in the English literature.

Telluric currents are induced in the earth by natural electromagnetic waves of extraterrestrial origin. The telluric method uses only the horizontal components of the electric field, E, associated with these currents, at the surface (*tellus* and *telluris* mean the earth in Latin). The magnetotelluric method uses both the horizontal components of E and the three orthogonal components of the magnetic field, H, associated with E, measured simultaneously at each measuring site.

These methods are based on the same theory, but are much different in cost. They are used to solve different kinds of exploration problems in pe-

*Now with Chevron Resources Company, P.O. Box 3722, San Francisco, California, U.S.A.

NOTATIONS

B	Base station
F	Field station
MT	Magnetotelluric
E (vector)	Electric field intensity, mV/km, in practical units
H (vector)	Magnetic field intensity, gamma, in practical units
$E_{/\!/}$, $H_{/\!/}$	Components parallel to the geologic strike
$E_\perp$, $H_\perp$	Components perpendicular to the geologic strike
ρ	Resistivity, ohm-m
ρ_e	Effective horizontal resistivity of a stack of horizontal layers
ρ_a	MT apparent resistivity
$\rho_\perp$	ρ_a derived from $E_\perp$ and $H_{/\!/}$
$\rho_{/\!/}$	ρ_a derived from $E_{/\!/}$ and $H_\perp$
S	"Horizontal unit conductance" of a stack of horizontal layers, mho
S zone	A frequency window in which instantaneous dc assumption is justified
T	Period, sec

troleum, geothermal, and mining geophysics.

The primary purpose of this paper is to survey the principles and procedures for a variety of telluric methods. Low-cost telluric methods will be emphasized, because the cost of telluric surveys, unjustly compared with that of gravity surveys, hampered their use in the past. The emphasis will be on methods and procedures with established economic usefulness, presented for users whose daily functions do not involve a great deal of mathematics. We shall assume that the reader is somewhat familiar with the magnetotelluric method (MT), which is extensively reviewed by Vozoff (1972).

Geophysicists not familiar with the telluric method believe that it has been replaced by MT. This paper will show the need for both, frequently used in conjunction. Recent experience, especially in prospecting for geothermal resources, supports this point of view (Morrison et al., 1975; Maas, 1975; and Hermance and Thayer, 1975).

The first practical telluric techniques were developed by Schlumberger (1936, 1941). The "relative ellipse area" method by Kunetz (1952a) constituted a milestone, in that scalar telluric anomalies could be assigned to measurement sites. This method is described by Boissonnas and Leonardon (1948); their article is probably the earliest significant English literature on this subject.

A comprehensive paper by Migaux (1951) describes the principles and geologic significance of the telluric method. A review paper by Kunetz (1958) contains many interesting case histories concerning petroleum exploration.

Another milestone was a book by Berdichevskii (1960) which contributed substantial quantitative information on the telluric method. This was done on the basis of then newly developed MT theory.

Other important contributions will be discussed or referenced under specific topics.

TELLURIC AND MAGNETOTELLURIC METHODS COMPARED

Figure 1a is a cross-section (a two-dimensional model) representing a salt ridge in a deep, unusually low-resistivity sedimentary basin, similar to the Texas Gulf Coast. The two near-surface inhomogeneities could represent fresh-water sands.

Figure 1c shows the computed MT sounding curves at stations *A*, *B*, and *C*. The dotted curves are the results obtained ignoring the near-surface inhomogeneities. The solid line curves have been computed for the complete model. Apparent resistivities obtained using that component of the electric field which is in the direction of geologic strike are designated $\rho_{\parallel}$; in the transverse direction, $\rho_{\perp}$. Data at *B* would be interpreted in a straightforward way, in terms of a one-dimensional model, and yield very valuable information; it would resolve some of the layers if they existed.

The dotted curves at *A* cannot be interpreted by themselves. Such curve pairs at a number of stations over the salt ridge have to be satisfied simultaneously by two-dimensional trial-and-error modeling. Such interpretations are laborious and the surveys are relatively expensive.

Including the near-surface inhomogeneities (the solid line MT sounding curves) makes the situation much worse; the $\rho_{\perp}$ curves diverge by a factor of about 10 if the station is displaced as little as a few hundred feet. The measuring axes can analytically be rotated to obtain $\rho_{\parallel}$, which is not much affected by the inhomogeneities, and $\rho_{\parallel}$ may be interpreted without the benefit of $\rho_{\perp}$. However, this is possible only if the near-surface inhomogeneities and deep structure are two-dimensional and have the same strike, which is unusual. A space-domain filtering of the data is not practical, because MT surveys used in petroleum exploration cost $ 1000 to $ 4000 per station.

Figure 1b shows a profile of normalized electric field components across the model for a sine wave whose period is 300 seconds. $E_{\parallel}$ is parallel and $E_{\perp}$ perpendicular to the strike. These data, which constitute essentially a telluric survey, are extracted from a survey made without knowing the strike direction. The effects of inhomogeneities can be filtered out if there are sufficient data points, and the salt ridge anomaly can be isolated and interpreted. One can have a high density of telluric stations, because the cost is about one-tenth that of MT. Choice of the proper solution from the infinite number available requires help from other kinds of data. This might be a few MT soundings at sites judiciously selected through the telluric data.

Another consideration is the search for relatively small three-dimensional features such as salt domes, reefs, and geothermal reservoirs (with or without near-surface inhomogeneities). Such surveys require many stations; Fig. 12 shows 287. An MT survey with the same number of stations would be very expensive. Also, most of the wealth of MT data thus obtained could not have been used effectively, because interpretation of MT data in terms of three-dimensional structures is not yet practical.

The telluric method is primarily a lateral exploration tool, similar to

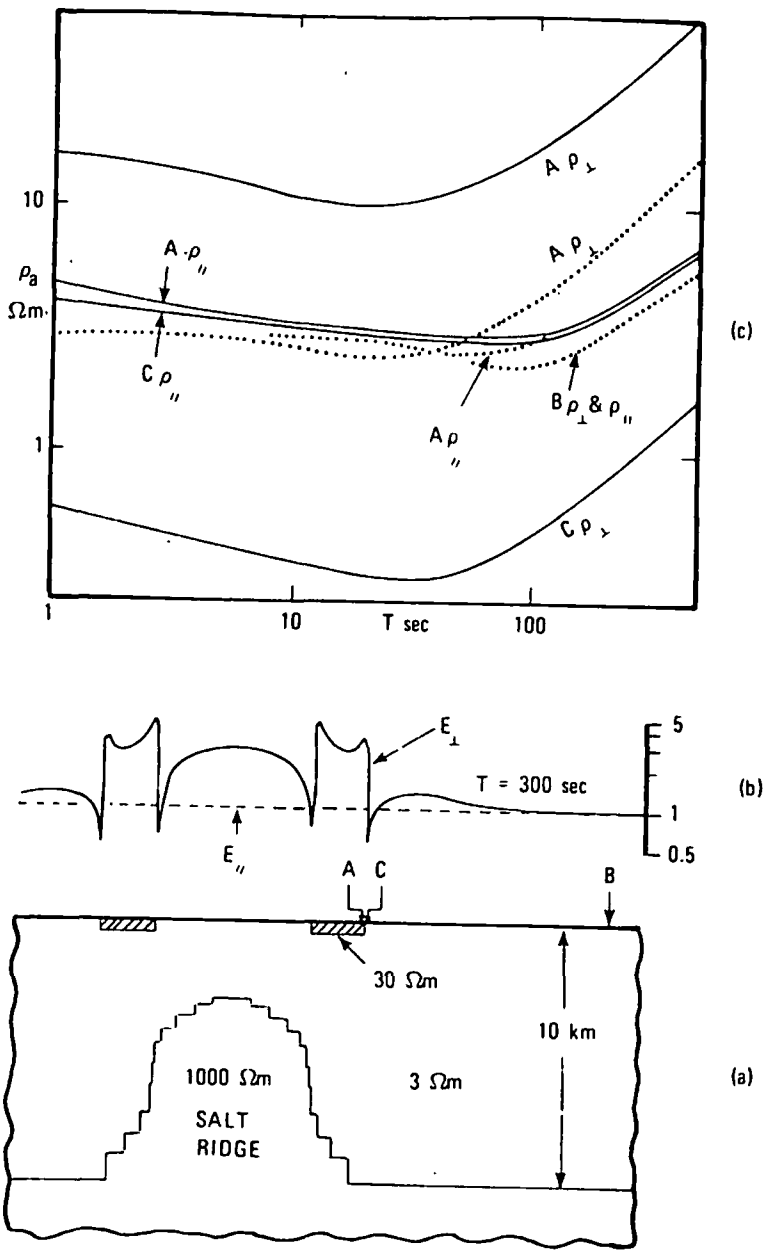

Fig. 1. Numerically computed magnetotelluric and telluric responses of a two-dimensional hypothetical structure. Dotted magnetotelluric sounding curves would have been obtained if the 30-ohm-m near-surface inhomogeneities were not present. (This model was originally constructed by this author in 1970 and a modified version of it was published by Ward et al., 1973.)

resistivity mapping with an immense feeding dipole length. The measured anomalies are almost entirely due to lateral variations in electrical resistivity. MT is, at its most effective, a vertical exploration tool similar to resistivity sounding, that yields well-log type information; the milder the lateral resistivity variations in sedimentary basins, the more rewarding the results.

The telluric method preceded MT by about two decades and led to it, but a quantitative understanding of the former was a by-product of the latter.

NATURAL ELECTROMAGNETIC FIELDS

The earth's natural electromagnetic fields have a very broad frequency range, from years per cycle to megacycles per sec. The telluric method, in its application to the study of sedimentary basins, usually makes use of the daytime electromagnetic signals with periods of about 5—600 sec. These "geomagnetic micropulsations" are generated through the interaction of ionized gas clouds from the sun with the earth's quasi-stationary magnetic field and atmosphere. Most telluric surveys employ a class of micropulsations called "continuous pulsations of type 3", designated Pc3, whose period range is about 10—45 sec.

Several thousands of papers (and many reviews) have been written on the micropulsations, especially in connection with research in space physics. Two recent publications are a book by Jacobs (1970) and a 50-page review paper by Orr (1973).

The phenomena are called magnetic instead of electromagnetic micropulsations because the amplitude of the electric field is highly dependent on local geology and does not clearly show the worldwide properties of the fields. The magnetic field, on the other hand, depends little on the local geology. This is why the telluric method uses E instead of H; the geological diagnostic power resides mainly in E. In MT the primary role of H is in normalizing E to the source strength, whereas in telluric work E at each field station is normalized to E at the base station. Amplitude of E, also affected by the frequency, time of the day, season, and latitude, is very roughly 1 mv/km. Telluric currents "scan" the subsurface from all directions, usually displaying a statistical elliptic polarization in a frequency band.

In sedimentary basins the signals can be considered plane waves (Madden and Nelson, 1964; and Srivastava, 1965). Also, the resistivity contrast between air and the earth is so large that waves with all angles of incidence are transmitted into the earth very nearly vertically. These considerations lead to the assumption that the signal is a vertically incident plane wave. This in turn implies that in a horizontally layered subsurface the telluric currents flow horizontally, that E is horizontally uniform (but amplitude and phase vary with depth), and that variations with horizontal distance are totally illogic. These assumptions are still controversial, especially for very long-period signals used in the study of the earth's crust beneath sedimentary basins (Tikhonov et al., 1974).

INSTRUMENTS AND EQUIPMENT

A horizontal component of E is measured by stretching an insulated wire on the ground, planting two electrodes at its ends, and measuring the potential difference between them. Two orthogonal components of E can be measured simultaneously by using three electrodes and an L-shaped wire.

Wire length largely depends on the nature of near-surface irregularities, which must be averaged out by using a sufficiently long wire; otherwise 100-ft. lengths would be suitable so far as instrument noise is concerned. It is possible to operate with 500-ft. lengths if the measuring sites are judiciously selected, but 1000-ft. lengths are recommended.

Electrodes used include non-polarizable (reversible) types of copper, cadmium, silver, or zinc. Bare copper pipes or lead plates are also used. This writer prefers weathered, paper-thin lead strips having no fresh surfaces, attached to the wire with an alligator clip. This seems to be the best compromise between precision and economics. The strips are expendable, so one does not have to walk to the end of the wire at the completion of measurements.

The instrument system for each channel consists of: a variable dc bias; a low-pass filter; a dc amplifier with an input impedance of at least 10 megohms; a band-pass filter; a strip-chart or "*X-Y*" recorder, depending on the technique used.

The amplifiers and recorders are off-the-shelf items; but the filters may be either homemade, to suit the geologic problem on hand or commercial variable pass-band filters. Overall system noise of less than about 3 μ V rms within the frequency band of interest is satisfactory, and not difficult to achieve. A two-channel system can be accommodated in a suitcase, less the power source.

PRINCIPLE OF THE TELLURIC METHOD

The structure analyzed in Fig. 2, shown in the upper left corner, is a horizontally layered sedimentary section overlying a high-resistivity half-space (the basement). Below it are shown the computed MT apparent resistivity (ρ_a) and phase (φ) curves as functions of T. The ρ_a curve minima and maxima on the left relate to the sedimentary layers; it then rises on the right to become asymptotic to the resistivity of the basement.

The section of the rising branch between T_1 and T_2 is close to a straight line having a slope of 45° in the logarithmic plot; let us assume that it is exactly so. This branch has to satisfy the well-known MT relationship (in the practical units mV/km, gamma, and ohm-m):

$$\rho_a = 0.2\, T\, |E_x/H_y|^2 \qquad (1)$$

A 45° straight-line relationship requires that in:

$$\log \rho_a = \log T + \log[0.2\, |E_x/H_y|^2] \qquad (2)$$

Fig. 2. Th
horizonta

the seco
impedan
zone" (Σ
mho's, o

$S = \sum_{i=1}^{n}$ (

where n
is depth
fective re
change s
layers an
Berdic

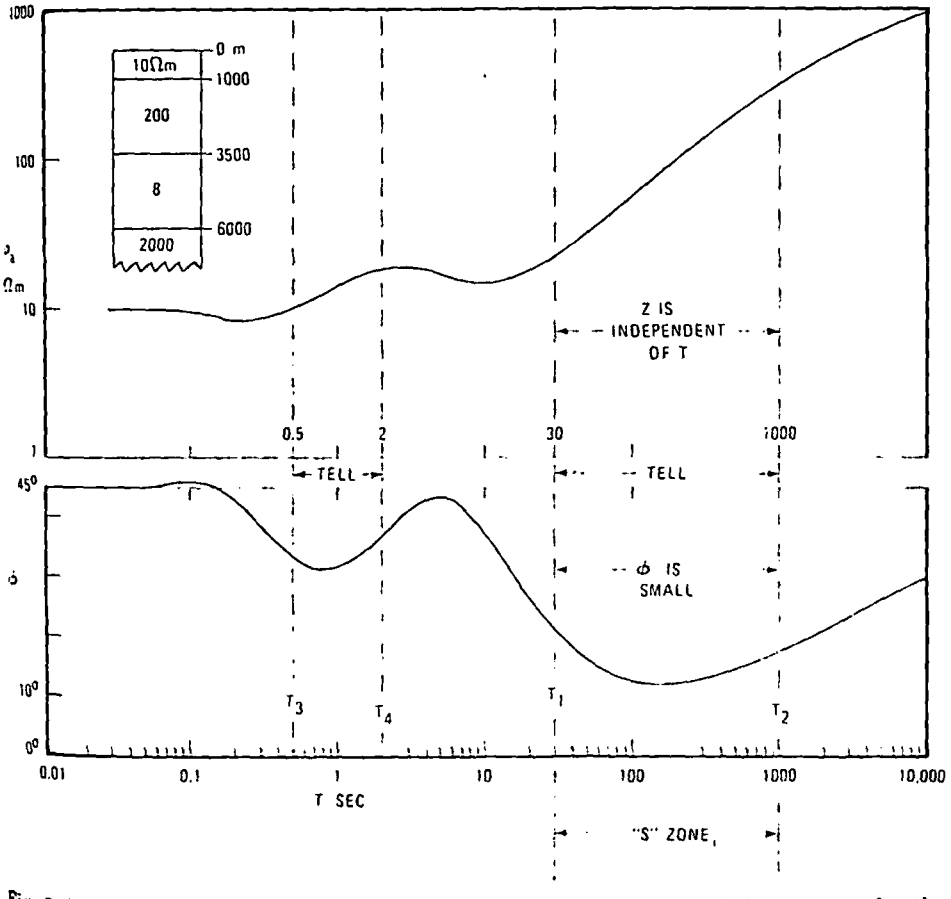

Fig. 2. Theoretical magnetotelluric sounding apparent resistivity and phase curves for the horizontally layered subsurface model shown at the upper left corner. Layers are isotropic.

the second term be independent of T. That is, within the T_1—T_2 range the impedance $Z = E_x/H_y$ is independent of T. The T_1 T_2 interval is called "S zone" (Berdichevskii, 1960); S is the "horizontal unit conductance", in mho's, of the sedimentary section:

$$S = \sum_{i=1}^{n} (h_i/\rho_i) = D/\rho_e \tag{3}$$

where n is the number of sedimentary layers, h_i are layer thicknesses, and D is depth to basement, both in m. This formula also defines ρ_e, called the "effective resistivity" of the sedimentary section. The 45° branch does not change substantially so long as S remains constant, no matter how many layers and what sequential combinations are considered.

Berdichevskii (1960) developed an asymptotic equation for Z for periods

longer than about T_1. His equation (in MKS units) is:

$$\dot{Z} = \frac{\dot{E}_x}{\dot{H}_y} = 1\Big/\left(S + \frac{10^3}{4\pi}\sqrt{\frac{T}{5\rho_b}}\, e^{i\pi/4}\right) \tag{4}$$

where ρ_b is basement resistivity, and dots represent complex quantities. Because Z is independent of T in the S zone, eq. 4 must then take the form:

$$Z = 1/S \text{ (in MKS)} \tag{5}$$

or:

$$Z \cong 796/S \text{ (in practical units)} \tag{6}$$

On the other hand the phase curve in Fig. 2 shows that the phase difference between E_x and H_y is small within the S zone and can be assumed to be zero. It follows that the impedance is approximately a real number (i.e., purely resistive); for instantaneous values the relationship between E and H is that of a dc electromagnetic field. The telluric field can be assumed to be an instantaneous dc field within the window T_1—T_2, and it will scan the total sedimentary section as such.

Figure 2 shows that another approximately dc window exists within the T_3 –T_4 range, for which the top of the 200 ohm-m layer would behave like a basement.

The S zone periods are such that the skin depth* for ρ_e is from about 1.5 to 10 times the depth to the basement.

So far we have based our argument on models of a horizontally layered subsurface. This would be valid if the measuring sites were far from lateral changes, or if the lateral changes were not abrupt. However, an important role of the telluric method is the study of abrupt changes, such as faults and subcrops. In reality, from the viewpoint of exact analysis, in such cases the dependence of Z on T, and the phase relationships become very complicated. However, theory and practice show that so long as one operates in the S zone, in terms of the average characteristics of the sedimentary section, the instantaneous dc assumption is still met satisfactorily, usually good enough for quantitative interpretation, as will be demonstrated later. When such is not the case, qualitative interpretation can be made. However, if the dc condition is met, the interpretation of measurements is drastically simplified.

Relationship between components of telluric field in S zone

In the general case, for one arbitrary frequency, f, of a plane wave in-

*The depth, z, at which the electromagnetic field reaches 1/e of its surface value:
$z = (1/2\pi)(10\rho T)^{1/2}$
where z is in km, ρ in ohm-m, and T is in sec.

cident to an arbitrary subsurface (inhomogeneous and anisotropic), the components of E and H are related by (Cantwell, 1960):

$$\dot{E}_x(t) = \dot{Z}_{xy}\dot{H}_y(t) + \dot{Z}_{xx}\dot{H}_x(t)$$

$$\dot{E}_y(t) = \dot{Z}_{yx}\dot{H}_x(t) + \dot{Z}_{yy}\dot{H}_y(t) \qquad (7)$$

where t is time, dots signify complex quantities, and Z's are the components of a surface impedance tensor. If we assume that within the S zone Z's are independent of frequency and the phases are negligibly small, $\phi \cong 0$, eq. 7 reverts to:

$$E_x(t) = C_1 H_y(t) + C_2 H_x(t)$$

$$E_y(t) = C_3 H_x(t) + C_4 H_y(t) \qquad (8)$$

where all quantities are real numbers, C's are constants depending only on the subsurface geology and the direction of the measuring axes, and $E(t)$'s are real-time series that include all frequencies within the S zone.

It follows that the components of E at two separate locations (measured along the x, y-axes at a base station B and along the u, v-axes at a field station F) are also linearly related:

$$E_u(t) = a\,E_x(t) + b\,E_y(t)$$

$$E_v(t) = c\,E_x(t) + d\,E_y(t) \qquad (9)$$

where constants a, b, c, and d depend only on the directions of the coordinate systems and subsurface geology.

RELATIVE ELLIPSE AREA METHODS

The relative ellipse and triangle methods

These methods were developed by Kunetz (1952a). In eq. 9 the instantaneous E-values can be replaced by synchronous increments between time intervals:

$$U = aX + bY \text{ and } V = cX + dY \qquad (10)$$

where capital letters signify components of a pair of conjugate variation vectors, ΔE_F at F and ΔE_B at B. These correspond to an arbitrary time interval, $\Delta t = t_2 - t_1$, as schematically shown in Fig. 3. Such strip chart records are called tellurograms.

The x, y-system at B and the u, v-system F are oriented arbitrarily. If a number of pairs of such conjugate variation vectors are determined, and those at F are normalized to the magnitudes of their conjugates at B, the normalized ΔE_F traces an ellipse whose area is equal to:

$$\pi J = \pi\,|ad - bc| \qquad (11)$$

where J is the Jacobian of the transformation from the x, y-system to the u,

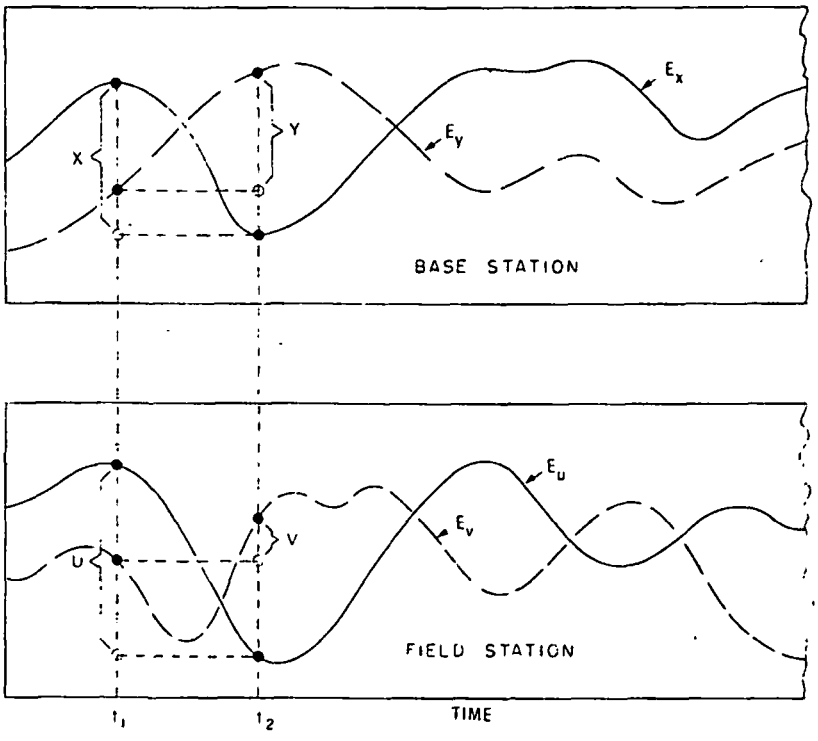

Fig. 3. Hypothetical tellurograms representing simultaneous recordings along orthogonal measuring axes x, y at base station and u, v at field station. (Reproduced from Yungul, 1968.)

v-system. Normalization is equivalent to assuming that ΔE_B traces a circle; and a circle at B transforms into an ellipse at F through eq. 10.

Experience shows that fairly regular ellipses are obtained, an indirect proof of the validity of eq. 10. The ellipse, and therefore J, is an invariant for a pair of measuring stations, depending only on the geology at F and B. The ellipse at F is called the "relative ellipse", and J is the "relative ellipse area".

Theoretically two pairs of conjugate vectors, determined by eight components, are sufficient to solve for J from eq. 10. The ratio of the areas of two conjugate triangles formed by these vectors is:

$$J = \frac{|U_1 V_2 - U_2 V_1|}{|X_1 Y_2 - X_2 Y_1|} \tag{12}$$

This is called the "triangle method", which yields J without constructing an ellipse.

Usually many triangles are constructed at each site, and a statistical value is determined among the selected ones. There is considerable scattering, due to: (1) experimental error; (2) cultural electrical noise; and (3) the fact that

eq. 10 is not rigorously satisfied. At least ten selected triangles must be used to obtain one J-value. This involves a total of eighty selected components. The procedure for the triangle method, described in detail by Berdichevskii (1960), is tedious, expensive, and requires considerable skill. It also requires at least 30-min record sections. It does not readily lend itself to digital computer processing, because favorable time intervals are visually selected first and then the resulting variation vectors are subjected to another visual selection.

Coefficients a, b, c, and d can be calculated graphically (Y-Shu, 1963), but the difficulties are essentially the same as in the triangle method.

The intrinsic ellipse method

Approximate values of J can be obtained by an automated version of Kunetz' (1952b, 1957) "intrinsic ellipse" method.

As with the triangle method, tellurograms are obtained at F and 3 along the u, v- and x, y-axes; a schematic one is shown in Fig. 4a. A synthetic tel-

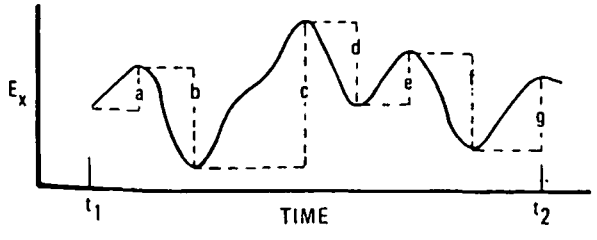

(a)

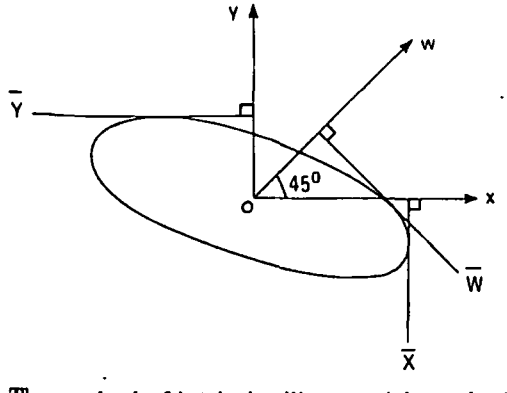

(b)

Fig. 4. The method of intrinsic ellipse. a. A hypothetical tellurogram. b. Determination of the intrinsic ellipse by means of its tangents.

lurogram is computed for the median direction of the measuring axes, such as along the w-axis (Fig. 4b). The median direction tellurogram can also be obtained directly in the field, by means of a third measuring line. The total variations on the tellugrams are computed for a selected time interval, say 15 minutes. On Fig. 4a the total variation along the x-axis is the numerical summation of the peak-to-trough excursions:

$$\bar{X} = a + b + c + d + e + f + g$$

A straight line perpendicular to the x-axis, drawn at distance $\bar{X}$ from the origin, constitutes a tangent to the intrinsic ellipse (Fig. 4b). The ellipse is determined by its origin and three tangents. Its area at F is (Kunetz, 1952b):

$$A_F = \frac{\pi}{2} \{[(\bar{X} + \bar{Y})^2 - 2\bar{W}^2]\ [2\bar{W}^2 - (\bar{X} - \bar{Y})^2]\}^{1/2} \tag{13}$$

The ratio of A_F to A_B is approximately equal to J. Kunetz' (1957) comparison of the intrinsic ellipse and triangle (or relative ellipse) methods shows a mean deviation of 7% between J's.

The intrinsic ellipse method can readily be processed by digital computer. The total variations can also be obtained directly in the field, by means of counters (Kunetz, 1957). I have found that for computerized automatic processing of 20-min tellurograms, the accuracy of J deteriorates as ellipticity increases. Sometimes eq. 13 yields imaginary values. This would be helped by using longer record sections and measuring the third component in the field. The procedures of this method are described in detail by Thieme (1963).

Azimuth and ellipticity of the intrinsic ellipse have some geological significance, as will be discussed under Absolute Ellipse Methods.

The vectogram method

I find that the most economical method of determining J, compared with the ellipse, triangle, and intrinsic ellipse methods, is polar diagram recording of E on "X-Y" recorders (Yungul, 1968).

Figure 5 shows a pair of vectograms, obtained approximately simultaneously at F and B, in about 1 min of recording time. The band-pass filter was peaked at T = 20 sec. The ratio of any single or combination of closed areas at F, including the tangents, to the conjugate at B is equal to J. This is in accordance with eq. 10. About a dozen J-values can be measured from this pair, but three, obtained from the contours (1, 2,3), (3, 4, 5), and (2, 3, 6), will suffice.

Normally a few such vectogram pairs are obtained at each field station. Many fewer J-values are needed than in the triangle method, because each closed area is equivalent to the average of several triangles. The measurement

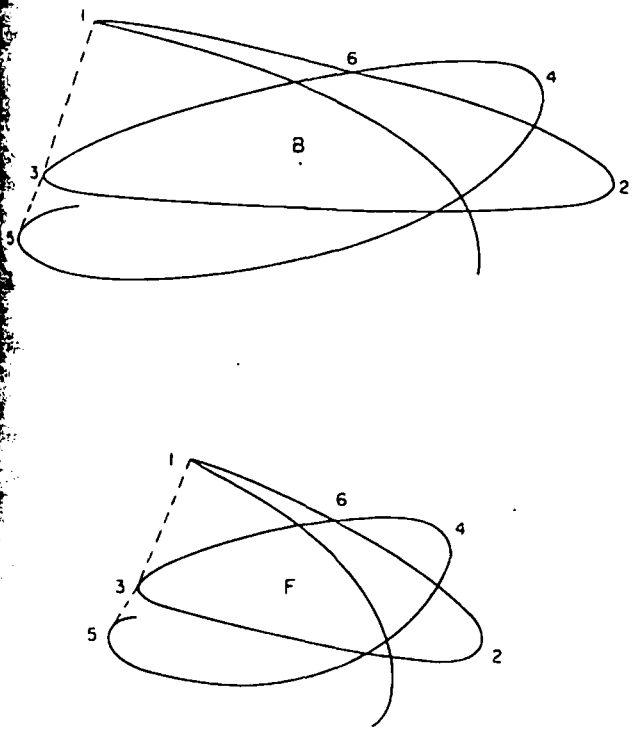

Fig. 5. A pair of actual vectograms, recorded simultaneously at base station (B) and field station (F), over a period of about one minute. (Reproduced from Yungul, 1968.)

of closed areas effectively integrates the undesirable signals and noise of relatively higher frequencies.

I have found that the standard deviation for the vectogram method is about one order of magnitude lower than for the triangle method, at the same 20-min recording interval (Yungul, 1968).

Approximately simultaneous vectograms can be obtained at F and B through oral communication by means of portable radio transmitters. One man at 3 can manage three or four F crews. The closed areas on the vectograms can be measured with a planimeter, without need for accurate time-tying.

At locations where E is somewhat linearly polarized the accuracy of J becomes low and sometimes unusable with the triangle method. Not so with the vectogram method; one can wait perhaps several minutes, until one or two nonlinear loops occur.

ABSOLUTE ELLIPSE METHODS

We have discussed the intrinsic ellipse method in terms of J only, but the ellipticity and azimuth of the intrinsic ellipse at F also have geological sig-

nificance. Ellipticity is large if dips are steep or F is near a lateral discontinuity, and small if the subsurface is nearly horizontally layered. Where F is on the axis of an anticline, the long ellipse axis tends toward perpendicular to the anticline's axis; where F is on the anticline's flank, the axis tends toward parallel to the anticline's axis (Kunetz, 1952b). This is entirely independent of the geology at B. However, ellipticity and azimuth at F depend on the polarization of the source field as well as the geology at F. In my experience, the azimuth may vary tens of degrees from one 15-min record section to another. Kunetz (1957) states that a record perhaps 1 month long would be needed to obtain stable ellipticity and azimuth, an "absolute ellipse". This procedure would, of course, have very little economic value, but it is possible to obtain one absolute ellipse at B and mathematically transform relative ellipses at F's into absolute ellipses (Tkachev, 1963; and Gugunava and Chernyavskii, 1964). Tkachev obtained the absolute ellipse at B by averaging the 15° beams of the variation vectors. This procedure is based on the assumption that a long time average at B cancels out source polarization effects, so that the absolute ellipse at B depends solely on the geology there (which probably cannot be guaranteed). We shall discuss this subject further under Hybrid Magnetotelluric Methods.

SINGLE-STATION METHODS

Statistical analysis of E-data obtained at one site over a relatively short time, say 3 hrs, can yield some geological information at that site (Yungul, 1961), but such techniques are primarily of academic interest. In what follows we shall confine ourselves to economical exploration methods.

Split-spread method

Figure 6 shows a field setup having a collinear and equally spaced three-electrode array. The two potential differences, each one being between the center electrode and one outer electrode, are simultaneously recorded on the same strip of paper for about 20 min. The result is a pair of somewhat meshing tellurograms at each setup.

Proceeding as with seismic reflection continuous profiling (overlapping spreads), hence the terminology "split-spread", one can determine J-values at midpoints of consecutive electrode pairs; e.g., at N with respect to M, and at 0 with respect to N, all normalized to M. Theoretically, determination of J requires two-dimensional (x, y) data, whereas this procedure provides only one-dimensional (x) data; nevertheless J-values are obtainable if ΔE scans the subsurface from various directions and if it is assumed that the subsurface is, piecewise, two-dimensional in the immediate vicinity of each spread (Yungul, 1965).

On each pair of tellurograms the peak-to-through amplitudes of somewhat meshing events are measured with an expanding-scale type of ruler, and the

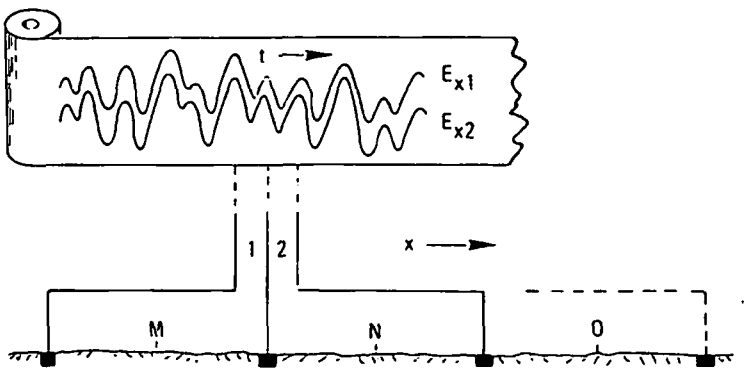

Fig. 6. The method of split-spread. Field setup and a hypothetical tellurogram.

ratio, R, of these amplitudes are computed:

$$R = \frac{\Delta E_{x1}}{\Delta E_{x2}} \tag{14}$$

About 30 R-values are obtained and plotted, either as dot histograms or sequentially (Fig. 7). In general, R has a large amount of dispersion. Then J-values are picked by visual inspection of these histograms, as explained below.

Suppose that the horizontal acute angle between the geologic dip direction and the spread is ϕ, which is arbitrary and unknown. In theory (unpublished) R varies, in general, from $-\infty$ to $+\infty$ for each setup. However, if ΔE_x's are taken from somewhat meshing events, the following theoretical and approximate relations are obtained:

If $\theta = 90°$ (spread along the strike), there is no dispersion in R; R and J equals J.

If θ is small, say 10°, dispersion in R is small; J equals average R.

If θ is large, say 20°–70°, dispersion in R is large; it varies from 1 to J; therefore J equals the maximum deviation of R from 1.

If θ is close to 90°, say 80°, dispersion in R is small; J equal the maximum deviation of R from 1.

If $\theta = 90°$ (spread along the strike), there is no dispersion in R; R and J equal 1.

Figure 7 shows four actual cases; also how J's are picked from R histograms. The histograms are plotted on a logarithmic R-scale, to reduce office work by applying the calibration factor to only the picked J-values.

The measurement of J is repeatable within about 5% if cumulative errors are adjusted by tilting long profiles, because random errors accumulate as $\sqrt{n}$, where n is the number of setups (stations). The J's are usually within about 10% of those obtained by the triangle method, if cumulative errors are adjusted.

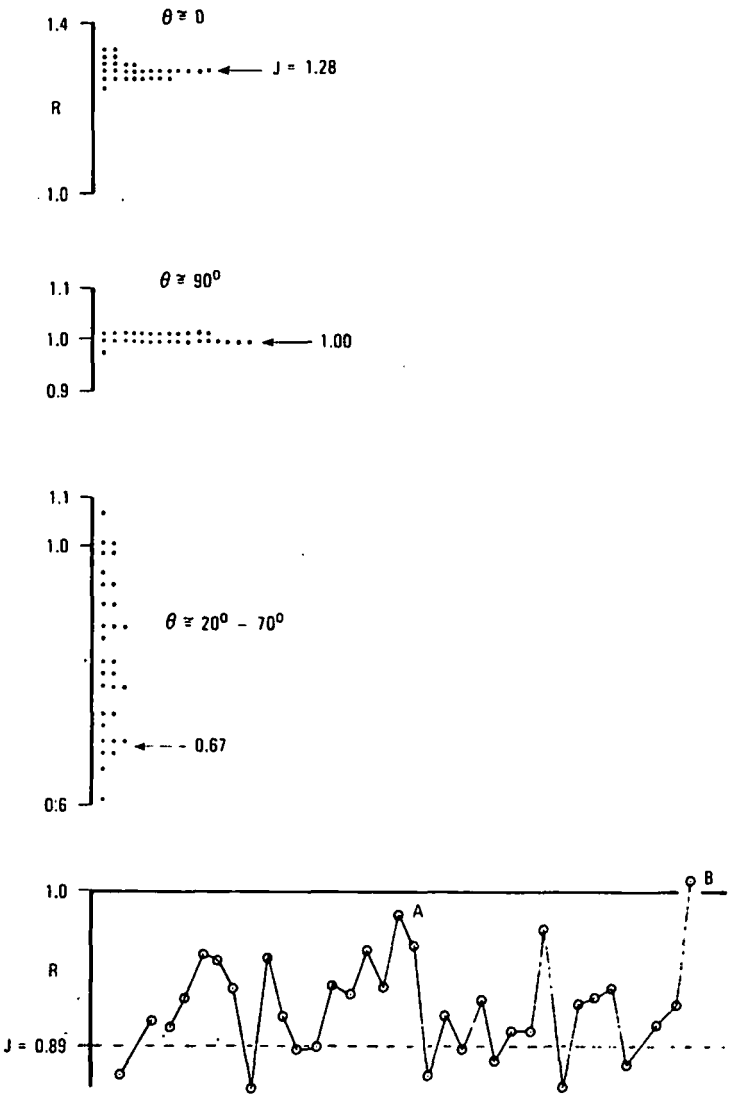

Fig. 7. Actual examples of processed data with the split-spread method. R is amplitude ratio; θ is angle between geologic dip direction and line of electrodes.

The split-spread method has very high resolution for local and very small anomalies associated with such features as pinchouts and minor faults, as will be shown under Interpretation (see Fig. 10); however, it suffers from long-distance and regional accuracy. Data processing at the office is extremely simple, but R-values can be obtained directly in the field, by means of special instruments.

The leapfrogging collinear three-electrode procedure was used by Neuenschwander and Metcalf (1942) and Dahlberg (1945), from 0.5 Hz to several

kHz. Their analyses were confined to extracting relative noise levels or average amplitude ratios, which would yield repeatable and geologically analytically significant data only when θ is either 0° or 90°.

T-spread method

It is sometimes desirable to obtain dip and strike information at an isolated field station. Here dip and strike pertain to the gross electrical anisotropy (macro- and micro-anisotropy combined). A third measuring wire spread is laid perpendicular to the split-spread from the middle electrode to form a T-shaped spread (Yungul, 1967). Three simultaneous tellurograms are recorded on the same strip chart. First, the split-spread data are obtained (Fig. 7). If the data turn out to be as in the example shown at the top of Fig. 7, no further analysis is needed: the split-spread is perpendicular to the strike, and the J-value indicates the dip azimuth. (J is less than unity on the down dip side, as will be explained under Interpretation.)

For an arbitrary orientation of the T-spread, the split-spread data will come out as shown at the bottom of Fig. 7. Here R-values A and B are close to unity, so for A and B the variation vector ΔE was nearly parallel to the strike. Now the direction of this ΔE can be determined by means of the third spread, and this will be the strike direction. The dip azimuth is determined by J, as explained above.

Cross-spread method

If the third recording channel that the T-spread method requires is not available, the dip and strike information can be obtained by making two consecutive split-spread measurements, obtaining J_1 first, and then J_2 from a spread formed by rotating the first spread 90° around the middle electrode. This method actually yields more precise results than the T-spread, although it requires a little more work. The data analysis is described below.

The boundary conditions show that any one telluric current sheet in the subsurface, say at a unit depth under the center electrode, can be replaced by the top of a fictitious insulating basement without perturbing E at the surface. If the top of this basement immediately under the cross-spread is assumed to be an arbitrarily inclined plane under a homogeneous and isotropic geologic section, then the J's are approximately inversely proportional to depths to the basement, as will be explained under Interpretation. Thus, it is a simple geometry problem to relate independently normalized J_1 and J_2 on one hand and the azimuth of the dip of this basement on the other. The basement is determined by a triangle having one corner vertically below the center electrode and two corners below the reference points of J_1 and J_2, at depths 1, D_1 and D_2 respectively, where:

$$D_1 = 2/(J_1 + 1) \text{ and } D_2 = 2/(J_2 + 1) \qquad (15)$$

HYBRID MAGNETOTELLURIC METHODS

Cagniard (1953) stated that MT data can be obtained at sea by measuring H at a base station (B) on land and E only at sea stations. Observations substantiate the theory that horizontal components of H should not change from one site to another, in particular if the geologic formations do not have steep dips and abrupt lateral variations. Let us call this modification a "roving MT".

It is now common practice to use this procedure to lower costs on land where logistics and surface conditions are difficult, such as in marshy or arctic regions. For instance, H is measured only at one station for all MT stations within about a 5-mi radius. However, H can change by a factor of about 1.5, in 5 mi, if the subsurface has major lateral variations (see, for instance, Hughes, 1974). This effect is frequency-dependent and can lead to serious errors.

I was able to modify and simplify Cagniard's roving MT so as to produce MT data with or without magnetic measurements (Yungul, 1966); in particular, by confining the E-measurements to the approximately $E_\perp$ components (perpendicular to the average strike of major geologic features). The subsurface at B is known from a dipole sounding, an MT sounding, or a well log. $E_\perp$ is measured simultaneously at B and F. It is well known in MT theory that for an exactly two-dimensional subsurface, $H_\parallel$ is exactly the same everywhere at the surface if the air resistivity is assumed infinite. All that is necessary is to obtain amplitude ratios of $E_\perp$ at F to those at B for the frequencies of interest. The square of this ratio multiplied by the $\rho_\perp$ of the theoretical (or actual) MT sounding curve at B yields the $\rho_\perp$-value at F.

Needless to say, this simple and inexpensive procedure is sensitive to deviations from two-dimensional tectonics, and the lack of complete MT data makes it difficult to cope with near-surface inhomogeneities. This method was evaluated by Crews (1972).

This method can be further extended, at least theoretically, to the case in which neither a theoretical nor a real MT sounding curve exists at B, for a subsurface consisting of n horizontal layers at B and m horizontal layers at F, if the parameters of only one layer are known (Yungul, 1966).

Another modification of Cangiard's roving MT (Hermance and Thayer, 1975) requires one set of MT measurements at B. The remainder of simultaneous measurements at B and F are confined to E. With reference to eq. 7, components Z^{ij} of the surface impedance tensor $[Z_B]$ can be determined at B from MT measurements by means of well-known procedures. (See, for instance, Vozoff, 1972.)

Equation 9 relates the components of E at B to those at F and, returning to complex quantities, defines a "telluric transfer tensor", [T], whose components are T_{ij}. This can be computed in the same manner as Z_{ij}. If it is assumed as before, that H is the same everywhere, impedance tensor $[Z_F]$ at F is equal to the product of [T] and $[Z_B]$; this is MT data at F.

This method seems to be a little more economical than Cagniard's roving MT, but involves one more assumption: the existence of an exact telluric transfer tensor [T] at all frequencies of interest.

In a book by Porstendorfer (1975, p. 65—80) the telluric and magnetotelluric tensor relationships are treated in a unified fashion.

In the Introduction we first discussed MT, then mainly considered the instantaneous dc condition, which can be called the "real telluric method". We have now come nearly full circle, back to MT.

I believe that the real telluric and real MT methods have definite and lasting places in applied geophysics: MT by its completeness, and telluric by the distinct factors of simplicity and economy. Simplicity is important in that it renders an occasionally used method readily available. Whether the hybrid methods also have definite and lasting places seems to be open to question.

INTERPRETATION

The geologic significances of the ellipticity and azimuth of an absolute ellipse have been briefly described under Absolute Ellipse Methods.

The ellipticity and azimuth of a relative ellipse also have some geologic significance; however, these depend on the geology at B as much as that at F. Their interpretation can be misleading unless B happens to be in a region of horizontally layered subsurface. Consequently, relative ellipses are generally not constructed; only their areas, J, are determined. In what follows we shall confine ourselves to the interpretation of J. Contour maps of J are called "telluric anomaly maps".

Qualitative interpretation

To facilitate understanding of the geologic significance of J, we shall confine discussion to two-dimensional structures. For a two-dimensional structure whose strike is in the y-direction, J at F is equal to the E_x-ratio at F to that at B:

$$J_F = E_{xF}/E_{xB} \tag{16}$$

For a dc field E_y is the same everywhere, and an E in the x-direction does not generate any y-component. This implies that in eq. 9, $b = c = 0$, $d = 1$, and $J = a$, hence eq. 16.

Approximately two-dimensional anomalies can be obtained by constructing J-profiles from a telluric anomaly map along directions substantially perpendicular to contours.

We can mentally construct a two-dimensional analog model that replaces: (1) the electric current by a nonturbulent fluid flow: (2) the electrical conductivity ($1/\rho$) distribution by a fluid permeability distribution; and (3) E by fluid velocity v. This can be done because both phenomena are governed by the same equations and boundary conditions. This anology is helpful in

visualizing qualitatively what kind of J-distribution to expect at the surface of the earth over certain geologic models. For most people water velocity is easier to visualize than E.

Figures 8 and 9 schematically show the J-anomalies associated with typical structures in sedimentary basins. Several of these characteristic effects may be included in one model. Let us now examine a few case histories corresponding to some of these schematic models.

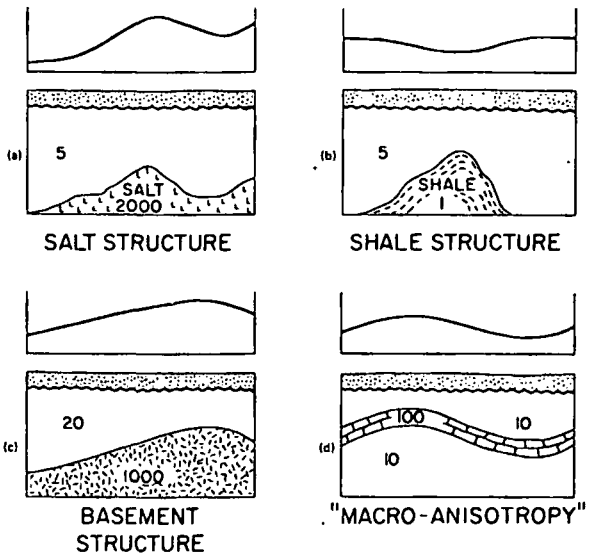

Fig. 8. Schematic telluric anomalies due to two-dimensional hypothetical structures. Numbers represent resistivities in ohm-m.

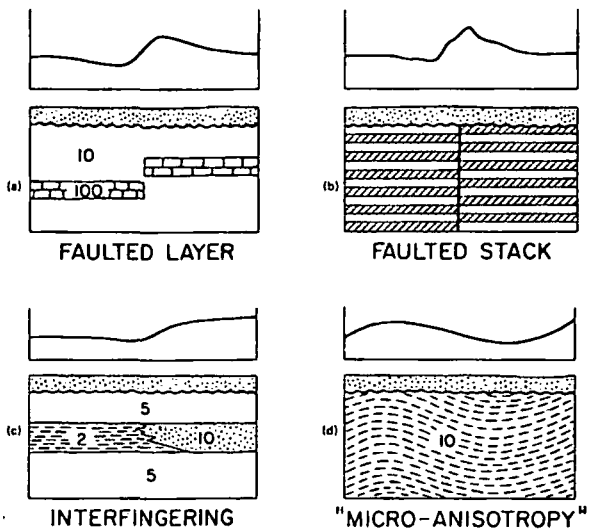

Fig. 9. Same notations as in Fig. 8.

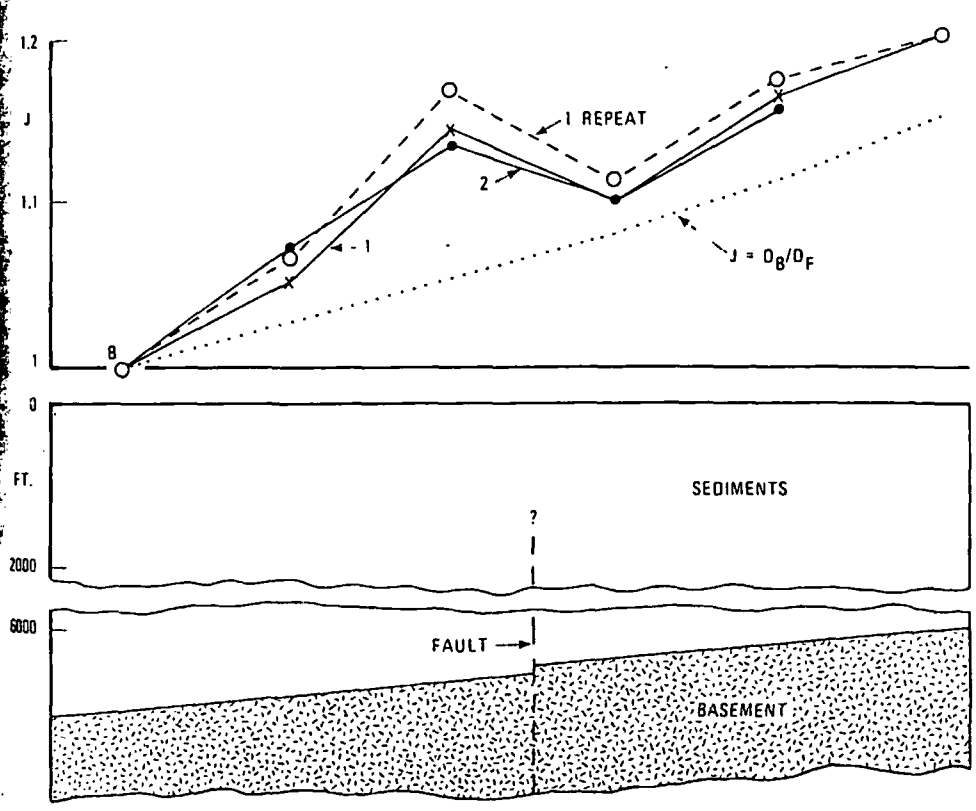

Fig. 10. A telluric anomaly obtained by the split-spread method, over a fault. Subsurface information came from seismic and well log data. Profiles 1 and 2 are 1 mi. apart. The dotted curve would have been obtained if the sediments were homogeneous and isotropic.

Figure 10 shows two telluric profiles over a fault. The subsurface information comes from detailed seismic and drilling data. The sedimentary section (under flat farmland) consists of gently dipping formations that include no major discrete resistivity layers. The effective resistivity is about 4 ohm-m. The telluric data were obtained by means of split-spread measurements. Profiles 1 and 2 are 1 mi. apart. A band-pass filter peaked at T = 20 sec was used. The repeat of Profile 1 was obtained at a different time and by different instrumentation than the other two profiles, to check repeatability.

The anomaly associated with the fault would have probably been within experimental error for another telluric method. It corresponds to Fig. 9b, "faulted stack". Constructing a model of this subsurface is practically impossible from well logs that could quantitatively account for this anomaly. This is because all of the microscopic and macroscopic properties of the sedimentary section enter into the picture. One has to consider this anomaly as a "signature" and be satisfied with it.

In Fig. 10 the regional rise in J to the right is primarily due to rising base-

ment. This corresponds to Fig. 8c, "basement structure". If the sedimentary section was homogeneous and isotropic, one would obtain the dotted curve; this will be explained under Approximate Interpretation. The steeper rise in J is due to increasing resistivity to the right, toward the basin margin.

The telluric anomaly shown in Fig. 11 was obtained over the Haynesville piercement salt dome in Texas (Boissonnas and Leonardon, 1948). The depth to the salt top is about 1200 ft. The salt outline near the top is shown by the dashed contour. This anomaly corresponds to Fig. 8a, "salt structure". It will be analyzed under Quantitative Interpretation.

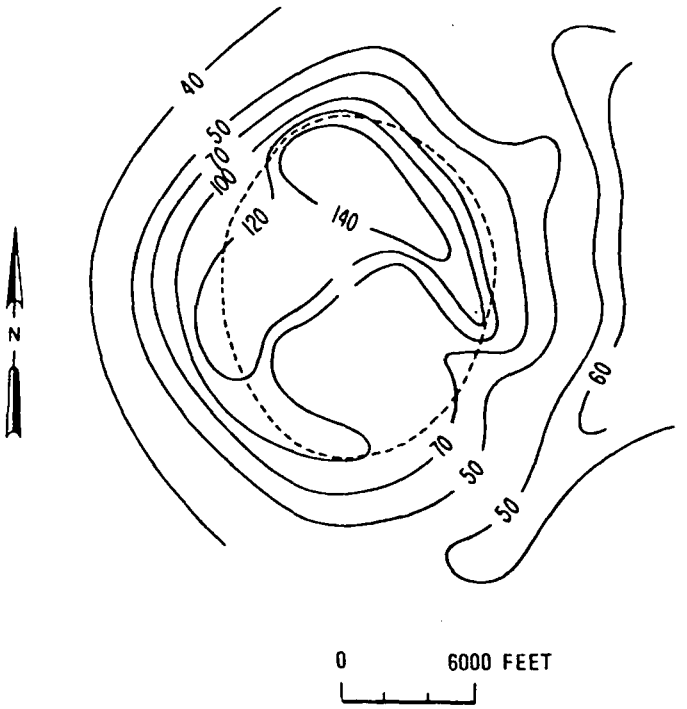

Fig. 11. Telluric anomaly map (J-contours), Haynesville piercement salt dome, Texas. (Modified from Boissonnas and Leonardon, 1948.)

Figure 12 is a telluric anomaly map of an area in the Midland Basin, Texas, comprising three major, isolated, known, and deeply buried reefs (Yungul et al., 1973). These are the Millican (M), Jameson (J), and IAB Reefs. The data were obtained mostly by the vectogram and partly by the split-spread methods. Only the vectogram stations, 287 of them, are indicated on the map, by heavy dots.

Figure 13 is an east—west cross-section and J-profile across the Millican Reef, showing the results of quantitative interpretation (as will be explained in the section so named). The numbers in the resistivity zones are the resistivity ratios. The known reefs are geographically associated with large telluric

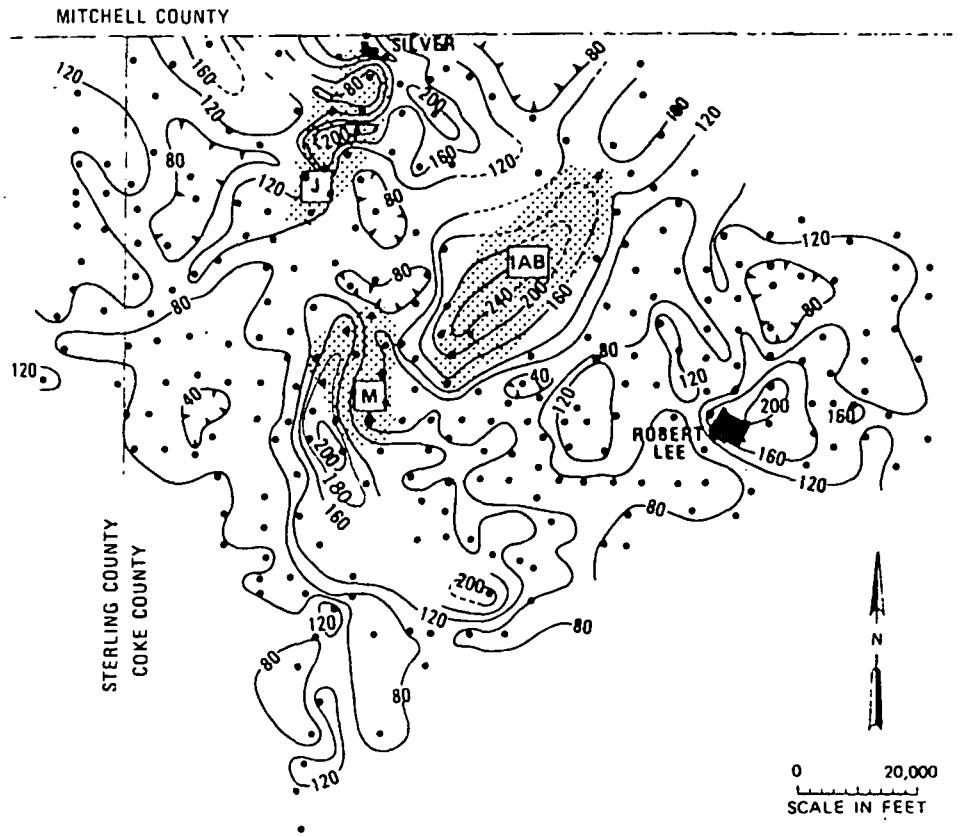

Fig. 12. Telluric anomaly map (*J*-contours), Midland Basin, Texas. Stippled areas show the known producing reef buildups: Jameson (J), IAB, and Millican (M). (Modified from Yungul et al., 1973.)

highs. However, the cause of these anomalies is lateral variation in resistivity within the post-reef sediments, which seem to be ordinary "layer-cake" types on the basis of extensive drill data. This anomaly is somewhat of the type of Fig. 9c, "interfingering". The effect of the reef mass on this very large anomaly is negligible.

Finally, Fig. 14, a classical example of a detail telluric survey, was done in the Aquitania Basin, southern France (Migaux, 1946). This is a detailed portion of a reconnaissance survey of a large area. Telluric stations are shown as heavy dots. The relative-ellipse method was used. An anticline lies unconformably under a horizontal section several hundreds of meters thick.

The subcrop of a limestone layer in the anticline creates "cuesta" type minor low and high telluric anomaly belts around the apex of the domal portion of the anticline, as shown by dotted and dashed lines, respectively. The anticline is represented by a telluric high that corresponds to a combination of Fig. 8d, "macro-anisotropy", and Fig. 9d, "micro-anisotropy".

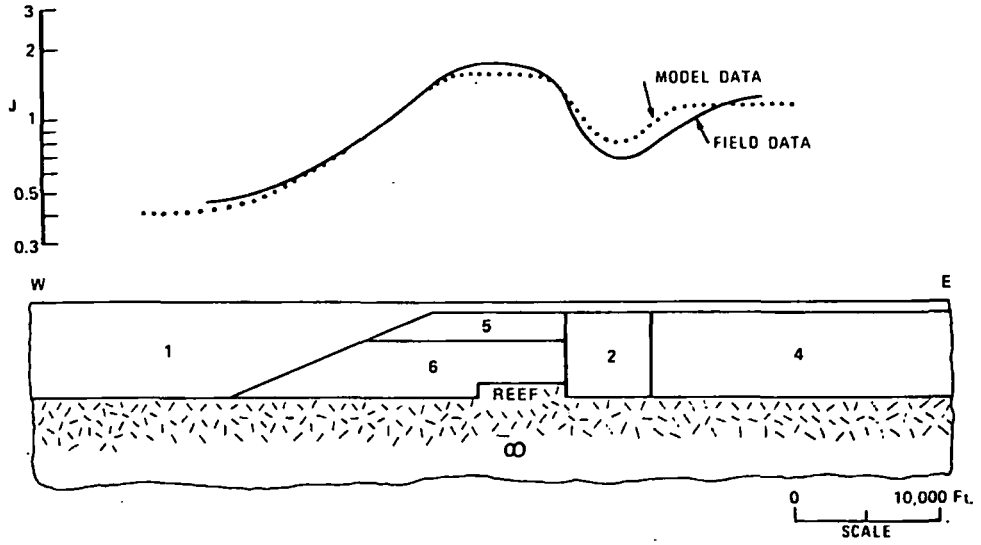

Fig. 13. Two-dimensional model of the Millican Reef, Midland Basin, Texas, east—west cross-section, and the theoretical (model) and actual (field) telluric data. The model resistivities are indicated as resistivity ratios. Resistivities in ohm-m are 7 times these ratios. Analog modeling with conducting paper and numerical modeling yielded practically the same results. (Reproduced from Yungul et al., 1973.)

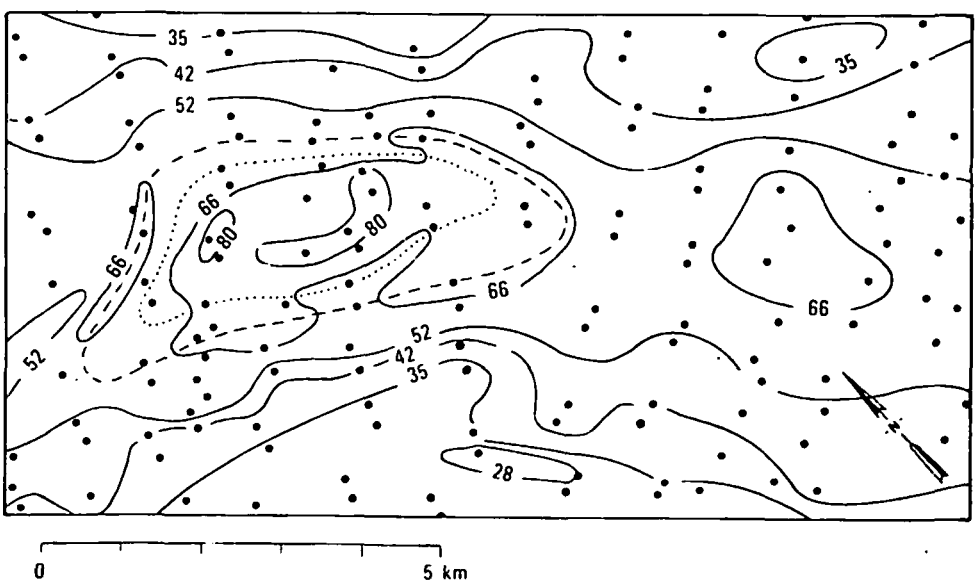

Fig. 14. Telluric anomaly map (J-contours) of an area in the Aquitania Basin, France, over the domal part of an anticline. The dotted and dashed curves are the minor low and high axes respectively, associated with a limestone subcrop. (Modified from Migaux, 1946.)

The limestone subcrop that creates the cuesta type anomaly constitutes another model type that is not included in Figs. 8 and 9. Here again, it would be extremely difficult to model this subsurface for quantitative interpretation, primarily due to the micro-anisotropy dependence.

Approximate interpretation

Smooth structures with low relief, and no high-resistivity "screening" layers within the sediments produce simple relationships between J and either the total horizontal conductance, S, of the sediments above basement, or depth, D, to basement.

For an arbitrary two-dimensional subsurface whose strike is in the y-direction, we have seen that:

$$J_F = E_{xF}/E_{xB} \tag{16}$$

and that H_y is the same everywhere at the surface. It follows that:

$$J_F = Z_{xyF}/Z_{xyB} = [\rho_{\perp F}/\rho_{\perp B}]^{1/2} \tag{17}$$

where Z_{xy} is the MT impedance obtained from E_x and H_y, and $\rho_\perp$ is the MT transverse apparent resistivity.

If it is assumed that B and F are away from abrupt lateral changes in the geology and overlie nearly horizontal layers, although in different sequences, we have, according to eq. 5:

$$Z_B = 1/S_B, \qquad Z_F = 1/S_F,$$

in the MKS system. Therefore, eq. 17 takes the following form:

$$J_F = S_B/S_F \tag{18}$$

where, as defined by eq. 3:

$$S = D/\rho_e$$

Therefore:

$$J_F = \frac{D_B}{D_F}\,\frac{\rho_{eF}}{\rho_{eB}} \tag{19}$$

If the structures are smooth and of low relief, even though three-dimensional, eq. 19 holds so long as stations are away from abrupt lateral changes. Another limitation is that there should be no high-resistivity screening inclusions in the sedimentary section, such as evaporite and carbonate layers of appreciable thickness. Such a layer accentuates the telluric effect of the section above it at the expense of that below (see Fig. 8d).

Equation 18 was derived by Migaux (1951), but the above derivation is similar to that of Berdichevskii (1960, p. 38–42).

Returning to eq. 18, if S_B is known, then J's can be converted into an S-map. Evidently this does not resolve D and ρ_e separately. However, if ρ_e's

are obtained at some locations by means of dipole or MT soundings or well logs, J's can be converted directly to D's. This requires empirically modified forms of eq. 18, from a statistical relationship between J's and sounding data. Berdichevskii (1960, p. 197–204) demonstrates the usefulness of such relationships in several case histories involving basin evaluation.

With reference to eq. 19, if ρ_e remains approximately the same in a region, then:

$$J_F = D_B / D_F. \tag{20}$$

This is how the dotted curve in Fig. 10 was obtained. Obviously ρ_e increases toward the basin margin, and eq. 20 does not hold quantitatively in this case.

The much publicized approximate interpretation techniques described above are too restrictive and yield crude quantitative information at best, unless they are combined with an adequate amount of sounding data. They cannot be used at all for interpretation of abrupt lateral discontinuities such as those in Fig. 13. These, as well as broad structure anomalies, can be interpreted by quantitative modeling, discussed next.

Quantitative interpretation

Quantitative interpretation is done by determining a theoretical telluric anomaly due to an assumed subsurface model (by means of analog or scale modeling, or by numerical or analytic methods). This model is modified until the theoretical anomaly matches the field measurements, which is called "the forward problem" procedure in geophysical terminology. Going directly from the measurements to the model by imposing some constraints on the model type, is called the "inverse problem" or "inversion".

Telluric interpretation at present is practically confined to the forward problem. With the exception of scale modeling, it is also confined to two-dimensional structures. The inverse problems and three-dimensional numerical methods constitute research projects at various organizations at present. MT model calculations also yield telluric anomalies for these models. However, since telluric anomalies represent the dc case, simpler solutions can be found for them by either experimental modeling (analog or scale modeling) or calculations.

With the dc assumption, telluric current flow is governed by Ohm's law:

$$\mathrm{i} = \mathrm{E}/\rho, \tag{21}$$

where i is the current density. This leads to Laplace's equation:

$$\nabla^2 V = 0 \tag{22}$$

where V is the electric potential of which E is the gradient. The subsurface model is confined between two half-spaces of infinite resistivity, namely the air and basement. The source is a primary uniform horizontal E. A solution of Laplace's equation that satisfies the boundary conditions of the model yields E (x, y), from which J-maps can be constructed. However, a straight-

forward analytical procedure is not practical, and recourse is made to mathematical "tricks" even for extremely simple models. Two early and significant papers of this nature are due to Baranov (1951), and Kunetz and Chastenet de Géry (1956).

Baranov's (1951) method deals with a two-dimensional basement configuration of arbitrary shape. The sedimentary section is homogeneous and isotropic. Starting with the current density at the surface (obtained from J's and assumed resistivity for the sediments), current lines are constructed in the subsurface by making use of Hermite polynomials. Any one of these current lines can constitute the solution, namely the top of the basement. Evidently this is a method of solving the inverse problem.

The method developed by Kunetz and Chastenet de Géry (1956) is applicable to the calculation of telluric anomalies due to a large number of two-dimensional structures. These are formed by two or more homogeneous media separated by surfaces of various shapes. The method uses the technique of conformal transformation.

These papers and many others now have historical value, in view of the developments in MT numerical calculations that we shall discuss later.

Experimental modeling

The only practical technique for three-dimensional interpretation now seems to be scale modeling in electrolytic tanks in which the surface of the electrolyte represents the surface of the earth. Utzmann (1954) describes in detail the instrumentation and the techniques of constructing the models and making the measurements for the case of instantaneous dc, although an alternating current source is used.

MT scale modeling facilities can also be used to determine telluric anomalies, but such systems have additional constrictions not necessary for telluric measurements. A review of MT scale modeling methods is given by Dosso (1973).

In certain cases master curves can be obtained by scale modeling for use in interpreting anomalies due to a certain type of model but for a wide range of geometric parameters. Such a case follows.

A piercement salt dome was modeled by an upright circular paraffin cylinder, placed on the tank bottom, which represented the basement. The electrolyte represented the sediments. The ratio of salt to sediment resistivity is practically infinite in this model. In reality (such as on the Gulf Coast) this is of the order of 1000, but whether it is 1000 or ∞ makes no appreciable difference in the results.

Even this simple model does not lend itself to analytic calculations. Three models were constructed for different ratios of salt height, h, to diameter, d, and telluric anomalies for each one were measured for several depths, z, to the top. The results were compiled in the form of master curves, as shown in Fig. 15. The solid curves represent maximum J's, which occur over the cylinder axis, as a function of depth-to-diameter ratio, z/d, for three dif-

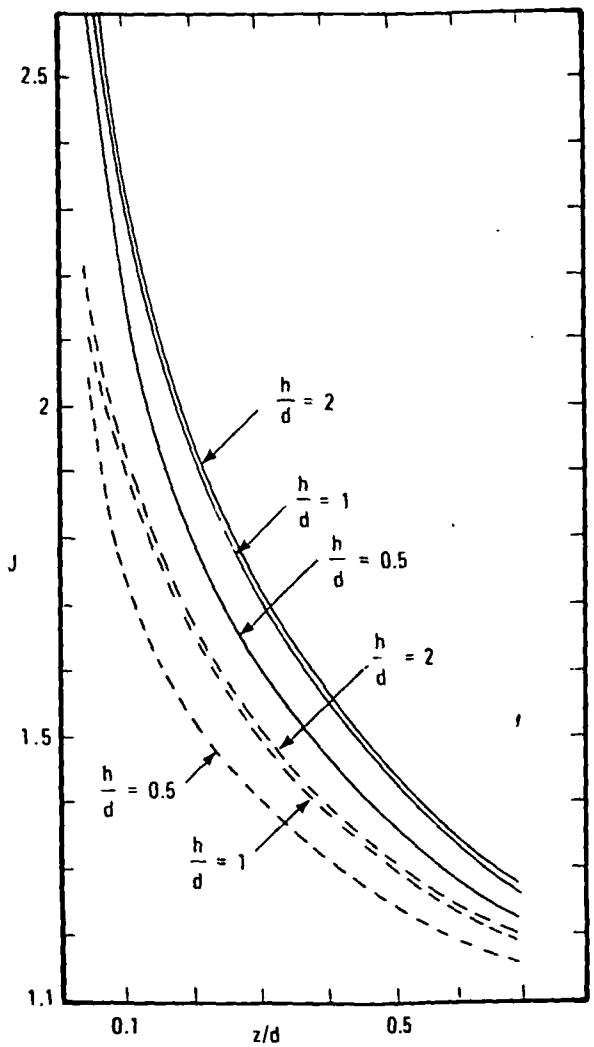

Fig. 15. Master curves for telluric anomalies due to an insulating upright circular cylinder, compiled from electrolytic tank scale modeling. The cylinder, resting on the tank bottom, represents a piercement salt dome. d is diameter, h is height, and z is depth to the top. Solid curves are maximum anomalies over the axis, and dashed curves are the anomalies at one radius from the axis.

ferent models characterized by heigh-to-diameter ratios, h/d. Similarly, the dashed curves are J's above the salt edge, that is, one radius away from the axis.

Interestingly, the curves are practically the same for models for which the heigh-to-diameter ratio, h/d, is equal to or larger than unity: a condition that applies to the piercement domes in the Gulf Coast area in general. Therefore, one solid curve and one dashed curve, say for $h/d = 2$, will suffice to interpret domes of all geometric parameters so long as $(h/d) \geqslant 1$.

Let us apply this to the interpretation of the anomaly shown in Fig. 11. If the J-contours are smoothed and normalized to the nonanomalous region and an average radial representative of the anomaly is obtained (not shown), the maximum J at the center is 2.4. This yields $(z/d) = 0.095$ from the solid curve for $(h/d) = 2$, and $J = 1.96$ over the edge from the corresponding dashed curve. On the telluric anomaly, $J = 1.96$ corresponds to a diameter of 14,500 ft. Therefore, the depth is 1,380 ft. According to the map given by Boissonnas and Leonardon (1948), the drill data indicates an average diameter of about 13,800 ft near the top, and an average depth of 1,200 ft. The interpreted depth and diameter figures are satisfactorily close to the actual data.

Apparently the anomaly of Fig. 11 was obtained by using signals whose periods were shorter than the S zone would require at Haynesville, Texas, if the total sedimentary section is considered. On the other hand, the curves of Fig. 15 are for the dc case (the S zone). Nevertheless, the interpretation results are good. This is because the anomaly is not sensitive to the entire height of the salt stock, as evinced from the h/d independence of the scale-model data. All that matters in this case is that enough of the salt stock lies within the depth of penetration, say within less than a skin depth. Evidently this example shows that quantitatively significant telluric data can be obtained even for periods shorter than those in the S zone.

Conductive paper modeling for two-dimensional structures is probably the most practical approach for occasional interpreters who do not have ready access to MT numerical modeling programs. The paper represents a vertical cross-section. The upper edge represents the air and the lower edge the basement. A uniform dc electric field at the left and right extreme edges is applied by means of strips of aluminum foil cemented with a silver paint to the edges. The electric field along the upper edge is measured by means of a high-impedance voltmeter having a two-electrode probe.

Finite resistivity ratios within the sediments can be obtained by stacking several layers of paper or by punching holes in regular patterns. Stacking allows a decrease in two-dimensional resistivity (in ohms per square) down to a factor of about 0.1. Punching holes allows an increase up to a factor of about 10. The stacking is effective only if the model is pressed under an insulated plate to about 0.25 lb/sq in.

Some conductive papers manufactured by telegraph companies for use in teleprinters are satisfactory. They usually have some anisotropy; resistivity is higher across the roll of paper than along it; but the results can easily be corrected mathematically.

The modeling results shown in Fig. 13 were done with conductive paper. Results with numerical MT modeling were practically the same.

Numerical modeling

Numerical two-dimensional telluric modeling consists of computing E_1's, normalized to a non-anomalous location where the subsurface is horizon-

tally layered, for the frequency with which telluric data had been measured. This constitutes one of the outputs of MT modeling computer programs. Normalized E_1's are equal to J's if the frequency is within the S zone, as shown by eq. 16. Obviously this requires that the model be in terms of resistivity values and not resistivity ratios.

We have seen that the S zone comprises a broad band of frequencies. According to the law of electromagnetic similitude, resistivity and frequency can be changed so long as their ratio is kept constant. Consequently, telluric modeling results will remain practically the same for a wide range of resistivities and frequencies so long as the resistivity ratios are correct.

As mentioned above, the model data shown in Fig. 13 represent numeric as well as paper modeling. The theoretical telluric and MT data shown in Fig. 1 also were obtained by numerical modeling.

The published two-dimensional numerical MT modeling methods fall into three main types: (1) transmission line analogy; (2) finite difference; and (3) finite element. These methods are extensively reviewed by Ward et al. (1973). The listing of a FORTRAN IV program using the finite-difference method was published by Jones and Pascoe (1971). Recent progress in numerical MT modeling is reviewed by Praus (1975).

REFERENCES

Baranov, V., 1951. Quantitative interpretation of measurements in prospecting by telluric currents. Proc., Third World Petroleum Congress. The Hague, Section 1: 646—653 (in French).

Berdichevskii, M.N., 1960. Electrical Surveying by Means of Telluric Currents. Gostoptekhizdat, Moscow. (English translation by Bradley, J.E.S., 1963, Boston Spa, England, National Lending Library, 141 pages; also by Keller, G.V., 1965, Quarterly of the Colorado School of Mines, v. 60, no. 1, 216 pages. Referenced pages are those of Keller's translation.)

Boissonnas, E. and Leonardon, E.G., 1948. Geophysical exploration by telluric currents, with special reference to a survey of the Haynesville salt dome, Wood County, Texas. Geophysics, 13: 387—403.

Cagniard, L., 1953. Basic theory of the magneto-telluric method of geophysical prospecting. Geophysics, 18: 605—635.

Cantwell, T., 1960. Detection and Analysis of Low-Frequency Magnetotelluric Signals. Ph. D. thesis, Massachussets Institute of Technology, 170 pp.

Crews, G.A., 1972. The Feasibility of Detecting Lithologic Variations Using a Modified Magnetotelluric Method. M. S. thesis, The University of Oklahoma.

Dahlberg, R.S., Jr., 1945. An investigation of natural earth currents. Geophysics, 10: 494—506.

Dosso, H.W., 1973. A review of analogue model studies of the coast effect. Phys. Earth Planet. Inter., 7: 294—302.

Gugunava, G.E. and Chernyavskii, G.A., 1964. The use of absolute ellipses in analysis of variations of the earth's natural electromagnetic field. Bull. Acad. Sci. USSR, Geophys. Ser., 7: 642.

Hermance, J.F. and Thayer, R.E., 1975. The telluric—magnetotelluric method. Geophysics, 40: 664—668.

Hughes, W.J., 1974. The polarization of micropulsations and geo-electric structure. Geophys. J.R. Astron. Soc., 38: 95—117.

Jacobs, J.A., 1970. Geomagnetic Micropulsations. Springer, New York, 179 pp.
Jones, F.W. and Pascoe, L. J., 1971. A general computer program to determine the perturbation of alternating electric currents in a two-dimensional model of a region of uniform conductivity with an embedded inhomogeneity. Geophys. J.R. Astron. Soc., 24 (1): 3—30.
Kunetz, G., 1952a. Method for the electrical investigation of the ground. U.S. Patent 2, 586,667; app. 1946.
Kunetz, G., 1952b. Method for the electric prospection of the subsoil. U.S. Patent 2, 623,097; app. 1947.
Kunetz, G., 1957. Application of statistical properties of earth currents in practical geophysics. Freiberg. Forschungsh., C32, Geophysik, p. 5—19 (in German).
Kunetz, G., 1958. Principles and applications of telluric prospecting. Erdöl-Z., Heft 9, Urban-Verlag, Hamburg, p. 3—15 (in German).
Kunetz, G. and Chastenet de Géry, J., 1956. Conformal representation and various problems of potential in media of different "permeability" (electrical conductivity). Rev. Inst. Fr. Pet., 11 (10): 1179—1192 (in French).
Maas, J.P., 1975. Telluric mapping over the Mesa geothermal anomaly, Imperial Valley, California. Presented at the SEG Pacific Section Meeting held in Long Beach, California, 1975.
Madden, T. and Nelson, P., 1964. A defense of Cagniard's magnetotelluric method. Massachusetts Institute of Technology, Geophysics Laboratory, Project NR-371-401.
Migaux, L., 1946. A new method of applied geophysics — prospecting by telluric currents. Ann. Géophys., 2: 131—146 (in French).
Migaux, L., 1951. Ten years of application of the telluric methods. Third World Petroleum Congress, The Hague Proceedings, Section 1: 624—645 (in French).
Morrison, H.F., Beyer, H., Clymer, R. and Lee, K.H., 1975. Telluric current exploration for geothermal reservoirs. Presented at the SEG Pacific Section Meeting held in Long Beach, California, 1975.
Neuenschwander, E.F. and Metcalf, D.F., 1942. A study of electrical earth-noise. Geophysics, 7: 69—77.
Orr, D., 1973. Magnetic pulsations within the magnetosphere — A review. J. Atmos. Terr. Phys., 35: 1—50.
Porstendorfer, G., 1975. Principles of Magneto-Telluric Prospecting. Borntraeger, Berlin-West, 118 pp.
Praus, O., 1975. Numerical and analogue modeling of induction effects in laterally non-uniform conductors. Phys. Earth Planet. Inter., 10: 262—270.
Schlumberger, M., 1936. Method for prospecting the undersoil. U.S. Patent 2,034,447; app. 1934.
Schlumberger, M., 1941. Method and apparatus for electrical underground prospecting. U.S. Patent 2,240,520; app. 1939.
Srivastava, S.P., 1965. Method of interpretation of magnetotelluric data when source field is considered. J. Geophys. Res., 70: 945—954.
Thieme, H.G., 1963. Problems and Successes of the Telluric Methods During the Investigation of High-Resistivity Anticline Structures in GDR. Dtsch. Verl. für Grundstoff-Industrie, Leipzig, 126 pp (in German).
Tikhonov, A.N., Chetayev, D.N., Morgunov, V.A., Chantladze, I.K., Shamanin, S.V. and Gerasimovich, Ye. A., 1974. Magnetotelluric study of the earth's crust. Dokl. Akad Nauk SSSR, Earth Sci. Sect., 217: 28—30.
Tkachev, G.N., 1963. Processing of tellurograms by the method of true ellipses. Geol. Geophys., Acad. Sci., USSR, 11: 114—120 (in Russian). (English translation: Defense Documentation Center, USA, AD 637-062.)
Utzmann, R., 1954. Electrical and telluric prospecting studies on scale models. Bull., Assoc. Fr. Tech. Pét., 107: 1—61 (in French).

Vozoff, K., 1972. The magnetotelluric method in the exploration of sedimentary basins. Geophysics, 37: 98—141.

Ward, S.H., Peeples, W.J. and Ryu, J., 1973. Analysis of geoelectromagnetic data. In: B.A. Bolt, B. Alder, S. Fernback, and M. Rotenberg (Editors), Methods in Computational Physics. Academic Press, New York, pp. 163—238.

Y-Shu, L., 1963. Calculating the parameters used in telluric current prospecting. Geophysics, 28: 482—485.

Yungul, S.H., 1961. Time variations of the ellipticity and preferred direction of the Pc telluric field. J. Geophys. Res., 66: 557—561.

Yungul, S.H., 1965. Telluric current method of determining ellipse area with a collinear three-electrode array. U.S. Patent, 3.188,559, app. 1961.

Yungul, S.H., 1966. Telluric sounding — a magnetotelluric method without magnetic measurements. Geophysics, 31: 185—191.

Yungul, S.H., 1967. Method for the determination of direction of effective strike and dip from telluric potentials utilizing a T-spread quadruple electrode array. U.S. Patent 3,309,607; app. 1964.

Yungul, S.H., 1968. Measurement of telluric relative ellipse area by means of vectograms. Geophysics, 38: 127—131.

Yungul, S.H., Hembree, M.R. and Greenhouse, J.P., 1973. Telluric anomalies associated with isolated reefs in the Midland Basin, Texas. Geophysics, 38: 545—556.